COMPUTATIONAL MODELING OF HEAT TRANSFER AND MICROSTRUCTURE DEVELOPMENT IN THE ELECTROSLAG CLADDING HEAT AFFECTED ZONE OF LOW ALLOY STEELS

Mengnie Li

B. E., Tsing Hua University, 1984

M. E., Beijing Institute of Aeronautical Materials, 1987

A thesis submitted to the faculty of the

Oregon Graduate Institute of Science & Technology

in partial fulfillment of the requirements for the degree

Doctor of Philosophy

in

Materials Science and Engineering

January 1996

The dissertation "Computational Modeling of Heat Transfer and Microstructure Development in the Electroslag Cladding Heat Affected Zone of Low Alloy Steels," by Mengnie Li has been examined and approved by the following Examination Committee:

Dr. David G. Atteridge, Dissertation Advisor
Professor

Dr. Lemmy Meekisho
Assistant Professor

Dr. Jack H. Devletian
Professor

Dr. William E. Wood
Professor, Department Chairman

To my family and friends

ACKNOWLEDGEMENT

The author wishes to express his indebtedness to Dr. David G. Atteridge for his invaluable guidance and encouragement throughout the course of this research work. Without his enthusiasm and firm stand for fundamental based modeling, this research work would not have been completed.

Special thanks are due to Prof. John S. Kirkaldy for the inspiration the author has received from his pioneering work and for his critiques on the dissertation. The author is very appreciative to Dr. Lemmy Meekisho for the many useful discussions on numerical analysis, the help in using ANSYS program, and his comments on the dissertation.

The author wishes to thank Dr. Jack H. Devletian and Dr. William E. Wood for their time and effort in evaluating the dissertation.

The author would also like to express his gratitude to the OGI faculty, staff, and fellow students who have made his years of staying at OGI joyful and memorable.

The author is grateful to the financial support provided by the National Center for Excellence in Metal Working Technology (NCEMT). NCEMT is operated by Concurrent Technologies Corporation under contract to the U.S. Navy as part of the U.S. Navy Manufacturing Technology Program.

Finally, but certainly not the least, the author wishes to thank his wife, Xiaoling (Charlene) for her love and support throughout the course of this research.

TABLE OF CONTENTS

LIST OF TABLES

LIST OF FIGURES

ABSTRACT

COMPUTATIONAL MODEL OF HEAT TRANSFER AND MICROSTRUCTURE DEVELOPEMENT IN THE ELECTROSLAG CLADDING HEAT AFFECTED ZONE OF LOW ALLOY STEELS

Mengnie Li, Ph.D

Supervising Professor: David G. Atteridge

The objective of this research work was to predict through modeling the microstructural development and resultant hardness in the heat affected zone of multipass electroslag cladding. Before this study, there were reported successes of using the Watt algorithm for such a purpose. The Watt algorithm is a combination of the austenite grain growth model developed by Ashby and Easterling and the reaction kinetics model for austenite decomposition developed by Kirkaldy and Venugopalan. The resultant hardness was then calculated using the predicted microstructure volume fractions and the rule of mixtures. Hardness of each microstructure constitute was calculated using empirically developed equations. Preliminary studies of this research involved using the Watt algorithm for the predication of Jominy hardness of steels and weld heat affected zone hardness. It was found that the reaction kinetics model for austenite decomposition developed by Kirkaldy and Venugopalan, on which the Watt algorithm was based, gives reasonably accurate predictions for steels with low alloy element additions but underestimates hardenability of steels with medium and high alloy element additions. Modifications were performed in some fundamental aspects of the Kirkaldy-Venugopalan model as well as the Watt algorithm. The new algorithm developed in this research is

an agglomerate of models with optimal balance of theoretical and empirical inputs and is generically applicable to low alloy steels. It embraces a two-dimensional finite element model for analyzing the heat transfer induced by multipass electroslag cladding, rigorous thermodynamics models for the computation of multicomponent Fe-C-M system equilibria, a semi-empirical model for the prediction of prior austenite grain growth, and a new reaction kinetics model for austenite decomposition which is a modification of original model developed by Kirkaldy and Venugopalan. The predicted heat affected zone microstructure and hardness in the heat affected zone of multipass electroslag cladding were found in excellent agreement with the microscopic observations and hardness measurements.

The two-dimensional finite element heat transfer analysis model emphasizes complete analysis of all clad passes in actual sequence and analysis of each pass individually in a synonymous fashion with a single pass weld. This was accomplished by defining a finite element mesh for analyzing each clad pass and remapping the interpass temperature distribution from the previous clad pass onto this new mesh so that the initial temperature distribution could be defined. This methodology is a natural extension of modeling technique for analyzing single pass weld to the analysis of multipass welds. This methodology overcomes the limitations of commonly used lumping techniques in modeling multipass welds. There is no theoretical limit of the number of passes that can be analyzed with this method. The predictions given by this model are in excellent agreement with experimental temperature measurements.

Thermodynamics based models for the computation of multicomponent Fe-C-M system equilibria in low alloy steels were incorporated into the microstructure prediction algorithm for the computation of critical temperatures and phase compositions for phase transformations. They are generically applicable to low alloy steels provided the total alloy addition do not exceed 8 at%. The accuracy of these models in computing Ae_3, Ae_1 and As_1 temperatures compared favorably with experimentally measured results in the literature.

A semi-empirical approach was adopted in this algorithm to model the prior austenite grain growth in the heat affected zone. The pinning effects from carbide and

nitride precipitates are incorporated into the model by the introduction of a modified Ashby-Easterling relationship. The maximum grain size in the heat affected zone was verified by the experimental measurements. Difficulties of using empirical grain growth kinetics equation in modeling austenite grain growth in weld heat affected zones are addressed in this thesis.

The core of this algorithm is the reaction kinetics model for austenite decomposition which was developed by modifying the original Kirkaldy-Venugopalan model. The original Kirkaldy-Venugopalan model was based on modeling time-temperature transformation diagrams. The model presented in this dissertation was calibrated to continuous cooling transformation diagrams and it gives much more reliable predictions to the reaction rates of austenite decomposition under continuous cooling conditions. With the predicted microstructure volume fractions, the resultant hardness was calculated using the rule of mixtures and empirically developed equations for the hardness of microstructure constituents. The reliability of this algorithm was verified with excellent agreement between the computed CCT diagrams and Jominy hardness curves and the experimentally measured ones.

CHAPTER 1
SCOPE OF THE THESIS WORK

1.1 Introduction

Electroslag cladding (ESC) with strip electrode is a unique surfacing technique first developed in 1971 by Seidal in Germany.[1] It is widely used in Europe and Japan because of its characteristics of high deposition rate and low dilution with uniform penetration.[2-6] However, it is just now beginning to enter the United States market.[7] The U.S. Navy is presently sponsoring an ESC technology development and transfer project at the Oregon Graduate Institute of Science & Technology (OGI) directed towards cladding nickel alloys onto carbon steel propulsion shaftings. Figure 1.1 is an illustration of electroslag cladding onto a proper shaft. Experimental studies at OGI[7-10] to date have demonstrated many advantages of strip electroslag cladding over strip submerged arc cladding from both economical and metallurgical perspectives. Economically, electroslag cladding offers higher deposition rate, and thus better cost-effectiveness.[7-9] Metallurgically, electroslag clads have lower dilution and lower inclusion content.[9-10]

Electroslag cladding is essentially a special welding application with high heat input. During the cladding operation, the base metal adjacent to the clad deposit undergoes intensive heating and fast cooling. This zone is referred to as the heat affected zone (HAZ), which is often a critical area due to the formation of undesirable microstructure. The heat affected zone has both an intriguing metallurgical complexity and considerable commercial significance. Mechanical properties of this area are different from, and usually inferior to, those of the base metal. It is the most common region of weld failures, and failures are mostly related directly to the microstructure.

Consequently, predicting the microstructure and mechanical properties in the heat affected zone is one of the most important problems in developing and optimizing a welding process.[11-15]

As with most welding processes, the state of art has been developed mainly by experience and extensive testing, rather than understanding the fundamental science behind it.[16] Mathematical modeling, which presumes the capability of accurate prediction of temperatures, microstructure, stress and strain, and residual deformation, has contributed little, but is anticipated to contribute more, to the understanding and solving of welding associated problems.[16-20] The objective of this study is to develop a numerical model that will predict the transient temperature profile, microstructure development and mechanical properties in the heat affected zone of electroslag cladding based on the known material behavior.

In the following section, a comprehensive literature review is presented on the early attempts in mathematical representation of welding operations, analytical and numerical methods for the heat transfer analysis in welds with special emphasis on finite element analysis models, and microstructure prediction models.

1.2 Literature Review on Welding Analysis

The critical first step in an accurate analysis of the microstructure formation in weld heat affected zone is to know thermal cycles induced by welding operations.[16-20] For the given base metal and filler material, the temperature field largely determines the size and resulting microstructure of the fusion zone and heat affected zone, as well as component residual stress and distortion. The temperature field, together with the chemical composition and transformation kinetics, provides the basis for predicting the microstructure in the heat affected zone. Therefore, predictions of many topics of interest require the knowledge of the transient temperature field during electroslag cladding operations.

Thermal cycles can be measured experimentally by putting thermocouples in the expected heat affect zone before cladding. However, experimental measurement is

difficult for several reasons. First, the location of thermocouples at the required positions in the HAZ must be done by trial and error, and it is only after sectioning and polishing that the true position can be determined accurately. Second, any thermocouple has a finite heat capacity and is of different composition to the base metal. It will itself create a thermal disturbance in the region to be measured. Third, the finite size of the thermocouple means that the measured result is actually some average over a distance of perhaps 0.5 ~ 1.0 mm rather than that related to a particular point in the HAZ. Alberry *et al.*,[21] and Christensen *et al.*[22] have discussed the difficulties encountered in measuring temperature during welding, particularly in interpreting the results. On the other hand, recent developments in mathematical modeling have enabled the heat transfer in real welding situations to be analyzed or simulated accurately, perhaps more accurately and consistently than experimental measurements.

1.2.1 Historical Background

Attempts at mathematical representation of welding operations date back to the 1930's. The failure of welded bridges in Europe in the 1930's and the American Liberty ships in World War II greatly stimulated welding research all over the world. Spraragen and Claussen[23] first reviewed the literature up to 1937 on the temperature distribution during welding. Prior to this date, investigators used different materials in their studies and most of the results were reported for mild steels in the form of maximum temperature distribution curves or cooling curves. Since then, numerous papers appeared on the thermal aspects of arc welding.

In 1943, Hess and his co-workers[24] measured cooling rates in low-carbon steel plates of various thicknesses. The effects of electrode diameter and coating, AC versus DC welding current, chemical composition of the plates, and latent heat of metallurgical transformation were considered. In the same year, Doan and Stout[25] established a correspondence between Jominy end-quench tests and cooling rates, which was previously discussed by Mahla *et al.*[26] in 1941. Also in 1943, Paschkis[27] established cooling curves of plates in the vicinity of welds by means of an analog computer and

postulated modes of heat transfer from the electrode and arc to the plate.

To gain some quantitative appreciation of the way in which the welding variables, weld component geometry and materials physical properties affect the metallurgical transformations in welds, considerable attention was given to the unique heat transfer phenomena associated with the movement of welding heat sources. The mathematics of heat transfer in solid from moving heat sources has been treated in classical works on heat conduction,[28,29] and, with the establishment of certain idealized boundary conditions, conclusions presented can be reasonably applied to the welding.

The solutions were first given by Roberts[30] in 1923, who considered some cases of convection, but they are usually associated with Rosenthal[31,32] for his efforts in developing and introducing the solutions into the welding literature. Boulton and Lance-Martin[33] developed the moving source equation independently and simultaneously with Rosenthal in the mid-1930's. Since then, quite a few analytical models have been suggested which in one way or the other pertain to the Rosenthal solutions. So it was Rosenthal's work which formed the essential basis for experimental and analytical studies to follow. The moving heat source theory reached its maturity with the comprehensive review by Myers *et al.*[34] in 1967. And even today the solutions given by Rosenthal are still the most popular analytical models for calculating temperature/time profile in welds.

1.2.2 Heat Transfer Analysis

Based on the principle of energy conservation, the heat conduction in any continuum is best described by the governing partial differential equation

$$\frac{\partial}{\partial x}(k_x\frac{\partial T}{\partial x})+\frac{\partial}{\partial y}(k_y\frac{\partial T}{\partial y})+\frac{\partial}{\partial z}(k_z\frac{\partial T}{\partial z})+Q=\rho c\frac{\partial T}{\partial t} \qquad (1.1)$$

where Q is the heat source or heat sink (W/m^3), k_X, k_Y, k_Z are thermal conductivities in principal axes x, y, z respectively ($W/m°C$), ρ is the density of material (kg/m^3), and c is the mass specific heat ($J/kg°C$). Most steels can be regarded as homogenous and isotropic continuum. Characteristic values of these materials can be mathematically

represented by $k_X = k_Y = k_Z = k$. If any of the thermal properties, k, ρ, or c is temperature dependent, Equation 1.1 is nonlinear.

On the boundary of the continuum domain Ω, either essential or natural boundary condition must be satisfied. The essential boundary condition is defined as

$$T(x, y, z) = T_S(x, y, z) \tag{1.2}$$

at the boundary S_I. This type of boundary condition prescribes temperature values at the boundary and is also called Dirichlet boundary condition or type I boundary condition in numerical analysis.

Natural boundary condition is defined by prescribing the heat flux, convection and radiation at the outward surface S_{II} of the domain

$$k_n \frac{\partial T_S}{\partial n} + q + h_C(T_S - T_A) + \sigma\varepsilon(T_S^4 - T_A^4) = 0 \tag{1.3}$$

In this equation, k_n is the thermal conductivity normal to the surface (W/m°C), q the prescribed heat flux at the boundary, h_C the film coefficient for convectional heat transfer at the boundary, T_S the surface temperature, T_A the ambient temperature, σ the Stefan-Boltzmann constant for radiative heat transfer, ϵ the thermal emissivity. The third and fourth terms are convective and radiative terms respectively. This type of boundary condition is often referred to as Cauchy boundary condition or type II boundary condition in numerical analysis. If convective coefficient h_C is temperature dependent or if radiation is included, this boundary condition is nonlinear.

In addition to these boundary conditions, the initial temperature conditions must also be specified in a transient analysis for all points in the domain

$$T(x, y, z, 0) = T_0(x, y, z) \tag{1.4}$$

If the partial differential Equation 1.1, the boundary condition Equation 1.2 and Equation 1.3, and the initial condition Equation 1.4 are all consistent, the problem is well posed and a unique solution exists. Solutions for the heat transfer in welds may be obtained from analytical studies based on some idealized simplifications or from numerical analysis.

Analytical Heat Transfer Models

To obtain compact analytical or closed form solutions for the heat conduction equation in welding situations, it is mandatory to simplify the heat source, geometry, boundary conditions and thermal properties. Rosenthal[31,32] argued that an observer moving with the electrode would see no change in temperature profile around him after the initial period of welding, a phenomenon termed as *quasi-steady* state of heat flow with respect to the moving arc. The coordinate system in Equation 1.1 was then transformed to the location of arc and analytical solutions were developed for moving heat source heat conduction problems. In early analytical models, following assumptions were made:

1. The material is solid at all times and at all temperature, no phase changes occur, and is isotropic and homogeneous.
2. The thermal conductivity, density, and specific heat are constant with temperature.
3. There are no heat losses at the boundaries, *i.e.*, the work piece is insulated.
4. The work piece is infinite except in the directions specifically noted.
5. Conditions are steady with time, *i.e.*, in the middle of a long weld, heat input, travel speeds, etc., are steady.
6. The heat source is concentrated in a zero-volume point, line or area.
7. There is no Joule (I^2R electric) heating.

Rosenthal gave the temperature T at a point lying a distance r from the weld line as a function of time t, for a given energy input q/v (q is the net heat input per unit time, and v is the welding speed). Two limiting solutions are presented here: those in an infinitely thick plate with a moving point heat source and those in a thin plate with a moving line heat source. In thick plate butt welds, heat transfer is three-dimensional and the first order solutions for temperature profile, peak temperature T_P and cooling time

between 800 to 500 °C $t_{8/5}$ in the heat affected zone can be expressed by

$$T = T_0 + \frac{q/v}{2\pi kt} \exp(-\frac{r^2}{4at}) \tag{1.5}$$

$$T_P = T_0 + \frac{2q/v}{\pi e\rho c r^2} \tag{1.6}$$

$$t_{8/5} = \frac{q/v}{2\pi k}(\frac{1}{773 - T_0} - \frac{1}{1073 - T_0}) \tag{1.7}$$

where T_0 is the initial temperature of the base metal, and a is the thermal diffusivity defined by $k/\rho c$ in m^2/sec. While in thin plate through-thickness butt welds, heat transfer is essentially lateral and following first order solutions were given:

$$T = T_0 + \frac{q/v}{d\sqrt{4\pi k\rho ct}} \exp(-\frac{r^2}{4at}) \tag{1.8}$$

$$T_P = T_0 + \frac{q/v}{2\sqrt{\pi e} d\rho cr} \tag{1.9}$$

$$t_{8/5} = \frac{(q/vd)^2}{4\pi k\rho c}[\frac{1}{(773 - T_0)^2} - \frac{1}{(1073 - T_0)^2}] \tag{1.10}$$

where d is the plate thickness in meters.

Tanaka[35] solved welding heat flow equation without neglecting surface heat transfer. Owing to surface heat transfer, Tanaka's solution is more complicated than Rosenthal's. However, surface heat transfer must be taken into account in welding heat conduction because it varies from welding process to process; it is very low in submerged arc welding due to covering flux, and is very high in electroslag and electrogas welding due to water cooling. Tanaka also proved that Rosenthal's solution can be derived from his solution. Naka and Masubuchi,[36,37] Masubuchi and Kusuda[38] also assumed line and point heat sources for two-dimensional and three-dimensional analytical solutions. They presented the solutions for the temperature distribution of

welded plates under transient state.

All these models were developed essentially based on the same assumptions and hence provide limited accuracy as they are too idealized to be used in practice. Wells[39] used the two-dimensional line heat source solution to predict the width of the melted zone in butt-welded steel plates. No surface heat loss was assumed and attempt was made to economize the heat input based on the weld size for a consumable electrode so that a flat weld is obtained. Assumptions implied were a constant value of thermal diffusivity and neglect of latent heat. Nippes *et al.*[40,41] found large discrepancies between Rosenthal's equation results and experimental results for cooling rates in the weld heat affected zone. The error became significant in the vicinity of the idealized point heat source.

Adams[42] modified the equations for calculating cooling rates in mild and low alloy steel welds. The major practical use of cooling rate equations is in the calculation of preheat requirements. If the plates are thick, requiring more than 6 passes to complete the joint, the cooling rate V_R can be approximated by:

$$V_R = \frac{2\pi k(T-T_0)^2}{q/v} \tag{1.11}$$

If the plates are thin, requiring fewer than four passes, the cooling rate V_R is then approximated by:

$$V_R = 2\pi k \rho c(\frac{d}{q/v})^2 (T-T_0)^3 \tag{1.12}$$

These equations are widely used in industry because of their simplicity and convenience of computing thermal cycles throughout the weld metal and heat affected zone. A pocket calculator is enough for the calculation. However, the distinction between thick and thin plates is often required because these terms have no absolute meaning. In other words, these solutions represent two extreme situations. Real welds often lie between these two limits, and may have more complex geometries. Jhaveri *et al.*[43] experimentally investigated the effect of plate thickness on heat flow in welds. Their study showed that heat flow is governed not only by the plate thickness, but also by the weld process used and even the type of material. For this reason, they proposed

a dimensionless quantity called "the relative plate thickness," τ, which is a function of material properties, plate thickness, heat input and temperature rise of a point:

$$\tau = d\sqrt{\frac{\rho c(T_C - T_0)}{q/v}} \tag{1.13}$$

Their experimental studies shows that the equations for thick plate applies when τ is greater than 0.9, and the thin plate equations when τ less than 0.6. When τ falls between 0.6 and 0.9, the upper bound of the cooling rate is given by the thick plate equation, and the lower bound by the thin plate equations. If an arbitrary division is set when τ is equal to 0.75, with larger values regarded as thick and smaller as thin, the maximum error may exceed 15% in a cooling rate calculation.

Christensen *et al.*[22] presented a thermal model essentially based on Rosenthal's equation for a point source in three dimension to predict peak temperatures and cooling rates. They established average arc efficiency values for the metal arc, metal inert gas and submerged arc welding processes. They also assumed constant material properties. Grosh *et al.*[44,45] neglected latent heat effect and assumed that thermal conductivity and the product of density and specific heat vary in the same manner with temperature. They solved the heat flow equation in two dimension analytically. Unfortunately this assumption of material behavior has very limited utility, especially with some aluminum alloys. Convection and radiation from the surfaces were also neglected. Kazimirov *et al.*[46] took into consideration linear variation of material properties and also allowed the surface heat losses. On comparison with experimental measurements, their results indicate that including the effect of temperature dependence of thermal conductivity and specific heat results in more accurate temperature distribution than the case when constant material properties are used. However, the assumption that the thermal diffusivity ($a = k/\rho c$) remains constant at all temperatures was made which is not true for most materials.

The accuracy of the analytical solutions is often called into question due to many assumptions made in the models, particularly of the point heat source and constant thermal properties. Nevertheless, these methods have provided a foundation for the

numerical methods that can take into account the nonlinearity involved in the process and provide a practical solution. Closed-form solutions are economical and useful for parametric study to get a general idea of behavior of processes.

Of the recent work in analytical models, the most interesting appears to be the incorporation of a diffuse or finite size heat source rather point heat sources.[47-51] These models are in the form of series which have the potential to improve the accuracy by increasing the number of terms to be evaluated. However, it is very sophisticated and not easy to compute thermal cycles using this method because of the number of terms to be evaluated and integrated. Meanwhile these models are still limited due to their reliance on constant thermal properties and they don't account for the convective and radiative heat losses. All these factors greatly complicate the heat flow equations and make the analytical solutions virtually impossible. Numerical techniques, on the other hand, can handle these situations without difficulty.

Numerical Heat Transfer Models

Numerical models in principle permit nearly any complexity to be taken into account although economic requirements set a limit in practical terms.[18] With the advancement in computer technology, most of the simplifying assumptions used in developing analytical solutions can be eliminated. Heat flow in welds can be analyzed more economically by computational weld mechanics than conducting experiments.

Finite difference, finite element, and boundary element analyses are the three strong candidates of numerical analysis. In the decade of mid-1960's to mid-1970's, finite element and finite difference methods were competing with each other. In 1973, Bonacina *et al.*[52,53] developed a finite difference model to solve non-linear heat conduction problems. They included variable material properties and phase change effects. In 1974, Comini *et al.*[54] included successfully nonlinear material properties and latent heat effects in their finite element model. Latent heat effect was incorporated as variation in heat capacity. Kohler *et al.*[55] reported a better stability of the solution for transient temperature field problems with finite element discretization of time. A

comparison in terms of accuracy, stability and computational cost of different numerical schemes for the finite element and finite difference methods in two-dimensional heat conduction problems was done by Thomas *et al.*[56]

Westby[57] was probably the first one who computed the temperature distribution in welds using finite difference method. He assumed that the weld energy was distributed throughout the molten zone with a constant power density. Pavelic *et al.*[58] also used finite difference method to compute temperature histories in gas tungsten arc welding of thin plates and compared with experimental data. But they modeled the welding heat source as a flux disc with Gaussian distribution. Provision was also made for inclusion of convective and radiative losses from the heat plate to the surroundings as well as variable properties of the metal. Much better agreement was obtained between experimental measurements and numerical computations than analytical models. In 1974, Parley and Hibbert[59] added several capabilities to Westby's finite difference model. They analyzed non-rectangular cross sections such as single and double V and U grooves in welding practice using non-uniform mesh. The welding heat source was simulated by designating one or more elements as heated elements with Gaussian distribution of heat flux. The model included temperature dependent material properties but failed to incorporate the heat loss from boundaries.

Much of the recent research in modeling and simulating arc welding processes involved finite element analysis (FEA). With FEA, the nonlinear features caused by the material properties as well as boundary conditions can be easily included in the computational models. Geometric complexity can also be easily included in the FEA solutions. Detailed aspects of heat transfer can be obtained through FEA because it can incorporate more details of the heat source, such as power density distribution, temperature dependent thermal properties, and nonlinear boundary conditions. In 1973, Hibbitt and Marcal[60] extended their finite element analysis to a complete thermal stress analysis for gas metal arc welding. The filler metal was added in steps at the end of the time interval and an intimate contact condition was assumed so that the interface of the base metal elements and filler metal elements attain a common temperature at the end of the time interval. Temperature dependent material properties, convective and radiative

heat losses and effect of latent heat by increasing the specific heat in the mushy zone were incorporated in the finite element analysis. The heat input was idealized as a linear increase from zero to a maximum value followed by a linear decrease to zero during the interval. The temperature history obtained from this uncoupled heat transfer analysis was later used as input to the stress analysis.

Based on the model developed by Hibbitt and Marcal,[60] Friedman[61] developed a two-dimensional thermomechanical model using finite element method for gas tungsten arc welding in 1975. The heat input distribution was modeled more realistically by a Gaussian distribution. In his later work, the latent heat was more accurately accounted for in each time step of the analysis.[62] In the mean time, Glickstein *et al.*[63] conducted extensive experimental parametric study of the effects of welding current, arc gap, torch speed, shielding gas and electrode shape on the width, depth and area of the weld bead of the nickel alloy 600. The data were used for comparison with computational predictions and for identifying the areas in which improvements could be made. They reported the need for including the effects of surface tension, arc pressure and the electro-magnetic Lorentz force in the weld pool mechanics.

Friedman and Glickstein[64] showed that the finite element welding thermal analysis is well suited to determine the response of the magnitude, distribution and duration of heat input in welds. Stationary gas tungsten arc welds were made on alloy 600 and good agreement between numerical prediction and thermocouple measurements of temperature histories at points outside the fusion zone and heat affected zone was obtained. Then Friedman[65] improved his previous model[61] by including the effect of weld puddle distortion. He examined the finite element heat conduction solution at the end of each time step and then included the effect of arc pressure and surface tension by allowing the nodes at temperatures above liquidus to move. He conducted the heat transfer analysis on deformed geometry of the weld pool. He found significant effects of weld pool distortion on weld penetration. Higher the arc pressure, earlier is the full weld penetration achieved in the gas tungsten arc welds. The model, however, was based on an axisymmetric geometry due to the stationary arc and the results are not necessarily true for a moving arc. Convective motion in the weld pool and the effect of

electromagnetic forces were not included in the model. Surface tension was considered only between liquid and atmosphere but it was ignored at the solid-liquid interface.

From a metallurgical perspective, Krutz and Segerlind[66] developed an approach to optimize a gas tungsten arc welding process with a two-dimensional finite element model. They first computed temperature distribution as a function of location and time. Then they used the empirical correlations between cooling rate and microstructure previously developed by Inagaki[67] to acquire optimum joint toughness and hardness. Welding parameters were then varied to obtain the desired cooling rate. The welding heat input was modeled with a Gaussian profile. Surface heat losses and latent heat effect were considered. The model, however, did not model the melting and addition of filler metal because of difficulty in element modeling.

Andersson[68] analyzed the thermal stresses in a submerged-arc weld considering the effects of phase transformation. The material was elasto-plastic with temperature dependent properties. The heating effect of the arc was modeled as a prescribed flux. Thermal stresses were not computed above some cut-off temperature.

In 1980's, Karlsson[69] analyzed the residual stress in welding large plates including the effects of tack welds. Argyris *et al.*[70,71] performed a visco-plastic stress analysis of a weld. They first performed an in-plane thermal analysis and then they coupled this with a cross-sectional thermal analysis and a plane strain stress analysis. Goldak *et al.*[72] published the first three-dimensional coupled temperature and stress analysis of a weld. Karlsson *et al.*[73] analyzed the stresses in a girth pipe weld also using a full three dimension transient analysis, coupling temperature and stress. Using shell elements, Lindgres and Karlsson[74] also analyzed the residual stress in the girth weld of a pipe. In all these models, the melting and addition of filler metal were treated in a simple way which assumes that the filler metal is in place at the start of the analysis and welding heat source is applied to remelt it.

Tekriwal and Mazumder[75] modeled the addition of filler metal in gas metal arc welding. Basically, the added metal was included in the original mesh. To add the metal the elements are turned on with a commonly used "birth and death" method in the finite element formulation. They assigned an initial temperature of 2300 °K (550 °K

above the melting point of the electrode) as the droplet temperature. Apparently, a part of the heat input from welding heat source is consumed to melt and superheat the filler metal electrode, thus it must be appropriately accounted. This method is a natural approach to simulate the physical process of welding.

Welding Heat Source Models

A significant advantage of finite element analysis is that the welding heat source can be diffuse or distributed in stead of being overly simplified as a point or a line assumed in deriving analytical solutions.[76] This has brought the heat transfer analysis closer to the reality of welding operation. However, a problem that emerged is how to model the welding heat source. Obviously, the accuracy of the heat source model largely determines the accuracy of the computed thermal cycles. The best heat source model depends on the analysts' point of view, knowledge and available resources.[77]

Early experimental measurements of stationary arcs in 1950's suggested a Gaussian distribution of energy.[22,78-80] Rykalin[81,82] dedicated two books to welding heat sources. Pavelic *et al.*[58] first incorporated distributed heat source into numerical analysis. In their approach, the heat from a welding arc is, at any given time, assumed to be deposited on the surface of weldment as a radially symmetric Gaussian distribution function. This flux disc model was followed by Friedman,[61-65] Krutz and Segerlind,[66] Andersson,[68] and many others.[69,73-75,83] Argyris *et al.*[70,71] modified the shape of the flux disc to be ellipsoidal with Gaussian distribution. In these works, significantly better temperature distributions in the fusion and heat affected zones were achieved than those computed with Rosenthal model. This model is certainly a significant step forward in modeling the welding heat source. However, the digging effect of the arc was not well incorporated.

A more comprehensive review of arc physics and weld molten pool behavior can be found in Lancaster's book.[84] In 1971, Wood and Milner[85] attempted to delineate the fluid motion in the weld pool of arc welding by introducing the concept of liquid phase convection. They found that the welding molten pool is stirred intensively. The models

proposed by Dilawari, Eagar, and Szekely[86,87] in 1978 and by Atthey[88] in 1980 are a notable advance. Oreper, Eagar, and Szekely[89,90] found that the convective motion in weld pool is driven by the combination of surface tension, electro-magnetic Lorentz forces and buoyancy forces. These initial efforts stimulated a great deal of interest and by the mid-1980's numerous elegant papers dealing with weld pool convection in two and three dimensions[91-101] have been presented.

Thus a rigorous analysis of all the heat transfer mechanisms would require solving the coupled equations of arc magneto-dynamics, fluid mechanics, and heat transfer. However, the method for attacking these problems hasn't been well established yet.[102] In the analysis of near weld region and far weld region, predicting the thermal cycles in the heat affected zone can be and is usually achieved without rigorous modeling of all heat transfer mechanisms taking place in the weld pool.[16,77] Many analysts prefer simpler heat source models which do not explicitly incorporate complex phenomena that happened in the weld pool but are capable of modeling heat transfer outside the fusion zone as has been done in the earlier numerical solutions.[16-20, 57-77] The decoupling of the heat transfer equation is not only possible, but also advantageous because it dramatically reduces computing cost without sacrificing accuracy.[77] The challenge for the analysts is to render it tractable. Obviously the least important phenomena must be neglected while only the essential physical phenomena remain. Thus the heat transfer equation can be decoupled from the physics of the weld pool. If the velocity is known, the fluid flow in the fusion zone can be easily coupled into the heat transfer equation by implementing a convective term. But in most cases, the velocity is not known. Many analysts have used artificially high values of thermal conductivity to compensate for the convective heat transfer in the fusion zone. This has been proven very effective. When the digging effect of the welding heat source is very strong, Goldak *et al.*[77] suggested a distributed heat source to compensate.

While the energy distribution of moving arcs has not been specifically measured, pictures suggest that the Gaussian distribution is probably skewed toward the trailing edge.[102,103] Therefore, Goldak and his coworkers proposed a double ellipsoidal heat source model[104] in 1984, which can be described by a double ellipsoidal disc with a

Gaussian distribution of flux on the surface of the weld, together with one double ellipsoid function of power density distribution to model the direct impingement of the arc and a second double ellipsoid with Gaussian distribution to model the energy distributed by the stirring of molten metal. This heat source model is generally regarded as a simple model which gives the most accurate temperature fields computed to date.[105,106]

Coupling Effect

Heat transfer analysis is usually simplified by uncoupling it from mechanical analysis so that it can be performed independently of the stress analysis. The assumptions for the uncoupling are based on the fact that the heating effect due to plastic deformation is small and negligible compared with the heating due to the welding heat source.[105] In the coupled thermal and stress analysis, the link is so weak that the temperature history is usually used as the thermal loading for stress computation.[19]

For carbon steels, solid state phase transformations in the heat affected zone often depend on the thermal history. As the microstructure changes, heats of phase transformations can contribute directly to the energy equation. Less directly, the conductivity and specific heat can also be microstructure dependent.

Several authors[54,107] have studied the effects of latent heat in the context of solidification problems where the phase change takes place at a single temperature and leads to a moving boundary problem at the solid-liquid interface. The inherent discontinuity in the spatial discretization requires continuous redefining the mesh of the moving boundary, which complicates considerably the computational problem in two- and three-dimensional situations. For this reason, the effects of melting and solidification had to be distributed over a finite temperature interval and incorporated either in the form of an equivalent increase of the specific heat[60] or by an equivalent spatial and time distribution of free enthalpy.[108] The effects of solid state phase transformations on the heat transfer are less significant and are often neglected although they can be analyzed in the same way as in analyzing melting and solidification.

Multiple Pass Welds

Multi-pass welds have been analyzed by Ueda,[20] Tekriwal and Mazumder,[75] Leung and Pick,[106] and Rybicki *et al.*[109] To reduce the cost of separate analyses for each pass, several passes have often been lumped together in different ways. Ueda[20] only analyzed the last pass in a specific layer. Tekriwal and Mazumder[75] used the element "birth and death" control method to turn on the passes to be analyzed. Leung and Pick[106] lumped thermal histories from several passes together, the temperature at any point, at any instant in time being the greatest value from any pass. All passes in a single layer, except the last, are lumped together. The last pass in any layer is treated separately. Rybicki *et al.*[109] lumped together the volume of weld deposit of several passes or layers of passes and imposed the thermal history of a single pass located in the middle of the deposit during the stress analysis. Lumping layers together is inadvisable with the possible exception that the lumped layers remain a small proportion of the total thickness. For extremely large numbers of passes these techniques are not adequate.

Goldak *et al.*[19] analyzed the surfacing of a thin plate which involved several hundred passes. Each pass was 10 cm long, groups of 20 passes were done sequentially to cover 10×10 cm rectangular surface patches. The orientation of each patch, and the patch sequence were varied in order to minimize the deformation. The residual stress pattern of the multipass case was created by superimposing the residual stress pattern of each individual weld and taking the largest value from any individual pass. By building up the stress pattern for each patch and sequentially applying this pattern to the plate it was possible to obtain qualitative agreement in both the deformed shape and optimum patch sequence.

The danger in all these lumping techniques is that the actual sequence of welding process is not simulated. Nevertheless, all these works were oriented towards modeling the residual stress and deformation induced by multipass welding. Accuracy of the heat transfer analysis is not critical for the subsequent structural analysis. Lumping techniques may be just adequate for this purpose and they provide an economic solution to complex engineering problems. It is very crucial, however, for a microstructural

analysis to have accurate results of thermal cycles.

1.2.3 HAZ Microstructure

As a consequence of the thermal cycle experienced, different microstructures are produced in layers of heat affected zone which is often characterized by peak temperatures between melting temperature and A_1 temperature in case of carbon steels. Primarily, transformation from $\alpha \rightarrow \gamma$ occurs on heating, with, depending on composition, the subsequent $\gamma \rightarrow \delta$ change, followed by the reverse reactions on cooling. Other thermally activated changes in microstructure will also occur in the heat affected zone, including precipitate dissolution, grain growth, particle pinning, recrystallization. The final microstructure will be largely determined by the $\gamma \rightarrow \alpha$ transformation during cooling.[110]

In principle, if the thermal cycle is known, all these metallurgical changes can be predicted based on the base metal chemistry and reaction kinetics. The prediction of microstructure and hardness in the heat affected zone is an interesting topic and has been established by the application of regression analysis, continuous cooling transformation (CCT) diagrams and computational models.[110,111]

Regression Analysis

With the development of modern computer technology, multiple regression analysis shows promise in microstructure and mechanical property predictions. Many regression models have been developed to date based on multiple regression analysis of the experimentally measured data and fitting into trend equations between variables such as hardness, martensite volume fraction, chemical composition, and welding parameters. These models show simple relationships among different variables and have been successfully employed in welding engineering.

Although mathematics varies from model to model and all models were relatively independent, they are all developed from the same hypothesis. It is said that for each

steel there exists a "characteristic hardness curve" as a function of cooling time. The characteristic hardness curve is unique for a given composition and is a measure of the HAZ hardening response to welding. In configuration, a characteristic hardness curve has two shelves; an upper hardness shelve for fast cooling rate which is correlated with martensite formation, and a lower hardness shelve for slow cooling which is correlated with no martensite formation. In between these two shelves, martensite volume fraction and hardness decrease as the cooling rate decreases.[112-114]

Different approaches were adopted to determine the characteristic hardness curve of a steel. Doan and Stout *et al.*[25] used Jominy end-quench method and extended it to the "weld test method."[115] Researchers in Creusot-Loire Works[116-118] developed their hardenability model based on their collection of CCT diagrams. Other more widely used approaches in welding engineering were based on the concept of carbon equivalent.

The prediction method based on Jominy end-quench test reported by Doan and Stout *et al.*[25,115] is experimentally based thus limited for computer implementation. This method is not considered in this study.

In Creusot-Loire hardenability model,[116-118] a parameter called austenization parameter, Pa, was defined to establish equivalence of time and temperature to accommodate rectangular heat treatment cycles for all the CCT diagrams. The expression of the austenitizing parameter Pa was derived from Fick's law of diffusion and is expressed by

$$Pa = \left(\frac{1}{T} - \frac{R}{Q}\ln t\right)^{-1} \qquad (1.14)$$

where T is the temperature in °K, t is austenitizing time in hr, R is the universal gas constant, 1.987 cal/mol°K, and Q is the activation energy for the grain growth which was found to be 110 kcal/mole for all steels. The hardness of a given alloy was assumed to be determined by a cooling rate weighted law of mixtures for microstructural constituents. Then they developed expressions for the critical cooling rates of steels in the basic form of

$$\log V_R = C_0 - \left(\sum_i K_i C_i + K_p Pa\right) \qquad (1.15)$$

where C_0 is a constant, C_i is the concentration of element C, Mn, Ni, Cr, and Mo, K_i and K_p are coefficients. They claimed to determine ten equations for different cooling rates based on regression analysis from CCT diagrams, five for separating martensite from bainite region, five for separating bainite from ferrite and pearlite region. However, only eight equations were given in their original publication.[117] Two equations for the cooling rates of forming 10% and 0% martensite were not given.

Similar approach was followed by DeAndrés and Carsí[119] from Spain. In their study, they established an equation to link ASTM grain size with austenitizing temperature and time. They differentiated steels with grain growth modifiers and those without to account for austenite grain growth

$$G = \frac{a}{T} + b\ln t + c \tag{1.16}$$

where G is the ASTM grain size number. They determined the coefficient in Equation 1.16 for steels with and without grain growth inhibitors. And then they were able to define austenization parameter from the grain growth perspective

$$Pa = (\frac{1}{T} - k\ln t)^{-1} \tag{1.17}$$

where k is defined as b/a, 1.47815×10^{-5} and 1.86202×10^{-5} for steels with and without grain growth modifiers respectively. They defined the same 10 cooling rates as in Creusot-Loire model and all the coefficients in the equations were given.

The development and application of models based on carbon equivalent is more straightforward and more widely used in welding industry. The concept of carbon equivalent was developed 50 years ago by Dearden and O'neill[120] as a means of characterizing the hardenability of steels during welding and may be regarded as a hardenability index of a steel from the compositional standpoint. Over the past 50 years, many formulae have been proposed to relate the chemical composition of base metal to the HAZ hardenability, critical hardness and the risk of cracking during welding.[121-123] More recently they have been used to rationalize the strength properties, microstructure and cracking tendencies of weld metals.[114] Later formulas have become more complex

involving cooling rate parameters, to allow hardness to be calculated directly, and hydrogen concentrations and restraint, to allow the cracking risk to be assessed. The development and application of carbon equivalent were recently reviewed by Düren,[125] Bailey,[126] and DeMeester.[127]

Carbon equivalent models[121-136] gave relationships to calculate the maximum $t_{8/5}$ cooling time for 100% martensite, hardness of martensite, the minimum cooling time for 0% martensite, and hardness for the structure without martensite. For cooling times beyond the 0% limit there is no martensite in the structure whereas the structure is all martensite when the cooling time is less than the 100% limit. In between these two limits, the HAZ hardness satisfies a unique relationship which is approximated by interpolation functions in different models.

Models proposed before 1980 did not cover the composition range for microalloyed steels and thus are limited in application. Among the new models which cover microalloyed steels, the models developed by Terasaki[136] based on weld CCT diagrams and by Yurioka[132-135] from hardness measurements in real weld heat affected zones are two excellent examples. The algorithms of these models are straightforward and there are no special computational difficulties. Calculation involved in these models is very simple and can be done using calculators. These models have been coded in the form of "HAZ-Calculator" type software systems[112-114,137] in recent years.

CCT Diagrams

The concept of using CCT diagrams to predict microstructural developments occurring during welding was developed in 1945 by Christenson *et al.*[138] Early weld CCT studies were concerned with solving weldability problems such as HAZ cold cracking or toughness. During welding operation, rapid heating and cooling thermal cycles ensure that austenite decomposition does not occur under equilibrium conditions. Consequently, the Fe-C phase diagram does not give a true indication of microstructural development. CCT diagrams, on the other hand, provide a convenient way of describing microstructural development under nonequilibrium conditions and an excellent method

of studying the complex interactions between the various factors such as chemical composition, cooling rate and prior austenite grain size.[110,139,140] The application of CCT diagrams for welding of steels is reviewed recently by Harrison and Farrar.[141]

The nature of fusion welding processes is such that a wide range of peak temperatures is experienced in the heat affected zone, resulting in a wide range of microstructural regions in the HAZ. The microstructural transformation resulting from the welding thermal cycles differs significantly from conventional heat treatment in respect of peak temperature and high temperature austenitizing time. Typically, the ferrite nucleation is retarded to much longer times and the amount decreases if the peak temperature becomes higher. Therefore accurate statements can only be made by using weld CCT diagrams[139,141] which are often related to higher austenization temperature. In principle, almost infinite number of CCT diagrams would be required to describe transformation behavior in every region of the HAZ. In practice, however, a good understanding of HAZ transformation behavior can be obtained by examining the grain refined region and the grain coarsened region using just one CCT diagram for each region.[141]

The grain refined zone of the HAZ experiences a peak temperature at, or a little above, the Ac_3 temperature. Peak temperatures of this order produce a fine austenite grains, which provide favorable sites for ferrite nucleation on cooling because of the high density of grain boundaries. The austenitization temperature of CCT diagram for this region is usually taken in the range 900-950 °C. The precise nature of the microstructure in the grain refined region depends on the exact chemical composition of the base metal and the complete thermal cycle. CCT diagrams produced for grain refined HAZ regions are generally similar to those produced for base metal to help in the correct selection of heat treatment cycles.[141]

The grain coarsened region of HAZ experiences peak temperatures from $\sim$1100°C up to the melting point of base metal. Peak temperatures of this order produce coarse austenite grains which tend to preclude extensive transformation to ferrite during cooling because of low density of grain boundaries. Microstructures in the grain coarsened region are generally more complex than those in the grain refined region or

base metal as a result of the much larger variety of transformation products that can be developed in these regions. The major phases observed in this region include equiaxed or polygonal ferrite, Widmanstätten ferrite, bainitic ferrite, and lath martensite. In addition to these, the carbon enriched phases, or minor phases, which are associated with the above mentioned ferrites may transform to pearlite, degenerate pearlite, carbides, or martensite-austenite (M-A) constituents.[141] The austenitization temperature of producing CCT diagram for this region is usually taken in the range of 1300-1350 °C.

The exact combination of microstructural constituents formed in the grain coarsened region depends on the chemical composition of base metal, weld cooling rate and the localized inclusion content. Three types of bainite in the grain coarsened HAZ were observed under normal weld cooling rate by Ohmori *et al.*[142] They were found at temperatures below 600°C and were termed: bainite I, bainite II, and bainite III. Bainite I was described as a carbide free bainitic ferrite, formed between 600 and 500°C in both the CCT and TTT diagrams. Bainite II was described as a ferrite lath structure, separated by layers of cementite, which formed between 500 and 450°C during isothermal transformation. During continuous cooling bainite II formed after bainite I but only at intermediate cooling rates. Bainite III was described as lath-like ferrite with a cementite morphology similar to high carbon, lower bainite, which formed between ~500°C and Ms temperature.

The grain coarsened region microstructure of low alloy steel HAZ was found dependent on the content of Nb in the base metal by Brownrigg and Boelen.[143] The Nb-bearing low alloy steels were found to consist of a mixture of bainite II (similar in microstructural appearance to upper bainite) and bainite III (similar in microstructural appearance to classical lower bainite), whereas the Nb-free steel consisted of bainite I (carbide free bainitic ferrite with M-A constituents between bainitic ferrite laths), and some periodic pearlite.

As an alternative, TTT diagrams of steels may be used for microstructure predictions. They are normally determined through metallographic examinations and the volumetric distribution of phase transformation products is less complicated. There is only one TTT diagram that exists for a steel when the austenite grain size and

composition are specified. Moreover, kinetics for grain growth and phase transformation under isothermal conditions are better established. Isothermal transformations which are the basis of TTT diagrams have a great theoretical advantage that one of the variables, temperature, is constant. Transformation diagrams under continuous cooling conditions, including welding, can be easily derived from TTT diagrams by fitting to transformation kinetics theories and using additivity rule.[145,146]

CCT diagrams can be and have been derived from TTT diagrams based on Scheil-Avrami rule[147-149] which is also known as the additivity rule. Grange and Kieffer[150] first offered a useful approximation which represents a geometric method of conversion of TTT to CCT diagrams. This conversion method was later coded into a computer program by Markowitz and Richman.[151] Hildenwall and Ericsson[152] pursued a semi-empirical approach. They fitted measured TTT diagrams to the Avrami equation[153,154] and then calculated CCT diagrams for microstructure predictions.

CCT diagrams were calculated with generic approaches. Researchers in Kawasaki Steel[155] have fitted C-curves for ferrite start, pearlite start and finish, bainite start and finish to the relevant part of the U.S. Steel Atlas[156] involving the composition ranges, $C=0.06$ to 0.79%, $Si<2.1\%$, $Mn=0.2\sim1.9\%$, $Ni<3.5\%$, $Cr<0.2\%$, $Mo<0.8\%$, and $Cu<1.5\%$. Intermediate volume fractions were interpolated according to a logarithmic formula which is equivalent to the Avrami equation. The TTT curves were thus used to predict CCT curves and microstructure via the additivity rule.

Kirkaldy and his coworkers[157-159] developed a comprehensive model for calculating TTT curves based on Fe-C-X thermodynamics which is accessible as multicomponent phase diagrams and isothermal phase transformation kinetics for ferrite, pearlite, and bainite. Zener-Hillert[160,161] type of kinetics formulas for phase transformation were used in this model and expressions for the coefficients were calibrated to the U.S. Steel Atlas[156] with a few adjustable parameters. This model accounts for explicit synergistic alloying effects. Phase transformations terminate at finite times and intermediate volume fractions are inherently defined. The model presented in ref. 159 is the most complete prior to this research.

Computational Models

The transformation behavior in weld heat affected zone can be described starting from chemical composition, austenitizing conditions and initial austenite grain size, proceeding with the thermodynamic equilibrium conditions of chemical potentials, and the laws of transformation kinetics in respect to incubation time, nucleation rate, grain, precipitate and phase growth rate (mainly diffusion controlled with the exception of martensite and bainite formation), ending with the integration over time of differential equations to obtain both the iron-carbon phase diagram and the isothermal TTT diagram. Consequently, the dependency of grain size, martensite content and hardness on peak temperature can be correctly calculated.[110,111]

Ikawa *et al.*[162-165] described the grain growth in the weld heat affected zone using empirical kinetics of grain growth

$$D^n - D_0^n = A t \exp(-\frac{Q}{RT}) \qquad (1.18)$$

Coefficients for the grain growth in the heat affected zone of a Cr-Mo steel (HT80) were determined,[163] n=4, $A=2.969\times10^{15}$ mm^4/sec, Q=137.7 kcal/mol/K. The computed grain size matched reasonably well with experimental measurements except at the fusion line.[162] They explained that grains on fusion line are partially melted at the grain boundaries in the base metal side which restrained further grain growth. Details of this unique phenomenon were discussed by Savage[167] in 1980. Excellent agreement was obtained when the grains on fusion line grow only during heating and do not grow during cooling.[162]

Alberry *et al.*[167] studied the grain growth in Cr-Mo-V steels using thermal simulation. They determined the coefficients in Equation 1.18 under isothermal conditions: n=2.73, $A=5.4\times10^{12}$ $mm^{2.73}/sec$, Q=460000 J/mol/K. This was later used by the authors to predict the microstructures in the weld heat affected zone.[168,169] The predicted grain size was found to be considerably larger than those actually observed. They attributed the differences to the steep thermal gradients in weld HAZ. They

introduced a thermal pining factor to the grain growth exponent n, such that the form of Equation 1.18 is retained:

$$D^{Nn} - D_0^{Nn} = 5.4 \times 10^{12} \sum_i \exp(-\frac{110{,}000}{RT_i}) \Delta t_i \qquad (1.19)$$

The value of thermal pining factor N was determined by matching the predicted grain size with the observed and was found to be 0.47 in their studies.

Ashby, Easterling, and Ion[170,171] used elementary grain growth kinetics to calculate austenite grain size in the weld heat affected zone. The kinetic equations for grain growth, precipitates dissolution and coarsening were integrated throughout a weld thermal cycle. The results were presented in the form of microstructural diagrams with cooling time $t_{8/5}$ as the ordinate and the maximum temperature reached as the abscissa. Kinetic constants which appear in such a treatment were determined by fitting the equations to data from real or simulated welds at certain fixed points.

The model proposed by Ashby, Easterling and Ion[170,171] provides a good basis, from which several refinements need to be implemented based on recent experimental and theoretical findings. Buchmayr[172] modified this model by taking into account the Gibbs-Thompson effect of precipitate dissolution, the influence of particle size on the dissolution time or solution temperature.[173,174] Suárez *et al.* applied this model to compute the grain size[175] and predict the HAZ microstructure of a HSLA microalloyed steel.[176]

Watt *et al.*[177,178] suggest an algorithm that combines Ashby and Easterling's model[170,171] for austenite grain growth with the austenite decomposition reaction kinetics model by Kirkaldy and Venugopalan.[159] Both the grain growth and the phase fraction formulations appear as ordinary differential equations in this method which were integrated numerically along the whole thermal cycle. The result of this approach is that microstructures can be tracked throughout the entire process. This in turn, permits the opportunity of coupling microstructure dependent thermal and mechanical properties to FEA temperature and stress computation. The mathematical ramification and solution techniques were presented by Bibby *et al.*[179]

1.2.4 Concluding Remarks

With the complexity of heat transfer induced by multipass electroslag cladding, only finite element analysis is considered adequate to give predictions with considerable accuracy. Commercial code ANSYS has been used at the Oregon Graduate Institute to conduct finite element analysis. It allows the analysts to focus on the physical details of the models. The analysis requires thermal properties of materials like thermal conductivity, enthalpy change, and density. One challenge in this study is that ESC is a dissimilar metal joining process. The thermal properties of the clad fusion zone were considerably different from those of the base metal and they were actually a function of dilution level. Accurate analysis of dissimilar metal joining processes requires modeling the advancement of solid/liquid interface and the thermal property change as a function of the composition in the fusion zone. The mathematical representation of the moving solid/liquid interface has not yet been well established and dynamic meshing may be necessary to solve the problem effectively.

Current state of art in computational weld mechanics has not addressed how to model the absorbing and releasing of latent heat of solid state phase transformations. The commonly used approach is to add the solid state phase transformation heat to the enthalpy change over the temperature range between Ac_1 and Ac_3. However, the release of phase transformation heat would not happen in the same temperature range during cooling, but at much lower temperatures for most steels when austenite decomposition reaction occurs. This may be part of the reasons that most of computed cooling rates in weld heat affected zone are faster than those measured.

Most of all, the biggest challenge in the finite element heat transfer analysis of this study is to incorporate the effects of multiple passes which include the addition of new material, shifting of thermal gradients from pass to pass, and interpass temperatures.

Regression models are developed based on large sets of data. They show simple relationships among different variables and can be easily employed in welding engineering. The implementation of regression models is straightforward and there are no special computational difficulties. They predict the average trend but may be subject

to substantial errors for a specific steel. One limitation of regression models is that they do not describe the process of microstructure evolution. Another limitation is that they all imply that welds of a given steel will have, in principle, the same HAZ hardness, if the $t_{8/5}$ cooling time (rate) is the same. Apparently this is a crude approximation and may lead to wrong conclusions. The weld HAZ microstructure is determined by the grain size and the entire thermal cycle, not just by the $t_{8/5}$ cooling time. The nonlinearity of cooling curves in the weld heat affected zone puts a practical limit to the accuracy of regression model application. For welding with preheating or multiple pass welding, the cooling curves in weld heat affected zone are very nonlinear at the temperature range for phase transformations. Application of regression models may lead to substantial errors.

The advantages of using weld CCT diagrams in the microstructure prediction lie in its simplicity and convenience in understanding phase transformation. They reveal the whole phase transformation process during continuous cooling. This approach is not limited by the steel composition and it only requires knowledge of the thermal history in the heat affected zone and does not need further computations for the microstructure and hardness prediction. Apparently, CCT diagrams for the heat affected zone must be available for predicting microstructure in the weld HAZ. If they can not be found in literature, they have to be measured experimentally. The international set of experimental CCT diagrams consists of some 1000 diagrams of highly varying quality. The smallest set has been determined by metallographic examinations of sequentially quenched specimens according to natural cooling regimes. The largest set has been determined by dilatometry at mostly constant cooling rates with a necessary ambiguity in interpretation as to relative volume fraction of constituents.[154.155] However, the cooling rates in weld heat affected zone are by no means constant. The nonlinearity of thermal cycle in weld heat affected zone increases with the decrease of temperature and with the preheat temperature in single pass welds or interpass temperatures in multipass welds. Application of CCT diagram approach may lead to substantial errors in these situations. Another nontrivial problem of this approach is that CCT diagrams of a same grade steel may be sensitive to the minor variation of chemical composition.

The most promising advantage of computational models is that it is based on first principles and the whole process of phase transformations can be tracked with respect to time. Consequently the state of microstructural development is known at any instant of time. It must be noted, however, parameters in computational models with no exceptions were calibrated with experimental measurements although they started with fundamentals of thermodynamics, austenite grain growth kinetics, and reaction kinetics of austenite decomposition. The formulation of a computational model as well as the database with which the model was calibrated would all contribute to the reliability of the model. The reaction kinetics model developed by Kirkaldy and Venugopalan has been often cited as the most comprehensive model to date, but the reliability of this model has never been extensively tested. Even Kirkaldy and Venugopalan have never used their model in the full scale for the quantitative prediction of steel hardenability. They only used the initial part of this model to calculate TTT and CCT diagrams. The application range for this model is not known. The only known limitation for this model is that it does not apply to microalloyed steels because they are designed for a different thermomechanical regime and the microalloying elements have different hardening and softening effects.

1.3 Thesis Outline

In this thesis, attempts have been made to develop a finite element heat transfer model for multipass electroslag cladding to compute the thermal cycles experienced in the electroslag cladding heat affected zone. The computed thermal cycles are then used for later microstructure predictions.

A comprehensive literature review has been presented in Section 1.2 regarding heat transfer analysis in welds and microstructure predictions. Electroslag cladding has never been analyzed in the literature before this study. Limited by the size of the problem and the computing power, the author decided to use a two-dimensional finite element model for the heat transfer analysis in multipass electroslag cladding. The theory and implementation of the finite element heat transfer analysis are presented in

Chapter 2 with special reference to multipass electroslag cladding. This model has the capability of literally analyzing as many clad passes as desired.

Chapter 3 is dedicated to the description of computing equilibrium phase diagrams based on thermodynamic model for multicomponent Fe-C-M systems, austenite grain growth kinetics of steels with special reference to the grain growth in weld heat affected zones of low carbon alloy steels, and a reaction kinetics model for austenite decomposition. All these models are based on first principles. All the models presented in Chapter 3 are referred to low alloy steels.

The two-dimensional finite element model presented in Chapter 2 is used to simulate the heat transfer during electroslag cladding onto carbon steels shafts. The computational heat transfer results are presented in Chapter 4. The depth of the heat affected zone, interpass temperatures, and $t_{8/5}$ cooling times in the heat affected zone will be discussed with respect to the cladding passes. The thermal effects from the two ends of experimental size shafts are discussed. The electroslag cladding process on a virtually long shaft is also analyzed. Optimal initial preheating temperature distribution is obtained from numerical simulations for the continuous cladding with the interpass temperature in the optimal range.

Chapter 5 presents the evaluation of the thermodynamics model for Fe-C-M multicomponent systems, and a model for microstructure and hardness predictions. The errors for computing austenite grain growth in weld heat affected zone are also discussed. Emphasized in this chapter are: Ae_3 temperature calculation, calculation of the temperature range for eutectoid reaction and the eutectoid composition, and the reliability of the reaction kinetics models presented in Chapter 3. The reaction kinetics model developed in this study as well as the model by Kirkaldy and Venugopalan are tested against the measured Jominy hardness curves. The results verifies the model developed in this study and errors in Kirkaldy-Venugopalan model are discussed.

Chapter 6 will be directed towards the applications of the computational models developed in this study. Chapter 7 will conclude the thesis work by identifying and suggesting areas of future research work. Following Chapter 7 will be the list of works that were referred to in the current work.

CHAPTER 2
FINITE ELEMENT HEAT TRANSFER MODEL

2.1 Introduction

The temperature field in any welding process is thermodynamically coupled with the mechanical field. The governing equation of heat flow follows the first law of thermodynamics which essentially states that the rate of heat change due to storage and conduction must be in equilibrium with the rate of internal heat generation, the rate of heat generation due to elastic and visco-plastic straining. However, heat due to elasto-visco-plastic straining of materials in welding operations is negligible in comparison to the heat input from welding heat sources. Heat due to phase changes is often incorporated into the heat transfer model with temperature dependent thermal properties of materials. Therefore, it is possible to analyze a welding process in three steps: the analysis of temperature filed, the analysis of microstructural changes, and the analysis of strain/stress fields. Heat transfer analysis is a necessary and usually the first step for any subsequent analysis including microstructural and mechanical analysis. The accuracy of heat transfer analysis may not be very crucial for the subsequent mechanical analysis, but is certainly imperative for microstructural analysis.

The objective of this study is to analyze the heat transfer in the heat affected zone induced by electroslag cladding of nickel alloys onto carbon steel propeller shafts. Commercial finite element code ANSYS was used for the heat transfer analysis since it was readily available as a general purpose finite element program. Although it is not a program specially written for solving welding problems, its use eliminates the time and cost in developing a project oriented program. The finite element code ANSYS contains

most of the necessary features to simulate welding processes, and in conjunction with user written subroutines, it is possible to simulate the nonlinear complex phenomenon of weld mechanics.

Attempts to model all aspects of the electroslag cladding process would lead to impractical computing requirements. Therefore, it is important to establish a reasonable heat transfer model with parameters which are essential for producing accurate thermal cycle results. Obviously some trivial phenomena must be neglected while only the essential heat transfer phenomena are retained. This can be achieved by modeling the fusion region as a "simple" heat source for the electroslag cladding instead of rigorously modeling all the heat transfer mechanisms taking place in the weld pool such as convection, magnetic stirring and heat losses from the weld heat source and the molten metal. The challenge is how to model the heat source and render it tractable.

2.2 Cladding Procedure

Extensive electroslag cladding experiments have been conducted at the Oregon Graduate Institute (OGI) to clad nickel alloys onto carbon steel propeller shafts of different diameters, wall thicknesses and lengths. A full size propeller shaft is normally 12 to 15 meters long, which is too long and too expensive for such preliminary experimental studies. Therefore, only short sections of shafts were actually used in the cladding experiments. The experimental setup is illustrated in Figure 2.1. Strip electrode was used in this project and it consists of nickel alloy 625, 30 mm wide and 0.5 mm thick. Cladding equipment was operated with constant voltage direct current power supply. The cladding current was 650 amperes and the voltage was 27 volts. The welding speed was 0.3 cm/sec. Strip electrode feeding rate was 3.0 cm/sec. Both uniform and non-uniform preheating were used in the cladding experiments. During the cladding experiments, the cladding head remained fixed, while the shaft was rotated by a gear system at a constant speed. One complete rotation was counted as one pass. A specially designed jogging technique was used to transit from one pass to the next. The time to finish one pass was thus determined by the shaft diameter.

2.3 Heat Losses

The heat supplied to an electroslag clad is primarily generated in the fusion pool and transferred to the base metal by conduction and convection within the weld pool. A simple approach commonly used by many analysts is to compensate the convective heat transfer in the weld pool with artificially high thermal conductivity values for the metal in the weld pool.[16-20,105] Typically, thermal conductivities an order of magnitude or sixfold higher than its value at the solidus temperature have been used. The difficulty associated with this technique is that various values of conductivity for the molten metal must be tried until a reasonable weld pool shape and temperature distribution within the weld pool are obtained.

On the exposed surfaces of the cladding shaft, heat is lost by the combination of convection and radiation. With ANSYS, incorporation of radiation into the heat transfer analysis requires radiation link elements and the calculation of a radiation matrix. This radiation matrix is then used in the thermal analysis to determine the temperature distribution in the model. This numerical implementation makes the analysis more complicated and computation intensive. Therefore, in this study, convection and radiation were incorporated into the analysis by introducing combined convection and radiation heat transfer coefficients.

Heat loss by free convection was assumed to obey Newton's cooling law

$$q_C = h_C(T_S - T_A) \qquad (2.1)$$

in which q_C is the convective heat flux in W/m^2, h_C is the convective heat transfer coefficient in $W/m^2 \cdot °C$, T_S and T_A are the surface temperature and ambient temperature in °C. Radiative heat loss was modeled with the Stefan-Boltzmann equation

$$q_R = \sigma \varepsilon (T_S^4 - T_A^4) \qquad (2.2)$$

where q_R is the radiative heat flux in W/m^2, σ is the Stefan-Boltzmann constant, 5.67×10^{-8} $W/m^2 \cdot °K^4$, ϵ is the emissivity of the free surface, T_S and T_A represent the surface temperature and ambient temperature in Kelvin respectively.

Equation 2.2 can be linearized into the form

$$q_R = h_R(T_S - T_A) \tag{2.3}$$

by introducing the radiation coefficient h_r:

$$h_R = \sigma \varepsilon (T_S^2 + T_A^2)(T_A + T_A) \tag{2.4}$$

It must be noted that radiation calculations are normally done in absolute temperatures (Kelvin) and the calculation involved T_S^4 terms which make radiation a highly nonlinear process. Also, because of the small value of σ, the effects of radiation may be neglected at low temperatures. At high temperature, however, radiation effects may be dominant. The linearization given by Equation 2.3 is somewhat deceptive in that the radiation coefficient, h_R, is highly temperature dependent.

The use of radiative coefficient h_R allows one to express, formally, the combined heat flow due to convection and radiation at the free surface as

$$q = q_C + q_R = h_{CR}(T_S - T_A) = (h_C + h_R)(T_S - T_A) \tag{2.5}$$

in which $h_{CR} = h_C + h_R$ is defined as the combined heat transfer coefficient. Equation 2.5 has the same form as Equation 2.1 for merely convection. Consequently, the combined heat transfer due to convection and radiation can be treated in the same way as convection in the finite element analysis. Combined heat transfer coefficients are used at free surfaces instead of the convective coefficients. This treatment has greatly reduced the complexity of incorporating radiation into the numerical model. There is no need to calculate radiation matrix and the convergence rate with combined heat transfer coefficients is much faster than a model using radiation link elements.

2.3.1 Convective Heat Transfer Coefficients

Considering the experimental setup for electroslag cladding, the cladding head remained fixed, while the shaft was rotated by a gear system at a rather low speed. The cladding was conducted in a closed room and no fan was used. It is justifiable to consider the convection as free convection or natural convection in air. The convective coefficient can be calculated according to the heat transfer theory of free

convection.[180,181]

For free convection in air, the significance of the buoyancy is described in terms of the Grashof number

$$Gr = \frac{L^3 g \beta \Delta T}{\nu^2} \tag{2.6}$$

Grashof number is an important dimensionless number for free convection. In Equation 2.6, L is the characteristic length of the surface subject to convection, g is the gravity acceleration, ν is the kinematic viscosity of air, ΔT denotes the driving temperature potential between the surface at T_S and the ambient fluid at T_A: $\Delta T = T_S - T_A$. The symbol β represents the coefficient of volume expansion of air and is the origin of the buoyant forces characteristic of free convection. The coefficient of thermal expansion is defined as the negative of the fractional change of the fluid density with respect to temperature:

$$\beta \equiv -\frac{1}{\rho}\left(\frac{\partial \rho}{\partial T}\right)_P \tag{2.7}$$

Thus β is determined by the governing pressure-density-temperature equation of state for the fluid involved. Like many gases, air may be adequately represented by the ideal gas equation

$$\rho = \frac{P}{R T_A} \tag{2.8}$$

where P is the pressure, R is the universal gas constant, T_A is the fluid temperature or ambient temperature in Kelvin. Thus thermal expansion coefficient β is readily calculated from

$$\beta = \frac{1}{T_A} \tag{2.9}$$

Another dimensionless parameter called the Prandtl number defined by

$$Pr = \frac{\nu}{\alpha} = \frac{\mu c}{k} \tag{2.10}$$

is often used for free convection heat transfer analysis, which arises from the rate laws

incorporated in the governing equations for shear stress and heat flux. In Equation 2.10, α is the thermal diffusivity, μ the dynamic viscosity, c the specific heat, k the thermal conductivity of air. Thus the Rayleigh number, which is the functional form for free convection, is defined simply by the product of the Grashof and Prandtl numbers

$$Ra = Gr \times Pr = \frac{L^3 g \beta \Delta T}{\nu^2} \times Pr \qquad (2.11)$$

In terms of the Rayleigh number, correlations for free convection are represented by valid Nusselt number expressions which vary from application to application. Then the convective heat transfer coefficient h_C is expressed by

$$h_C = Nu \frac{k}{L} \qquad (2.12)$$

All the thermal properties of air at atmospheric pressure, ρ, c, μ, ν, and k, are readily available in the literature.[180,181]

Outside Surface

The convective coefficient on the outside surface of the shaft can be calculated by treating the shaft as a horizontally laid cylinder. In this application, the characteristic length is represented by the outside diameter of the shaft, D_{out},

$$L = D_{out} \qquad (2.13)$$

Based on extensive studies, Churchill and Chu[182] recommended the Nusselt number expression for horizontal cylinders

$$Nu = \{0.60 + 0.387 Ra^{1/6} [1 + (\frac{0.559}{Pr})^{9/16}]^{-8/27}\}^2 \qquad (2.14)$$

which is valid for a wide range of Rayleigh number. The temperature dependent file coefficient of free convection at the outside surface of a horizontal shaft can be thus calculated from Equation 2.12. It is only dependent upon shaft diameter and temperature. The quantification of free convection presented above is based on the

theory of heat transfer and has been verified by the experimental studies.[180,181]

Edge Surfaces

Practically, convective and radiative heat loss through two ends of a full size shaft during cladding may be negligible because they are considerably far away from the cladding heat source. However, shaft sections used in cladding experiments were much shorter than actual submarine propeller shafts, and normally whole sections were preheated in the cladding experiments whereas only local preheating is considered feasible in the cladding onto full size shafts. Convection and radiation through these shaft ends may be of concern in the simulation of electroslag cladding experiments. In this research, the convective coefficient for the two edge surfaces are incorporated by considering the two shaft ends as vertical plane surfaces. In this application, the characteristic length can be specified as the wall thickness of the shaft

$$L = \frac{D_{out} - D_{in}}{2} \tag{2.15}$$

where D_{out} and D_{in} are the outside and inside diameters of the shaft. It must be noted this is only an approximation which may be subjected to trivial errors.

Churchill and Chu[183] have performed an extensive correlation of a great number of works. They recommended the following Nusselt number expressions for the vertical plane surface:

$$Nu = 0.68 + 0.670\,Ra^{1/4}\left[1 + \left(\frac{0.492}{Pr}\right)^{9/16}\right]^{-4/9} \tag{2.16}$$

when $0 < Ra < 10^9$, and

$$Nu = \left\{0.825 + 0.387\,Ra^{1/6}\left[1 + \left(\frac{0.492}{Pr}\right)^{9/16}\right]^{-8/27}\right\}^2 \tag{2.17}$$

for $Ra > 10^9$. Actually Equation 2.17 may be applied over the entire range of Ra. However, better accuracy was reported by the use of Equation 2.16 for small Ra values.[180] The film coefficient of free convection at the two end surfaces of a shaft is

dependent on its wall thickness and temperature.

Inside Surface

For the inside surface of the shaft, it is justifiable to consider only convective heat loss. There is no theoretical solution for the free convection on the inside surface of a pipe or shaft. Thus in this research, the solution for a horizontal heated plate facing down is used for the approximation. In this application, the characteristic length is expressed by

$$L = \frac{\pi D_{in} L_0}{2(\pi D_{in} + L_0)} \tag{2.18}$$

where D_{in} and L_0 are the inside diameter and the length of the shaft respectively.

Based on the work of McAdams,[184] Goldstein *et al.*[185] and Lloyd and Moran[186] recommended the Nusselt expression for the heated plate facing down as

$$Nu = 0.27\, Ra^{1/4} \tag{2.19}$$

for $3\times10^5 < \text{Ra} < 3\times10^{10}$.

2.3.2 Radiative Heat Transfer Coefficients

The only unknown parameter for calculating the radiative heat transfer coefficient was the emissivity ϵ in a certain ambient temperature. Siegel and Howell[187] discussed radiative properties of metals as functions of directional variations, wavelength, surface temperature, surface roughness, and surface impurities. Modern heat transfer analysis theory has not been able to rationally correlate the surface radiative emissivity with all these factors. Thus radiative heat transfer analysis has to be largely dependent on experimental measurements. However, there have been limited data for the emissivity of steels with wide range of values. It is not difficult to conjecture that all the reported data are subject to different degrees of errors. Steel composition and surface conditions may be considerably different from the real objects in applications, for example, carbon

steel propeller shafts in this study. Consequently, the emissivity value in the heat transfer analysis has to be chosen carefully or to the best knowledge of the analysts.

In this research, the outside shaft surface was machined before cladding. Thus the surface would be expected to be clean but could be still rough. The shaft is preheated before cladding and the vicinity of the clad was exposed at high temperature for short period of time during the cladding operation. It is reasonable to suspect that there is a very thin layer of oxide on the surface. In this study, emissivity value of 0.30 was chosen for the outside surface.

While, for the two ends of the shaft, the surface is rather rough and there is considerable amount of oxides on the surface. This type of surface is known to have higher emissivity. An emissivity value of 0.80 is assumed.

2.3.3 Combined Heat Transfer Coefficient

For each shaft used in the electroslag cladding experiment, the convective coefficient, radiative coefficient and combined coefficient of each surface are calculated. Of the material types analyzed in this study, only the results for shaft E290 are shown in Figure 2.2, 2.3 and 2.4. The ambient room temperature was assumed to be 20 °C. The geometric parameters of this shaft are: D_{out}=61 cm, D_{in}=35.5 cm, and L_0=104 cm. Other experimental shafts with different geometry have similar results and the results are used in the finite element heat transfer analysis of each shaft. Figure 2.2 and 2.3 clearly demonstrated the dominant effect of radiative heat loss over a wide range of temperature. The significance of radiation should not be ignored.

During the electroslag cladding, the top of clad was covered by fused flux until about two minutes after the cladding heat source passed. The area covered by the flux is assumed to be adiabatic in the finite element analysis.

2.4 Cladding Heat Input

The net heat input to a clad (weld) is generally calculated from the energy

supplied (the product of welding amperage and voltage) and heat efficiency of the process,

$$Q = \eta I V \tag{2.20}$$

The loss of energy that occurs from welding heat source is extremely complex in nature. Because of this, the heat efficiency η can be perceived as a complexity factor which is used to quantify the energy input from the welding heat source. A wide range of efficiencies have been reported in the literature for arc welding processes.

However, the efficiency of electroslag cladding is not known exactly and is hard to measure experimentally because of its high heat input. In this study, the heat efficiency of the process was obtained using numerical tests to match the computed interpass temperatures with the experimentally measured ones. This is a reasonable approach because the interpass temperatures, at $6 \sim 11$ minutes after welding depending upon the diameter of the shaft, are believed to be dependent only upon the shaft geometry, initial temperature distribution, material thermal properties, and the net heat input from the cladding heat source. The details of the heat source will not affect interpass temperatures. Excellent agreement was observed with a heat efficiency value of 0.81.

2.5 Heat Source Model

Perhaps the most critical input data required for finite element heat transfer analysis in welds are the parameters necessary to describe the heat input from the heat source to the weldment. Not only the magnitude, but the distribution of the heat input will also influence the dimensions of the weld metal and heat affected zones, the cooling rates, and the peak temperature distribution, as well as the temperature gradients necessary to calculate microstructure evolution and residual stress/strain field.

Most of the heat for electroslag cladding is believed to be generated in the slag pool which covers the molten metal pool. The mechanism of the heat generation is known to be caused by Ohmic heating. However, energy distribution in the slag pool

is not yet clearly understood thus it has to be approximated with a reasonable heat source model.

Welding heat source models with reference to electric arcs have been extensively reviewed in Chapter 1. The general guideline in model welding heat source can be summarized here. For welding operations where the effective penetration depth is small, the heat flux disc type of model originally proposed by Pavelic *et al.*[58] have been found very successful and efficient in computing temperature profiles in welds.[59-67] While for welding operations with deep penetrations, such as submerged arc welding, electron beam welding, etc., the three dimensional double-ellipsoidal model originally proposed by Goldak *et al.*[104] is more effective in predicting the contour of the fusion zone. Apparently, strip electroslag cladding belongs to the first category with shallow penetration and the heat source can be modeled as a heat flux disc acting on the top of the clad. To compensate for the convective heat transfer in the fusion zone, artificially high values of thermal conductivity have been proven effective.

In this research, because strip electrode was used which has a cross section of 30 mm in width and 0.5 mm in thickness, uniform heat flux distribution was assumed in the cross sectional direction at the top of the clad. It linearly diminished to zero along the two sides of the clad deposit. In the cladding direction, the heat flux was assumed to satisfy two Gaussian distribution functions; the front part to model the strong interaction between the molten pool and slag pool, and the rear part to model the thermal impingement from the slag pool in the trailing tail. The heat flux profile along the welding direction is shown in Figure 2.5 and is expressed in the coordinate system moving along with the welding torch by

$$q(x) = \frac{2\sqrt{3}\,\eta_1 IV \exp[-3(x/d_1)^2]}{\sqrt{\pi}\, w d_1} \tag{2.21}$$

for the front part where $x < 0$, and

$$q(x) = \frac{2\sqrt{3}\,\eta_2 IV \exp[-3(x/d_2)^2]}{\sqrt{\pi}\, w d_2} \tag{2.22}$$

for the rear part where $x > 0$. In these two equations, w is the width of the clad bead, d_1 and d_2 are the characteristic distances of the front and rear part of Gaussian distribution functions at which the Gaussian distribution function value equals to 0.05 of its peak values, I and V are the cladding current and voltage respectively, η_1 and η_2 are fractions of the heat source efficiency η for the front and rear part respectively

$$\eta = \eta_0 + \eta_1 + \eta_2 \tag{2.23}$$

where η_0 is the fraction of heat which was consumed to melt the cladding strip and superheat the filler metal droplets.

The melting and addition of filler metal has been modeled by Tekriwal and Mazumder.[75] The added material was included in the original mesh using element birth and death control method. To add metal, the elements are simply turned on with an assigned initial temperature, 500 ~ 1000 °C above the liquidus of the filler metal. To deactivate an element, the thermal conductivity of the element was multiplied with a very small value and the specific heat and enthalpy change were zeroed out. The commercial finite element code ANSYS has this element birth and death control feature. However, preliminary studies showed that convergence rate is significantly lowered when element birth and death control method was used and the computed results showed no apparent difference. Thus the element birth and death control method was not used in this research. Instead, the clad deposit was assumed to be in place in the beginning of each pass. An initial temperature of 1950 °C was assigned to the fusion zone elements. This served as a natural approximation to the addition of melted filler metal. All the nodes at the original interface between fusion zone and substrate were assigned with initial temperatures which were averages of droplet temperature 1950 °C and preheating temperature for the first pass clad or the interpass temperature for subsequent passes.

Heat source parameters were tried out to match the computed results with experimental measurements. The efficiency of the heat source, η, was the first one to be determined, and has been estimated using numerical tests by matching interpass temperature in the heat affected zone. The second parameter determined was the fraction of heat to melt and superheat the clad deposit metal to the droplet temperature.

Calculations showed that it consumes 25% of the nominal heat input IV to heat the clad deposit from room temperature to 1950 °C. The next parameter to be determined was the characteristic distance for the front part of the heat source, d_1. Numerical tests showed that the distance between the electrode tip and the substrate base metal gives a good approximation for the parameter d_1. Then the values of η_1 and η_2 , and d_2 were all estimated *via* trial and error to obtain reasonable penetration predictions and comparable thermal cycles in the weld heat affected zone with the experimental measurements. In this research, η_1 and η_2 were found to be 0.15 and 0.30 respectively, and d_1 and d_2 were 6 and 60 mm respectively.

The heat flux profile was captured by 5 and 20 load steps for the front and rear parts of the heat source model respectively. Stepped loads were assumed for fast convergence rate and small initial time integration steps were used to guarantee convergence, 0.034 sec and 0.1 sec before and after the fusion zone solidifies. In each load step, the integration time step was automatically adjusted by the ANSYS program for convergence.

2.6 Dimensionality of the Analysis

The heat transfer in electroslag cladding is spatially three dimensional. However, performing a three-dimensional finite element heat transfer analysis in welds with details requires a tremendous amount of computing power and could be unbearably expensive. In this research, a two-dimensional heat transfer analysis can be justified by assuming that the heat flow was constrained in the plane normal to the welding direction. Physically this is a reasonable assumption because the weld pool is approximately 32 mm wide and 78 mm long, and isotherms near the fusion zone are significantly elongated along the cladding direction. By assuming that cladding has achieved a steady-state that temperature distribution can be observed moving with the heat source, a two dimensional model can be used in which the analysis is conducted in a plane section normal to the welding direction at a location far from the ends of the clad. The heat flow in the welding direction can be simulated by modeling a three-dimensional heat source moving

through the plane of analysis.

2.7 Material Thermal Properties

It is true that one of the greatest advantages of using finite element analysis is that temperature dependent material properties can be incorporated in the numerical model. And, as a matter of fact, many analysts have realized that with the proper modeling of real applications, the accuracy of the numerical analysis can be only limited by the accuracy of the material properties used in the analysis.[18] Therefore, the importance of having accurate material properties in numerical analysis should never be ignored.

Finite element heat transfer analysis with ANSYS requires accurate values of the density, thermal conductivity, and enthalpy change of materials. Low temperature data is readily available for most low alloy carbon steels,[190-192] but high temperature data must be estimated or extrapolated from the low temperature data because little high temperature data exists in the literature. Above the melting point, the complex convective heat transfer mechanisms in the weld pool are so far too difficult to model even with accurate thermal properties. Instead the thermal conductivity above melting is increased sixfold to compensate for the convective mechanism as recommended by many analysts.[16-20]

The electroslag cladding process to be analyzed in this research involves joining of two distinctively different metals, nickel alloys and carbon steels. The thermal properties of the clad fusion zone are considerably different from those of the base metal. They are largely dependent upon the deposit material and the dilution rate from the base metal. Accurate analysis of dissimilar metal welding processes requires modeling the advancement of solid/liquid interface and the thermal property change as a function of the composition in the fusion zone. The mathematical representation of the moving solid/liquid interface has not yet been established and dynamic meshing may be necessary to solve the problem effectively. These two phenomena are too complex to model at the present state of computer software and hardware. They are not considered in this research.

Because strip electroslag cladding has a low dilution rate, approximately 10%, and shallow penetration, about 0.5 mm in comparison to the clad height 5.5 mm, the fusion zone was assumed to have the same composition and thermal properties as the filler metal. The original interface between the cladding deposit and base metal was assumed to remain.

The densities of materials were assumed to remain constant at the room temperature value of 7860 kg/m^3 for the shaft steel and 8440 kg/m^3 for the fusion zone. This is a reasonable assumption because density has only minor effects on the heat transfer analysis. Probably more importantly, the thermal expansion effect has been ignored because of decoupling from mechanical analysis.

Temperature dependent thermal properties of nickel alloy 625 have been provided by Inco Alloy International.[193] Based on the provided specific heat data, the enthalpy change of nickel alloy 625 can be readily obtained by integration

$$^0H(T)=\int_0^T \rho\, c\, dT \tag{2.24}$$

where ρ is density in kg/m^3, c is the mass specific heat in J/kg°C, and T is temperature. There is no heat for solid state phase transformation assumed in the numerical analysis for nickel alloy although it is possible that there might be some precipitates formed in the clad metal during cooling. This is because the total precipitate volume fraction is very small according to the microscopic observations, less than 5%.[9,10] High temperature data were extrapolated from lower temperature values. The latent heat of fusion was estimated to be 324 kJ/kg and was incorporated into the numerical analysis by adding it to the enthalpy change over the mushy zone.

Temperature dependent thermal properties of the shaft steel were not available. Thus thermal properties of steel with similar chemical composition were used in the numerical analysis. The latent heat of fusion for the shaft steel was estimated to be 275 kJ/kg from the thermodynamics model of Fe-C-M multicomponent equilibria which is to be presented in Chapter 3. It was added to the enthalpy change over the mushy zone of the steel. Similarly, the heat for solid state phase transformations can be treated in

the same manner except that the quantity is smaller and less significant. It is debatable though how this is going to affect the accuracy of the analysis because the quantity and the temperature for absorption during heating and releasing during cooling of the solid state phase transformation heat are different. During heating, this phase transformation occurred between temperature range from As_1 up to Ae_3. The definition of As_1 and Ae_3 temperatures and the heat for austenite formation from ferrite and pearlite were estimated from the thermodynamic model to be presented in Section 3.2. During cooling, however, austenite may decompose over a much wider temperature range depending on steel hardenability and cooling rate. The total quantity of the heat released during austenite decompositions may be different from the heat absorbed for austenite formation during the heating. The only way to model this effect is to have full scale coupled thermal/microstructural analysis where explicit expression of material properties in terms of microstructure constituents is essential. However, this is not possible at the present time. All the coupled analysis, no matter thermal/mechanical or thermal/microstructural analysis, have singled out thermal analysis and used the results of thermal analysis as input data for further analysis.

Rolphe and Bathe[194] presented a simple way to include the latent heat effect. Whenever a nodal temperature crosses a transformation temperature, this is noted whether it occurred during cooling or heating. A volume or mass is associated with each node and the corresponding heat of transformation is computed. If a node has transformed, its temperature is reset to the transformation temperature and the heat subtracted from the heat of transformation until it is reduced to zero. At that time the node is set free. In all other respects, it is a standard finite element analysis. The algorithm is simple, relatively easy to code, and efficient if and only if the analyst is developing a project oriented code. But for a user of commercial finite element codes, this is a rather difficult problem.

This study did not attempt to solve, but only to point out this problem. Obviously, simplifications have to be made to deal with solid state phase transformation in a rational fashion. Any simplification is just an approximation to the reality and is subject to errors.

Ideally, different thermal properties can be used for the heat affected zone during heating and cooling respectively. In this study, enthalpy change of the heat affected zone was kept the same during heating and cooling because of the concern of discerning heat affected zone boundary and energy conservation. Different thermal conductivity was used for the HAZ during heating and cooling. During heating, typical thermal conductivity values of ferrite structure from the literature was used until As_1. Thermal conductivity values of austenite structure were used for temperatures higher than Ae_3. While during cooling, the thermal conductivity was defined with the information provided by experimentally measured CCT diagrams of the shaft steels. CCT diagrams of the shaft steels revealed that only bainite and martensite reactions would happen under a wide range of the cooling rates. Thus the thermal conductivity of the heat affected zone under cooling was assumed to have the values of austenite structure at all temperatures above the isothermal bainite start temperature, and the values of ferrite structure at temperatures below the martensite start temperature of the shaft steels. Values from linear interpolation were used at temperatures between Bs and Ms points. Calculations of these temperature points may be found in Chapter 3.

When thermal properties of a steel are not known, it is justifiably to use thermal properties of another steel with similar chemical composition. Alternatively the enthalpy change of steels may also be obtained by the thermodynamic definition

$$^0H = {}^0G - TdS = {}^0G - T(\frac{d^0G}{dT})_{T,P} \qquad (2.25)$$

where ^0H and ^0G are standard enthalpy and Gibbs free energy respectively, T is the temperature, S is the entropy. With this definition, the enthalpy change can be expressed as a function of Gibbs free energy only. And, in Section 3.2, all the data for calculating Gibbs free energy of steels as solid solutions are presented. This is another option when the specific heat of the steel is not accurately known. This method has a advantage of being a generic approach and the results are sensitive to the chemical composition of steels. It is very likely that the enthalpy change calculated based on thermodynamics model is more reliable than estimated from the measured specific heat because enthalpy

is a well defined state function of a thermodynamic system, whereas high temperature specifici heat data of steels are rare.

Thermal conductivity and enthalpy change of the materials used in this study are shown in Figure 2.6 and 2.7 respectively. An artificially high value of thermal conductivity, 125 W/m°C, is assigned to the metal above its solidus to compensate for the convective heat transfer mechanism in the weld pool. This approach has been proven effective by many analysts.

2.8 Modeling Multipass Cladding

The state of art in modeling multipass welds has been reviewed in Chapter 1. It was noted that the commonly used lumping techniques are limited by the number of passes to be analyzed and the area covered by the welds. Most of all, lumping of welds does not simulate the actual process. Therefore, lumping techniques are not considered in this study to model multipass electroslag cladding.

Instead, a specially devised remapping technique was developed by the author in this research. This method emphasizes complete analysis of all weld passes in actual sequence and analyzing each clad pass individually in a synonymous fashion with a single weld pass. This was accomplished by defining finite element mesh for analyzing each clad pass and remapping the interpass temperature distribution from previous clad pass onto the new mesh so that the initial temperature distribution of analyzing the current clad pass could be defined. By doing this, the finite element mesh for each clad pass was customized to take into account the new added deposit material and the mesh density was optimized according to the thermal gradients. Remapping interpass temperature distribution from one mesh to another mesh does not pose any problem in finite element code ANSYS and can be done rather efficiently with a user defined subprogram called macro. This methodology is a natural approximation to the heat transfer in multipass welds and it overcomes the limitations of lumping techniques. There is no theoretical limit of the number of passes that can be analyzed with this method.

The approach used by Tekriwal and Mazumder[75] to model the melting and

addition of welding deposit took advantage of a special capability in finite element analysis, called "element birth and death" control. Essentially, the added material was included in the original mesh. To achieve the "element death" effect, the "killed" elements are not actually removed from the model, rather, their thermal conductivity was multiplied with a severe reduction factor. Elements loads associated with deactivated elements are zeroed out in the load vector. Similarly, mass, damping, specific heat, and other such effects are set to zero for deactivated elements. To reactivate the "killed" elements, all these constraints, thermal conductivity, mass, element loads, damping, specific heat, etc. return to their original values. The drawback of the element birth and death control is that sudden changes in the conductivity matrix cause convergence problems. Preliminary studies showed that using element birth and death significantly reduced convergence rate and it costs more computing time, while the results are just about the same as those without using element birth and death control method. Therefore, a much simpler approach was used in this study. The added material, the clad, was included in the original mesh with a initial temperature 1950 °C, 500 °C above its liquidus temperature. And the heat source, a flux disc with double Gaussian distribution, was applied on top of the clad.

The finite element mesh of the clad and the adjacent region used in analyzing the first and second pass clads are shown in Figure 2.8 and 2.9.

2.8 Model Implementation with ANSYS

When performing finite element analysis using ANSYS, three major steps are to be followed. The first step is called preprocessing. In this step, the finite element model is built by defining the element types, material properties, model geometry and by discretizing the finite element model. In this study, 8-node isoparametric thermal elements (Plane55) were used to discretize the finite element model. This element type has optional quadratic and linear (no mid-nodes) formulations. A element can be either quadrilateral or triangular. These formulation options have added a lot of flexibility to the use of this element type. All the information of the finite element model is written

into a database file.

The second step is to define initial and boundary conditions, to apply loads, and to obtain solutions. In this step, the history of loads is discretized in load steps, and options for solving the equations are also specified. The equations are then solved and the results are written to the results file. Database file is updated in this step too. Equations are usually solve with wave front method.

The last step in the finite element analysis is called postprocessing in which one reviews the results. One can obtain contour displays, deformed shapes, and tabular listings to review and interpret the results of the analysis. Other capabilities, including error estimation, load case combinations, calculations among results data, and path operations are also available. Graphics can be exported to postscript files and listings can be exported to ASCII files for further analysis.

A few parameters are defined here for the computational results in order to compare the computational results with the experimental measurements. The depth of penetration is defined by the maximum distance from the original clad/substrate interface to the computed fusion line. The computed fusion line is composed of points in the substrate base metal where the peak temperature experienced is equal to the solidus of the material. The size of the Heat affected zone is defined by the maximum distance from the fusion line to the points where the peak temperature experienced equal to the Ae_1 point of the steel. Furthermore, the size of the coarse grain region is defined by the distance from the fusion line to the points where the peak temperature experienced equal to 1100 °C according to Harrison and Farrar.[141]

Computers used in the finite element analysis were IBM and HP work stations. The results of computer simulation for the experimental cladding shafts and the optimized initial temperature distribution for different shaft sizes are presented in the Chapter 4.

CHAPTER 3
MICROSTRUCTURE PREDICTION MODEL

As identified in Chapter 1, the major objective of this research is to predict the microstructural development in the heat affected zones of multipass electroslag cladding. Thermal analysis is important and necessary for the overall analysis because it generates the thermal cycles experienced by the heat affected zones. However, the principal focus of this research is to analyze the microstructural development that occurs in the electroslag cladding heat affected zones so that the resultant microstructure will be predicted.

A brief overview of the microstructural changes in the heat affected zone of low alloy steels is presented in Section 3.1. A comprehensive computer algorithm has been developed in this research to model the whole process of phase changes in the heat affected zones. The global algorithm embraces thermodynamics based models for computing multicomponent Fe-C-M system equilibria, a semi-empirical model for austenite grain growth in weld heat affected zone, and a reaction kinetics model for austenite decomposition reactions. Details of these models are presented in Section 3.2, 3.3 and 3.4. Empirically based formulas for the calculation of weld heat affected zone hardness are presented in Section 3.5.

3.1 Microstructural Changes in the Heat Affected Zone

The microstructure development in electroslag cladding heat affected zone depends predominately on the thermal cycle and steel composition. Shown in Figure 3.1 is a cross sectional photograph of a single pass electroslag clad and its adjacent heat affected

zone. The microstructure in the heat affected zone changes from location to location depending primarily on peak temperatures experienced in local areas.

An equilibrium phase diagram of binary Fe-C metastable system as well as a typical thermal cycle in the heat affected zone are given in Figure 3.2 to indicate the transformations that must be considered in the computational modeling. It must be noted that the equilibrium phase diagram of a low alloy steel will differ from that in Figure 3.2. Any low alloy steel is a multicomponent thermodynamics system. The eutectoid reaction in such a multicomponent system would occur in a temperature range. In other words, the eutectoid region in the multi-dimensional phase diagram is represented by a multi-dimensional region. The author has designated Ae_1 and As_1 temperatures as the upper and lower limits of eutectoid reaction in a low alloy steel. A detailed model for the computation of critical temperatures for phase transformations in low alloy steels are presented in Section 3.2.

In this study, the base metal steel was provided in normalized condition, which consisted of ferrite and pearlite. It is reasonable to assume the initial amounts of ferrite and pearlite are at their equilibrium quantities. On heating the steel is assumed to be in equilibrium and the microstructure would not change until temperature reaches As_1 temperature. At As_1 temperature, pearlite in the steel starts to change into austenite and all pearlite will be completely transformed to austenite at Ae_1 temperature. Ferrite would transform into austenite at temperatures from As_1 to Ae_3. At Ae_3 temperature, all ferrite has been transformed into austenite.

At temperatures above Ae_3 temperature, only austenite exists. Newly formed austenite has very fine grains. For most low alloy steels, the average size of newly formed austenite grains is approximately 5 microns.[117] These grains have strong tendency to grow larger so that the surface energy at grain boundaries would be reduced. Growth of austenite grains is very stagnant at temperatures slightly above the Ae_3 temperature of steel due to the pinning effect of carbide and nitride precipitates until the precipitate dissolution temperature, T_{DISS}, is reached.[170] Austenite grains would grow at temperatures higher than the dissolution temperature T_{DISS}.

As the temperature goes below Ae_3 during cooling, austenite starts to decompose

into ferrite. Ferrite is a body-centered crystal structure. Should appreciable amount of ferrite be formed, it would appear as a network or in parallel laths. It is a fairly soft and ductile structure.

At temperatures below Ae_1, ferrite formation continues and pearlite formation starts. Should appreciable amount of pearlite be formed, it would appear in colonies and each colony consists of alternate plates of $(FeM)_3C$ and ferrite, with ferrite being the continuous phase. Pearlite is not a phase, but a mixture of two phases.

Both ferrite and pearlite reactions are nucleation and growth transformations controlled by the diffusion of elements. Ferrite and pearlite are usually recognized as high temperature decomposition products. In the welding heat affected zone of low alloy steels, it is very rare for these two reactions to go to completion. The lower the welding heat input and the better the steel hardenability, the harder for these two reactions to reach completion.

At temperatures below Bs temperature, the formation of bainite would take precedence over ferrite and pearlite. The untransformed austenite would start to transform into bainite. Bainite reaction is also a nucleation and growth transformation. Depending on the temperature at which bainite is formed, bainite is often further classified as upper bainite and lower bainite and they have different morphologies. Upper bainite is formed at higher temperatures and it consists of needles or ferrite laths with cementite precipitates between the laths. Lower bainite is formed at lower temperatures and it consists ferrite plates with very fine carbide dispersed in the plates. Like pearlite, bainite is not a phase but a mixture of ferrite and carbide and it is slightly harder than ferrite+pearlite structure.

As the temperature goes below Ms temperature, the untransformed austenite starts to transform into martensite and bainite formation would most likely continue until there is no untransformed austenite. Martensite reaction is known to be athermal. The transformation is a function of temperature only. It is produced by shear movements of the austenite lattice, producing a body-centered tetragonal lattice. Martensite is considered a phase and is the hardest of all austenite decomposition products in steels.

Accurate modeling of the microstructure development would require knowledge

of the critical temperatures of phase transformations and the kinetics of austenite grain growth and decomposition reactions. The following sections are dedicated to the description of thermodynamics based models for computing multicomponent Fe-C-M system equilibria, a semi-empirical kinetics model for austenite grain growth, and an reaction kinetics model for austenite decompositions. All these models are with special reference to low alloy steels.

3.2 Thermodynamics of Multicomponent Fe-C-M System Equilibria

There is more experimental information on phase equilibria in iron-base alloys than in any other system. Nevertheless, it is still far from having full information on the iron-base alloy phase diagrams. Thus it is always desirable to treat the available information in such a way that the unknown parts of phase diagrams could be predicted based on reasonable mathematical representations.

Mathematical representation for each individual phase in equilibria is of crucial importance for success. It is always possible to describe the available information with a desired precision and to obtain an adequate interpolation between the experimental points. However, it is vital to work with a mathematical representation which is based on a sound theoretical model so that reasonable extrapolations outside the experimental range can be obtained. In developing such a mathematical representation, it is practically impossible to work with a model which accounts for all the effects involved with a satisfactory accuracy. Even if there exists such a description for a simple system, it may be practically impossible to use it in a treatment of a system with more components. Therefore, all the trivial aspects have to be eliminated while only the essence of the thermodynamic equilibria remains. In general, one must accept working with fairly simple expressions and it is always advisable not to use many parameters in order to obtain good agreement with the available experimental information.[195] The present state of art in thermodynamic modeling has not gone beyond regular solution model with Wagner formulation[196] and subregular solution model by Hillert and Staffansson.[197]

Scientists have observed three types of equilibria in low alloy steels. The

common perception of equilibrium requires full partitioning of all alloying elements. This type of equilibrium is often known as "ortho-equilibrium" (OE).[198] However, substitutional alloying elements in low alloy steels diffuse much slower than interstitial elements such as carbon. Thus partitioning of substitutional alloying elements will be limited during $\gamma \rightarrow \alpha$ transformation at normal commercial cooling and transformation rates. Two distinct limiting cases have been recognized. The first is designated as "para-equilibrium" (PE) by Hultgren,[198] Hillert,[199] and Aaronson *et al.*[200] The second is designated as "no-partition local equilibrium" (NPLE) by Hillert,[201] Popov and Mikhalev,[202] and Purdy *et al.*[203] PE is defined by a uniform carbon chemical potential and a continuous substitutional alloying element to iron mole fraction ratio at the transforming interface. NPLE is define by a no-partition local equilibrium for all components at the interface which requires a corresponding steep diffusion profile spike of alloying elements ahead of the interface. In this research, only the ortho-equilibrium and para-equilibrium are considered and analyzed.

The austenite-ferrite equilibrium can be analyzed using the regular solution model with Wagner formalism,[196] which, given the dilute nature of all alloying element additions and using empirical interaction parameters, is rigorous. The austenite-stoichiometric cementite equilibrium can be quantified using an integral of the Gibbs-Duhem equations together with empirical partition coefficients, or analyzed using the subregular solution model proposed by Hillert and Staffansson.[197]

Kirkaldy and Baganis[204] first successfully computed ortho-equilibrium Ae_3 temperature of steels with additions of Mn, Si, Ni, Cr, Mo and Cu based on Wagner formulation. They offered an analytical solution for low concentrations (total alloying element additions up to 2.5 wt%) and a general non-analytical computer solution for higher composition limits (total alloying element additions up to 7.0 wt%). In their computation, equilibrium equation for iron was treated as the key equation and was solved using Newton-Raphson method. Other equilibrium equations for carbon and alloying elements were solved using iteration schemes. Their computations compared favorably with observations on over 200 steels from international compendium.

Thermodynamic data of W, V, Nb, and Co were added to the model by Kirkaldy,

Thomson, and Baganis.[205] They devised a scheme based on Gibbs-Duhem equation to represent the deviation of Acm curve from the binary Fe-Fe_3C phase diagram. To calculate the eutectoid point, they kept the carbon content in austenite as a main variable. The eutectoid point was defined as the common point of the computed Ae_3 curve and Acm curve. The temperature at this point was called Ae_1 temperature of the steel. The carbon content at this point was termed eutectoid composition. The computation was considerably simplified by introducing analytical approximations for binary Fe-Fe_3C phase diagram and by neglecting self interactions in computing equilibria of carbon and substitutional alloying elements. Based on these assumptions, they proposed an simple equation to compute the partitioning coefficient of alloying elements for α-γ equilibrium.

It must be noted that the computed eutectoid "point" as defined by Kirkaldy, Thomson and Baganis[205] was not based on strict sense of thermodynamic equilibria in a multicomponent system. In a multicomponent Fe-C-M system, eutectoid reaction does not occur at a fixed temperature and composition point, but within a temperature range. Further austenite decomposition to ferrite at temperatures lower than Ae_3 is not restrained in the isopleth of the same alloying element concentrations. The compositions of austenite and ferrite at a certain temperature can only be defined theoretically by a tie-line passing through the steel composition point in the multi-dimensional space. There is an α-γ-cementite three phase region in the multicomponent phase diagram. If projected into three-dimensional Fe-C-X spaces, this region is made up of a stack of tie-triangles; the positions, at various temperatures, of the tie-lines bounding the triangles, mark out the boundary surfaces of the region and the corresponding corner positions of the triangle mark out the boundary curves. Each corner of the tie-triangle represents the composition of a phase.

All the aforementioned three types of equilibria were modelled by Hashiguchi *et al.*[206] with the regular solution model for the α-γ equilibria with Wagner formalism and a regular solution model for γ-cementite equilibria. The algorithms have been devised in their formulations to account for different equilibria. Better accuracy and consistency have been reported. Simplifications made by Kirkaldy, Thomson, and Baganis[205] regarding the partitioning of alloying elements were also adopted in the work of

Hashiguchi *et al.*[206] They defined Ae_1 temperature as the upper limit of the temperature range for the $\alpha+\gamma+$cementite three phase region in a steel. Their computed Ae_1 temperatures were consistently higher than the measured ones which actually designated the lower limit of this range. They did not define nor compute the lower limit of this three phase eutectoid reaction region in steels.

A comprehensive review on computing multicomponent iron-base phase diagrams for hardenable steels and HSLA steels has been recently presented by Kroupa and Kirkaldy.[207] The algorithm developed by Kirkaldy, Thomson and Baganis[205] was used by Sugden and Bhadeshia[208] and some citation and printing errors in the original publication[205] were corrected. The computation accuracy was reportedly improved by introducing iteration method.

In this research, Ae_1 temperature is defined as the upper limit of the $\alpha+\gamma+$cementite three phase region in the n-dimensional equilibrium phase diagram. The temperature at which austenite is completely decomposed to $\alpha+$cementite is defined as As_1, which represents the lower limit of the $\alpha+\gamma+$cementite three phase region in the n-dimensional phase diagram. The austenite composition at the As_1 temperature is thus defined as the eutectoid composition. Physically, Ae_1 and As_1 temperatures represent two limiting cases where steel composition point is located at tie-lines for α-γ equilibrium and α-cementite equilibrium. The practical significance of Ae_1 and As_1 temperatures is that they represent the asymptote of pearlite start and pearlite finish curves in a TTT diagram.

3.2.1 Basic Concept

This section is committed to the description of the computational thermodynamic model of multicomponent Fe-C-M equilibria for the prediction of equilibrium diagrams of steels with addition of alloying elements Mn, Si, Ni, Cr, Mo, Cu, W, V, Nb. The advantages of the thermodynamic method lie in its theoretical validity and simplicity, and its computation economy in predicting phase transformation related thermodynamic quantities such as Ae_3, Ae_1 temperatures and the eutectoid composition, and equilibrium amount of ferrite, cementite and austenite and the composition in each phase.

Simplifications made by Kirkaldy *et al.*[204-207] are tested in this research by including newly available thermodynamic data.[209]

In the following description, all the elements are designated with numbered subscripts, Fe the solvent as 0, C as 1, and substitutional alloying elements such as Mn, Si, Ni, Cr, Mo, Cu, W, V, and Nb as i=2,3,....n respectively. The chemical potentials of iron and alloying elements are expressed using the regular solution model with Wagner[206] expansions for the activity coefficients

$$\mu_0 = {}^0G_0 + RT\ln X_0 - \frac{RT}{2}\sum_{i=1}^{n}\epsilon_{ii}X_i^2 - RTX_1\sum_{i=2}^{n}\epsilon_{1i}X_i \qquad (3.1)$$

$$\mu_1 = {}^0G_1 + RT\ln X_1 + RT\sum_{i=1}^{n}\epsilon_{1i}X_i \qquad (3.2)$$

$$\mu_i = {}^0G_i + RT\ln X_i + RT(\epsilon_{1i}X_1 + \epsilon_{ii}X_i) \qquad (i=2 \text{ to } n) \qquad (3.3)$$

where ${}^0G_i$ is the standard free energy of element i in infinite dilute iron solution, and X_i denotes the mole fraction of element i, ϵ_{ij} the interaction coefficient between element i and element j.

The Gibbs free energy of carbides (cementite) is described by the subregular solution model originally proposed by Richardson[210] and by Hillert *et al.*[211] This model is used in this research to model the γ-cementite equilibrium. In the formulation of this model, all thermodynamic quantities are referred to one mole of metal atoms. The carbide formula M_3C are thus rewritten as $MC_{1/3}$. The chemical potentials of the carbides are expressed by

$$\mu_{FeC_{1/3}} = \mu_{Fe} + \frac{1}{3}\mu_1 = {}^0G_{FeC_{1/3}} + RT\ln Y_0 + \sum_{i=2}^{n}A_{0i}Y_i^2 \qquad (3.4)$$

$$\mu_{MC_{1/3}} = \mu_i + \frac{1}{3}\mu_1 = {}^0G_{MC_{1/3}} + RT\ln Y_i + A_{0i}(1-Y_i)^2 \qquad (3.5)$$

In Equation 3.4 and 3.5, Y_0 and Y_i (i=2 to n) are concentrations of metal elements in cementite expressed by $Y_i = X_i/(1-X_1) = 4X_i/3$ for i=0, 2 to n, which represents the

fraction of lattice sites occupied by element i. The parameter A_{0i} is the interaction coefficient between iron and the substitutional alloying element i in the carbides. Interactions between substitutional alloying elements are justifiably neglected.

3.2.2 $\alpha+\gamma$ Equilibria

Ortho-Equilibrium

By definition, Ae_3 temperature designates the temperature at which, under equilibrium conditions, the γ iron or austenite (fcc) solution for a given steel composition begins to decompose into α iron or ferrite (bcc). Consequently the Ae_3 temperatures of a multicomponent system defines the bottom floor of the austenite field. It can be computed according to the rigorous thermodynamic model for multicomponent system.

The ortho-equilibrium between α and γ phases is defined by

$$\mu_i^{\alpha} = \mu_i^{\gamma} \qquad (i=0 \text{ to } n) \qquad (3.6)$$

In the computation of Ae_3 temperature of a steel, X_i^{γ} are all known as the steel composition. In these n+1 equations, there are n+1 unknowns which include n number of X_i^{α} and temperature. Theoretically, all these unknowns can be determined from the n+1 equations.

The key equation in computing Ae_3 temperature of steels is the equilibrium equation for iron (i=0) to which all alloying elements contributed

$$\frac{\Delta^0 G_0^{\alpha\to\gamma}}{RT} + \ln\frac{1-\sum_{i=1}^{n} X_i^{\alpha}}{1-\sum_{i=1}^{n} X_i^{\gamma}} + X_1^{\alpha}\sum_{i=2}^{n}\epsilon_{1i}^{\alpha}X_i^{\alpha} - X_1^{\gamma}\sum_{i=2}^{n}\epsilon_{1i}^{\gamma}X_i^{\gamma} + \frac{1}{2}\sum_{i=1}^{n}\epsilon_{ii}^{\alpha}(X_i^{\alpha})^2 - \frac{1}{2}\sum_{i=1}^{n}\epsilon_{ii}^{\gamma}(X_i^{\gamma})^2 = 0 \qquad (3.7)$$

This equation is nonlinear and can be solved using Newton-Raphson method. At each

trial temperature, equations for alloying elements (i=1 to n) are first solved using iteration method to obtain the mole fractions of alloying elements in ferrite phase. To reduce the number of iterations, the iteration starts with the first order approximations provided by Kirkaldy *et al.*[207]

$$X_1^{\alpha} = \frac{X_1^{\gamma} \exp\left(\frac{\Delta^0 G_1^{\alpha\to\gamma}}{RT} + \epsilon_{11}^{\gamma} X_1^{\gamma}\right)}{1 + \epsilon_{11}^{\alpha} X_1^{\gamma} \exp\left(\frac{\Delta^0 G_1^{\alpha\to\gamma}}{RT}\right)} \tag{3.8}$$

and

$$X_i^{\alpha} = \frac{X_i^{\gamma} \exp\left(\frac{\Delta^0 G_i}{RT} + \epsilon_{11}^{\gamma} X_1^{\gamma}\right)}{1 + \epsilon_{1i}^{\alpha} X_1^{\alpha}} \tag{3.9}$$

Iterations are then conducted for the equilibria of alloying elements (i=1 to n) until converged solutions for X_i^{α} are obtained. Normally convergence is obtained within 10 iterations. Convergence may become a problem for steels with more than 1.5 wt% Si addition and with medium or high carbon concentration.

Solutions obtained in this method are considered more accurate than those computed by Kirkaldy *et al.*[206,207] because this algorithm accounts for the self interaction of alloying elements in different phases and interaction between carbon and alloying elements in different phases. The simplifying assumptions made by Kirkaldy *et al.* in deriving approximations for alloying element partitioning coefficients are therefore released.

Two equations regarding the mole fraction of iron in different phases are then added to the system

$$X_0^{\gamma} = 1 - \sum_{i=1}^{n} X_i^{\gamma} \tag{3.10}$$

$$X_0^{\alpha} = 1 - \sum_{i=1}^{n} X_i^{\alpha} \tag{3.11}$$

Then computed X_i^{α} and X_i^{γ} (i=1 to n) are substituted into Equation 3.7 to determine the only unknown variable, T, the Ae_3 temperature.

Para-Equilibrium

Para-equilibrium is defined in Equation 3.12, 3.13, 3.14 according to the free energy construction by Gilmour[212]

$$\mu_1^{\gamma} = \mu_1^{\alpha} \tag{3.12}$$

$$X_i^{\alpha}/X_0^{\alpha} = X_i^{\gamma}/X_0^{\gamma} = X_i/X_0 = k_i \tag{3.13}$$

$$X_0^{\gamma}(\mu_0^{\gamma} - \mu_0^{\alpha}) + \sum_{i=2}^{n} X_i^{\gamma}(\mu_i^{\gamma} - \mu_i^{\alpha}) = 0 \tag{3.14}$$

The carbon mole fraction in ferrite can be determined using the same approach as in computing ortho-equilibrium Ae_3 temperature.

Summing X_i from i=2 to n using relations in Equation 3.13 yields

$$\sum_{i=2}^{n} X_i = 1 - X_0 - X_1 = X_0 \sum_{i=2}^{n} k_i \tag{3.15}$$

Solving for X_0, one obtains

$$X_0 = \frac{1 - X_1}{1 + \sum_{i=2}^{n} k_i} \tag{3.16}$$

$$X_i = \frac{k_i(1 - X_i)}{1 + \sum_{i=2}^{n} k_i} \tag{3.17}$$

Equation 3.16 and 3.17 are true in both α and γ phases. Thus all the terms in Equation 3.14 are solved from Equation 3.12, 3.16 and 3.17 using iteration method. The temperature for α-γ para-equilibrium, defined as Ap_3, can then be obtained by solving Equation 3.14 using Newton-Raphson method. It was also noted that convergence becomes a problem for steels with more than 1.5 wt% Si addition and with medium or high carbon concentration.

3.2.3 $\alpha+\gamma+$cementite Equilibria

Ortho-Equilibrium

At temperatures below Ae_3, further decomposition of austenite into ferrite will change the composition of both phases. These composition changes in α and γ phases under equilibrium can still be described by Equation 3.7, 3.8, and 3.9. Same approaches described in section 3.2.2 are used for computing α and γ equilibrium. The only difference is that in this case, both X_1^{γ} and temperature are set as trial parameters.

In the computation of Ae_1 and As_1 temperatures, n more unknowns, X_i^{γ}, are added to the nonlinear equation system. But they are related to the steel composition and X_i^{α}. In the computation of Ae_1 temperature, points (X_1^{α}, X_i^{α}) and (X_1^{γ}, X_i^{γ}) are at the two ends of a tie-line in the n-dimensional phase diagram going through the alloy composition (X_1, X_i). Thus these coordinates are related by the lever rule:

$$X_i^{\gamma} - X_i = \frac{X_i^{\gamma} - X_i^{\alpha}}{X_1^{\gamma} - X_1^{\alpha}} (X_1^{\gamma} - X_1) \qquad (3.18)$$

This adds n-1 more equations to the system and they can be solved along with Equation 3.8 and 3.9. Similarly in the computation of As_1 temperature, points (X_1^{α}, X_i^{α}) and (X_1^{cem}, X_i^{cem}) are at the two ends of a tie-line for α-cementite equilibrium in the n-dimensional phase diagram going through the alloy composition (X_1, X_i). Equations

$$X_i^{cem} - X_i = \frac{X_i^{cem} - X_i^{\alpha}}{X_1^{cem} - X_1^{\alpha}} (X_1^{cem} - X_1) \tag{3.19}$$

are added to the equation system and they are solved along with Equation 3.8 and 3.9.

The equilibrium between cementite and γ is expressed by substituting Equation 3.1 and 3.3 into 3.4 and 3.5. This yields

$$\frac{1}{3}(3^0G_{FeC_{1/3}}^{cem} - 3^0G_{Fe}^{\gamma} - {}^0G_C^{\gamma}) + RT\ln\frac{Y_0^{cem}}{X_0^{\gamma}} - \frac{1}{3}RT\ln X_1^{\gamma} + \sum_{i=2}^{n} A_{0i}^{cem} Y_i^{cem^2} + RT\sum_{i=1}^{n}(\frac{1}{2}\epsilon_{ii}^{\gamma} X_i^{\gamma^2} - \frac{1}{3}\epsilon_{1i}^{\gamma} X_i^{\gamma}) = 0 \tag{3.20}$$

$$\frac{1}{3}(3^0G_{MC_{1/3}}^{cem} - 3^0G_i^{\gamma} - {}^0G_1^{\gamma}) + RT\ln\frac{Y_i^{cem}}{X_i^{\gamma}} - \frac{1}{3}RT\ln X_1^{\gamma} + A_{0i}^{cem}(1 - Y_i^{cem})^2 - \epsilon_{1i}^{\gamma} X_1^{\gamma} - \epsilon_{ii}^{\gamma} X_i^{\gamma} - \frac{1}{3}\sum_{i=1}^{n}\epsilon_{1i}^{\gamma} X_i^{\gamma} = 0 \tag{3.21}$$

The key equations for the computation of Ae_1, As_1 temperatures are Equation 3.7 and 3.20. They are solved together with Newton-Raphson method. For each trial temperature and carbon mole fraction in austenite, X_1^{γ}, mole fractions of alloying elements in ferrite and austenite phases are computed by solving Equation 3.18 or 3.19, and 3.6 for i=1 to n using iteration method. The computed mole fractions of alloying elements in austenite, X_i^{γ} are then substituted into Equation 3.21 to solve for the values of all the molar ratios of alloying elements in cementite, Y_i's, using iteration method. Note that Y_{Si} and Y_{Cu} are set to zero because both Si and Cu and known not to dissolve in cementite. Thus Equation 3.7 and 3.20 only contain two unknown variables, T and X_1^{γ}, which are the Ae_1 or As_1 temperature and the austenite composition at this temperature. The austenite composition at As_1 is defined as the eutectoid composition in this research.

Para-Equilibrium

The definitions of Ae_1, As_1 and the eutectoid composition under ortho-equilibrium are also adopted in para-equilibrium computation. In a similar method as for ortho-equilibrium, they are determined using Newton-Raphson method.

The para-equilibrium conditions for γ and cementite are expressed as

$$X_i^\gamma / X_0^\gamma = Y_i / Y_0 = X_i / X_0 = k_i \tag{3.22}$$

except for Si and Cu, (Y_{Si} and Y_{Cu} are set to zero) and

$$X_0^\gamma (\mu_{FeC_{1/3}}^{cem} - \mu_0^\gamma - \frac{1}{3}\mu_1^\gamma) + \sum_{i=2}^{n} X_i^\gamma (\mu_{MC_{1/3}}^\gamma - \mu_i^\gamma - \frac{1}{3}\mu_1^\gamma) = 0 \tag{3.23}$$

In a similar procedure as for $\alpha \rightarrow \gamma$ para-equilibrium, equation 3.22 results in

$$X_i^\gamma = \frac{(1 - X_1^\gamma) k_i}{1 + \sum_{i=2}^{n} k_i} \tag{3.24}$$

and

$$Y_i^{cem} = \frac{k_i}{1 + \sum_{i=2}^{n} k_i} \tag{3.25}$$

in which Y_i is constant and X_i^γ is a function of X_1^γ only. Thus Equation 3.14 and 3.23 only contain two unknowns, T and X_1^γ. They are solved using Newton-Raphson method.

3.2.4 Thermodynamics Data

There are considerable discrepancies in the reported experimental and calculated thermodynamic values for Fe-C-M multicomponent systems. There exist a number of errors in the thermodynamic data cited by Kirkaldy, Thomson and Baganis[207] and some of those have been pointed out and corrected by Sugden and Bhadeshia.[211] The accuracy

and consistency of the thermodynamic data set significantly affect the accuracy of predictions. Therefore careful evaluation of the thermodynamic data set is necessary and has been done in this research.

The temperature dependent standard Gibbs free energy change Δ^0G for the $\alpha \rightarrow \gamma$ phase change of pure iron solution have been calculated by Weiss and Tauer,[213] Smith and Darken,[214] Kaufman, Clougherty, and Weiss,[215] Orr and Chipman,[216] and Harvig.[217] The results of different sources compare very well with each other. The data presented by Harvig[217] are tabulated in Table 3.1 and are used in this research.

The standard molar Gibbs free energy changes Δ^0G_i (i=1,2.....n) for alloying element i in infinite dilute iron-base solution for $\alpha \rightarrow \gamma$ phase change have been experimentally measured from binary Fe-M phase diagrams using different mathematical formulations.

The data provided by Kirkaldy and his coworkers[206-208] were evaluated based on commonly used regular solution model

$$\mu_i = {}^0G_i + RT\ln X_i + E_{G_i} \tag{3.26}$$

The first order Taylor expansion due to Wagner applied to the logarithm of the activity coefficient of every element in the dilute iron-base solution yields

$$E_{G_i} = RT\ln\gamma_i = \sum_{j=1}^{n} \epsilon_{ij} X_j \tag{3.27}$$

which accounts for the deviation from the ideal solution for element i. Equation 3.26 is the general form of Equation 3.1, 3.2 and 3.3. Wagner interaction parameter ϵ_{ij}'s are normally used effectively as empirical parameters in thermodynamic analysis of alloy systems. Considering a system composed of solvent 0 and n alloying elements, $\Delta^0G_i^{\alpha\rightarrow\gamma}$ can be evaluated by

$$\frac{\Delta^0 G_i^{\alpha\rightarrow\gamma}}{RT} = \ln\frac{X_i^{\alpha}}{X_i^{\gamma}} + \ln\frac{\gamma_i^{\alpha}}{\gamma_i^{\gamma}} \tag{3.28}$$

In their computation, Kirkaldy and his coworkers[206-208] neglected the interactions

of different substitutional alloying elements. They argued that the interactions of different substitutional elements should be small compared to those between metal and carbon. Also, due to the different signs of the interaction parameters, the interactions may very well cancel each other. Their computation results showed that the interaction parameters affected the Ae_3 temperature by only a few degrees, thus the error introduced by not including interactions between substitutional alloying elements is of the same order as the experimental uncertainty in measuring the Ae_3. Furthermore, Kirkaldy and Baganis had taken ϵ_{11}^{α} as zero. This is a justifiable assumption because eventually ϵ_{11}^{α} is multiplied by the very low concentration of carbon in ferrite. With or without this assumption, the computational result is essentially the same. Also because the interactions between alloying elements and carbon are normally not known, they are assumed to be the same as those in austenite. The thermodynamic data set used by Kirkaldy and Baganis[206,207] are tabulated in Table 3.2

Probably the most complete and accurately measured thermodynamic data to date were presented by Uhrenius.[209] All the data in this compendium were measured based on the subregular solution model originally developed by Hillert and Staffansson.[197] This model is a generic representation for ionic melts and interstitial solid solutions and is based on the use of atomic ratios rather than atom fractions. Thus the concentration of an interstitially dissolved element is expressed by the fraction of interstitial sites occupied by that element. As an example, ferrite has three interstitial sites for carbon per metal atom (lattice site) whereas austenite has only one. This means that a certain carbon content should be expressed differently in these two cases. This is done by the ratio c/a where a denotes the number of metal atoms per mole and c the corresponding number of interstitial sites per mole of metal atoms available. Thus $c/a=1$ for austenite and $c/a=3$ for ferrite. The molar ratios Y_i are defined by

$$Y_M = X_M/(1-X_C) \tag{3.29}$$

and

$$Y_C = a/c \cdot X_C/(1-X_C) \tag{3.30}$$

The subscript M stands for iron and substitutional alloying elements and C for carbon.

X_i denotes the mole fraction of element i. The chemical potential of the components can be derived from the expression for the integral Gibbs free energy as given by Hillert and Staffansson[197]

$$\mu_{Fe} = {}^0G_{Fe} + RT\ln Y_{Fe} + c/aRT\ln(1-Y_1) + E_{G_{Fe}} \tag{3.31}$$

$$\mu_C = {}^0G_C + RT\ln[Y_C/(1-Y_C)] + E_{G_C} \tag{3.32}$$

$$\mu_M = {}^0G_M + RT\ln Y_M + c/aRT\ln(1-Y_1) + E_{G_M} \tag{3.33}$$

The excess energies terms are given by

$$\begin{aligned} E_{G_{Fe}} = & -Y_M Y_C[\Delta G_M + {}^0L^C_{FeM} - {}^0L^v_{FeM} + L^M_{Cv} - L^{Fe}_{Cv} + (1-2Y_M)({}^1L^v_{FeM} - {}^1L^C_{FeM})] \\ & + Y_M^2[{}^0L^v_{FeM} + (3-4Y_M){}^1L^v_{FeM}] + Y_C^2 L^{Fe}_{Cv} + 2Y_M Y_C^2(L^M_{Cv} - L^{Fe}_{Cv}) \\ & + 2Y_M^2 Y_C[{}^0L^C_{FeM} - {}^0L^v_{FeM} + (2-3Y_M)({}^1L^C_{FeM} - {}^1L^v_{FeM})] \end{aligned} \tag{3.34}$$

$$\begin{aligned} cE_{G_C} = & (1-2Y_C)L^{Fe}_{Cv} + Y_M(\Delta G_M + {}^0L^C_{FeM} - {}^0L^v_{FeM} + L^M_{Cv} - L^{Fe}_{Cv}) \\ & + 2Y_M Y_C(L^{Fe}_{Cv} - L^M_{Cv}) + Y_M^2({}^0L^v_{FeM} - {}^0L^C_{FeM}) \end{aligned} \tag{3.35}$$

$$\begin{aligned} E_{G_M} = & Y_{Fe} Y_C[\Delta G_M - {}^0L^v_{FeM} - {}^0L^C_{FeM} + (1-2Y_M)({}^1L^v_{FeM} - {}^1L^C_{FeM}) + L^M_{Cv} - L^{Fe}_{Cv}] \\ & + Y_{Fe}^2[{}^0L^v_{FeM} + (1-4Y_M){}^1L^v_{FeM}] + Y_C^2 L^M_{Cv} + 2Y_{Fe} Y_C^2(L^{Fe}_{Cv} - L^M_{Cv}) \\ & + 2Y_{Fe}^2 Y_C[{}^0L^C_{FeM} - {}^0L^v_{FeM} + (1-3Y_M)({}^1L^C_{FeM} - {}^1L^v_{FeM})] \end{aligned} \tag{3.36}$$

The parameter ΔG_M is a difference between four standard states.

$$\Delta G_M = {}^0G_{Fe} + {}^0G_{MC_{c/a}} - {}^0G_{FeC_{c/a}} - {}^0G_M \tag{3.37}$$

Two of these, $MC_{c/a}$ and $FeC_{c/a}$, are hypothetical because all the interstitial sites in ferrite and austenite cannot be filled with carbon. Instead, the whole expression for ΔG_M may be regarded as a parameter representing the interaction between carbon and the substitutional alloying element. The L parameters are also interaction parameters, *e. g.*, L_{Cv}^{Fe} represents the interaction between carbon atoms and vacancies when the metal lattice is completely filled with iron atoms.

Comparing Hillert and Staffasson's subregular solution model to the regular solution model with Wagner formulation, the standard Gibbs free energy change of element i in infinite dilute iron-base solution for $\alpha \rightarrow \gamma$ phase change can be derived by the limiting case $Y_0 \rightarrow 1.0$ and $Y_i \rightarrow 0$ (i=1,2,...n).

$$\Delta G_1^{\alpha \rightarrow \gamma} = {}^0G_1^{\gamma} - {}^0G_1^{\alpha} + \ln(a/c)^{\gamma} - \ln(a/c)^{\alpha} \tag{3.38}$$

$$\Delta {}^0G_M^{\alpha \rightarrow \gamma} = {}^0G_M^{(\gamma)}(p.c.) - {}^0G_M^{(\alpha)}(p.c.) + {}^0L_{FeM}^{\nu(\gamma)} + {}^1L_{FeM}^{\nu(\gamma)} - {}^0L_{FeM}^{\nu(\alpha)} - {}^1L_{FeM}^{\nu(\alpha)} \tag{3.39}$$

$$\epsilon_{11} = \frac{a+c}{c} + \frac{1}{RT}\frac{\partial E_{G_1}}{\partial X_1} = \frac{a+c}{c} - \frac{2L_{Cv}^{Fe}}{c^2 RT} \tag{3.40}$$

$$\epsilon_{ii} = \frac{\partial E_{G_i}}{\partial X_i} = -\frac{2({}^0L_{FeM}^{\nu} + 3 \times {}^1L_{FeM}^{\nu})}{RT} \tag{3.41}$$

$$\epsilon_{1i} = \frac{1}{RT}\frac{\partial E_{G_1}}{\partial X_i} = \frac{\Delta G_M + {}^0L_{FeM}^{C} - {}^0L_{FeM}^{\nu} + L_{Cv}^{M} - L_{Cv}^{Fe}}{cRT} \tag{3.42}$$

${}^0G_i^{\alpha \rightarrow \gamma}$ data set evaluated from Equation 3.38 and 3.39 are tabulated in Table 3.3. They are in good numerical agreement with the values presented in Table 3.2. In this research, the ${}^0G_i^{\alpha \rightarrow \gamma}$ values in Table 3.2 are used in the computations because they are more consistent with the formulation of this model.

Other thermodynamics data used in the computations are tabulated. The standard magnetic entropy of α iron is taken from the tabulation of Weiss and Tauer[19] (Table 3.4). Interaction coefficients evaluated from Equation 3.40, 3.41, and 3.42 are tabulated in Table 3.5 and 3.6 based on the data presented by Uhrenius.[209] With the availability of these data, it is possible to evaluate and release the simplifications made by Kirkaldy and his coworkers[204-206] in their calculations. The standard free energy change between cementite and γ phase are presented in Table 3.7 from the data presented by Uhrenius.[209] Interaction coefficients between iron and substitutional alloying elements in cementite are presented in Table 3.8. They were evaluated from the values by Uhrenius.[209]

3.3 Austenite Grain Growth

The austenite grain size is a very important microstructure factor for austenite decomposition reactions because grain boundaries provide nucleation sites for phase transformations. Thus it is always desirable to predict prior austenite grain growth in order to predict the microstructure development. This section is to present the kinetics theory and parameters for austenite grain growth in low alloy steels.

There are basically two types of grain growth, *normal* and *abnormal*. Normal grain growth begins with a structure of uniformly distributed and randomly oriented fine grains. All grains would literally grow at the same rate and the distributions of grain size and grain shape do not change with time. Literally, normal growth is equivalent to photographic enlargement. The driving force for normal growth is the energy contained in grain boundaries. Occasionally abnormal grain growth, which is characterized by the growth of just a few grains, can occur when normal grain growth has been slowed or stopped either by fine precipitates or other interfaces. These grains, usually larger than the surrounding ones or in better orientation, grow and consume the surrounding fine grains until all the original fine grains are replaced. The grain growth after unpinning is dramatically different from that during inhibition.[218]

It is well understood that grain growth in polycrystaline metals is controlled by the migration of atoms and is a thermally activated process. Hence grain growth has been studied from kinetic perspectives.

In a single-phase metal, the rate at which the mean grain diameter increases with time depends on the grain boundary mobility and the driving force for boundary migration. Burke[219,220] established that the driving force of grain growth in annealed copper and copper alloys was essentially the surface energy of the grain boundaries, which impelled the boundaries to migrate towards their respective centers of curvature. His work was followed by Feltham *et al.*[221,222] It was assumed in this type of elementary model that the mean curvature radius of all the grain boundaries was proportional to the mean grain diameter D, and the mean driving force for grain growth will be proportional to $2\gamma/D$. This was expressed by

$$v = \frac{dD}{dt} = \alpha M \Delta G = \alpha M \frac{2\gamma}{D} \tag{3.43}$$

where υ is the moving velocity of the grain boundary, α is a proportionality constant of the order of unity, M is the mobility of the boundary, γ the surface energy of the grain boundary, t is the time.

This equation states that the rate of grain growth is inversely proportional to D and increases rapidly with increasing temperature due to increased boundary mobility, M. Taking $D = D_0$ when $t = 0$, integration of Equation 3.43 gives

$$D^2 - D_0^2 = Kt \tag{3.44}$$

where $K = 4\alpha\gamma M$.

Theoretically Equation 3.44 can only be used to describe normal grain growth. To bring this equation closer to reality, like the grain growth in weld heat affected zone, Ashby and Easterling[170,171] introduced a fudge factor to deal with the pinning of grain boundary by precipitates. They took a simple thermodynamic approach to compute the precipitate dissolution temperature T_{DISS} based on the type of precipitates and steel composition. Also incorporated in their algorithm is the superheating factor, f, to account for the superheating caused by fast heating during welding. When temperature is lower than T_{DISS}, grain growth is neglected. When temperature exceeds T_{DISS}, grain growth is then described by Equation 3.44.

Experimentally, Beck *et al.*[223,224] found that grain growth in aluminum alloys follows a relationship of the form

$$D^n - D_0^n = Kt \tag{3.45}$$

where K is a proportionality constant which increases with temperature. Since grain growth is a thermally activated diffusional process, K in both Equation 3.44 and 4.45 is usually expressed in Arrhenius rate equation

$$K = K_0 \exp\left(-\frac{Q}{RT}\right) \tag{3.46}$$

where K_0 is a constant, Q is the activation energy for the grain growth, R is the gas

constant, T is temperature in Kelvin.

Allegedly Equation 3.45 can be used to describe normal grain growth, abnormal grain growth after unpinning and during inhibition. The value of n for metals are found to be temperature dependent and decreases with temperature approaching a minimum of 2 as the melting temperature is approached. Elementary kinetics model is equivalent to experimental kinetics model with n=2. This corresponds to the limiting case where the grain boundary migration rate is directly proportional to the driving force. However, the experimentally determined values of n are usually greater than 2, vary from 2 to up to 20, and only approach 2 in very pure metals and at very high temperatures.[219,225] The reasons for this are not fully understood. The most likely explanation is that the velocity of grain boundary migration rate v is not a linear function of the driving force, ΔG. This means that the grain boundary mobility M in Equation 3.43 is not a constant but varies with ΔG and therefore also with the instantaneous grain size D. Such variation of M could arise from solute drag effects.[218,225]

Studies of grain boundary migration by Hu and Rath[226,227] in zone-refined aluminum crystals have shown that the boundary velocity is a power function of the driving force:

$$v = \alpha M(\Delta G)^m \tag{3.47}$$

They have shown that the exponent n and m are related by the expression

$$m = n - 1 \tag{3.48}$$

Empirical models are more generalized and adjustable for modeling the growth of austenite grains. However, because of the complications caused by different microstructure constituents in steels, the growth of austenite grains have not been studied thoroughly. Wide range of kinetic values n, Q, and K_0 have been reported in the literature and they are compiled in Table 3.9 regarding austenite grain growth in different types of steels.

Hannerz and Kazinczy[228] first studied kinetics of austenite grain growth in cast and forged steels containing various amounts of grain refining elements. The investigated temperature range was 950 to 1250 °C and the time range 10 to 10^7 seconds.

They found grain growth inhibition at two grain size levels, 15-25 μm and $\sim$ 100 μm. The former was attributed to the dispersion of carbide or nitride precipitates, the latter to slag inclusions which are normally very stable oxides. The types of grain growth were observed and were characterized by different n values. It was reported $n=6$ for normal grain growth, $n \approx 1 \sim 2$ for abnormal grain growth after unpinning. A very slow grain growth with $n \approx 20$ occurring during inhibition. Grain growth inhibition at 100 μm was also observed by Meyers in his air melted steels and attributed to fine dispersion of refractory oxides.[229]

Maynier and his coworkers at Creusot-Loire[116-118] found the activation energy for austenite grain growth to be dependent on molybdenum content. The activation energy was found to be 110 kcal/mol for low alloy steels. They did not, however, report their K_0 value.

Ikawa, *et al.*[164,165] studied grain growth in the weld heat affected zone of HT80 steel using grain growth equation they derived with $n=4$. They observed 60-80% of the total amount of grain growth occurred in heating cycle. In cooling cycle, grain growth was nearly completed when temperature falls to 90-95% of peak temperature. During welding thermal cycle, grain growth rate increased rapidly as temperature rose, taking a maximum value just before the peak temperature and decreases rapidly as temperature falls. Their calculated grain size is larger than measured in the region adjacent to the fusion line. They attributed this to the partially melting of the grain boundaries at fusion line which restrains grain growth in the adjacent region in the HAZ side. Savage[230] has also articulated this theory based on the solidification characteristics of weld fusion zone.

Saito and his coworkers at the Kawasaki Steel[155] devised the grain growth equation based on $n=10$ for C-Mn hot rolled steels. Different activation energy and K_0 values are used for temperatures above and below 1100 °C.

Alberry and his collaborators[167] conducted probably the most comprehensive investigation on austenite grain growth of Cr-Mo-V steels in the temperature range from 1118 to 1303 °C using thermal simulation technique. They measured all the grain growth parameters under isothermal conditions. However, their so derived grain growth equation predicted much larger weld HAZ grain sizes than they had measured

experimentally. They attributed this discrepancy to the steep thermal gradients in the weld heat affected zone. Thus they modified the grain growth equation by optimizing exponent n to match the calculated grain size with the measured in weld HAZ.

Based on their studies on austenite grain growth during heat treatments, DeAndrés and Carsí[119] developed a simple relationship to link ASTM grain size with austenitizing temperature and holding time. They differentiated the steels with grain growth modifiers from those without to account for the grain size effect. The ASTM grain size of prior austenite is calculated by

$$G = \frac{a}{T} + b \ln t + c \tag{3.49}$$

where a, b, and c are constants depending on whether the steel has grain growth modifiers. Their austenizing temperature range was 800 to 950 °C and time range 30 minutes to 4 hours. Equation 3.49 is identical to and can be derived from Equation 3.45. Thus the n, Q and K_0 values can be derived from their published a, b, c values. Meanwhile, the reported n, Q and K_0 values can also be fitted into Equation 3.49 to obtain constants in Equation 3.49.

Rétz, Bobok and Gergely[230] presented a computational method for the austenite grain growth of carbon steels during non-isothermal conditions based on their isothermal studies. Their grain growth equation is the same as the empirical grain growth model and they have incorporated this model into a comprehensive computerized system for properties prediction and technology planning in heat treatment of steels.[231]

Akselsen *et al.*[232] discussed the assumptions of predicting weld HAZ grain size by integrating isothermal grain growth equation and the inconsistency of reported grain growth parameters. They pointed out the fact that much wider temperature range is experienced by weld HAZ than regular heat treatment, and in this wide temperature range, all the grain growth parameters are not necessary constant and are normally temperature dependent. Although this problem can be overcome by calibrating n to 2 and fitting integral at fixed points to specific data through adjusting Q value,[223] an experimental verification of the various approximations involved is lacking.

Consequently they called for closer examination of the mechanisms controlling austenite grain growth.

Based on the austenite grain growth studies in the literature, it is recognized that there exists no simple grain growth model which can be generically applied to the prediction of austenite grain growth in heat treatment workpieces or in the welding heat affected zones. Austenite grain growth kinetics varies from steel to steel and has to be characterized individually if accurate information is required

In this research, a semi-empirical approach is adopted to model the growth of austenite grains in the heat affected zones. Newly formed austenite grains are assumed to be pinned by carbide or nitride precipitates until complete dissolution. A modified Ashby-Easterling relationship is used to calculate the dissolution temperature

$$T_{DISS} = \frac{B}{A - \log(C_M^a C_C^b)} + \Delta T \tag{3.50}$$

where A and B are the constants of the solubility product, C_M and C_C refer to the concentration of metal and non-metal species in the material being used to form the precipitates, indexed by their respective precipitate stoichiometries, a and b, ΔT is the superheating temperature required for the complete dissolution of precipitates in welding heat affected zone due to fast heating rates. Parameter A and B for the computation of T_{DISS} are tabulated in Table 3.10.[170]

It is assumed that the austenite grain size in the intercritical region and up to the dissolution temperature, T_{DISS}, remain at the as-recrystallized size of the steel, D_0, which is approximately 5 microns for most modern steels.[177] A not unreasonable superheating value ΔT of 200 °C is used in this research. After complete dissolution of carbide and nitride precipitates at T_{DISS}, austenite grains are assumed to grow during the heating cycle and the growth of austenite grains satisfy Equation 3.45. Parameters reported by Ikawa *et al.*[163-165] are used. Austenite grain growth in weld heat affected zones is assumed to take place only during the heating. This assumption is based on the experimental observation and computational studies by Ikawa *et al.*[163-165]

Even with such restrictions, the predicted austenite grain sizes are still too big

comparing to the experimentally observed in the grain coarsened region where peak temperatures exceed T_{DISS}. Experimentally it was found that the prior austenite grain sizes are quite uniform in the grain coarsened heat affected zone and the average grain size is 105 microns independent of the preheat temperature or interpass temperatures. This may be related to the pinning effect caused by the dispersion of oxides in the steel.[228,229] Consequently, austenite grain growth is assumed to stop whenever grain size reaches 105 microns.

The approach used in this research to model the austenite grain growth is semi-empirical and is applicable to the specific steel. It is believed that its methodology should generically applicable in the modeling of austenite grain growth in weld heat affected zones. Experimental verification should be conducted whenever possible.

3.4 Reaction Kinetics of Austenite Decomposition

When austenite is cooled below Ae_3 temperature, it will start to decompose. The possible transformation products which may be obtained, depending on the cooling rates and composition, include ferrite, pearlite, bainite and martensite. Ferrite and pearlite are normally regarded as equilibrium transformation products at room temperature for low alloy steels. They are actually metastable. The stable equilibrium phases at room temperature for most carbon steels are carbon as graphite and iron. Ferrite and pearlite are formed at high temperatures through diffusional transformations. Martensite, on the other hand, is formed at low temperatures through so-called shear or diffusionless mechanism. Bainite is formed at medium temperatures. There has been considerable debate regarding the mechanisms of bainite transformation. It is well known that bainite transformation has some of the characteristics of both diffusional and shear (martensitic) transformations.

3.4.1 Basics of Phase Transformation Kinetics

A very closely associated term for diffusional transformation is nucleation and

growth. Ferrite, pearlite, and bainite reactions may all be classified as nucleation and growth reactions. A nucleation and growth reaction may be *continuous* or *discontinuous*. In a continuous reaction, the transformation product is of different composition and the untransformed material has gradually changing composition. While in a discontinuous reaction, the transformation product has the same average composition as the untransformed material, and the untransformed material has the original composition except for a short distance from the advancing interface. An excellent review on the phase transformation kinetics has recently been published by Kirkaldy.[233]

The first mathematical model for phase transformation was derived by Johnson and Mehl.[153] This model pertains to reactions in which nuclei form at random throughout the matrix, without regard for the matrix structure and is limited to the process of congruent freezing and to recrystallization in pure metals and in one-phase alloys. Also assumed in their derivation are that the nucleation rate N_v and the radial growth rate G are constant throughout the reaction. The reaction products were assumed to be growing spheres before impinging others. Thus they derived the reaction rate equation

$$X(t) = 1 - \exp(-\frac{\pi}{3} N_v G^3 t^4) \tag{3.51}$$

where X is the fraction of transformed metal, and t is the time. Equation 3.50 is often referred to as Johnson-Mehl relation.

Almost at the same time as Johnson-Mehl developed their expression for phase transformation, Avrami[148,149] derived a similar but more general expression for phase transformations

$$X(t) = 1 - \exp(-kt^n) \tag{3.52}$$

where k and n are constants depending on the nucleation sites. This equation is often called Avrami equation.

Cahn[154] examined the assumptions made in deriving Johnson-Mehl relation and Avrami equation and he made some modifications to account for time dependent and time-independent nucleation rates. He concluded that the reaction rate is independent

of the nucleation rate at high nucleation rates but approaches Johnson-Mehl relation at low nucleation rates. The conditions which determine which type of site will produce the most nuclei, and hence determine the reaction rate, were discussed. Experimental studies showed that nucleation in many systems occurs early in the reaction at grain boundaries. This fact is called site saturation. Cahn[234] demonstrated that this type of system will quite often obey the additivity rule originally proposed by Avrami[148,149] and Scheil.[147]

It must be noted that rate laws expressed by Johnson-Mehl[153] and by Avrami[148,149] are not limited to steels but discontinuous phase transformations. Avrami equation has been used by many researchers using a semi-empirical approach to model austenite decomposition in eutectoid steels.[152,235-238] The constants in Avrami equation, k and n, were either calibrated to existing TTT diagrams or approximated with empirical from a rather large diagram database. Obviously, the restriction of Avrami equation to discontinuous phase transformations has been relaxed or ignored in these works.

3.4.2 Kirkaldy's Theory of Steel Hardenability

Zener[160] analyzed the kinetics of austenite decomposition. For the first time he incorporated thermodynamics and diffusional effect in the derivation of reaction rate law. Hillert[161] undertook a synthesis of isothermal growth theory as pertaining particularly to steels, with emphasis on Widmanstätten plates, the eutectoid pearlite and bainite. He incorporated thermodynamics including capillarity effects in a rigorous fashion. The work by Zener and Hillert laid a foundation for the quantitative study of austenite decomposition.

In numerous publications, Kirkaldy *et al.*[157-159] have reiterated the classical theory of hardenability which can be summarized briefly as follows: the additions of alloying elements in hardenability steels can be generally classified as either raising or lowering the Ae_3 temperature of the steel. Carbon, manganese, copper and nickel lower the Ae_3 temperature of steels and enlarge austenite region. They are called austenite stabilizers. While silicon, molybdenum and vanadium increase the Ae_3 temperature of steels and are

called ferrite stabilizers. Chromium is an austenite stabilizer at low concentrations (8 wt%) and a ferrite stabilizer at high concentrations. The austenite stabilizers decrease the supersaturation (super cooling) for a given transformation temperature. Consequently the reaction rates are retarded and higher hardenability is expected. Ferrite stabilizers, on the other hand, have strong effect of partitioning through phase boundary diffusion. The diffusion rates decrease exponentially with temperature. Therefore, ferrite stabilizers are very effective in depressing reaction rates. The best combination for designing hardenable steels would thus be a combination of austenite stabilizers and ferrite stabilizers.

Realizing those elements which would partition during austenite decomposition (C, Cr, ferrite stabilizers, and to a less extent, austenite stabilizers) will play a major role in determining the reaction rate, Kirkaldy *et al.*[205] developed a general Zener-Hillert type formula to approximate ferrite start curve ($\tau_{0.1\%}$) in the absence of bays. This formula was calibrated to the U.S. Steel Atlas.[156] Assuming prompt site saturation which eliminates the complication of nucleation effects, and taking the temporal start curve as proportional to the inverse of the steady state velocity at a spherical front, this formula is expressed as

$$\tau_{0.1\%} = \frac{60C + 90Si + 160Cr + 200Mo}{2^{G/8}(Ae_3 - T)^3 \exp(-20000/RT)} \tag{3.53}$$

where G is the ASTM grain size number. This formula eventually led to the Minitech Computerized System.[239] This formula was still primitive because it needs to be expanded if full time-temperature dependence of phase transformation is required.

In the expansion, Kirkaldy and Venugopalan[159] adopt Kennon's proposition[240] that separate C and sigmoidal volume fraction curves be associated with ferrite, pearlite and bainite reactions. The philosophy which led to this expansion was well presented by Kirkaldy and Sharma.[158]

It is important to understand that the kinetics formulas presented by Kirkaldy and Venugopalan in their 1983 publication[159] had a number of errors as pointed out by Kirkaldy in a recent conversation with the author. In the originally published formulas

by Kirkaldy and Venugopalan, the effect of grain size was incorporated into the kinetics equations by a term $2^{(G-1)/2}$ where G is the ASTM grain size index. Physically this term represents the number of grains per square inch at 100x magnification. Recently this term was adjusted by Kirkaldy[203] to $6\times2^{G/8}$ which assumes an incubation transient as grain diameter to the 1/4 power. These two terms are equivalent at G=8. Mathematically, this adjustment indicate less significant effect of prior austenite grain size.

Moreover, Kirkaldy has recently notified the author that the right side of all the kinetics equations in their original publication[159] should have been multiplied by 1/0.3. After all these changes, the kinetics equations can then be expressed as

$$\tau_F = \frac{60Mn + 2Ni + 68Cr + 244Mo}{1.8\times2^{G/8}(Ae_3 - T)^3 \exp(-23500/RT)} I(X) \qquad (3.54)$$

for ferrite reaction and

$$\tau_P = \frac{1.79 + 5.42(Cr + Mo + 4MoNi)}{1.8\times2^{G/8}(T_{Ps} - T)^3 D_P} I(X) \qquad (3.55)$$

for pearlite reaction. where τ_F and τ_P are the transient time for ferrite and pearlite reactions respectively. In these two equations, the term I(X) is incorporated to account for the sigmoidal effect of the transformed volume fraction

$$I(X) = \int_0^X \frac{dX}{X^{2(1-X)/3}(1-X)^{2X/3}} \qquad (3.56)$$

In Equation 3.55, 1/ D_P is the effective diffusional resistance for pearlite reaction and is evaluated by

$$\frac{1}{D_P} = \frac{1}{\exp(-27500/RT)} + \frac{0.01Cr + 0.52Mo}{\exp(-37000/RT)} \qquad (3.57)$$

where T_{Ps} represents the $\tau=\infty$ asymptote of pearlite start curve which in many cases is not known *a priori*, whether it is determined by multicomponent equilibrium limit Ae_1 or the para-equilibrium limit Ap_1. Therefore they proceeded with the interpolation

procedure for the pearlite asymptote

$$T_{Ps} = Ap_1 + (Ae_1 - Ap_1)\frac{Cr}{Cr + Mo + Ni} \tag{3.58}$$

where Ae_1 and Ap_1 were calculated using the method by Hashiguchi *et al.*[206]

Their model for ferrite and pearlite reactions was reported as working very well[203] for determination of ferrite and pearlite start and finish curves but failed for bainite termination. They partially corrected this problem in an *ad hoc* way via empirically modified integral $I'(X)$. The formula for bainite reaction is expressed by

$$\tau_B = \frac{(2.34 + 10.1C + 3.8Cr + 19Mo)\times 10^{-4}}{1.8\times 2^{G/8}(Bs - T)^2 \exp(-27500/RT)} I'(X) \tag{3.59}$$

where

$$I'(X) = \int_0^X \frac{Z\,dX}{X^{2(1-X)/3}(1-X)^{2X/3}} \tag{3.60}$$

$$Z = \exp(BX^2) = \exp[X^2(1.9C + 2.5Mn + 0.9Ni + 1.7Cr + 4Mo - 2.60)] \tag{3.61}$$

For negative B values, the correction term $Z=\exp(BX^2)$ is deleted, or set to one. In this case and only in this case, $I'(X)=I(X)$.

The supercooling for computing bainite reaction is calculated from the bainite asymptote of TTT diagrams. Based on linear regression analysis from U.S. Steel Atlas and Steven and Haynes,[241] Kirkaldy and Venugopalan[159] developed an empirically based formula to calculate bainite asymptote of carbon steels

$$Bs(^\circ C) = 656 - 58C - 35Mn - 75Si - 15Ni - 34Cr - 41Mo \tag{3.62}$$

Kirkaldy and Venugopalan assumed all the diffusion-controlled austenite reactions stop when temperature gets lower than the isothermal martensite start Ms temperature of the steel. They adopted the empirically derived equation for Ms temperature by Steven and Haynes[241]

$$Ms(^\circ C) = 561 - 474C - 33Mn - 17Ni - 17Cr - 21Mo \tag{3.63}$$

In other words, all austenite will instantaneously transform to martensite at temperature

below Ms temperature. This assumption poses no problem in modeling quenching of steels.

The above equations explicitly described the isothermal reaction kinetics for austenite decompositions. Phase transformations under continuous cooling can thus be computed by incorporating the isothermal reaction kinetics with the additivity rule. In many computational phase transformation studies, the reaction kinetics theory is normally applied in an incremental form to allow prediction of transient and residual microstructures. In the computation of phase transformations under continuous cooling, Kirkaldy and Venugopalan assumed that no bainite forms for all temperatures above the intersection of pearlite start curve (Ps) with bainite start curve (Bs) and that no pearlite forms below the intersection. If the intersection of ferrite start curve (Fs) with Bs occurs below the intersection of Ps with Bs, they assumed that below the Fs-Bs intersection only bainite forms. For alloys for which a segment of Ps proceeds both Fs and Bs, they assumed that within that segment pearlite goes to 100% completion as some sort of degenerate structure. These assumptions have little effect on the prediction of CCT product quantities or hardness.

One must be cautious about the precise meaning of X in Equation 3.54, 3.55, 3.56. It was assumed in Kirkaldy-Venugopalan model that the phantom reaction goes to completion. The actual ferrite fraction for any phantom X(t) is $X_F = X \cdot X_{FE}$ where X_{FE} is the attainable equilibrium amount of ferrite. Thus if τ in Equation 3.53 is to be expressed as an explicit function of X_F, one must set

$$X = \frac{X_F}{X_{FE}} = \frac{X_F}{1 - X_{PE}} \tag{3.64}$$

everywhere in Equation 3.54 for the calculation of ferrite reaction. Similarly, one must set

$$X = \frac{X_P}{X_{PE}} = \frac{X_P}{1 - X_{FE}} \tag{3.65}$$

everywhere in Equation 3.55 for the calculation of pearlite reaction. The equilibrium

amount of ferrite and pearlite X_{FE} and X_{PE} can be estimated from the thermodynamics model for Fe-C-M multicomponent system.

3.4.3 Reaction Kinetics Model of Austenite Decomposition

During the pursuit of this research, the author was aware of the work by Bhadeshia who took a thermodynamic approach to model the microstructure development in low alloy steels.[242-244] On fitting TTT diagrams to Russell's linked-flux nucleation equation,[245,246] Bhadeshia developed a computer program to predict the transformation start curves for both diffussional (ferrite) and displacive (bainite) transformations. The details of this program, particularly those thermodynamics and kinetics parameters, however, are not presented in open literature publications. The mathematics of this model is more complicated. Moreover, the model was based on Johnson-Mehl[153] type kinetics equations developed by Umemoto,[146] which is theoretically applicable to discontinuous reactions only. Pearlite and martensite reactions can be considered as discontinuous. However, ferrite and Bainite reactions are obviously continuous. Therefore, the author believes that the methodology developed by Kirkaldy,[158,159] which was based on reaction kinetics models by Zener[160] and Hillert,[161] is more theoretically correct and was thus adopted in this research.

Preliminary studies by the author involved using Kirkaldy-Venugopalan model to predict the Jominy hardness curves of steels[247,248] and weld heat affected zone microstructure.[249] It was found that Kirkaldy-Venugopalan model gives considerably accurate predictions for steels with low hardenability which is associated with little addition of alloy elements. The performance of Kirkaldy-Venugopalan model is less satisfactory for steels with medium or high hardenability which is associated with more alloy element additions.

In this research, the author has developed a new reaction kinetics model for austenite decomposition by modifying the original Kirkaldy-Venugopalan model. This new model was developed based on a hypothesis on the effects of alloying elements on

steel hardenability. It was conjectured that the effects of alloying elements on steel hardenability can be classified in thermodynamic and kinetic perspectives. Thermodynamically, they affect steel hardenability by influencing the multicomponent Fe-C-M system equilibria. Thus they either enlarge or suppress the temperature regions for each austenite decomposition reaction. The kinetic effects of alloying elements are that they all uniquely retard phase transformations through partitioning at the phase boundaries For many alloying elements, the kinetic effects on steel hardenability are more significant than their thermodynamic effects.

The general form of TTT curve chosen in accordance with the analysis is described by Zener-Hillert type formula

$$\tau(X,T) = \frac{F(C, Mn, Si, Ni, Cr, Mo, G)}{\Delta T^n \exp(-Q/RT)} S(X) \qquad (3.66)$$

where F is a function of steel composition C, Mn, Si, Cr, Mo in wt%, and ASTM grain size G of prior austenite, ΔT is the undercooling, Q is the activation energy of the diffusional reaction. The exponent of undercooling n is an empirical constant determined by the effective diffusion mechanism (for pearlite, n=2 for volume and n=3 for boundary diffusion). S(X) is the reaction rate term which is an approximation to the sigmoidal effect of phase transformations. S(X) in this model is expressed in the same type of equation as in I(X) in Kirkaldy-Venugopalan model

$$S(X) = \int_0^X \frac{dX}{X^{0.4(1-X)}(1-X)^{0.4X}} \qquad (3.67)$$

except constant 2/3 in Equation 3.56 has been replaced by 0.4. When $X \to 0$, Equation 3.67 would predict $X \propto \tau^{1.67}$ which corresponds to the empirical observation $\tau_{1.0\%} = 4\tau_{0.1\%}$ by Kirkaldy, Thomson and Baganis.[205]

Computing phase transformations under continuous cooling is very straightforward with the application of additivity rule. Equation 3.66 and 3.67 can be rewritten as

$$\frac{dX}{dt} = \frac{\Delta T^n \exp(-Q/RT) X^{0.4(1-X)}(1-X)^{0.4X}}{F(C, Mn, Si, Ni, Cr, Mo, G)} \qquad (3.68)$$

which can be used to predict critical cooling rates for ferrite, pearlite, and bainite reactions. Thus it became possible to correlate this model with the empirical formulas in DeAndrés and Carsí model which was developed based on CCT diagrams and to develop a new set of kinetics equations. This method is considered equivalent to calibrating the model with CCT diagrams. CCT diagrams were normally measured with dilatometry method and were reported to have better accuracy than TTT diagrams measured with metallurgraphic examinations.[144]

To avoid complications in the model calibration process, volume fractions of transformed products were directly used for the computation of ferrite and bainite reactions. Phantom fraction was used for the computation of pearlite reaction. It was assumed that one reaction reaches to its completion when its equilibrium amount is attained.

Under isothermal conditions, ferrite reaction can be represented by

$$\tau_F = \frac{FC}{2^{0.41G}(Ae_3 - T)^3 \exp(-27500/RT)} S(X_F) \tag{3.69}$$

where the effects of alloying elements on ferrite reaction are expressed by

$$FC = \exp(1.00 + 6.31C + 1.78Mn + 0.31Si + 1.12Ni + 2.70Cr + 4.06Mo) \tag{3.70}$$

The volume fraction of transformed ferrite X_F is directly used in the calculation. Ferrite reaction is assumed to reach completion when its equilibrium amount is reached.

Pearlite reaction is represented by

$$\tau_P = \frac{PC}{2^{0.32G}(Ae_1 - T)^3 \exp(-27500/RT)} S(X_P/X_{PE}) \tag{3.71}$$

where the effects of alloying elements on pearlite reaction are expressed by

$$PC = \exp(-4.25 + 4.12C + 4.36Mn + 0.44Si + 1.71Ni + 3.33Cr + 5.19\sqrt{Mo}) \tag{3.72}$$

In the calculation of pearlite reaction, it is presumed that the phantom reaction goes to completion.

Bainite reaction under isothermal condition is represented by

$$\tau_B = \frac{BC}{2^{0.29G}(Bs - T)^2 \exp(-27500/RT)} S(X_B) \qquad (3.73)$$

where the effects of alloying elements on bainite reaction are expressed by

$$BC = \exp(-10.23 + 10.18C + 0.85Mn + 0.55Ni + 0.90Cr + 0.36Mo) \qquad (3.74)$$

It was found in this research that Equation 3.62 overpredicts the effect of Si on suppressing isothermal bainite asymptote temperature. For most low alloy steels, Si content is kept around 0.25 wt%. This poses no problem for the using of Equation 3.62. The predicted Bs temperatures for steels with higher Si content, ~ 1 wt% or above, are too low when compared with isothermal bainite asymptote temperatures in measured TTT diagrams.[156] Earlier work by Steven and Haynes[241] suggested that the effect of Si on Bs temperature is negligible comparing to other alloying elements. Therefore, they did not include Si in their equation for the calculation of Bs temperature. The author thus normalized Equation 3.62 to Si=0.25. Bs temperature is then evaluated from

$$Bs(^\circ C) = 637 - 58C - 35Mn - 15Ni - 34Cr - 41Mo \qquad (3.75)$$

It is well understood that martensitic reaction starts at a critical temperature called martensite start, Ms. Martensite reaction is not a nucleation and growth type of reaction, but is produced by a shear movement of the austenite lattice, producing a body-centered tetragonal lattice. No diffusion occurs in martensite reaction. Thus martensite reaction is only a function of temperature. In this research, however, martensite reaction is represented using Koistinen-Marburger relationship[250]

$$X_M = 1 - \exp[-0.011(Ms - T)] \qquad (3.76)$$

where T denotes the temperature which is below the martensite start temperature Ms.

There exists no theoretical method in determining the martensite start temperatures of steels. Estimating Ms temperatures thus has been made through empirically derived formulas.[241,251-254] The accuracy of all these formulas was evaluated by Krauss[255] in 1978 and by Kung and Rayment[256] in 1982. Krauss concluded that the formula developed by Andrews[254] presented the most accurate results. Kung and Rayment[256] modified the existing Ms temperature equations by including the effects of

Co and Si. The modified Andrews' linear equation and Steven and Haynes' equation[241] both were found to give reasonably good predictions for both low and high alloy steels. However, the Andrews' linear equation slightly overestimated the case for high chromium alloys steels, whereas Steven and Haynes' equation, on the other hand, underestimated the case for high molybdenum alloy steels. In this research, The martensite start temperature Ms is calculated from the modified Andrews' linear equation by Kung and Rayment[256]

$$Ms(^{\circ}C) = 539 - 423C - 30.4Mn - 12.1Cr - 17.7Ni - 7.5Mo + 10Co - 7.5Si \quad (3.77)$$

which is expected to be the most accurate formula for calculating Ms temperature to date.

An important assumption made in this model is that bainite would continue to form even at temperatures below Ms until all austenite is transformed. This assumption has little effect in the microstructure and hardness computation of steels during conventional quenching. However, it does influence the results of microstructure predictions in weld heat affected zone, particularly when the cooling rates below Ms temperature are very slow. This is very common when preheating is practiced or interpass temperatures are elevated in multiple pass welding.

The author has not thoroughly tested the application range of this reaction kinetics model. But it is believed that this model is valid at least within the same range of Creusot-Loire model: $0.1 < C < 0.5$, $Si < 1.0$, $Mn < 2$, $Ni < 4$, $Cr < 3$, $Mo < 1$, $V < 0.2$, $Cu < 0.5$, $Mo + Ni + Cr + Mo < 5$, $0.01 < Al < 0.05$. It could be valid over a slightly wider range.

3.5 Hardness Calculation

In principle, weld HAZ microstructure can be observed with optical or even electronic microscopes and measured with advanced quantitative microscopy techniques. However, modern optical microscopy has not been able to effectively distinguish martensite from bainite since they have very similar lath structure. And the accuracy of measurements with computerized image analyzing system is often called into question.

An effective method of differentiating martensite from bainite or ferrite+pearlite is from their hardness values. Normally, martensite is much harder than bainite or mixed ferrite+pearlite structure. Therefore, hardness measurements and prediction can be readily used as an index for the accuracy of microstructure predictions.

One can expect that weld HAZ microstructure of a low alloy steel consists a mixture of martensite, bainite, or even ferrite and pearlite. To estimate the hardness of weld HAZ, the rule of mixture is used in this research which is expressed by

$$Hv = X_M Hv_M + X_B Hv_B + X_{FP} Hv_{FP} \tag{3.78}$$

where X_M, X_B, and X_{FP} are volume fraction of martensite, bainite and ferrite+pearlite respectively, Hv_M, Hv_B, and Hv_{FP} are hardness of martensite, bainite and ferrite+pearlite respectively.

3.5.1 Hardness of Martensite

Researchers at Creusot-Loire[117] first developed empirical expressions to calculate hardness of different microstructure constituents as function of chemical composition and cooling rate at 700 °C. They expressed the hardness of martensite as a linear function of the alloying elements C, Si, Mn, Ni, and Cr. The cooling rate Vr at 700 °C in °C/hr was introduced into the formula as a logarithmic function

$$Hv_M = 127 + 949C + 27Si + 11Mn + 8Ni + 16Cr + 21\log Vr \tag{3.79}$$

From this equation, significant effect of carbon can be noticed. Other alloying elements also contribute to the hardness of martensite too. Experimental studies did show effects of alloying elements on the hardness of martensite.[253] The author found this formula quite accurate in the computation of Jominy hardness of low alloy steels.[246,247] However, it seems to overpredict martensite hardness in weld heat affected zones.[248]

While in DeAndrés-Carsí model,[119] martensite hardness was expressed as a function of carbon and cooling rate Vr

$$Hv_M = 121.15 + 902.6C + 26.68 \log Vr \tag{3.80}$$

The effects of substitutional alloying elements on the hardness of martensite was totally

ignored. Comparing the coefficients of Equation 3.79 and 3.80, one may expect that Equation 3.79 predicts consistently higher hardness values than Equation 3.80.

The application range of DeAndrés-Carsí model was not reported in their original publication.[119] It is believed that this model is valid in the same range of Creusot-Loire model: $0.1<C<0.5$, $Si<1.0$, $Mn<2$, $Ni<4$, $Cr<3$, $Mo<1$, $V<0.2$, $Cu<0.5$, $Mo+Ni+Cr+Mo<5$, $0.01<Al<0.05$.

Weld heat affected zone models only express martensite hardness as a function of carbon content of the steel. Terasaki[136] expressed the martensite hardness in weld heat affected zone by

$$Hv_M = 293 + 812C \tag{3.81}$$

The formula was developed based on simulated CCT diagrams for weld heat affected zones. It is reportedly valid within the range: $0.05 \le C \le 0.40$, $Mn \le 1.52$, $Si \le 1.76$, $Ni \le 9.33$, $Cr \le 4.75$, $Mo \le 1.24$, $Cu \le 1.42$, $V \le 0.56$, $Nb \le 0.05$, $Al \le 0.72$, $B \le 0.004$, $Ti \le < 0.04$.

Yurioka *et al.*[132-135] expressed the martensite hardness in weld heat affected zone *via*

$$Hv_M = 294 + 884C(1 - 0.3C^2) \tag{3.82}$$

This formula was developed based on Y groove weldability tests. Yurioka *et al.* claimed that this model is valid over a wide range: $C \le 0.8$, $Mn \le 2.0$, $Si \le 1.2$, $Ni \le 10$, $Cr \le 10$, $Mo \le 2$, $Cu \le 0.9$.

It has been reported that there is considerable scatter of the experimentally measured hardness values of martensite for low and medium carbon alloy steels.[255] The scatter band may have been caused by factors including the amount of retained austenite, auto-tempering, room temperature aging, prior austenite grain size, and packet size of lath martensite.[255] Therefore, one should choose formulas accordingly in the hardness calculations. It was found for the steel involved in this research, all these formulas, except Equation 3.80, overpredicts martensite hardness in the weld heat affected zone. Consequently, Equation 3.79 and 3.80 were used in the calculation of martensite hardness in heat treatment specimens and weld heat affected zones respectively. One

change made in this research is that the Vr at 700 °C in Equation 3.79 and 3.80 is replaced by the cooling rate at Ms temperature, the cooling rate at which martensite is formed.

3.5.2 Hardness of Bainite

Both Creusot-Loire model and the DeAndrés-Carsí model used the same equation to calculate the hardness of bainite structure

$$Hv_B = -323 + 185C + 330Si + 153Mn + 65Ni + 144Cr + 191Mo + \log Vr(89 + 53C - 55Si - 22Mn - 10Ni - 20Cr - 33Mo) \quad (3.83)$$

The effect of cooling rate Vr at 700 °C (in °C/hr) on hardness may be interpreted by its effect on decreasing the size of substructure, *i.e.*, the size of the pearlite and bainite laths. This formula was found to be considerably accurate in the computation of Jominy hardness of steels,[246,247] but overpredict bainite hardness in weld heat affected zones.[248]

Terasaki[136] developed a simple equation for the calculation of bainite hardness based on his experimental results

$$Hv_B = 150 + 188C_{EQ} \quad (3.84)$$

where C_{EQ} is the carbon equivalent of a steel expressed by

$$C_{EQ} = C + \frac{Si}{3} + \frac{Ni}{26} + \frac{Cr}{9} + \frac{Mo}{3} + V \quad (3.85)$$

Yurioka *et al.*[132-135] proposed a similar formula for the calculation of bainite hardness in weld heat affected zone. The carbon equivalent in Yurioka's model for the calculation of bainite hardness is expressed by

$$C_{EII} = C + \frac{Si}{24} + \frac{Mn}{5} + \frac{Cu}{10} + \frac{Ni}{18} + \frac{Cr}{5} + \frac{Mo}{2.5} + \frac{V}{5} + \frac{Nb}{3} \quad (3.86)$$

If a steel carbon equivalent, C_{EII}, is low ($C_{EII} \leq 0.75$ %), bainite hardness is calculated using

$$Hv_B = 117 + 197\,C_{EII} \tag{3.87}$$

When the steel carbon equivalent, C_{EII}, is high, another formula is used for the calculation

$$Hv_B = 145 + 130\tanh(2.65C_{EII} - 0.69) \tag{3.88}$$

In this research, Equation 3.83 was found to predict consistently higher bainite hardness values than Yurioka *et al.*'s model and Terasaki model. The formulas in Yurioka *et al.*'s model were used to calculate the hardness of bainite in weld heat affected zones. The calculated bainite hardness values are in good numerical agreement with the calculated results with Terasaki model for the vast majority of low alloy steels.

3.5.3 Hardness of Ferrite+Pearlite

Creusot-Loire model expressed the hardness of ferrite+pearlite structure as

$$\begin{aligned} Hv_{FP} = {} & 42 + 223\,C + 53\,Si + 30\,Mn + 12\,Ni + 7\,Cr + 19\,Mo \\ & + \log Vr(10 - 19\,Si + 4\,Ni + 8\,Cr + 130\,V) \end{aligned} \tag{3.89}$$

Whereas, DeAndrés-Carsí model expressed the hardness of ferrite+pearlite structure as

$$\begin{aligned} Hv_{FP} = {} & -437 + 3300\,C - 5343\,C^2 \\ & + \log Vr(1329\,C^2 - 744\,C + 15\,Cr + 4\,Ni + 135.4) \end{aligned} \tag{3.90}$$

Predictions given by these two equations are in reasonably good agreement. In this research, Equation 3.89 was selected to calculate the hardness of ferrite+pearlite structure in weld heat affected zone. The cooling rate Vr at 700 °C in Equation 3.89 is replaced by the cooling rate at which appreciable amount, *i.e.*, 1% volume fraction, of ferrite+pearlite structure is formed.

It must be noted that the aforementioned Creusot-Loire formulas as well as DeAndrés-Carsí formulas were all developed based on CCT diagrams or hardness measurements after heat treating. They are all reported quite successful in hardness predictions after heat treatments. However, researchers at Creusot-Loire found that these

formulas predicted considerably higher hardness values than the measured in weld heat affected zone of steels. Consequently, they developed another formula to calculate the martensite hardness in weld metal and heat affected zone[257,258] using the same approach. Also proposed in their study was a slightly different formula for the calculation of bainite hardness in weld metal and heat affected zone. These two formulas are expressed by

$$Hv_M = 97 + 949C + 27Si + 11Mn + 8Ni + 16Cr + 20\log Vr \tag{3.91}$$

$$\begin{aligned} Hv_B = &-348 + 185C + 330Si + 153Mn + 66Ni + 144Cr + 191Mo \\ &+ \log Vr(89 + 54C - 55Si - 22Mn - 10Ni - 20Cr - 33Mo) \end{aligned} \tag{3.92}$$

and they are expected to have better accuracy than Equation 3.78 and 3.83 in weld metal and heat affected zone. However, the reported composition range for these two equations are very narrow:[257,258] $0.02 < C < 0.15$, $Si < 0.9$, $Mn < 2.0$, $Ni < 2.5$, $Cr < 2.5$, $Mo < 1$, $V < 0.1$, $Ni + Cr + Mo + V < 5$. This has seriously limited the application of these formulas. So these two equations were not considered in this research.

3.6 Remarks

The thermodynamics model for computing equilibria in multicomponent Fe-C-M systems have been well established and tested with the experimentally measured Ae_3, Ar_3, Ac_3, Ae_1, Ar_1, and Ac_1 temperatures. The mathematics of the regular solution model with Wagner formulation is simple and proven efficient in Kirkaldy and his coworkers' computations. The contribution made by the current author is to eliminate some assumptions regarding interaction coefficients made by Kirkaldy *et al.*[204-206] by incorporation the thermodynamic data set which were measured systematically and presented by Uhrenius.[209]

It is for the first time that the three phase $\alpha+\gamma+$cementite eutectoid reaction in a low alloy steel was recognized to occur in a temperature range. The upper and lower limits of this region were designated as Ae_1 and As_1. The significance of Ae_1 temperature is that it represents the temperature at which austenite starts to decompose into pearlite. In a TTT (IT) diagram, it illustrates the asymptote of pearlite start C

curve. The significance of As_1 is that it represents the temperature at which austenite would start forming during heating or equilibrium austenite decomposition into ferrite and pearlite reaches completion. Therefore, it represents the asymptote of pearlite finish C curve and also ferrite finish C curve if ever plotted.

The growth of prior austenite grains in steels is, at current state, too complex to be modeled with a simple relationship. Empirical grain growth kinetics equation has been used by many researchers in this regard. However, wide range of kinetics parameters have been reported. It is concluded in this study that grain size measurement should be recommended if the characteristics of prior austenite grain growth is not known.

One may notice the similarity between the reaction kinetics models for austenite decomposition developed in this thesis and by Kirkaldy and Venugopalan. One significant modification made in the development of the model presented in Section 3.4.3 is that the effects of alloying elements on diffusional reactions are expressed in exponential forms. They imply that the effect of alloying elements on steel hardenability is multiplicative. Whereas Kirkaldy-Venugopalan model suggests the effect of alloying elements on steel hardenability is additive. Detailed discussion on the modifications will be presented in Section 5.5.

It must be noted that the Kirkaldy-Venugopalan model[159] was developed in 1983. Despite its great advantages of being a generic reaction kinetics model based on first principles of phase transformation theories, the accuracy and reliability of the model were never tested extensively limited by the computing power at that time. Kirkaldy and Venugopalan never used this model to a full scale for the predictions of steel hardenability. They only used this model to calculate TTT and CCT diagrams of steels. The application range of this model is not known yet. Although Watt and Henwood *et al.*[177-179] coded this model into a program later in 1987 to predict the microstructure development in weld heat affect zone of steels, they simply assembled this model along with the model by Ashby and Easterling[170,171] for austenite grain size predictions. They did not test the reliability and applicability of this model.

The viability and reliability of the models described in this chapter will be

evaluated in Chapter 5.

CHAPTER 4
THERMAL EFFECTS OF MULTIPASS ELECTROSLAG CLADDING

The results of temperature measurements and numerical analysis on the heat transfer induced by multipass electroslag cladding are presented in this Chapter. Section 4.1 delineates the techniques used to measure temperatures in the expected heat affected zones. Section 4.2 presents the comparison between the computed and experimentally measured results on a shaft during cladding experiment. Section 4.3 is dedicated to the predictions of thermal effects of electroslag cladding on the same experimental size shaft under ideal conditions: no operation errors and a lot more passes onto the shaft. The limitations in the implementation of the results from experimental size shafts to full size shafts are discussed in section 4.4 in terms of the difference in their lengths and cladding locations. Section 4.5 presents useful information on the optimal preheating temperature distribution for electroslag cladding on a full size shaft.

4.1 Temperature Measurement

Chromel-alumel thermocouples were buried in the expected heat affected zone for temperature measurements. Accurately locating thermocouples in the heat affected zone is generally not an easy task, especially in this study, because of the shape and size of the shafts. A number of techniques have been tried in this project to locate thermocouples. The first one required drilling through wall thickness holes in the radial directions of the shaft, through 7.6 to 12.7 cm thick material, and then spot welding thermocouples at the expected locations. The holes were sealed on top before electroslag cladding. Thermal disturbances are expected to occur in the vicinity of thermocouples

due to geometric discontinuities. This technique was very time consuming and labor intensive. Moreover, some thermocouples did not survive. They were melted during either the sealing or cladding process.

Another technique involved machining trenches on the shafts. Slanted holes were drilled from the shaft outside surface to the edge of the trenches which were 1.25 cm wide and 1.90 cm in depth. Thermocouples were mounted through these holes, spot welded at the expected locations, and set in high temperature cement. Thermocouples were connected to a data acquisition system through the holes and underneath trenches. The trenches were sealed with previously machined steel bars. This "trench" technique for temperature measurements was found to provide the most consistent and reliable results.

Acquisition of the temperature data from thermocouples was processed by a commercial program called Viewdac. Data acquisition started at cladding initiation and continued throughout the pass. Since Viewdac data acquisition program allows a variable sampling rate, the data acquisition rate was maximized at the time the cladding head passed over the thermocouples, 3 Hz, and was the lowest during the latter stage when the thermal gradient was low, 1 Hz. The data collected by the Viewdac program was post-processed using the PC based QuattroPro commercial software. They were also downloaded into IBM and HP work stations for comparative studies with the computational results.

4.2 Heat Transfer in Cladding Experiment on Shaft E290

The average length of full size propeller shafts is about 12 to 15 meters. Therefore, a full size propeller shaft is too long and too expensive to be used for experiments. Only small sections of shafts were used in practice for conducting experiments. In this section, results of finite element heat transfer analysis of electroslag cladding on a section of a propeller shaft, E290, are presented along with the results from experimental measurements. In the cladding onto this shaft, E290, preheating temperature was almost uniformly distributed. The welding parameters which were

optimized from cladding experiments on plates and then used in the cladding on shafts have been presented in Chapter 2, section 2.2. These parameters are recapitulated in Table 4.1. The outside diameter of the shaft was 61 cm (24 in.), and its wall thickness was 12.7 cm (5 in.). The shaft used in the cladding experiment was a section of a long propeller shaft and its length was 104.1 cm (42 in.).

In the two-dimensional finite element analysis in this study, the cladding process was assumed to start from the left end of the shaft. During the cladding experiment, the first clad pass was started 8.9 cm (3.5 in.) away from the left end (to the centerline of the clad bead. Each clad pass was simplified to have a rectangular cross section. The bead width was assumed to be equal to the distance between two adjacent clad beads at the centerline which was determined experimentally to produce a smooth clad top surface. The bead width on this shaft was found to be 2.92 cm (1.15 in.). The height of clad was calculated from the measured deposition rate in the finite element analysis.

The experimental setup for electroslag cladding on shafts has been presented in Chapter 2, section 2.2. It should be mentioned, however, that operation errors happened during the cladding of shaft E290. The "jogging" equipment which was used for the transition from one cladding pass to the next failed to give the right jogging distances for the first four cladding passes. The spacing distances between the first and second, second and third were twice as what was expected. While the fourth cladding pass was laid right on top of the third pass. Errors were corrected after the fourth pass. For completeness, these errors were simulated in the finite element analysis in order to compare the computed results from finite element analysis with the experimentally measured.

Results of the numerical simulations are generally more compatible for comparative studies and they are also easy to be interpreted than thermocouple measurements. However, one commonly encountered difficulty in comparing computational thermal cycles with the experimentally measured results is how to locate thermocouples accurately and to interpret the measured results. In this study, determining the position of thermocouples along the shaft axial direction posed no problem because it did not affect the accuracy of temperature measurements significantly.

Isotherms in the heat affected zone underlying the clad deposit were almost parallel to the axial direction of the shaft and the thermal gradients in this direction were found to be low in this area. However, the exact locations of thermocouples in shaft radial direction are very critical and could not be determined accurately. Since the thermal gradients in this direction were very high, a slight error in locating thermocouples had potentially large differences in measured temperature results. Therefore, comparative study for the computed and measured temperatures was performed by matching their peak temperatures at the same axial locations.

For each individual clad pass, thermal cycles experienced in the heat affected zone are not different from those induced by a single pass cladding process. A typical comparison between computed and measured thermal cycles in the heat affected zone of electroslag cladding is shown in Figure 4.1 from which one can observe excellent agreement over the whole process, particularly at low temperatures.

One most commonly used parameter in describing the cooling rate and to correlate with the microstructure in welding heat affected zone is the cooling time from 800 to 500 °C ($t_{8/5}$), which greatly influences the microstructure development in the weld heat affected zone. The computed $t_{8/5}$ cooling times are shown in Figure 4.3 in comparison with the measured results for shaft E290. The computed results are in fairly good agreement with the experimentally measured results with the trench technique. Measured $t_{8/5}$ cooling times from thermocouples through wall thickness holes are consistently higher than the results of both the computation and measurements using trench technique. It is almost universal that computed $t_{8/5}$ cooling times in weld heat affected zones are always shorter than those experimentally measured. Figure 4.3 suggests that a microstructure gradient in the heat affected zone may be expected along the shaft.

The computed results in this study have smaller scatter bands than the experimentally measured results. This observation suggests that the computed results have better consistency, and may have better accuracy than the experimentally measured data.

It is well known that temperature in the heat affected zone changes dramatically with position and time. The finite size of thermocouples indicates that the measured

results are some average over a distance of 0.5 ~ 1.0 mm rather than that related to a particular point. With very steep temperature gradients at high temperatures in the heat affected zone, the size of thermocouples may lead to substantial errors. Improved accuracy can be expected at low temperatures. All these factors affect the accuracy and the interpretation of measured temperatures, and consequently make it considerably difficult to compare the computed with measured temperatures, particularly at high temperatures.

The computed heating rates in the heat affected zone are not as high as those of experimentally measured, but they are very close. This success was attributed to the method of modeling the melting process and accounting for filler material in the finite element analysis. This was accomplished by assigning an initial droplet temperature 500 °C above the solidus of strip electrode to the fusion zone elements. Another method often used by Goldak and his coworkers[16] was to include the deposit material into the original mesh and the fusion zone elements were assigned the same initial temperature as the base metal. Preliminary studies found that the computed heating rates in the heat affected zone with this method were much lower than those experimentally measured, and the computed thermal cycles are displaced by a certain time difference during cooling. This may be acceptable for modeling single pass welding process, but certainly not desirable in this study for modeling a multipass cladding process because interpass temperature computation is considered critical. In fact, one major concern in this study was the interpass temperatures because they change the cooling conditions of cladding passes. Small errors in interpass temperature computation could be accumulated over the many clad passes. The computed and measured interpass temperatures in the heat affected zone are overlaid in Figure 4.2. The agreement is excellent.

It is not surprising that the computed $t_{8/5}$ cooling times in the heat affected zone are consistently smaller than the measured ones. This may be attributed to the thermal conductivity values of the heat affected zone used in the analysis. In this finite element analysis, thermal conductivity of the heat affected zone was partially corrected by extrapolating thermal conductivity of austenite to bainite start temperature. This treatment may not be enough because microstructure analysis revealed that the final

microstructure in the heat affected zone consists of about 85% martensite and 15% bainite. Further extrapolation may be expected to improve the discrepancy between the computed and measured $t_{8/5}$ cooling times. The difficulty associated with further extrapolation is the uncertainty of the temperature range for the austenite decomposition reactions. At present state, the author is satisfied with the results obtained.

4.3 Predictions of Cladding on Shaft E290

The results of finite element heat transfer analysis clearly demonstrated the accuracy of the model. With finite element analysis, it is feasible to achieve what experimental studies did not or could not. Predictions were made for the cladding onto the same shaft E290 as if there were no operation errors and more clad passes on the shaft. Finite element analysis was conducted to simulate the electroslag cladding on shaft E290 without operation errors. Twenty continuous clad passes onto shaft E290 were analyzed. The trends of interpass temperature changes and their effect on the $t_{8/5}$ cooling times are of particular interest. More information on the heat transfer induced by electroslag cladding onto the shaft are revealed through finite element analysis.

Trends of interpass temperature change in the heat affected zone as the cladding proceeds were investigated. The results of finite element analysis showed that the initial temperatures in the heat affected zone of each pass were within ± 2 °C from the temperature at the center of the heat affected zone. For simplicity, the interpass temperature was defined as the initial temperature at the center of the expected heat affected zone of each pass. The trends is shown in Figure 4.4 along with the temperature change at both ends of the experimental shaft. It is clear that the interpass temperatures increased rapidly in the first four passes. After that, interpass temperatures still kept increasing but at lower rate. Temperature at the right end dropped almost 30 °C after finishing the first 12 clad passes as a result of convection and radiation. After that, the heat from the cladding started reach the right end, and its temperature started to go up. This effect will be discussed in next section.

The $t_{8/5}$ cooling times in the heat affected zone of each pass were found within 1.5

seconds from the value at the center. Figure 4.5 shows the change of $t_{8/5}$ cooling times in the 20 passes. Figure 4.6 shows the dependency of the $t_{8/5}$ cooling times on the interpass temperatures.

In the finite element heat transfer analysis, the original interface between clad deposit and the substrate was assumed to remain. Three parameters are defined to interpret the computed temperature results. First, the penetration depth was estimated by the depth at which the computed peak temperature was equal to the solidus of the substrate material. Second, the boundary between coarse grain region and fine grain region of heat affected zone is defined as locations where the computed peak temperature equal to 1100 °C. Third, the outside boundary of heat affected zone was defined at locations where the computed peak temperature equal to As_1 of the substrate material. The predicted heat affected zone depths of all clad passes in the experimental shaft are shown in Figure 4.7 which are in good agreement with the experimental observation.

4.4 Limitations of the Experimental Data

As mentioned before, full size propeller shafts are too long and too expensive for conducting experiments. Therefore, only short sections of long shafts were used in actual experimental studies. Over years of research, a lot of experimental data have been collected from preliminary process tests, microscopic examinations, temperature measurements, and mechanical tests. These data are readily available to be implemented to the cladding of nickel alloys onto full size propeller shafts. The question is then how the experimental data obtained from experimental size shafts represent the cladding onto full size shafts. Obviously it is required to verify the size difference on the cooling conditions during electroslag cladding.

The rate at which interpass temperatures increase represents the rate for the welding heat to build up. The rate for the heat to build up depends on the rate the heat is dissipated or diffused. The most dominant mechanism of heat transfer in this application is conduction in the shaft. Heat loss at free boundaries through radiation and free convection is less significant. During cladding onto experimental size shaft E290

as shown in Figure 4.4, some of the reasons for the fast heat build up in the first four passes include the fact that these clads were very close to the left end of the shaft. The heat conducted from the cladding heat source to the left end echoed back. Consequently the interpass temperatures in the first few passes were artificially elevated. This is associated with end effects. The change of temperatures at both ends of the shaft effectively indicated end effects. End effects from the left end of the shaft was found very significant in the first a few passes in this cladding experiment. End effects from the right end of the shaft were observed after 12 passes.

End effect from left end of the experimental size shaft for the first few passes can easily be verified. This was done with finite element analysis by investigating the effect of the starting distance to the temperature in the heat affected zone of the first clad pass as well as the left end. The starting distance was defined as the distance from the left end to the centerline of the first clad pass. The shaft was assumed to be uniformly preheated to 225 °C. The temperature at the center of heat affected zone and at the left end, by the end of first clad pass, are plotted in Figure 4.8 as a function of the starting distance. It can be seen that end effects become negligible when the starting distances are longer than 16 cm. It was also found that this minimum starting distance for end effect free cladding for the first few passes was only dependent on the thermal properties of the shaft material and the time to complete one cladding pass. This minimum starting distance can be approximated by

$$S_0 = 2\sqrt{at} = 2\sqrt{\frac{kt}{\rho c}} \qquad (4.1)$$

where S_0 is the minimum starting distance fore end effect free cladding, a, k, ρ, and c are the thermal diffusivity, thermal conductivity, density, and specific heat of the shaft steel, t is the time to complete one pass of cladding on the shaft. Taking the values of a, k, ρ, and c at the preheating temperature, 225 °C, this equation would give 16 cm, which is in excellent agreement with the determined minimum starting distance value with finite element analysis.

End effect from right end of the shaft can be quantified in a similar fashion.

However, such an analysis is only of limited interest because it is dependent on the initial preheating temperature distribution and the length of the shaft. For electroslag cladding on experimental size shafts with uniform preheating temperature distribution, the temperature change at the right end of the shaft can serve as a good indication of end effects. This matter becomes more complicated for cladding with non-uniform preheating temperature distribution. Although it is still possible to evaluate the end effect from right end with numerical analysis, results of such an analysis is not likely to have general application values.

4.5 Optimization of Cladding onto a Long Shaft

The ultimate goal in this project was to optimize the electroslag cladding process onto full size propeller shafts. With other factors fixed, interpass temperature during multipass electroslag cladding played an important role in determining the cooling condition and thus the microstructure and mechanical properties in the heat affected zone. Mechanical tests revealed that optimal heat affected zone properties were achieved when the interpass temperatures were within the optimal range of 200 to 250 °C. The objective of this study was to define the conditions which would allow electroslag cladding to be conducted continuously such that the interpass temperatures during cladding remained within the optimal range.

Applications of electroslag cladding onto full size shafts include cladding multipass layers of nickel alloys at the bearing locations. Each bearing is approximately 22.9 cm (9 in.) wide. It would take eight clad passes to cover the area. There is also a need to clad a whole layer of nickel alloys onto a propeller shaft for better corrosion resistance. At any event, electroslag cladding should start and finish with sufficient distance away from the shaft ends so that no end effects would be expected. The results of experimental measurements and finite element analysis presented in previous sections based on a uniform preheating temperature at 150 °C demonstrated that it is impossible to keep the interpass temperatures within the optimal range without interrupting the cladding process for at least eight passes. Also because of the length of propeller shafts,

it is not feasible to preheat the whole shaft with uniformly distributed temperatures. Therefore, local preheating has to be used.

Finite element analysis was performed to predict the interpass temperature change of electroslag cladding onto a long shaft. The objective of this study was to determined the optimal preheating temperature distribution so that electroslag cladding would be continuous and the interpass temperature would be kept within the optimal range from 200 to 250 °C.

Practically speaking, simulating a full size shaft which is 12 to 15 meters (~ 40 ft.) long is not feasible or economical. A four meter long shaft section was analyzed with the finite element method in this study. Results of this study showed that a shaft of this length can be considered as being infinitely long for any of the cladding applications. No end effect would be expected and this is confirmed from the numerical analysis.

The optimal preheating temperature distribution was determined through trial and error with finite element modeling. The initial preheating temperature was assumed to be uniform through wall thickness of the shaft. Cladding was assumed to start one meter away from the left end of the shaft. During the numerical analysis, an area starting from 30 cm left of the first clad pass to two bead widths on the right side of the first clad pass was uniformly preheated to 210 °C. The size of the preheated area corresponds to the size of electric blankets commonly used for preheating in welding laboratories. At both sides of the preheated area, temperature distribution diminished to room temperature, assumed 20 °C, over a distance S which needed to be determined.

The value of the distance S was determined with finite element analysis on a trial and error basis. This distance was found to be 65 cm. The optimal preheating temperature distribution so determined along the axial direction of the shaft is presented in Figure 4.9.

Thirty cladding passes on this shaft were analyzed. The predicted interpass temperatures for these thirty passes with initial temperature shown in Figure 4.9 are presented in Figure 4.10. They are kept well within the optimal range. It is very likely that interpass temperature will continue to remain in the optimal range 200 to 250 °C if the shaft was longer and more cladding passes were required because interpass

temperatures became stabilized after the first 10 passes. Examinations on the temperature changes at two shaft ends revealed no significant end effects occurred for these 30 clad passes.

Although the shaft section simulated in this study is only four meters long, not as long as a full size shaft, the temperature changes at the two ends of the shaft during cladding clearly demonstrated that no end effects played a role. Therefore the parameters used in this numerical verification regarding the optimal preheat temperature distribution for multipass electroslag cladding can be applied justifiably to the cladding on full size shafts with the same diameter.

CHAPTER 5
MICROSTRUCTURE PREDICTION MODEL EVALUATION

Computational modeling in materials science and engineering is not directed towards eliminating experimental studies, but to reduce the amount of tests and to reach beyond the limitations of experimental measurements. It is important to have a model which is based on scientific principles. It is, however, probably more important to have the model verified by experimental observations. A model will not be a good one until proven to give reliable predictions. A good model will provide more thorough understanding to the subject and be able to predict the behaviors of materials.

The global model assembly presented in Chapter 3 for microstructure and hardness predictions consists of thermodynamics models for computing Fe-C-M multicomponent system equilibria, austenite grain growth, and reaction kinetics for austenite decomposition. This chapter is dedicated to the verification and justification of these models by comparing the predictions with experimental measurements. The performance of the models are also compared with other empirical models. In depth discussion about the reaction kinetics model developed in this research and the model by Kirkaldy and Venugopalan is presented.

5.1 Thermodynamics of Low Alloy Steels

There have been two types of models used in the thermodynamics study of multicomponent Fe-C-M systems. The regular solution model with Wagner formulation used by Kirkaldy and his coworkers[204-206] is definitely a simple one with special reference to low alloy steels. It generates accurate predictions provided that

concentrations of alloying elements in the steel are low. The only disadvantage of this model is that thermodynamics data were derived from binary Fe-C and Fe-M equilibrium phase diagrams. These data are not complete in the sense that they provide molar free energy changes of alloying elements in a phase transformation but the free energy values of each individual phase are lacking. The subregular solution model by Hillert and Staffansson[197] has more complicated formulation and is essentially developed based on ternary systems for much wider composition range. Computational implementation of this model for multicomponent systems is more troublesome. The advantage of this model, however, is that it has the capability of modeling the formation of all different kinds of intermediate phases, and that all the thermodynamics data were measured systematically and consistently.

In this research, the author took the advantage of the simplicity of regular solution model with Wagner formulation and the accuracy and consistency of thermodynamics data based on Hillert-Staffansson model. The method of evaluating required thermodynamics data for this study has been presented in Section 3.2.3. With all these thermodynamics data, the free energy change of each individual phase can be analyzed so that free energy diagrams of steels can be constructed. Another advantage of this approach is that the enthalpy change of a steel, which is an important thermal property of a material in heat transfer analysis can also be computed.

5.1.1 Ae_3 Temperature

The model used in this study for computing Ae_3 temperature of steels has been presented in Chapter 3.2 in terms of ortho-equilibrium and para-equilibrium. This model was developed based on the work by Kirkaldy and his coworkers.[204-206] A progress was made in this thesis work to eliminate some simplifications in their original work by introducing more complete and consistent thermodynamics data in the literature. The accuracy of different approaches in calculating Ae_3 temperatures of steels are presented in this section. Empirical formulas developed by Grange and Andrews are also evaluated in this research.

Before discussing these results, the question of terminology should be discussed with reference to experimental measurements. When the lower and upper limits of austenite formation in hypoeutectoid steels are measured by continuously heating at some specified rate, they are called Ac_1, and Ac_3, respectively. In either instance, the temperature which is determined varies with the rate of heating. It is lower with slower heating rate, the closest approach to equilibrium being attained when the steel is heated at the slowest possible rate. However, a less tedious method, which yields essentially the same value, has been used in practical experimental measurements. This method consists of holding specimens at each of a series of constant temperatures for varying periods of time up to several hours, or at least until doubling the holding times causes no appreciable change in the amount of austenite formed, and then quenching to room temperature. The lower and upper limits of austenite formation determined by this isothermal technique have usually been designated Ae_3, and Ae_1. Subscripts 1 and 3 referring to the A_1 and A_3 lines of the binary Fe-Fe_3C phase diagram.

Grange[259] pointed out some ambiguities in the using of Ae_3, Ae_1 temperatures in question of terminology. In steels which contains three or more elements, the A_1 "line" becomes a three-phase field. Furthermore, the subscript "e" implies true equilibrium conditions which are rare if ever attained in steels of commercial purity. For these reasons, experimental measurements were conducted to measured the lower and upper limits of austenite formation, call A_S and A_F. A_S is defined as the temperature at which a barely detectable amount of austenite forms during prolonged holding at constant temperature and A_F is the temperature at which the last trace of ferrite transforms to austenite on prolonged isothermal holding. Practically speaking, A_S constitutes a ceiling for tempering and A_F a floor for austenizing hypoeutectoid steels. In other words, A_S is the doom of α+cementite two phase region, and A_F is the floor of single phase austenite region.

The A_F defined by Grange[259] can be thus regarded as Ae_3. Based on experimental measurements from 19 steels, Grange developed an empirical formula for the calculation of Ae_3 temperature. This formula was derived by regression analysis from his own experimental measurements of 19 steels within the composition range:

0.30~0.63%C, 0.37~1.85%Mn, 0.16~0.30%Si, 0~3.41%Ni, 0~0.98%Cr, 0~0.33%Mo. This formula is expressed in the form

$$Ae_3(^\circ C) = 854.4 - 179.4\,C - 13.9\,Mn + 44.4\,Si - 17.8\,Ni - 1.7\,Cr \qquad (5.1)$$

Another formula for the calculation of Ae_3 temperature was developed by Andrews[254] in 1965 from binary phase diagrams and calibration of the constants with the experimentally measured Ae_3 temperatures by Grange,[259]

$$\begin{aligned} Ae_3(^\circ C) = 913 &- \Delta T - 25\,Mn - 11\,Cr - 20\,Cu + 60\,Si \\ &+ 60\,Mo + 40\,W + 100\,V + 700\,P \end{aligned} \qquad (5.2)$$

where ΔT accounts for the effects of carbon and Ni, by adding Ni/10 to C as given in Table 5.1.

Watt and Henwood *et al.*[177-179] used the empirically developed formulas for Ac_3 by Andrews[254] in their microstructure prediction algorithm for weld heat affected zone

$$\begin{aligned} Ac_3(^\circ C) = 912 &- 203\sqrt{C} - 15.2\,Ni + 44.7\,Si + 104\,V + 31.5\,Mo + 13.1\,W \\ &- (30\,Mn + 11\,Cr - 20\,Cu - 700\,P - 400\,Al - 120\,As - 400\,Ti) \end{aligned} \qquad (5.3)$$

This formula was reportedly valid within composition range:[254] 0.08~0.59%C, 0.04~1.98%Mn, 0.09~1.78%Si, 0~5.0%Ni, 0~4.48%Cr, 0~1.05%Mo, 0~4.10%W, 0~0.07%V, and 0~0.072%As.

Probably the most accurately measured Ae_3 temperatures of steels were those reported by Grange,[259] and then those in U.S. Steel Atlas.[156] The computed Ae_3 temperatures using the model presented in this thesis, for the 19 steels measured by Grange[259] and 72 steels in U.S. Steel Atlas,[156] are presented in Figure 5.1 and 5.2 in comparison with the experimental measurements. The performance of the models developed in this research, the model by Kirkaldy and Baganis,[204] and the empirical formulas described above were evaluated by comparing the predicted with the experimentally measured Ae_3 temperatures for the 19 steels by Grange[259] and for 72 steels in U.S. Steel Atlas.[156] Statistics analysis of the computed results were performed to evaluate the accuracy of different models in terms of mean difference, root mean square (R.M.S.) difference, and standard deviation. The results are listed in Table 5.2 and 5.3 against the 19 steels measured by Grange[259] and 72 steels in U.S. Steel Atlas.[156]

The results in this study clearly demonstrated that all models gave reasonably good predictions to the Ae_3 temperatures of steels. Overall, the thermodynamics model presented in this thesis, Andrews' Ae_3 formula, and Grange's Ae_3 formula, all gave excellent predictions to Ae_3 temperatures of steels. Statistically, the calculated Ae_3 temperatures using Andrew's Ae_3 formula were slightly higher than the experimentally measured. The calculated Ae_3 temperatures using the model presented in this thesis and Grange's Ae_3 formula were slightly lower than the experimentally measured. The model developed by Kirkaldy and Baganis also has considerable accuracy. It is interesting that calculated Ac_3 temperatures using Andrews' Ac_3 formula were consistently lower than the experimentally measured, quite contradictory to one's expectation that the calculated Ac_3 temperatures might be slightly higher than the experimentally measured Ae_3 temperatures. This may be associated with uncertainties of the coefficients of elements in the parenthesis in Equation 5.3 as mentioned by Andrews.[254]

The model presented in this thesis is an improvement of the originally model by Kirkaldy and Baganis.[204] This study has demonstrated that this improvement offers better accuracy particularly at high temperatures which are associated with low carbon contents. This was attributed to the elimination of some simplifications made in Kirkaldy-Baganis model by introducing more updated thermodynamics data.

It is interesting to investigate the partition of alloying elements during austenite decomposition to ferrite under equilibrium condition. The iterative nature of the algorithm used in the thermodynamics model of this thesis made it difficult to evaluate the partition of alloying elements because of their interactions. With the assumption that the term $\epsilon_{ii}^{\gamma}X_i^{\gamma}-\epsilon_{ii}^{\alpha}X_i^{\alpha}$ was negligible in the equilibrium of each substitutional alloying elements in the two phases, Kirkaldy, Thomson and Baganis[205]] proposed relationship to calculate partition coefficients of alloying elements

$$A_i = \frac{\exp\left(\frac{\Delta^0 G_i}{RT} + \epsilon_{1i}^{\gamma} X_i^{\gamma}\right)}{1 + \epsilon_{1i}^{\alpha} X_1^{\gamma} \exp\left(\frac{\Delta^0 G_1}{RT}\right)} \qquad (5.4)$$

which is a first order approximation to the partition of alloying elements. Close data analysis during the computation revealed that the partitioning coefficients calculated using Equation 5.4 were indeed in fairly good agreement with the computed results in this study which has eliminated those assumptions. The computed partitioning coefficients of alloying elements during $\gamma \rightarrow \alpha$ decomposition at 1000 °K using Equation 5.4 are presented in Table 5.3. It is clear that all alloying elements have significant partition coefficients. The partition of alloying elements not only affects the thermodynamics of the multicomponent system, but also has profound effects on the austenite decomposition kinetics which will be discussed later in Section 5.4.

5.1.2 Ae_1, As_1 Temperatures and Eutectoid Composition

In the original work by Kirkaldy, Thomson, and Baganis,[205] Gibbs-Duhem equation was used to compute the compositional deviation of Acm from binary Fe-Fe_3C phase diagram. To calculate the eutectoid point, they set the carbon content in austenite as a variable and defined the common point of computed Ae_3 curve and Acm curve as the eutectoid point. This approach can only be treated as an approximation. The concept of this approach to determine eutectoid point is incorrect because this point does not represent the eutectoid point of a steel. The inaccurate assumption is that austenite decomposition path to ferrite is restrained in the isopleth of the steel composition of alloying elements instead of a unique curve in the multi-dimensional space determined by thermodynamics equilibrium. This assumption has been corrected by Hashiguchi *et al.*[206] However, Hashiguchi *et al.* did not compute the temperature range for the eutectoid decomposition. They only calculated the temperature for austenite to decompose into eutectoid. This temperature represents the upper limit of the $\alpha+\gamma+$cementite three phase region.

As identified in Chapter 3, eutectoid reaction occurs in a temperature range instead of at a fixed point as in binary Fe-Fe_3C phase diagram. There is a three phase (ferrite+austenite+cementite) region in the n-dimensional phase diagram. The Ae_1 temperature defined by the author as well as by Hashiguchi *et al.* represents the upper

limit of this region. It is not comparable to the A_S temperature defined by Grange in his experimental measurements. The As_1 temperature defined in this research correlates to the lower limit of this region, which should be comparable with the A_S temperature defined by Grange.[254] The significance of As_1 and Ae_1 is that, in a TTT diagram, they represent the asymptote of pearlite start curve and pearlite finish curve respectively.

Grange[259] developed an empirical formula for the calculation of A_S temperatures of the 19 steels based on his measurements. This formula is expressed by

$$A_S(^\circ C) = 723 - 13.9\,Mn - 14.4\,Ni + 22.2\,Si + 23.3\,Cr \qquad (5.5)$$

This equation is valid within the same composition range as that of his A_F formula, Equation 5.1.

In the algorithm by Watt *et al.*[177-179] Ae_1 temperature was approximated with the empirical formula for Ac_1 developed by Andrews[254]

$$Ac_1(^\circ C) = 723 - 10.7\,Mn - 16.9\,Ni + 29.1\,Si + 16.9\,Cr + 290\,As + 6.38\,W \qquad (5.6)$$

which was derived within the composition range: $0.08 < C < 1.43$, $0.04 < Mn < 1.98$, $0.06 < Si < 1.78$, $Ni < 5.0$, $Cr < 4.48$, $Mo < 2.61$, $W < 4.10$, $V < 2.51$, $As < 0.072$.

The computed Ae_1 and As_1 temperatures for the 19 steels measured by Grange[259] and 66 steels in U.S. Steel Atlas[156] are shown in Figure 5.3 and 5.4. It is clear from these two figures that the computed Ae_1 temperatures are consistently higher than the measured A_S temperatures and the computed As_1 temperatures are consistently lower than the measured A_S. Most of the measured A_S temperatures are within the range from As_1 to Ae_1. The computed Ae_1 temperatures by Hashiguchi, *et al.*[206] were also consistently higher than the measured A_S temperatures. This is because the computed Ae_1 temperature represents the upper limit of the three phase region, whereas the measured A_S temperatures represents the lower limit of this region.

The calculated A_S temperatures using Grange's A_S formula, and Ac_1 temperatures using Andrews' Ac_1 formula were found in excellent agreement with experimental measured A_S temperatures.

The difference between computed As_1 temperatures in this study and the measured As temperatures by Grange and in the U.S. Steel Atlas are within the accuracy of

experimental measurements. For the technique mentioned by Grange,[259] one can always expect that the measured A_S temperatures be higher than the actual ones because of the criterion used in the measurement. To detect the formation of austenite, there must be appreciable amount of austenite formed which can only be achieved by heating a sample above its actual As_1 temperature. In the meantime, the author admits that the model presented in this thesis may also be subjected to errors because of neglecting the formation of carbides and other intermediate phases. The formation of carbides and other minor phases may change the composition of austenite and thus affect the multi-phase equilibria in the eutectoid reaction region. Nevertheless, thermodynamics data for the computation of Ae_1, As_1 are still lacking, particularly for those strong carbide formers.

In this research, the eutectoid composition was defined as the austenite composition at As_1 temperature in this research. The model presented in this study is so far the only one which computes As_1 and the eutectoid composition in a rational fashion. The computed results are in considerable agreement with Bain's experimental measurements.[260] Consequently the equilibrium amount of ferrite and pearlite of a hypoeutectoid steel at room temperature can be accurately determined by

$$X_{FE} = \frac{C_{Eut} - C}{C_{Eut} - C_F} \tag{5.7}$$

$$X_{PE} = 1 - X_{FE} = \frac{C - C_F}{C_{Eut} - C_F} \tag{5.8}$$

where C_{Eut}, C and C_F are the carbon content in the eutectoid, steel, and in ferrite.

Watt *et al.*[177-179] combined Equation 5.3 and 5.6 to determine the common carbon concentration and they defined this concentration as the eutectoid point. The whole concept is limited in a binary system. The estimated carbon content in the eutectoid with this method was often found to be unreasonably high for many steels. This contradicts a well known fact that almost all the alloying elements in steels would reduce the carbon content in the eutectoid.[260] This was caused by extrapolating the Ac_3 formula outside

its valid range: $0.08 < C < 0.59$. Thermodynamically this method is incorrect because further austenite decomposition to ferrite will not follow Equation 5.3 once it gets started. In principle, an estimated eutectoid carbon content higher than 0.59 using this method should be discarded.

5.2 Austenite Grain Growth

Austenite grain growth in heat treating of steels has been studied with empirical kinetics model

$$D_t^n - D_0^n = A t \exp(-\frac{Q}{RT}) \tag{5.9}$$

where t represents time, R is the gas constant, A, n, and Q are the kinetics parameters for the grain growth. Reported kinetics parameters in the literature for different class of steels have been compiled and presented in Table 3.9. These parameters are known to be dependent on the steel chemistry and metallurgical processes. Austenite grain growth kinetics varies from steel to steel and kinetics parameters were normally measured under isothermal conditions. Application of these parameters may lead to overpredictions of prior austenite grain size in weld heat affected zone. Experimental examination should be conducted if there is any doubt about the accuracy of austenite grain size predictions.

Microscopical examinations of the cladding heat affected zone of the steel involved in this study in this research revealed that prior austenite grain sizes were quite uniform in the coarse grain heat affected zone. The average diameter of prior austenite was 105 microns. The predicted austenite grain sizes with any set of the compiled kinetics parameters in Table 3.9 are much larger than the actual grain size in the heat affected zone. This discrepancy may have been attributed to the following factors:

1. steep thermal gradients,[167]
2. pining effects caused by partially melted zone,[164,165,230]
3. pining effects from oxides.[228]

Another possible error may have been caused by integrating grain growth kinetics equation for the whole time when temperatures were above Ae_3 or T_{DISS} temperature. Ikawa *et al.*[164,165] observed that 60-80% of grain growth occurred in the heating period, and the grains stop growthing when temperatures become lower than 90% of the peak temperature during the cooling. This is a phenomena which the author has difficulty to understand. As a thermally activated process, austenite grain growth is strongly dependent on temperature and time. However, the heating part of the thermal cycle in weld heat affected zone is only a very small part of the whole cycle at high temperatures. A natural expectation is that the cooling cycle would contribute more to the austenite grain growth. Maybe because of this, numerical predictions of austenite grain growth in weld heat affected zone using empirical kinetics model with parameters measured isothermally are doomed to failure. At present state, grain growth in welding heat affected zone is too complicated to be simulated with a simple model of empirical kinetics.[225] Any predictions on this subject have to be verified by experimental measurements.

The method presented in this thesis to model the growth of prior austenite is a semi-empirical method. The predicted prior austenite grain size profile is in reasonable agreement with microscopical observations. Before better understanding about the austenite grain growth in welding heat affected zones is attained, this method is a reasonable choice for computational modeling.

5.3 Predictions of Jominy Hardness Curves

It is practically easier to compare predicted hardness with experimental measurements than microstructure. The reaction kinetics model of austenite decomposition developed in this research has been presented in Chapter 3, Section 3.4, along with the model originally developed by Kirkaldy and Venugopalan.[159] In this section, the reliability of these two computational reaction kinetics models are evaluated by applying them to the prediction of Jominy hardness of steels. Also evaluated in this research was the empirical model by DeAndrés and Carsí[119] based on CCT diagrams.

Thermal data needed for the microstructure and hardness predictions in Jominy end-quench bars were obtained from finite element analysis. The predicted Jominy hardness curves were then compared with the experimental hardness measurements.

Four steels were selected in this part of the study which include two C-Mn steels (A36 and A588), and two hardenable low alloy steels (4140 and Class 1 steel for submarine propeller shafts). The composition of these steels are shown in Table 5.7. The austenization temperature and holding time used in the end quench tests are listed in Table 5.8. Jominy hardness was measured in Rockwell C and then converted to Vickers. When the Rockwell C hardness values become less than 20, undetectable with Rockwell C, hardness was then measured in Vickers.

Finite element analysis was performed to simulate the heat transfer during Jominy end quench test. Results of the heat transfer analysis provided the needed information for the microstructure and hardness predictions. Because of the axisymmetry of Jominy bars, two dimensional thermal elements with axisymmetric formulation option were used to discretize the Jominy bar. The finite element mesh is presented in Figure 5.5. The density of Jominy bars was assumed to remain constant at the room temperature value, 7860 kg/mm^3. Temperature dependent thermal conductivity and enthalpy change of materials were used in the analysis and are presented in Figure 5.6 and 5.7, respectively. The heat of solid state phase transformation was ignored in the finite element heat transfer analysis because of the difficulty in determining the temperature range which the heat is released during cooling. Cooling rate in Jominy bars changes dramatically with the Jominy distance and consequently the temperature range for austenite decomposition to take place is different from location to locations.

The convective film coefficient at the quenching end is assumed to have a very high value,[260.261] 10000 W/m^2°C, at surface temperature higher than 100 °C, see Figure 4. The other free surfaces of the bar are subject to free convection in air and radiation which was incorporated in the analysis by introducing combined heat transfer coefficient. An emissivity value of 0.3 was used in this analysis. Free convection at the cylindrical surface of Jominy bars was approximated by the solution for vertical cylinders. The solution is the same for a vertical plane surface as shown in Equation 2.16 and 2.17.

Free convection at the top surface of Jominy bars was approximated by the solution for heated plate facing up. The solution was provided by Goldstein *et al.*[185] and Lloyd and Moran[186] based on the work of McAdams[184]

$$Nu = 0.54\,Ra^{1/4} \tag{5.10}$$

for $2.6\times10^4 < \mathrm{Ra} < 10^7$ and

$$Nu = 0.15\,Ra^{1/3} \tag{5.11}$$

for $10^7 < \mathrm{Ra} < 3\times10^{10}$ with the characteristic length expressed by Equation 2.18. The combined heat transfer coefficient at the cylindrical surface of Jominy bars is shown in Figure 5.8 which clearly indicates the dominant effect of radiation.

The results of finite element heat transfer analysis of the end quenching of Jominy bars were used as the thermal history input for microstructure predictions. Consequently, the microstructure distribution profile along the Jominy bar was calculated. By incorporating the hardness calculation formulas in Creusot-Loire system, presented in Section 3.5, the hardness distribution along the Jominy bar can be calculated.

The thermodynamics parameters for these four steels, which are needed in the microstructure prediction using the reaction kinetics model presented in this thesis and the model by Kirkaldy and Venugopalan, are presented in Table 5.9 and 5.10. Table 5.9 contains the important temperatures for austenite decomposition in these steels. Table 5.10 presents the predicted equilibrium amount of ferrite and pearlite at As_1 temperatures of these steels.

The predicted Jominy hardness curves are presented in Figure 5.9 to 5.12 in comparison with the experimentally measured results. Obviously all models gave reasonable predictions for A36 and A588 steels. Kirkaldy-Venugopalan model[159] gave less accurate predictions for steels with higher hardenability, 4140 and Class 1 steels. The reaction kinetics model presented in this thesis, as well as empirically based DeAndrés-Carsí model, however, gave better predictions to 4140 and Class 1 steels. The agreement between the predicted Jominy hardness with the thesis model and the experimental measurements is excellent. The DeAndrés-Carsí model[119] seems to

overpredicts the rate of ferrite reaction when one compares the predicted hardness at the quenching end of A36 and A588 samples and the other end of 4140 and Class 1 steel samples.

The model presented in this thesis was developed based on modifications on the original Kirkaldy-Venugopalan model. A detailed discussion on the rationales of these modifications and their effects will be presented in Section 5.4.

5.4 Discussion on Empirical Models

The results of this study clearly demonstrated that the predicted Jominy hardness curves using the model presented in this thesis and the model by DeAndrés-Carsí are quite comparable. The DeAndrés-Carsí model is a good representative of empirically based models, such as Creusot-Loire model and weld HAZ models developed based on the concept of carbon equivalents. Thus the discussion in this section pertains to all the models of this type.

DeAndrés-Carsí model gave reasonable predictions to the Jominy hardness curves of steels and was reported quite successful in predicting final microstructure and hardness of quenched steels. Its mathematics is very simple and easy to be incorporated into a computer program. Thus one may question the necessity or desirability of developing the reaction kinetics based computational model presented in this thesis. The arguments for this development are three fold. First, the model presented in this thesis is a generic computational model, formulated based on the first principles of reaction kinetics of austenite decomposition. Second, this model has the capability of simulating the whole process of phase transformations, thus provide a complete picture of the microstructure development, versus only predictions of the final microstructure given by DeAndrés-Carsí model. Third, this model can account for any nonlinear cooling rates whereas the DeAndrés-Carsí model is limited to linear or quasi-linear cooling rates.

In the practice of microstructure prediction, DeAndrés-Carsí model bears a serious limitation. It uses only one parameter, Vr, cooling rate at 700 °C, to represent the cooling condition for the whole thermal cycle. This may be a reasonable

approximation to the quenching of steels, where cooling rates are quite fast and linear. When the cooling rate in an area is very nonlinear, like in weld heat affected zone, this model will generate substantial errors, because all CCT diagrams measured with dilatometry method, the data base on which this model was developed, were usually measured with linear or quasi-linear cooling rates. In the welding of hardenable steels, preheating has been a common practice to reduce the risk of hydrogen assisted cracking. During a multipass welding operation, interpass temperatures are normally elevated. In either of these situations, the cooling rates in the temperature range for bainite and martensite reactions considerably slowed down and are much smaller than the cooling rates at 700 °C. Hence, DeAndrés-Carsí model will not give accurate predictions in these applications. Only computational models can account for the nonlinearity of cooling curves properly.

5.5 Discussion on Reaction Kinetics Models

Jominy hardness computations in this research confirmed an earlier observation by Lee and Bhadeshia:[244] Kirkaldy-Venugopalan model works reasonably well for C-Mn steels and steels containing lower alloy content, but less satisfactory for higher alloyed steels. The reaction kinetics model presented in this thesis was developed based on modifications of original Kirkaldy-Venugopalan[159] model. This section is to discuss the rationales behind the modifications made in the development of the thesis model.

The thesis model and Kirkaldy-Venugopalan model, as well as the model developed at Kawasaki Steel,[155] all started with modeling isothermal reaction kinetics. The predicted incubation and completion times at the nose temperatures of ferrite and bainite reactions may be considered as good indications of steel hardenability. The predicted results of 4140 steel are listed in Table 5.11 and 5.12 for ferrite and bainite reactions respectively. The prior austenite grain size in this sample was predicted using DeAndrés-Carsí model,[119] G=8.

It is interesting to notice that both Kirkaldy-Venugopalan model and Kawasaki Steel model were calibrated with the same data base, U.S. Steel Atlas, but they give

quite different predictions. The predicted incubation times using these two models are quite short for both ferrite and bainite reactions comparing to those predicted with the thesis model. Kirkaldy-Venugopalan model would predict short completion times. Kawasaki Steel model, on the other hand, predicted quite long completion times. The discrepancies caused by these two models motivated the author to re-evaluate the accuracy of their database, U.S Steel Atlas. A reasonable speculation is that either there exist systematic errors in the data base, U.S. Steel Atlas, or systemic errors were introduced in Kirkaldy-Venugopalan model during the calibration process, or even the mathematical formulation of Kirkaldy-Venugopalan was not quite right.

Another indication of predicted steel hardenability is the critical cooling rate for the formation of 100% martensite. The predicted results for 4140 steel using different models, including some empirical models, are presented in Table 5.13. All models, except Kirkaldy-Venugopalan model, predicted that the critical cooling rate for the formation of 100% martensite for 4140 steel is determined by suppressing bainite reaction. It is clear from the results in this research that Kirkaldy-Venugopalan model overestimated the rates of ferrite reaction in hardenable steels which led to the underestimation of steel hardenability.

Although Kirkaldy-Venugopalan model failed to give accurate predictions for the Jominy hardness of hardenable steels, one can not deny or underrate the great contribution made by Prof. Kirkaldy in this life time research in steel hardenability. The philosophy presented in his numerous publications is highly regarded by the author as the most comprehensive to date. Therefore, the author has put a lot of effort in recognizing the sources of errors in this model and sought ways to modify this model. The modifications are considered as an important step to perfect this model so that the modified model can be used for microstructure predictions in a full scale without introducing artificial fudge factors.

Careful examinations on the mathematics formulation of Kirkaldy-Venugopalan model suggested that its accuracy was affected by the following factors:

- accuracy of the database used in the model calibration,
- expression of I(X) term,

- accounting for the effects of alloying elements,
- accounting for the effects of austenite grain size.

Following discussion is focused on the implications of the original Kirkaldy-Venugopalan model and the justifications of modifications carried out in this research towards minimizing errors.

5.5.1 Accuracy of Database

Any theoretically based model has to be calibrated with some experimental data, and the predictions given by a model is only as reliable as the data with which the model was calibrated. The Kirkaldy-Venugopalan model was calibrated with the TTT diagrams from U.S. Steel Atlas.[156] It is reasonable to speculate that systematic errors were introduced into the Kirkaldy-Venugopalan model from this database. The U.S. Steel Atlas was the oldest, and probably most familiar compilation of TTT diagrams. This collection contains more than one hundred TTT diagrams, taken from work done at the U.S. Steel Research Laboratory and also from open literature at the time of publication. Because of the variety of sources for this data, a variety of experimental procedures were involved. Most of the diagrams, however, were based on metallographic observation and hardness measurements of specimens transformed for various times at different temperature and quenched.

The first edition of U.S Steel Atlas was published in 1943 prompted by the growing realization on the part of producers, heat treaters, and users of steel that such information can be of great practical value. Continued requests for copies of the Atlas led to a second edition, issued in 1951, containing additional diagrams and data. The third edited was published in 1963.[156] The U.S. Steel Atlas is now out of print. However, the American Society for Metals has issued publications[263,264] containing many of the TTT diagrams from the U.S. Steel Atlas, supplemented with some CCT diagrams. Among these TTT diagrams, there are many TTT diagrams for low alloy steels which reportedly have incubation times at the nose temperature less than one second, or a few seconds. Such things as reporting incubation times of no more than 2 seconds for

forming 0.1% volume fraction of transformation product were particularly suspicious. It is practically impossible to quench a sample at a theoretically infinite fast cooling rate to the nose temperature and hold the sample at the temperature to less than one second, or a few seconds, and then quench the sample to room temperature at a theoretically infinite fast cooling rate. This was also notified in the Appendix of the third edition:

> "The principal curves of the I-T diagram have been drawn as broad lines, not only so that they will stand out among fainter coordinate lines, but also to emphasize that their exact location on the time scale is not highly precise, even for the particular steel sample they represent. Portions of these lines are often shown as dashed lines to indicate a much higher degree of uncertainty. Thus all portions of lines extending to the left of the 2-second coordinate are dashed lines because, for times less than about 2 seconds, reliable and accurate measurements were not possible by the methods used."
>
> "In this connection, it should be recognized that the I-T diagram is designed to represent the over-all pattern of transformation in a particular composition and, particularly in regions in which transformation occurs rapidly, should not be regarded as being always a summary of a complete set of highly precise quantitative measurements, the principal fundamental difficulty, of course, is that even a very small piece of steel requires some appreciable time interval to cool throughout to the temperature of the isothermal bath...."

A very important notification in the appendix of U.S. Steel Atlas, which could often be neglected, is that many beginning lines which represent short incubation times were not actually measured, even in the "nose" region of rapidly transforming steels, but estimated from measured data for longer times using the method proposed by Austin and Rickett.[265] Therefore, considerable judgment is often required in constructing an TTT diagram from experimental data and equal judgment is required in its interpretation with respect to conditions different from those under which it was determined. An experienced scientist or metallurgist should not read into an TTT diagram an unduly high

degree of accuracy nor condemn it because it is not always based upon a complete set of highly precise measurements.[156]

It is commonly believed that CCT diagrams measured with dilatometry method may not be able to give accurate volume fractions of transformation products, but they have better accuracy in determining the temperature range for austenite decomposition reactions during continuous cooling at certain rates.[144] CCT diagrams are also a natural approximation for the phase transformations under most of the cooling conditions in heat treating or welding operations. Thus the author sought a way to calibrate the phase transformation model with CCT diagrams. The critical formulas presented in DeAndrés-Carsí model were developed based on regression analysis on CCT diagrams. They provided a convenient means for the model calibration in this research. This may partially explain why the model developed in this research performed better than the Kirkaldy-Venugopalan model. The calibration of the model presented in this thesis was performed around a pseudo steel composition: C=0.3%, Mn=0.5%, Si=0.25%, Ni=1.05%, Cr=0.5%, Mo=0.25.

5.5.2 Reaction Rate

The model developed in this study, as well as Kirkaldy-Venugopalan model, indicates that all diffussional austenite decomposition reactions terminated in finite time. The Kirkaldy-Venugopalan model used the I(X) expression

$$I(X) = \int_0^X \frac{dX}{X^{2(1-X)/3}(1-X)^{2X/3}} \tag{5.12}$$

to simulate the sigmoidal effect of phase transformations. In this research, an equivalent expression

$$S(X) = \int_0^X \frac{dX}{X^{0.4(1-X)}(1-X)^{0.4X}} \tag{5.13}$$

was used. The constant 2/3 in I(X) expression was replaced by 0.4 to match with the empirical observation, $\tau_{1.0\%}=4\tau_{0.1\%}$ mentioned by Kirkaldy, Thomson and Baganis.[205] Equation 5.12 would, on the other hand, predict $\tau_{1.0\%}\approx 2.2\tau_{0.1\%}$.

Numerical integration was performed with $\Delta X=10^{-5}$ for these two expressions. The results are shown in Figure 5.13 and one can notice the similarity of the profiles of these two curves. Some typical values are presented in Table 5.14.

It is interesting to note the ratio between the time to finish (X=1.0) and the time to start (X=1.0%) a reaction. The Kirkaldy-Venugopalan model predicts I(1.0)/I(0.01)=7.24, *i.e.*, $\tau_{Ff}/\tau_{Fs}=\tau_{Pf}/\tau_{Ps}=7.24$ at any temperature. The model presented in this thesis, however, predicts S(1.0)/S(0.01)=19.9. This characteristics of I(X) and S(X) expressions is very critical in predicting accurately the incubation time for a reaction. Since all the computational models were calibrated to the incubation times, cautions must be taken very carefully in the calibration process. The small ratio between the time to finish and to start a reaction in Kirkaldy-Venugopalan model has seriously worsened the predictions for steels with reported small incubation times. This may be the reason which forced Kirkaldy and Venugopalan to include an empirical term in the I'(X) expression for the calculation of bainite reaction.

The reaction kinetics model presented in this thesis shared a common misconception with Kirkaldy-Venugopalan model.[159] The mathematical formulation of these two models suggest the time for a diffusional reaction to reach completion is directly proportional to its incubation time at any temperature. This is inherent in the derivation of Zener and Hillert's reaction kinetics.[160,161] The natural deduction of this formulation is that both the start curve and finish curve of a reaction in a TTT diagram would have same profile. This is not true. All the experimentally measured TTT diagrams would demonstrate that the nose temperatures of finish curves for bainite and pearlite reactions are always lower than those of the starting curves. A reasonable explanation is that all the diffusional phase transformations have different equilibrium temperatures to start and complete the reactions. For example, austenite starts to decompose into pearlite at Ae_1 temperature and the reaction is completed at As_1 temperature under equilibrium condition. Consequently, the start curve and finish curve

have different asymptotes: Ae_1 for the start curve, As_1 for the pearlite finish curve. The same analogy would apply to ferrite and bainite reactions. At the current state, however, the Zener-Hillert[160-161] type formulation offers the best foundation for computational modeling.

5.5.3 Effects of Alloying Elements

The mathematical formulation of Kirkaldy-Venugopalan model suggests that the effects of alloying elements on steel hardenability are additive. This is contradictory to the common perception which says that the effects of alloying elements on steel hardenability are multiplicative.[116-119,266,267] This was introduced into the model through the approximation of the effective diffusion coefficient for the phase transformation[157-159]

$$\frac{1}{D_{eff}} = \frac{1}{D_C} + \sum_{i=2}^{n} \frac{k_i C_i}{D_i} \tag{5.14}$$

provided the mechanism for all elements is the same. How many terms correlated to different alloying elements should be incorporated in the approximation for effective diffusion could be a very critical problem in deriving a valid and general formula for a phase transformation.

In this research, the author classified the effects of alloying elements on steel hardenability in thermodynamic and kinetic perspectives. Thermodynamically, they affect steel hardenability by influencing the equilibria of Fe-C-M multicomponent system. Thus they either enlarge or suppress the temperature regions for each austenite decomposition reaction. The kinetic effects of alloying elements on steel hardenability are that they all uniquely affect phase transformation through partitioning at the phase boundary. Theoretically speaking, all the alloying elements which would partition during austenite decomposition will affect the effective diffusion coefficient. Table 5.3 lists the computed partition coefficients of alloying elements at 1000 °K. It is very clear that all alloying elements will partition during ferrite reaction and thus they will influence the effective diffusion coefficient.

The question is then how to model the kinetics effects of alloying elements on effective diffusion coefficient for a austenite decomposition reaction. If the effective diffusion coefficient is expressed in Arrehnius rate equation, a reasonable speculation is that alloying elements affect both the activation energy and proportion coefficient. It was conjectured that the addition of alloying elements in low alloy steels would not change the mechanism of a diffussional austenite decomposition reaction, and the diffusion of each alloying element at the phase boundary has an activation energy close to the self diffusion of iron atoms during the reaction. Therefore the author has adopted a methodology of using a fixed value of activation energy for austenite decomposition reaction and incorporating the kinetics effects of alloy elements in the term of proportion coefficient.

The methodology of modeling the effective diffusion coefficient in this thesis is similar to but slightly different from that presented in Kirkaldy and Venugopalan model. A very significant difference between these models is that the effects of alloying elements are multiplicative in the thesis model but additive in the Kirkaldy-Venugopalan model. Experimental observations[116-119,266,267] clearly support the formulation of the thesis model. This formulation difference can partially explain why Kirkaldy-Venugopalan model works very well for steels with poor hardenability, but so satisfactorily for steels with higher hardenability which is associated with more alloying element additions.

5.5.4 Effects of Austenite Grain Size

The original Kirkaldy-Venugopalan model[159] assumed nucleation site saturation at grain boundaries. For each diffusional reaction, there is thus a grain size term $1/2^{(G-1)/2}$ which literally represents the number of grains per square inch at $100\times$ magnification. A difference of 2 in ASTM grain size will affect rates of austenite decomposition reactions by a factor of 2. This term was later adjusted by Kirkaldy[233] to $1/2^{G/8}$ which represent the 1/4 power of the austenite grain diameter. A difference of 2 in austenite grain size thus affects steel hardenability by a factor of 1.18. Mathematically, this adjustment suggests less significant effects of austenite grain size.

The rationale behind this adjustment was claimed to match the incubation time transient predicted by Cahn[154] for nucleation and growth from grain boundary. Actually, the classical phase transformation kinetics theory developed by Johnson-Mehl,[153] Avrami,[148,149] and Cahn[154] is more complicated than this. Cahn[154] studied four types of nucleation sites: homogeneous nucleation, grain boundaries, grain boundary edges, grain boundary corners. He analyzed the half time of a reaction and its dependence on the austenite grain diameter D. He concluded that the half time of a reaction is proportional to the $D^{1/4}$ for grain boundary nucleation, $D^{1/2}$ for edge nucleation, $D^{3/4}$ for corner nucleation, D^{1} for site saturation and D^{0} for homogeneous nucleation.

It is the author's perception that all these nucleation sites are competing with each other. The overall effect of the austenite grain size on each reaction may thus be considered some kind of average among all these nucleation mechanisms. The coefficients of grain size term in the model developed in this research may be interpreted as the overall effects of grain size. The coefficients in Equation 3.68, 3.70, and 3.72 indicate that ferrite reaction is close to the site saturation, pearlite and bainite reactions are between edge nucleation and corner nucleation.

5.5.5 Activation Energy

The exponent of undercooling n in these two models and the activation energy Q for a phase transformation determine the shape of a curve. It is not unreasonable to assume one single value of activation energy for austenite decomposition reactions. The challenge is how to find this value with optimal fit which would predict reasonable shape of C curves combined with the exponent of undercooling term. One can expect to somehow correct the errors introduced by this simplification in later stage of model calibration. At the nose of each C curve, there exists a simple relationship

$$Q = \frac{nRT_N^2}{\Delta T} \tag{5.15}$$

where T_N is the temperature at the nose of a C curve. In this study, an activation energy value of 27500 cal/mol°K was adopted. This correlates to the activation energy of self diffusion of iron atoms at phase boundaries. If the activation energy of a reaction is known, the nose temperature, at which shortest incubation time is expected, can be expressed by

$$T_N(^\circ K) = \frac{-Q + \sqrt{Q^2 + 4nQRAe_3(^\circ K)}}{2nR} \tag{5.16}$$

The calculated T_N values based on Q=27500 cal/mol°K for many steels are in good agreement with the experimentally measured nose temperatures for ferrite, pearlite, and bainite reactions in TTT diagram compendiums.[156.263.264] This has justified the use of a single value of activation energy for austenite decomposition reactions.

The author did not find it necessary to incorporate another empirically derived term to simulate the sluggish bainite reaction. The error introduced by I(X) expression in Kirkaldy-Venugopalan model and determination of bainite reaction incubation time may be the reasons which forced them to use their correction term in I'(X) expression.

5.6 Concluding Remarks

The verifications and justifications of the model presented in this thesis for microstructure and hardness predictions developed in this research have been presented in this chapter. The results of this study clearly demonstrated improvements of the models by Kirkaldy and his associates. The thermodynamics models for computing Fe-C-M multicomponent system equilibria and the reaction kinetics model developed in this research are very successful in the microstructure predictions. And they are expected to give more reliable predictions for the microstructure development in weld heat affected zone.

The author attributes the success of the model presented in this thesis to the inspiration from the continuous work of Prof. Jack Kirkaldy on steel hardenability. The philosophy and the modifications of the models in this thesis is an extension or

continuation of his work and a necessary step towards perfection. The author is fully aware of the fact that Kirkaldy himself did not use the Kirkaldy-Venugopalan model to the full scale for the prediction of microstructural development in steels. Instead, he only used this model to predict TTT and CCT diagrams of steels. He developed a unique method for the calculation of Jominy hardness of steels with considerable accuracy.[268-271]

It was concluded from current studies that the growth of austenite grains is too complex to be modeled with a single relationship based on empirical grain growth kinetics. This conclusion is particularly true for the prediction of austenite grain size in weld heat affected zone. As a matter of fact, modeling prior austenite grain growth is a universal problem in modeling microstructure development in welds. The author adopted a semi-empirical approach in this research to model the austenite grain growth. Before more understanding of austenite grain growth in weld heat affected zones is obtained, this approach remains to be a reasonable choice. Experimental evaluations are recommended to guarantee accuracy of final microstructure predictions.

Applications of the models developed in this research will be demonstrated in next Chapter, which include computation of TTT and CCT diagrams, prediction of weld heat affected zone microstructure and hardness, and characterizing steel weldability.

CHAPTER 6
MICROSTRUCTURE AND HARDNESS IN THE HEAT AFFECTED ZONE

The models for the prediction of microstructure development in weld heat affected zones of steels have been presented in Chapter 3. The reliability of the models for predicting multicomponent Fe-C-M system equilibria has been verified in Chapter 5 with the experimental measured data in the literature. The accuracy of the reaction kinetics model for austenite decomposition in low alloy steels has been confirmed in Chapter 5 by the prediction of Jominy hardness of steels. This Chapter is mainly dedicated to the prediction of microstructure and hardness in the heat affected zones of electroslag cladding. Applications of these models in predicting TTT and CCT diagrams, with specific reference to the grain coarsened and grain refined regions of HAZs, are also presented in this Chapter for the purpose of help understanding the phase transformation behavior in the heat affected zones.

A steel for manufacturing submarine propeller shafts, MIL-S-23284 Class 1 steel, was selected in this study. The composition of this steel has been presented in Table 4.7. Thermodynamics parameters of this steel are shown in Table 4.9.

6.1 TTT Diagrams for the HAZ

Computation of TTT curves with the models presented in Chapter 3 was done in three steps. The first step was to compute Ae_3, Ae_1, As_1, Bs, and Ms temperatures, as well as the eutectoid composition of the steel using the thermodynamics model. Consequently the equilibrium amount of ferrite and pearlite at room temperature could

also be estimated. The second step was to define the volume fraction of each phase transformation product which each C curve would represent. In this research, ferrite start, pearlite start, and bainite start curves were all associated with the formation of 1% volume fraction of transformed product. Thus the value of S(X) term was calculated. For both ferrite and bainite reactions, calculation of S(X) is straightforward since transformed volume fraction is directly used, thus $S(X)_{X=0.01}=0$. For pearlite reaction, numerical integration was performed to evaluate $S(0.01/X_{PE})$ because phantom fraction $X=X_P/X_{PE}$ is used in the calculation. For both pearlite finish and bainite finish curves, $S(1.0)=2.05$ is used. The third step involved the calculation of C curves using the kinetics equations presented in Chapter 3 and the plotting of C curves in a TTT diagram. These procedures can be used for the computation of TTT diagrams with reference to many applications which include heat treating and welding heat affected zones.

TTT diagrams with specific reference to the two distinct regions of heat affected zone, grain coarsened and grain refined regions, were computed. The only extra parameter needed in the computation was the austenite grain size. Metallographic examinations revealed that the average diameters of prior austenite grains in grain coarsened region and grain refined region were 105 and 5 microns respectively. The computed TTT diagrams are presented in Figure 6.1 and 6.2 for these two regions respectively.

From the predicted TTT diagram for grain coarsened region, Figure 6.1, one can see that ferrite and pearlite reactions are very retarded. Only martensite and bainite would expected to form in this region. The TTT diagram for the grain refined region, however, shows a good possibility to form ferrite in this region. The only difference in this two distinct regions is the prior austenite grain size. As the prior austenite grain size increases, all C curves are pushed to the right side which means for longer reaction times. The degree of this retarding effect of austenite grain size varies from reaction to reaction. It is more notable for ferrite reaction than for pearlite and bainite reactions. As the austenite grain size changes from 5 microns to 105 microns, ASTM grain size index changes from 12.3 to 3.55. The grain size term changes from 0.03 to 0.36 for ferrite reaction, 0.07 to 0.46 for pearlite reaction, 0.08 to 0.49 for bainite reaction.

6.2 CCT Diagrams for the HAZ

Computation of CCT diagrams for the clad HAZ were conducted using similar procedures. The first two steps were the same as in the computation of a TTT diagram. The third step, however, required approximation of the cooling curves. To be more comparable to the cooling cycles which were commonly used in the experimental measurements with dilatometry method, constant cooling rates were assumed in this research for computing CCT diagrams. The simulated samples were assumed to be austenized at 900 °C and were allowed to cool down with constant cooling rates to room temperature. The C curve which represented the start of a phase transformation is associated with the formation of 1% of transformed product.

The computed CCT diagram for the grain refined and grain coarsened regions of the heat affected zone are presented in Figure 6.3 and 6.4. They are in good agreement with the experimentally measured ones using dilatometry method. From these CCT diagrams, one can expect that only bainite and martensite would form in grain coarsened region over a wide range of cooling rates.

6.3 HAZ Microstructure and Hardness

The models presented in this thesis were applied to the prediction of microstructure development and hardness in the electroslag cladding heat affected zone of Class 1 steel. The predicted microstructure and hardness were first compared with the results from earlier experimental studies[272,273] which were conducted at OGI using small blocks prior to the author's work. Then the models were applied to predictions of microstructure and hardness in the multipass electroslag cladding heat affected zone of Class 1 steel propeller shafts.

6.3.1 Comparison with Results from Experimental Studies

In the experimental studies which were directed towards characterizing the

microstructure in the electroslag cladding, single pass bead-on-plate clads were prepared on small plates, 10 cm thick, 16 cm wide and 50 cm long. Three different preheating temperatures were used: 93 °C (200 °F), 150 °C (300 °F), 204 °C (400 °F). Post weld stress relieve heat treatment were also conducted at 649 °C (1200 °F). Only as-welded hardness profile was compared in this research.

Hardness profiles were measured along the centerline of clad in Knoop hardness values. For comparison, the Knoop hardness values were converted to Vickers in this research.

A hardness profile was measured by Zhao[272] from a specimen with 93 °C preheat temperature. The heat transfer in such a specimen during electroslag cladding was simulated with the model presented in Chapter 2. The thermal cycles experienced in the heat affected zone were then used for the microstructure and hardness predictions. The predicted and measured hardness profiles in the heat affected zone as a function of the distance from the fusion line is presented in Figure 6.5. Excellent agreement is observed.

Only the microstructure in grain coarsened heat affected zones were characterized with both optical and electronic microscopic examinations. It was reported by Zhao[272] that the microstructure in the grain coarsened heat affected zone of the 93 °C preheated sample was consisted primarily of lath martensite and lower bainite. The computation yielded a microstructure of approximately (90% martensite + 10% bainite). For the 150 °C preheated sample, microscopic examinations revealed that the microstructure was dominated by upper bainite and auto-tempered martensite. The computation predicted approximately (80% martensite + 20% bainite). For the 204 °C preheated sample, microscopic examinations suggested that the microstructure was mainly composed of auto-tempered martensite. The computation produced approximately (60% martensite + 40% bainite). Again the computational predictions are in good agreement with the microscopic examinations.

One must be aware that it is difficult using transmission electronic microscope examination to quantify microstructural constituents. And computational modeling, at current state, is not able to distinguish upper bainite from lower bainite and to model the

tempering of martensite in a rigorous fashion.

Gao[273] conducted more extensive hardness measurements in samples with different preheating temperatures. He investigated the effect of preheating temperatures on the hardness profile in weld heat affected zone. However, he only reported the measured hardness range in the heat affected zone. The author is not sure of the accuracy of his data. His results are presented in Figure 6.6 along with the predicted heat affected zone hardness profiles for different preheat temperatures. The agreement between these two data sets is fairly good.

As the interpass temperature increases, the cooling rates around Ms temperature decrease substantially. This causes potential uncertainty in the calculation of martensite hardness using Equation 3.80. One can speculate that cooling rates which were used to develop Equation 3.80 from CCT diagrams were much higher than the cooling rates in weld heat affected zone, particularly when the interpass temperature is elevated.

6.3.2 Microstructure and Hardness in the Multipass Electroslag Cladding Heat Affected Zones

Thermal cycles experienced in the heat affected zone of electroslag cladding onto shaft E290 are presented in Figure 6.7 as a function of the distance from the original clad/substrate interface. The predicted martensite volume fraction and hardness in the heat affected zone are plotted in Figure 6.8 and 6.9 as functions of the distance from the original clad/substrate interface. The increased amounts of bainite and ferrite formed as the distance increases were mainly attributed to the change of prior austenite grain size. The predicted austenite grain sizes are plotted in Figure 6.10. Similar results as in Figure 6.8 to 6.10 can be predicted for heat affected zones with different interpass temperatures. Based on such results, the effects of interpass temperatures on the microstructure formation and final hardness in the heat affected zone can be analyzed.

The major concern in the electroslag cladding is the microstructure and mechanical properties in the grain coarsened region of the heat affected zone. It has been articulated repeatedly in this thesis that interpass temperatures played a key role in

determining the microstructure formation and hardness in the heat affected zone of multipass electroslag cladding on carbon steel propeller shaft. The major reason is that cooling rates at temperatures for bainite and martensite reactions are severely reduced by the elevated interpass temperatures. This section is dedicated to the investigation of the effects of interpass temperatures on the microstructure and hardness in the heat affected zone.

According to Harrison and Farrar,[141] weld heat affected zone is normally characterized into grain coarsened region and grain refined region. Grain coarsened region experienced peak temperatures from ~1100 °C up to the melting point of base metal. The calculated precipitate dissolution temperature of the Class 1 steel, T_{DISS}, is 1091 °C which correlates very well the mentioned lower peak temperature limit for the grain coarsened region. Grain refined region experienced peak temperatures a little above the Ae_3 temperatures. It was assumed in this research that the austenite grain size would remain at its as-recrystallized size until T_{DISS} temperature is reached. Commonly used CCT diagrams for weld heat affected zones are normally measured with austenization temperature in the range 900 to 950 °C for the grain refined region and 1300 to 1350 °C for the grain coarsened region. In this research, representative thermal cycles with peak temperatures values of 1300 and 900 were taken as references to evaluate the effects of interpass temperatures on cooling rates, microstructure and hardness in the grain coarsened region and grain refined region respectively.

The effects of interpass temperature on the cooling rates in grain coarsened and grain refined heat affected zones are presented in Figure 6.11 and 6.12. It can be seen from these two figures, that the cooling curves are very nonlinear at temperatures around the Ms point of the steel. With non-linear cooling curves like these, using CCT diagrams, most of which were measured with constant cooling rates using dilatometry method, is doomed to giving unreliable predictions. Empirical models developed based on the concept of carbon equivalents have the same limitations. Only computational model can take the nonlinearity of cooling curves into proper consideration.

The predicted volume fractions of martensite in the grain coarsened and grain refined heat affected zones are plotted in Figure 6.13 and 6.14 as functions of interpass

temperatures. The differences were caused by the prior austenite grain sizes. The predicted hardness in the grain coarsened and grain refined heat affected zones are plotted in Figure 6.15 and 6.16 as functions of interpass temperatures. The predicted HAZ hardness values are in good agreement with the experimentally measured.[274]

The success in the microstructure and hardness predictions in this research may be well attributed to the capability of computational modeling in accounting for the nonlinearity of cooling curves and proper modeling of bainite and martensite reactions. In this research, bainite was assumed to continue forming at temperatures below Ms temperature as long as austenite remained. These are reasonable approximations to the reality of bainite and martensite reactions, particularly in the cladding heat affected zones where cooling rates were severely reduced at temperatures below Ms temperature by the elevated interpass temperatures. In this research, the rate of martensite formation was appropriately estimated with Koistinen-Marburger relationship,[250] Equation 3.76. It is a good mathematic representation of martensite transformation based on experimental observations. It is well understood that the formation of martensite is only a function of temperature. A common perception about the formation of martensite has been summarized by Steven and Haynes[241] as follow: 10% martensite formed at a temperature 10 °C below Ms temperature, 50% martensite formed at a temperature 47 °C below Ms temperature, 90% martensite formed at a temperature 103 °C, and 100% martensite formed at temperature 215 °C below Ms temperature. It is very clear from Figure 6.11 and 6.12 that elevated interpass temperatures prolong the cooling time in the temperature range for the formation of martensite, consequently left more time for the bainite to be formed.

6.4 Re-evaluation of Empirical Weld HAZ Models

This research has offered a negative appraisal to the application of empirically based weld heat affected zone models, such as the ones developed by Yurioka *et al.*,[133] and by Terasaki.[136] When these two models were applied to the heat affected zone of electroslag cladding, the predicted HAZ hardness values were consistently 60 to 90

Vickers higher than the experimental measurements. The error would increase as the interpass temperature. Should these two models be applied to the determination of preheat temperature, they predicted preheat temperature unreasonably higher than the actual Ms temperature of the steel to avoid the formation of martensite in the heat affected zone.

Although they are reported quite successful in welding industry, the empirically based weld heat affected zone models bear a very serious limitation by taking only $t_{8/5}$ cooling time as the thermal input to the prediction of microstructure and hardness. There exists a significant difference between electroslag cladding process in this research and conventional welding process. Convectional welding processes normally have the heat input as the major factor affecting the $t_{8/5}$ cooling time in weld heat affected zone. Whereas electroslag cladding in this research has fixed heat input, the interpass temperature is probably the only factor which influence the cooling rate in the heat affected zone. Finite element analysis in this research demonstrated that the $t_{8/5}$ cooling time in the heat affected zone would increase moderately as the interpass temperature goes up. The cooling time from 500 to 300 °C, $t_{5/3}$, on the other hand, would be significantly lengthened as the interpass temperature increases. As the interpass temperature increases from 20 to 275 °C, the $t_{8/5}$ cooling time increases from 23 to 69 seconds, while $t_{5/3}$ increases from 28 to 523 seconds. $T_{8/5}$ may be a good index for ferrite and bainite reactions. It is certainly not a good index for bainite reactions. Cooling time from 500 to 300 °C, $t_{5/3}$, however, is a better index for the cooling rate in the range for bainite reaction.

CHAPTER 7
SUMMARY AND SCOPE OF FUTURE RESEARCH

A complete analysis of microstructure development in the heat affected zone of electroslag cladding of nickel alloys onto low alloy steels consists of analysis of the heat transfer induced by the cladding, thermodynamic modeling of multicomponent Fe-C-M system equilibria for low alloy steels, kinetics model for the austenite grain growth, and reaction kinetics model for austenite decomposition. This research has tackled every issue in the related disciplines.

7.1 Finite Element Analysis

The heat transfer analysis requires weld geometry, material properties, the cladding procedures and parameters as input and provides temperature distribution history, cooling rates for later microstructure and hardness predictions. A macro file was generated to discretize the finite element model so that the meshing can be conducted automatically. The mesh density was optimized according to the expected thermal gradients during the cladding. This macro file takes into account parameters of the weld geometry.

As stated earlier, the finite element analysis has taken many details of the heat transfer into proper consideration. It is believed that the accuracy of the current analysis is limited by the accuracy of the material properties. The cost of incorporating temperature dependent thermal conductivity in finite element analysis is trivial and it should be used whenever the data is available. Thermal properties of nickel alloy 625 were obtained from the manufactures.[193] They should be reasonably accurate. The

reported thermal conductivity and specific heat of this material are found to be a linear function of temperature. The accuracy of these data was not reported. The enthalpy change of this material was integrated from the specific heat data.

The enthalpy change of the shaft steel was computed according to the thermodynamics of the multicomponent Fe-C-M system. The computed results should have better accuracy than those commonly used in finite element analysis which were actually analytical approximations for pure iron.[16,17,177-179] For the first time, enthalpy change of steels was computed in a rational method and incorporated into finite element analysis. Thermal conductivities of materials, however, have more uncertainties in the accuracy in terms of their dependence on steel composition and microstructure.

It was well understood that thermal properties of materials are not only temperature dependent, but also dependent on their composition and thermal history, which is associated with the microstructure state. For example, austenite has smaller thermal conductivity and higher specific heat than ferrite at the same temperature. The dependence of thermal properties on the composition and microstructure may hinder the accuracy of finite element heat transfer analysis. Many researchers used the same thermal properties of materials in the heat transfer analysis in welds during heating and cooling. The interactive effects of phase transformations on the heat transfer were ignored. The author, however, used modified thermal conductivity in the heat affected zone during cooling. This is just a step closer to the interaction between heat transfer and phase transformation in the heat affected zone. This treatment offsets, to a certain extent, a common problem in computational weld mechanics: computed cooling rates are often found to be greater than the experimental measured. A more complete treatment would require the enthalpy change of the heat affected zone be modified during cooling. The current analysis in this research did not chose a complete treatment because of concerns in energy balance in HAZ boundary elements and the lack of information on the latent heat of bainite and martensite formation.

The heat transfer analysis was conducted with a two-dimensional finite element model. This was the best choice under the current circumstances. It is true that the heat transfer in clads is three dimensional. A three-dimensional finite element analysis of

such a full size multipass cladding problem, however, requires tremendous amount of computer hours. To make a three-dimensional analysis tractable at a reasonable cost, much coarser mesh sizes have to be used and the heat source model has to be simplified drastically. While development of faster and enhanced performance computers is ever desirable, the finite element analysis for now has to be limited in size and yet, most of the weld features have to be predicted. An accurate three-dimensional analysis and predictions of weld features in a multipass welding is a real task. A two dimensional model, on the other hand, may have much finer mesh and it has the capability of incorporating more details of the heat transfer into the finite element analysis. Physically this is a reasonable approximation because most of the heat flows perpendicular to the cladding direction when isotherms are sufficiently elliptical. The accuracy of such a two-dimensional analysis increases as the cladding speed increases, as the thermal diffusivity decreases.

The finite element analysis in this research is based on a purely heat conduction analysis. Weld pool convection effects have been simulated by using effective values of thermal conductivity. A more accurate representation of the phenomenon would be a combined model of convective and fluid flow in weld pool region and conduction outside weld pool in the solid material. Alternatively, parameters controlling heat flow such as thermal conductivity and heat transfer coefficient can be determined based on weld pool convection model and then used in the heat conduction analysis. The newly added feature for fluid mechanics analysis in the ANSYS revision 5.1, called FLOTRAN, gives the possibility of performing such an analysis. However, since the objective of this research is to analyze the microstructure development in the heat affected zone, it is only considered critical for the analysis to predict accurate thermal history in the heat affected zone. The author found the results in the research rather satisfactory.

It is important that the finite element heat transfer analysis accommodate and simulate the real physics of welding process. For example, as done in this research, the analysis must be able to accommodate the dynamically changing finite element mesh due the addition of filler metal and subsequent cladding passes. Initial and boundary conditions must be appropriately adaptable and accurately incorporated as the process

demands.

7.2 Thermodynamics Model for Computing Multicomponent Fe-C-M System Equilibria

The thermodynamics model presented in this research for computing multicomponent Fe-C-M system equilibria is an extension of the original work by Kirkaldy and his coworkers.[204-206] This model was oriented towards low alloy steels with addition of Mn, Si, Ni, Cr, Mo, Cu, W, V, and Nb. More alloying elements can be incorporated if thermodynamics data become available.

In this research, more consistent thermodynamics data regarding the self interactions of alloying elements and interactions between alloying elements and carbon in both austenite and ferrite are introduced so that some assumptions made by Kirkaldy and his coworkers[204-206] can be eliminated. These data were derived from the Uhrenius's compendium.[209] The computer algorithm of the thermodynamics model in this research uses iterative scheme and forced convergence Newton-Raphson method. The simplified equation for estimating partitioning of alloying elements in computing γ-α equilibrium, derived by Kirkaldy, Thomson, and Baganis,[205] was eliminated. Consequently, the accuracy of the thermodynamics model has been improved. The computed Ae_3 temperatures in this research are in better agreement with the experimentally measured ones than the results previously presented by Kirkaldy and his coworkers.[204-206]

Probably the most distinguishable contribution made in this research is to recognize that the α-γ-cementite three phase equilibrium in steels occurs over a temperature range. In this research, both the upper limit and the lower limit of this region in steels were computed. The upper limit was defined by the composition point of a steel located on the tie line for α-γ equilibrium of the tie-triangle designated for the α-γ-cementite three phase equilibria. This temperature was defined as A_1 temperature of steel. Its significance stands for the temperature at which pearlite starts forming during cooling. It is the real asymptote of pearlite reaction in a TTT diagram. This temperature was later used for the calculation of supercooling in predicting pearlite

reaction. The lower limit was defined by the composition point of a steel located on the tie line for α-cementite equilibrium of the tie-triangle designated for the α-γ-cementite three phase equilibria. This temperature was defined as As_1 temperature of steel. It represents the upper limit of tempering heat treatment. It is also the temperature at which austenite starts forming during heating. It correlates to the experimentally defined and measured A_S temperature, which represents austenite start. It was found that most of the experimentally measured A_S temperatures lie between the computed As_1 and A_1 temperatures.

A reasonable assumption made in this research was that the austenite composition at As_1 temperature represents eutectoid composition point of steels. The equilibrium amount of ferrite and pearlite at all temperatures below As_1 were than computed according to the composition of the eutectoid point and of the steel. This poses no problem for most low alloy steels, particularly the shaft steel involved in this research, because both ferrite and pearlite reactions will not go to completion under ordinary cooling conditions. Conceptually, this is a significant advance.

7.3 Austenite Grain Growth Prediction

Accurate prediction of the austenite grain growth in the cladding heat affected zone, or in any weld heat affected zone, has never been an easy task. The empirical kinetics model for grain growth may be used to simulate the grain growth in weld heat affected zone. However, parameters in such models were normally measured under isothermal conditions and they are different from steels to steels. A rational explanation to this is that these parameters are dependent on steel chemistry, particularly some minor elements, and the melting method. When they are applied to the prediction of austenite grain growth in weld heat affected zone, they often overpredict the grain growth by large factors. This may have been caused by the failure of accounting for the effects of thermal gradients, pinning effects from the partially melted zone, and some other possible pinning effects. The observation made by Ikawa *et al.*[163] was very interesting, which says, 95% austenite grain growth in weld heat affected zone occurs during the heating.

Virtually only a negligible part of the grain growth takes place during cooling. In a computational model for austenite grain growth, a commonly used method is to integrate the kinetics equation over the time when temperatures are above the Ae_3 temperature or T_{DISS} temperature for carbides and nitrides to dissolved in the austenite matrix. In the weld heat affected zone, the area under the cooling curve is much larger than that under the heating curve. The author finds this hard to rationalize with the expectation of essentially all grain growth taking place in the heating cycle.

It was concluded by the author that computational modeling of austenite grain growth in weld heat affected zone is so far too difficult to be accomplished with a simple kinetics equation. In this research, the author has adopted a semi-empirical approach to model the growth of prior austenite grains. Austenite grain growth was assumed to remain at its as-recrystallized size, approximately 5 microns for modern steels, until T_{DISS} temperature is reached. Austenite grains start growing T_{DISS} up to the peak temperature during heating. Austenite grain growth during cooling is ignored. Computation of austenite grains is terminated whenever its size reaches its maximum size, 105 microns. The kinetics parameters for austenite grain growth by Ikawa *et al.*[163] were used to simulate the growth of austenite grains. The author would leave this part of modeling work open for future improvements.

7.4 Prediction of Austenite Decomposition

The reaction kinetics model for austenite decomposition developed in this research was based on modifying the original Kirkaldy-Venugopalan model.[159] Besides some minor changes, a significant difference between the model presented in this thesis and the Kirkaldy-Venugopalan model was the data base for the coefficient calibration. The original Kirkaldy-Venugopalan model[159] was calibrated with TTT diagrams in U.S. Steel Atlas.[156] In this research, the reaction kinetics model was calibrated with empirical formulas developed by DeAndrés and Carsí[119] which were developed based on regression analysis on CCT diagrams. Therefore, the model presented in this research can be considered calibrated with CCT diagrams.

The thesis model and Kirkaldy-Venugopalan model have different formats in accounting for the effects of alloying elements. The model presented in this thesis suggests that all alloying elements contributed to the hardenability and their effects on steel hardenability are multiplicative. The original Kirkaldy-Venugopalan model, however, virtually accounts for ferrite stabilizers only and the model suggests that their effects on steel hardenability are additive. Theoretically, the reaction kinetics model developed in this research has corrected a number of inaccurate assumptions made in the Kirkaldy-Venugopalan model. Prediction of Jominy hardness curves with these two models clearly demonstrated that the modifications are effective and have significantly improved the accuracy of predictions for hardenable steels.

The model developed in this research is comparable with the DeAndrés-Carsí model[119] in the prediction of Jominy hardness of steels. However, it overcomes the limitations of the DeAndrés-Carsí in predicting phase transformations under nonlinear cooling. Moreover, it provides the whole picture of phase transformations. Since the DeAndrés-Carsí model was a generic empirical model, the model in this research can also be regarded as a generically applicable model for low alloy steels. Application range of the original DeAndrés-Carsí was believed to be the same as the Creusot-Loire model[116-117] in weight percent: $0.1 < C < 0.5$, $Si < 1.0$, $Mn < 2.0$, $Ni < 4.0$, $Cr < 3.0$, $Mo < 1.0$, $V < 0.2$, $Cu < 0.5$, $Mn + Ni + Mo < 5.0$, and $0.01 < Al < 0.05$. The same application range may be applied to the model developed in this research.

The current model only accounts for alloying elements C, Mn, Si, Ni, Cr, and Mo. Further modifications will be considered to account for alloying elements Cu, W, V, and Nb. Since concentrations of these alloying elements in low alloy steels are normally minor, they are not expected to have substantial effects on the reaction kinetics of austenite decomposition.

At current state, the computational modeling in this research only predicts the as-welded microstructure and hardness in the heat affected zone. It is felt not adequate to model the tempering of martensite and bainite in a rigorous fashion. The author would like anticipate future development in the theoretical modeling of tempering process of martensite and bainite.

7.5 Suggestions for Future Work

Current microstructure and hardness predictions have been performed using FORTAN programs coded by the author. The results of finite element heat transfer analysis were output to local files for the predictions. The new release of ANSYS revision 5.1 has the capability of incorporating user developed subroutines for special analysis. Thus it is possible to code the thermodynamics model, austenite grain growth model, and reaction kinetics model for austenite decomposition into subroutines and link them with ANSYS program. Thus microstructure and hardness predictions may be performed after the heat transfer analysis by simply calling these subroutines. Limited by the time frame, the author regrets that this can only be done in the future.

Although the reliability of the reaction kinetics model presented in this thesis has been tested with Jominy hardness measurements on limited number of steels, and it is believed to be generically applicable to low alloy steels, it is the author's wish that the reliability of this model be tested more extensively. This may be considered in the future work.

Table 3.1 Temperature dependent values of $\Delta^0G_0^{\alpha\rightarrow\gamma}$ (cal/mol) for iron[217]

T (°K)	$\Delta^0G_0^{\alpha\rightarrow\gamma}$	T (°K)	$\Delta^0G_0^{\alpha\rightarrow\gamma}$	T (°K)	$\Delta^0G_0^{\alpha\rightarrow\gamma}$
750	412.50	960	119.9	1170	2.52
760	396.10	970	109.3	1180	0.74
770	379.90	980	99.3	1184	0.00
780	364.00	990	89.8	1190	-0.89
790	348.40	1000	80.80	1200	-2.40
800	333.00	1010	72.18	1210	-3.82
810	317.80	1020	64.16	1220	-5.15
820	302.80	1030	56.75	1230	-6.39
830	288.10	1040	50.15	1240	-7.55
840	273.50	1050	44.31	1250	-8.63
850	259.10	1060	39.11	1260	-9.63
860	244.70	1070	34.21	1270	-10.55
870	230.80	1080	29.92	1280	-11.40
880	217.30	1090	26.07	1290	-12.17
890	204.10	1100	22.22	1300	-12.87
900	191.10	1110	18.37	1350	-15.29
910	178.30	1120	14.92	1400	-16.10
920	166.00	1130	11.84	1450	-15.64
930	154.10	1140	9.10	1500	-13.95
940	142.40	1150	6.66	1600	-7.20
950	142.40	1160	4.48	1668	0.00

Table 3.2 Molar free energy change for solid state phase transformations

Element	$\Delta^0G_i^{\alpha\rightarrow\gamma}$ (cal/mol)	$\Delta^0G_i^{\gamma\rightarrow\delta}$ (cal/mol)
C	-15323+7.686T	15940-5.7T
Mn	$-26650+42.69T-0.017T^2$	430-0.305T
Si	-5954+38.799T-4.7244TlnT	5954-38.799T+4.7244TlnT
Ni	-4545+3.233T	1330-0.26T
Cr	-367-4.646T+0.6568TlnT	367+4.7T-0.6568TlnT
Mo	565+0.15T	-565-0.15T
Cu	$-25500+41.183T-0.017T^2$	-1450-0.8T
W	1290-0.30T	-2500-0.15T
V	$8357+13.8T-0.0051T^2$	$-8357-13.8T+0.0051T^2$
Nb	5162-2.875T	-5162+2.875T

Table 3.3 Molar free energy change for melting

Element	$\Delta^0G_i^{\gamma\rightarrow L}$(cal/mol)	$\Delta^0G_i^{\delta\rightarrow L}$(cal/mol)
C	-5360+0.6T	-21300+6.3T
Mn	3070-2.03T	3500-2.308T
Si	-2246-34.899T+4.7244TlnT	-8200+3.9T
Ni	-790-0.64T	-2120-0.38T
Cr	-4233+6.89T-0.6568TlnT	-4600+2.19T
Mo	-7165+2.14T	-6600+2.29T
Cu	-2650+0.8T	-1200
W	-8790+3.95T	-7500+3.65T
V	$3257-11.5T+0.0051T^2$	-5100+2.3T
Nb	-10661+5.175T	-5500+2.3T

Table 3.4 Standard magnetic entropy of pure iron $({}^0S_{Fe}{}^{\alpha})_{mag.}$ from Weiss and Tauer[213]

T(°K)	$({}^0S_{Fe}{}^{\alpha})_{mag.}$	T(°K)	$({}^0S_{Fe}{}^{\alpha})_{mag.}$
400	0.05	1200	1.84
500	0.09	1300	1.94
600	0.16	1400	1.99
700	0.28	1500	2.02
800	0.45	1600	2.04
900	0.72	1700	2.05
1000	1.16	1800	2.06
1100	1.67		

Table 3.5 Self interaction coefficients of alloying elements

Element	$\epsilon_{ii}^{\alpha}=\epsilon_{ii}^{\delta}$	ϵ_{ii}^{γ}	ϵ_{ii}^{L}
C	1.3	4.786+5066/T	0.389+7810/T
Mn	$3.082+4679/T+1519.8({}^{0}S_{Fe})_{mag.}/T$	2.406-175.6/T	31.4/T
Si	−16.35−44829/T	26048/T	24751/T
Ni	$2.013+4595/T+385.5({}^{0}S_{Fe})_{mag.}/T$	−2839/T	312.6/T
Cr	2.819-6039/T	7.655−3154/T−0.661lnT	9.8/T
Mo	$-0.219-4472/T+402.6({}^{0}S_{Fe})_{mag.}/T$	-2330/T	-1343/T
Cu	$0.634-11270/T+1006.5({}^{0}S_{Fe})_{mag.}/T$	−1.376−5766/T	11011/T
W	−9058/T	0.453-7851/T	-4289/T
V	1.564+4811/T	11.987+20473/T	6056/T

Table 3.6 Interaction coefficients between alloying elements and carbon[209]

Element	$\epsilon_{1i}^{\alpha}=\epsilon_{1i}^{\delta}$	ϵ_{1i}^{γ}	ϵ_{1i}^{L}
C	1.3	4.786+5066/T	0.389+7810/T
Mn	0.464−4989/T	−4811/T	-5060/T
Si	0.464+17049/T	14794/T	-0.428+18740/T
Ni	0.464+6377/T	5533/T	5340/T
Cr	2.022+5316/T	14.193−30209/T	-9500/T
Mo	0.464−9869/T	−10714/T	−7490/T
Cu	7.080−4689/T	6.615−5533/T	7586/T
W	0.464−2603/T	−10342/T	-12230/T
V	0.464-20806/T	−21650/T	-30100/T
Nb	-28770/T	-28770/T	-46615/T

Table 3.7 Standard free energy change between cementite and γ phase[209]

Element	${}^0G_{MC_{1/3}}^{cem}$ - ${}^0G_M^{\gamma}$- 1/3${}^0G_C^{\gamma}$ (cal/mol)
Fe	-493.1-14.370T+1.788TlnT
Mn	-6910.9+4.594T
Ni	-201.6+0.966T
Cr	-3879.9-1.953T
Mo	1923.2+2.597T
W	11428.5+6.845T
V	-6727.1-1.897T

Table 3.8 Interaction coefficient between iron and alloying elements in cementite[209]

Element	A_{0i} (cal/mol)
Mn	$1995.7-3.633T-956Y_{Mn}^{cem}$
Ni	0
Cr	427.8
Mo	0
W	0
V	-6742.4

Table 3.9 Reported Austenite Grain Growth Parameters

	n	Q (kcal/mol)	K_0 (mm^n/sec)	Steels	Ref.
Cole *et al.*	2	30	5×10^{-2}	plain eutectoid steel	222
Hannerz *et al.*	6	NA	NA	cast and forged steels	228
Manyior *et al.*	2	110	NA	low alloy steels	116
Ikwa *et al.*	4	137.7	2.969×10^{15}	HT80	163
Alberry *et al.*	2.73 1.28	110 110	5.4×10^{12} 5.4×10^{12}	Cr-Mo-V steels weld HAZ	167
Ashby *et al.*	2	$16RT_M$	NA	C-Mn steels	170
Saito *et al.*	10	95.6 218.5	3.87×10^{22} for $T\geq1100$ °C 1.31×10^{22} for $T<1100$ °C	hot rolled steels	155
DeAndrés and Carsí	5.05	106.7 134.4	2.72×10^{27} 9.80×10^{-14}	without inhibitors with inhibitors	119
Gergely *et al.*	2.44	75.8	6.087×10^{7}	low alloy steels	230

Table 4.1 Electroslag cladding parameters

Current	650 A
Voltage	27 V
Cladding Speed	29.6 cm/sec
Strip Electrode Feed Rate	296 cm/sec

Table 5.1 Undercooling ΔT due to C and Ni in Andrew's Ae_3 formula[254]

C+Ni/10 (wt%)	ΔT (°C)	C+Ni/10 (wt%)	ΔT (°C)	C+Ni/10 (wt%)	ΔT (°C)
0.05	24	0.25	93	0.45	137
0.10	48	0.30	106	0.50	145
0.15	64	0.35	117	0.60	160
0.20	80	0.40	128	0.70	173

Table 5.2 Statistics analysis of computed Ae_3 temperatures for the 19 steels measured by Grange[259]

Model	Mean Difference	R.M.S Difference	Standard Deviation
Thesis Model	-1.823	5.523	5.213
Kirkaldy and Baganis	-8.573	10.432	5.944
Grange's Ae_3 Formula	-1.004	3.748	3.611
Andrews' Ae_3 formula	1.184	13.871	13.820
Andrews' Ac_3 formula	-10.614	13.572	8.459

Table 5.3 Statistics analysis of computed A_3 temperatures for 72 steels in U.S. Steel Atlas[156]

Model	Mean Difference	R.M.S Difference	Standard Deviation
Thesis Model for Ae_3	-6.184	11.925	10.196
Kirkaldy and Baganis	-14.847	19.036	11.914
Grange's Ae_3 Formula	-9.842	14.634	10.830
Andrews' Ae_3 formula	2.214	30.558	30.478
Andrews' Ac_3 formula	-15.288	21.309	14.844

Table 5.4 Computed partition coefficients ($A_i=X_i^{\alpha}/X_i^{\gamma}$) of alloying elements as functions of carbon content in austenite at 1000 °K

Element	C=0.02	C=0.04	C=0.06
Mn	0.59	0.57	0.54
Si	1.27	1.45	1.65
Ni	0.54	0.57	0.60
Cr	0.68	0.59	0.51
Mo	1.30	1.18	1.08
Cu	0.52	0.53	0.53
W	1.50	1.37	1.25
V	0.98	0.81	1.47

Table 5.5 Statistics analysis of computed A_1 temperatures for the 19 steels measured by Grange[259]

Model	Mean Difference	R.M.S. Difference	Standard Deviation
Thesis Model for Ae_1	7.669	-11.280	8.272
Thesis Model for As_1	-7.317	11.315	8.630
Grange's A_S Formula	2.096	3.653	2.992
Andrews' Ac_1 formula	2.706	4.625	3.750

Table 5.6 Standard deviation of computed versus measured A_1 temperatures for 66 steels in U.S. Steel Atlas[156]

Model	Mean Difference	R.M.S. Difference	Standard Deviation
Thesis Model for Ae_1	9.7	13.4	9.2
Thesis Model for As_1	-4.7	11.2	10.2
Grange's A_S Formula	3.6	8.9	8.1
Andrews' Ac_1 formula	4.4	9.1	8.0

Table 5.7 Composition of steels (wt%) for Jominy end-quench tests

Steels	C	Mn	Si	Ni	Cr	Mo	Cu	V
A36	0.20	1.01	0.1	0.02	0.02	-	0.05	0.002
A588	0.24	0.98	0.1	0.02	0.02	-	0.04	0.001
4140	0.38	0.81	0.28	0.11	0.98	0.22	0.11	0.003
Class 1	0.24	0.31	0.20	3.04	0.39	0.44	0.09	0.052

Table 5.8 Austenizing temperature and holding time for samples

Steel	Austenizing Temperature (°C)	Holding Time (min)
A36	838	66
A588	868	30
4140	845	30
Class 1	838	42

Table 5.9 Important temperatures for austenite decomposition in steels

Steel	Ae_3(°C)	Ap_3(°C)	Ae_1(°C)	Ap_1(°C)	As_1(°C)	Tps(°C)
A36	827	826	719	719	710	719
A588	815	814	720	720	711	720
4140	775	725	731	708	713	725
Class 1	762	728	703	677	686	680

Table 5.10 Equilibrium amount of ferrite and pearlite at As_1 temperatures

Steel	C_{Eut}(wt%)	C_F(wt%)	X_{FE}	X_{PE}
A36	0.760	0.013	0.750	0.250
A588	0.760	0.013	0.750	0.250
4140	0.767	0.012	0.507	0.493
Class 1	0.594	0.009	0.607	0.393

Table 5.11 Predicted incubation and completions times of ferrite reaction at nose temperature in steel 4140

Model	T_{NFs} (°C)	$\tau_{1\%F}$ (sec)	τ_{Ff}(sec)
Thesis Model	607	82.4	825
Kirkaldy-Venugopalan Model	587	4.8	28.0
Kawasaki Steel Model	635	26.8	1230

Table 5.12 Predicted incubation and completion times of bainite reaction at nose temperature in steel 4140

Model	T_{NBs} (°C)	τ_{Bs} (sec)	τ_{Bf}(sec)
Thesis Model	464	4.8	96.1
Kirkaldy-Venugopalan Model	462	5.6	242
Kawasaki Steel Model	512	2.8	527

Table 5.13 Critical cooling rates for 100% martensite formation and martensite hardness in steel 4140

Models	Cooling Rate (°C/sec)
Thesis Model	23.6
Kirkaldy-Venugopalan Model[159]	108
Kawasaki Steel Model[155]	156
Creusot-Loire Model[116-118]	22.9
DeAndrés-Carsí Model[119]	24.1
Terasaki Model[136]	30.4
Yurioka Model[142-145]	43.1

Table 5.14 Some typical values of I(X) and S(X)

	X=0.01	X=0.5	X=0.99	X=1.00
I(X)	0.588	2.127	3.666	4.254
S(X)	0.103	1.025	1.946	2.050

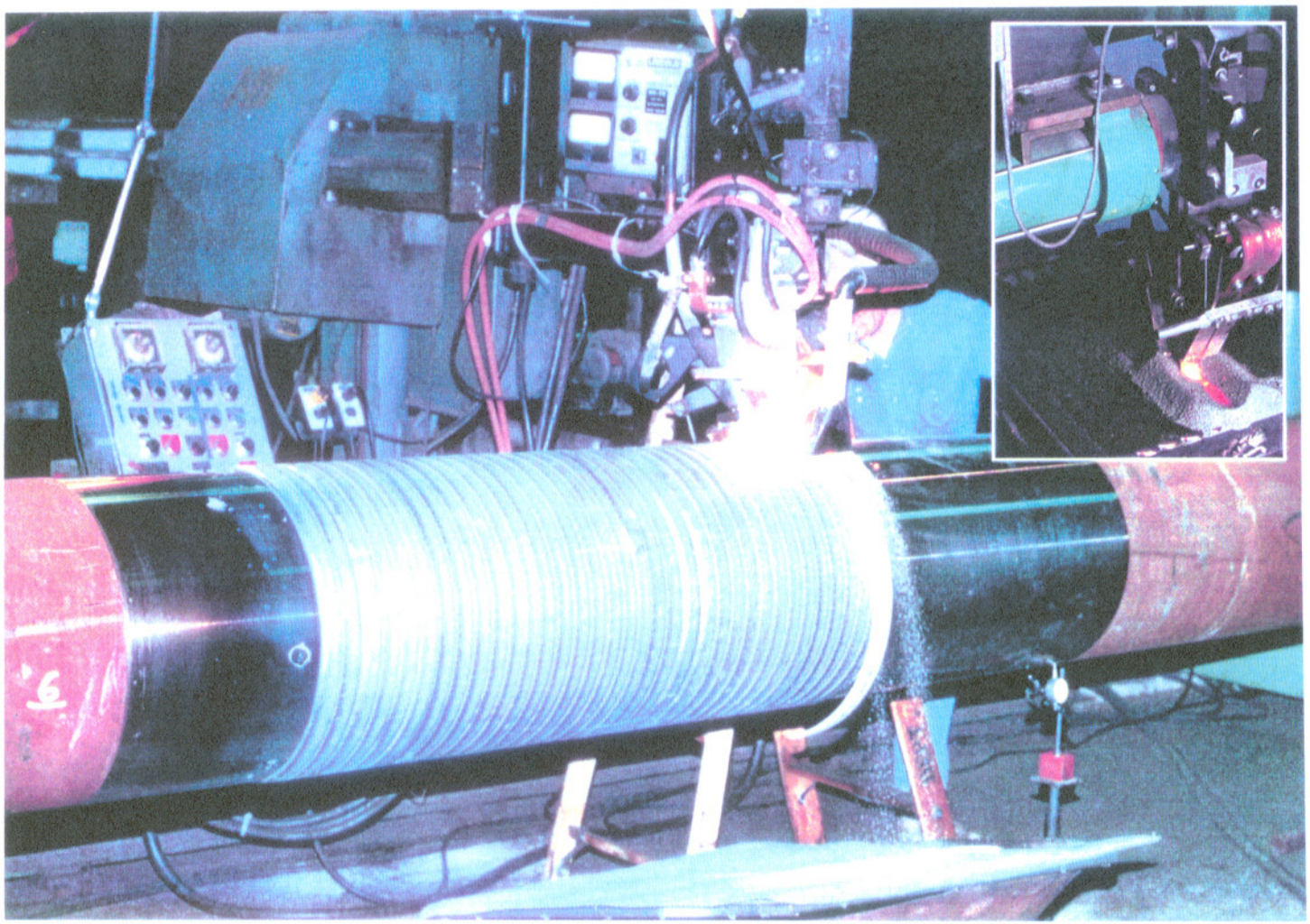

Figure 1.1 Electroslag cladding onto a propeller shaft and a flat workpiece (insert photo).

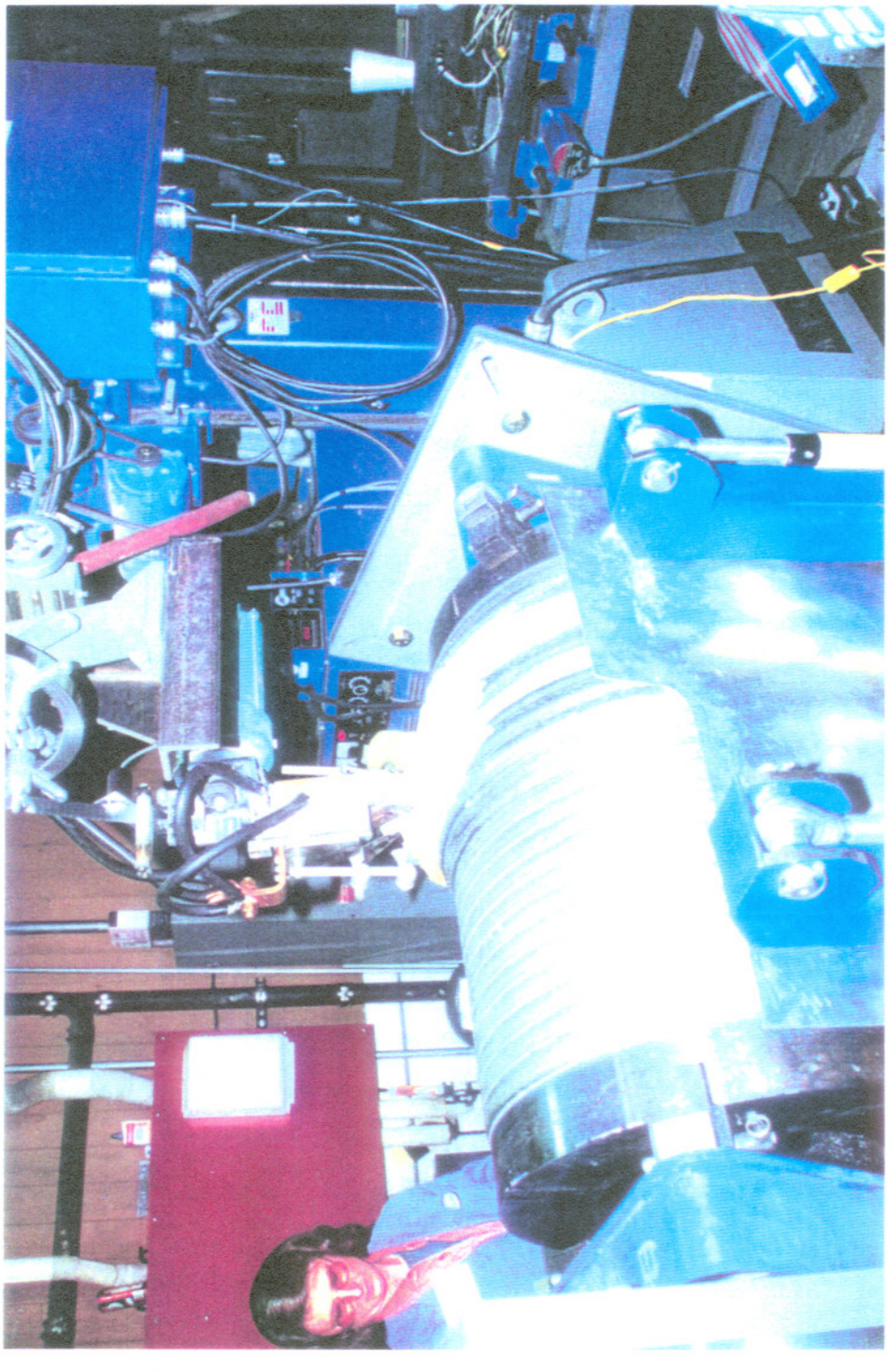

Figure 2.1 Experimental setup of electroslag cladding.

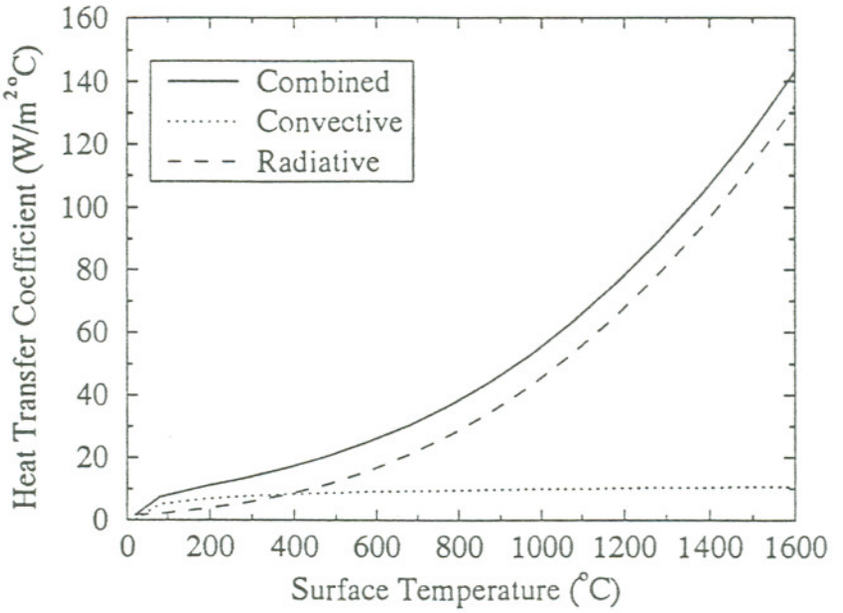

Figure 2.2 Heat transfer coefficients on the outside surface of shaft E290.

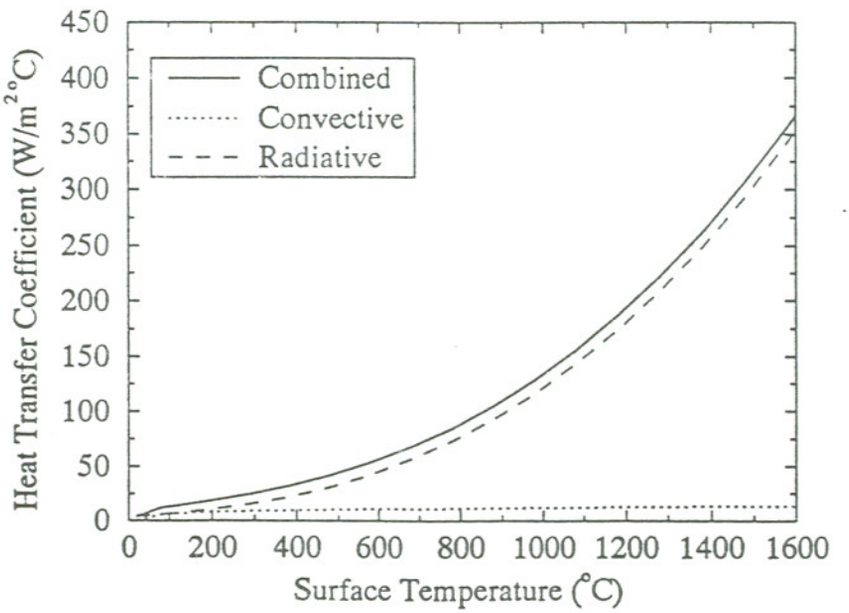

Figure 2.3 Heat transfer coefficients on the ends of shaft E290.

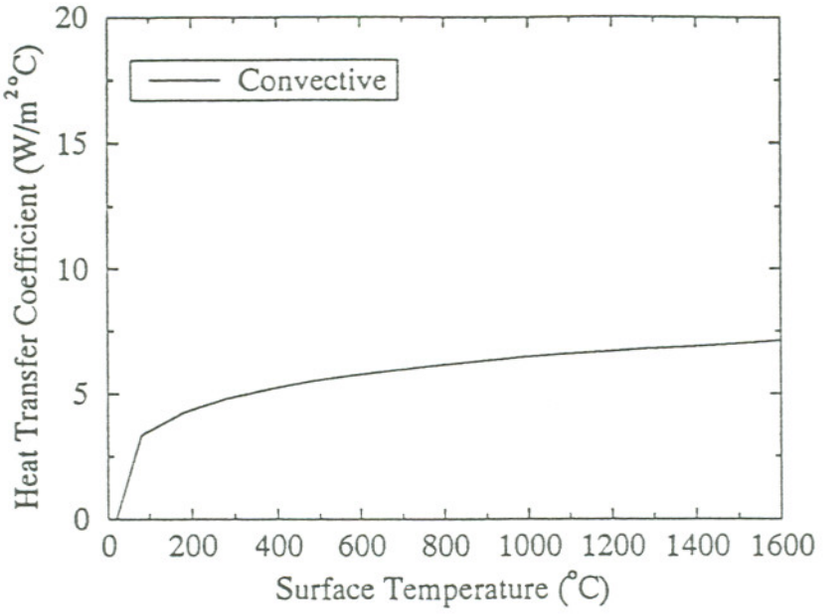

Figure 2.4 Heat transfer coefficient on the inside surface on shaft E290.

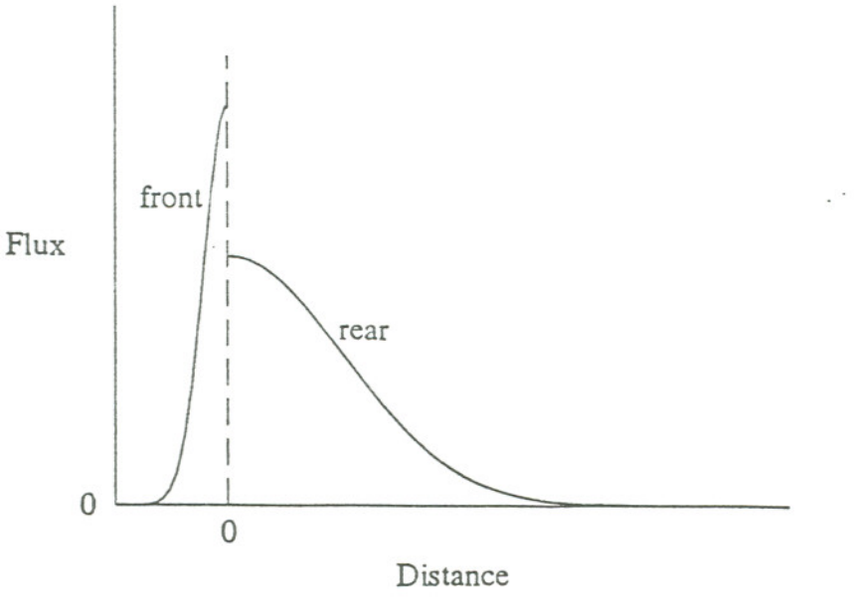

Figure 2.5 Heat flux profile of the electroslag cladding heat source model along the cladding direction.

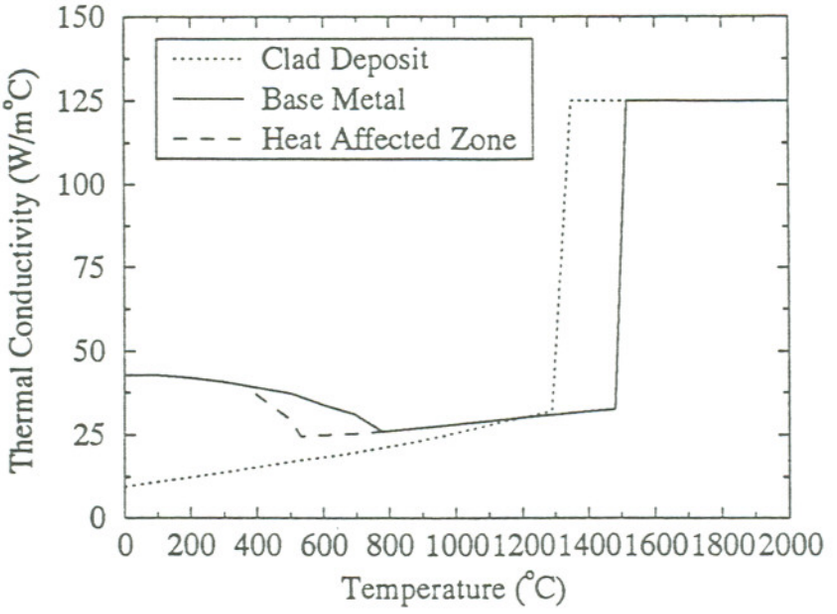

Figure 2.6 Thermal conductivity of materials.

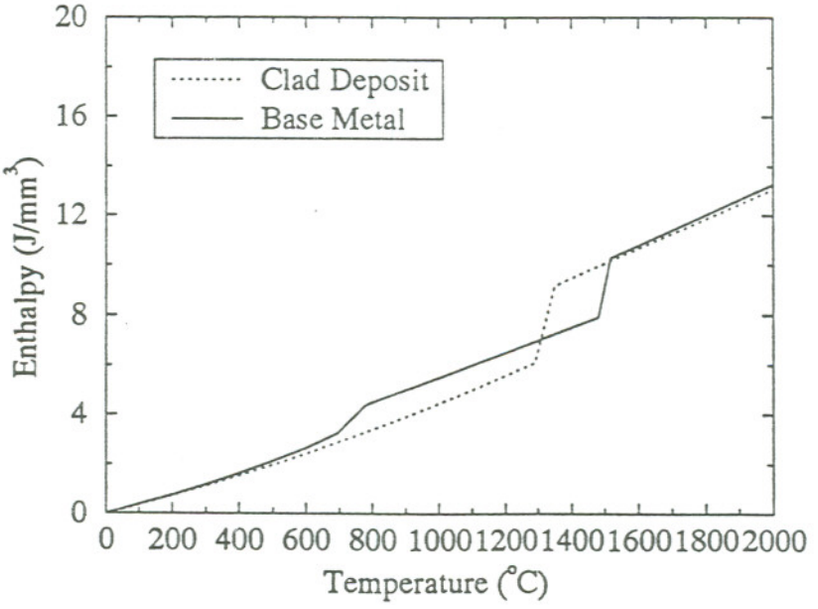

Figure 2.7 Enthalpy change of materials.

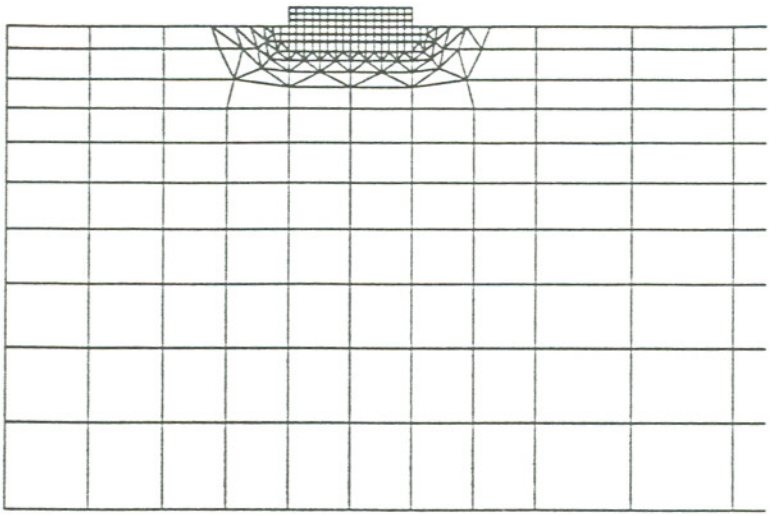

Figure 2.8 Finite element mesh of the clad and adjacent region for analysis the first clad pass.

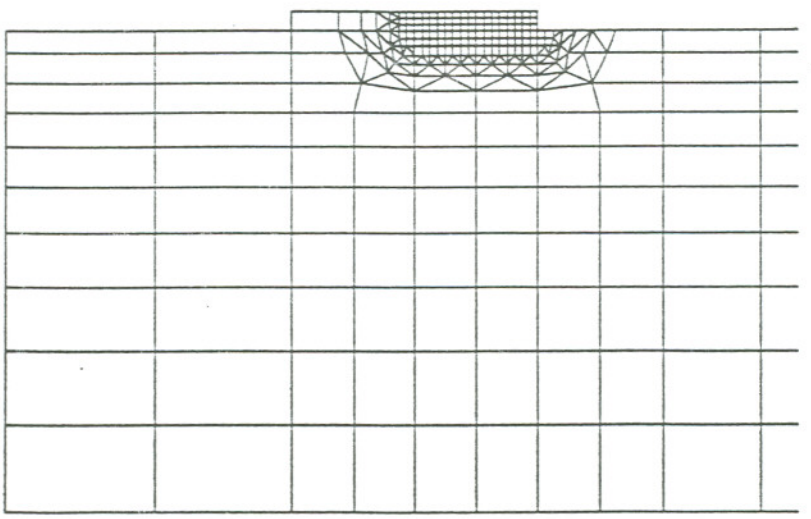

Figure 2.9 Finite element mesh of the clad and adjacent region for analyzing the second clad pass.

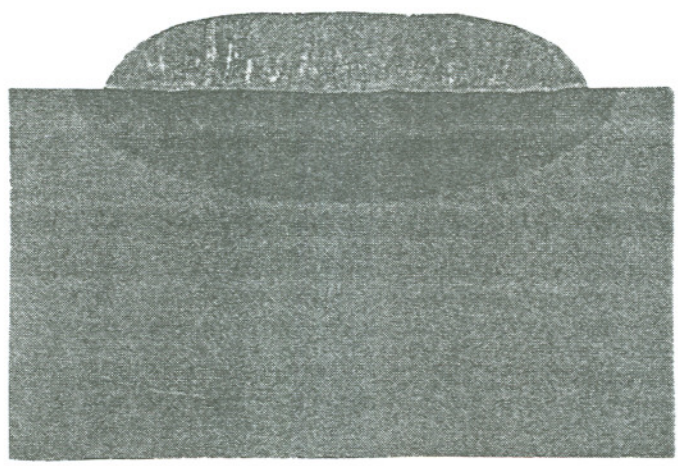

Figure 3.1 Photograph of a single pass clad and its adjacent heat affected zone. (courtesy of Y. P. Gao[273])

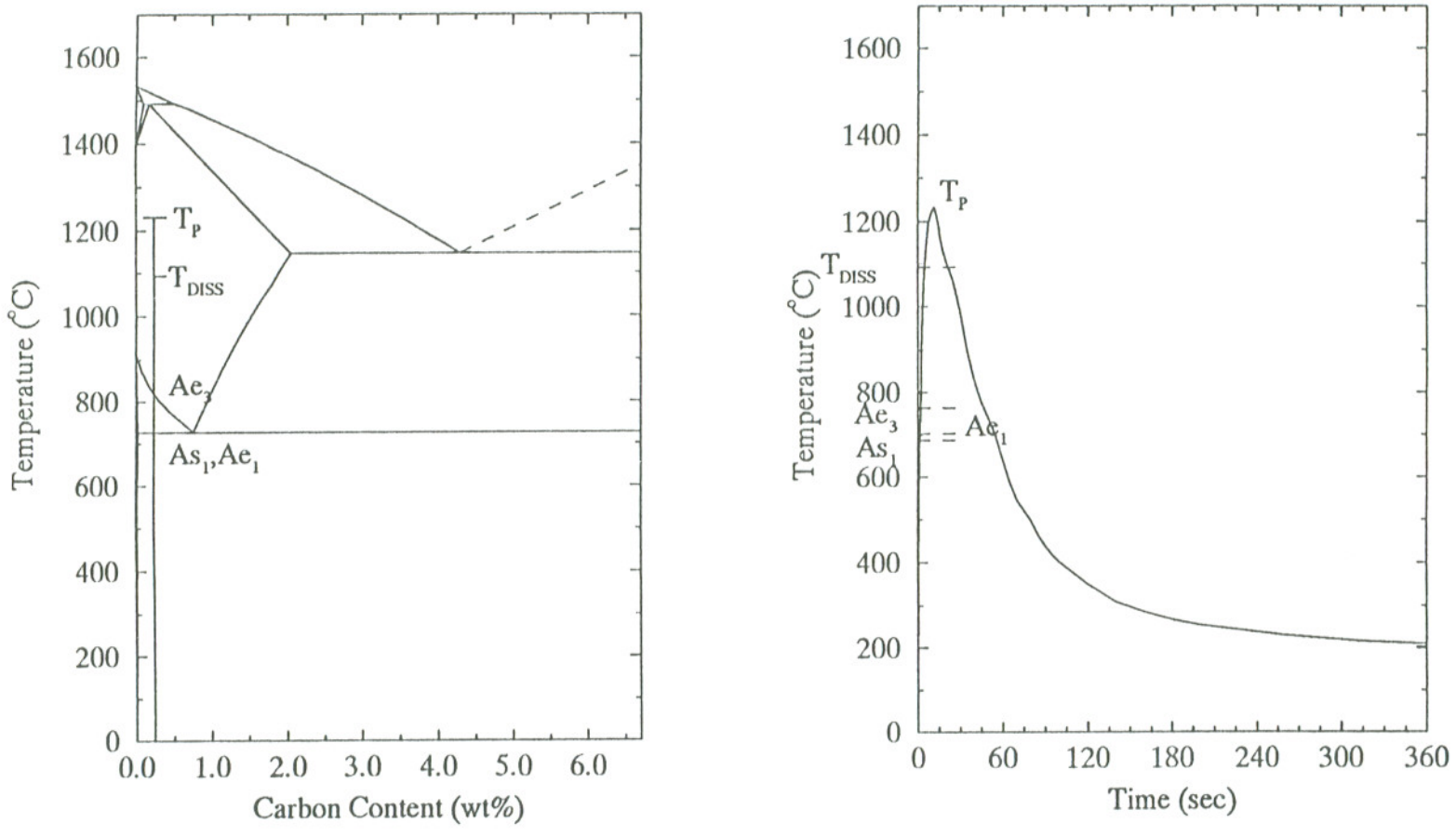

Figure 3.2 Illustration of microstructural changes in the heat affected zone

(a) Fe-Fe_3C phase diagram, and (b) typical thermal cycle in the heat affected zone.

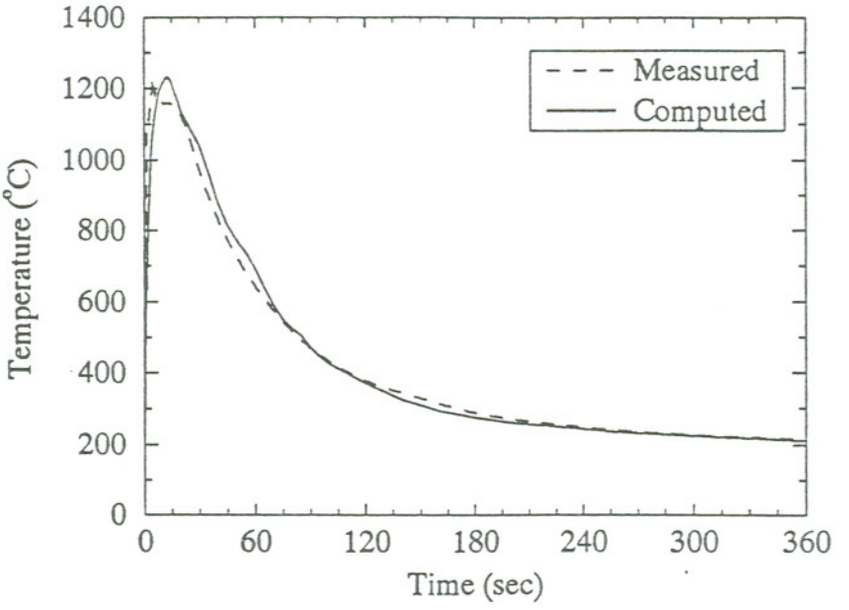

Figure 4.1 Typical comparison between the computed and measured thermal cycles in the cladding heat affected zone.

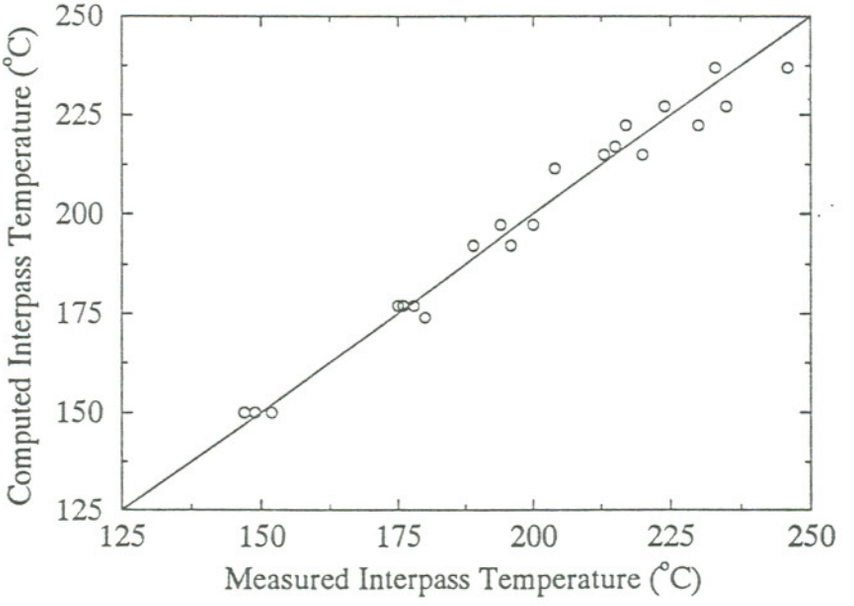

Figure 4.2 Comparison between computed and measured interpass temperatures during cladding on shaft E290.

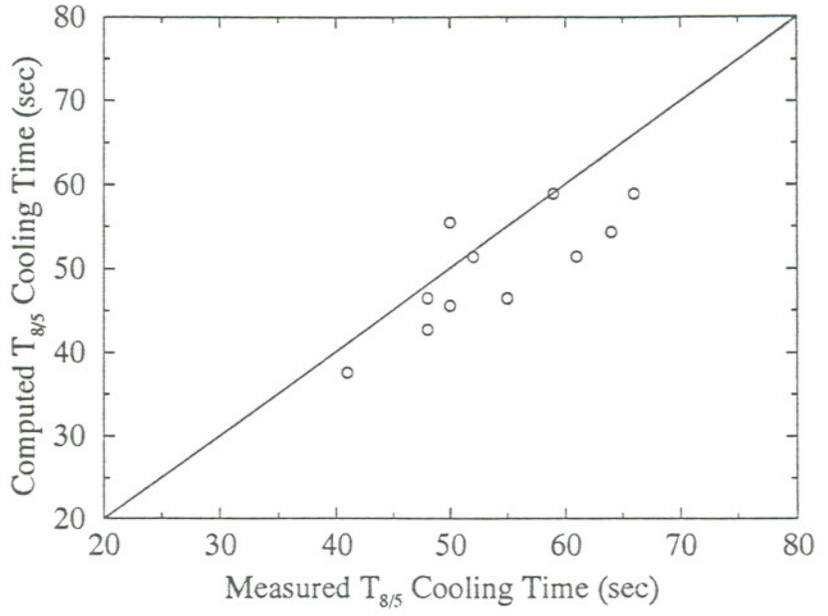

Figure 4.3 Comparison between computed and measured $t_{8/5}$ cooling times in the heat affected zone of shaft E290.

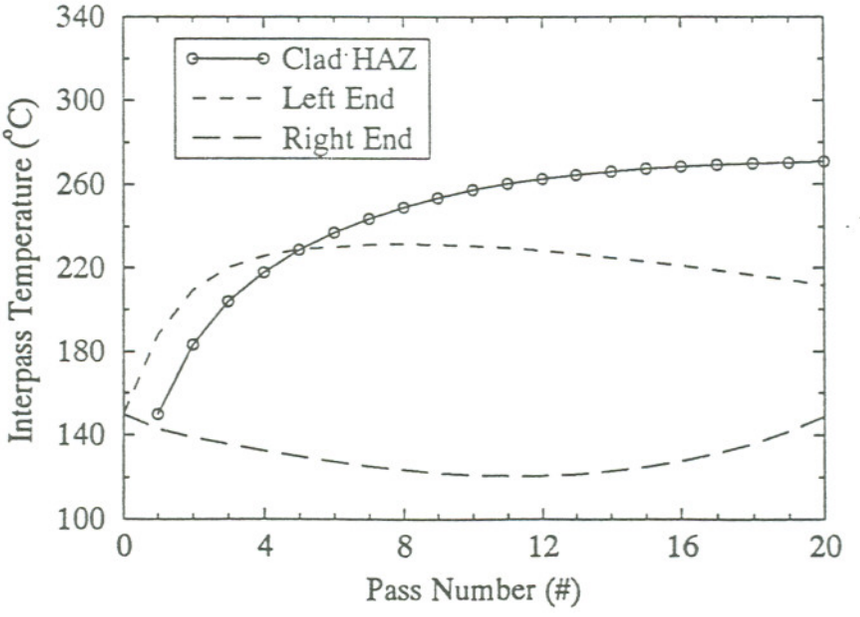

Figure 4.4 Predicted interpass temperatures for the cladding on shaft E290.

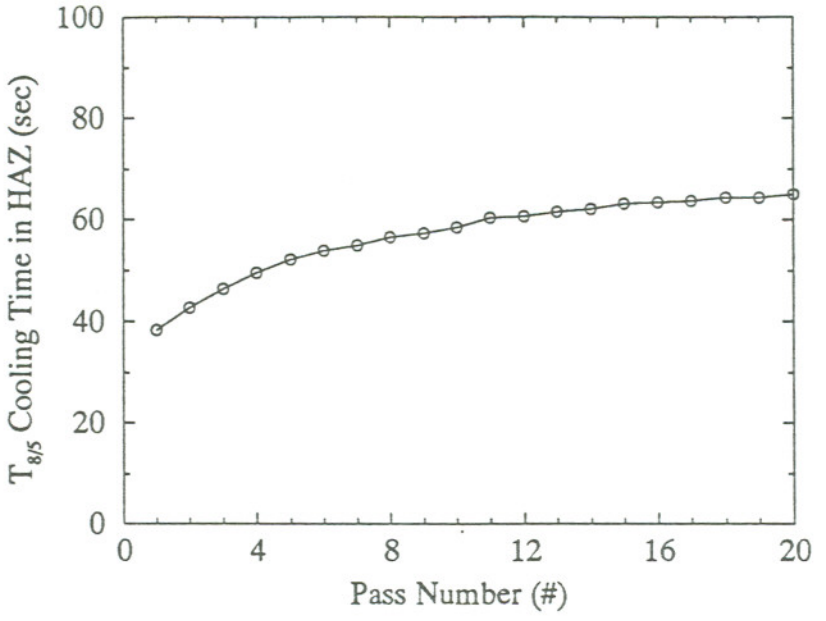

Figure 4.5 Predicted $t_{8/5}$ cooling time for the cladding on shaft 290.

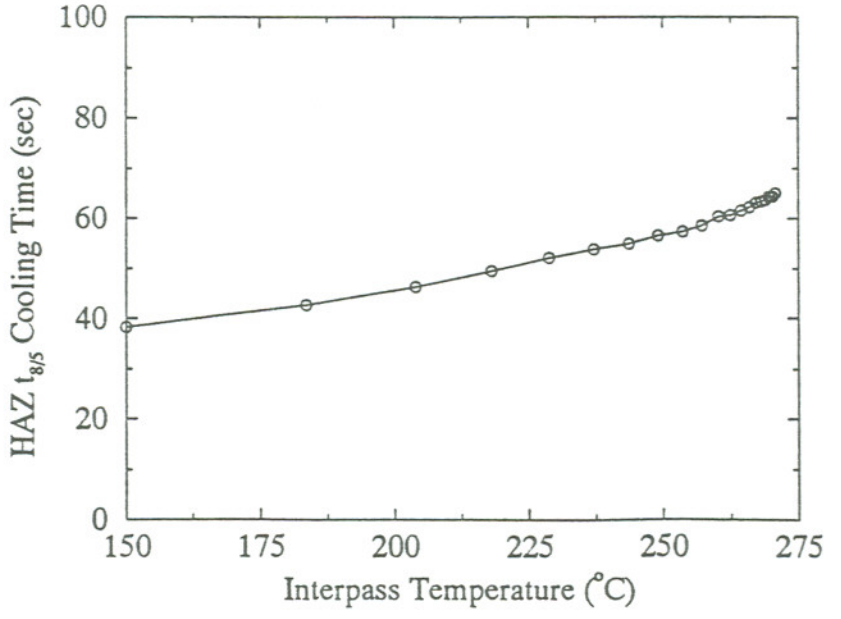

Figure 4.6 Predicted $t_{8/5}$ cooling time a function of interpass temperatures.

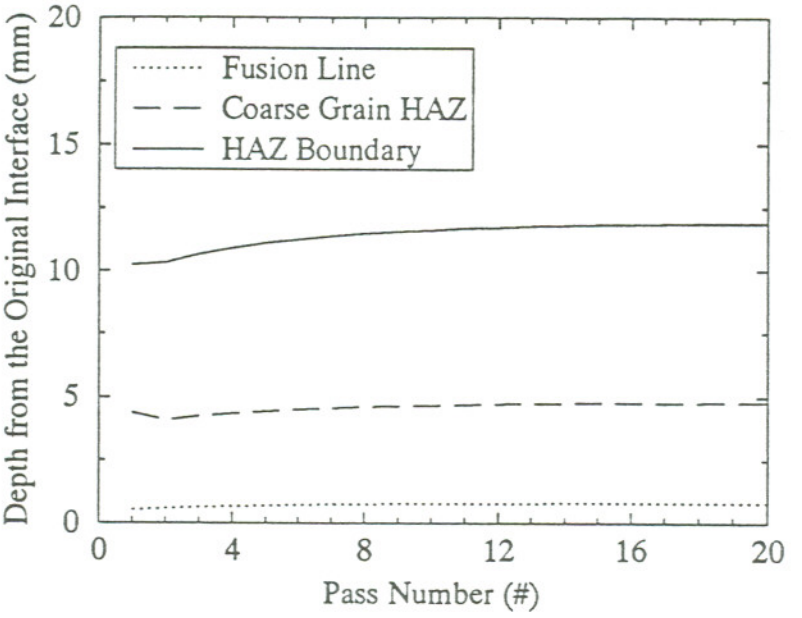

Figure 4.7 Predicted HAZ size for the cladding on shaft E290.

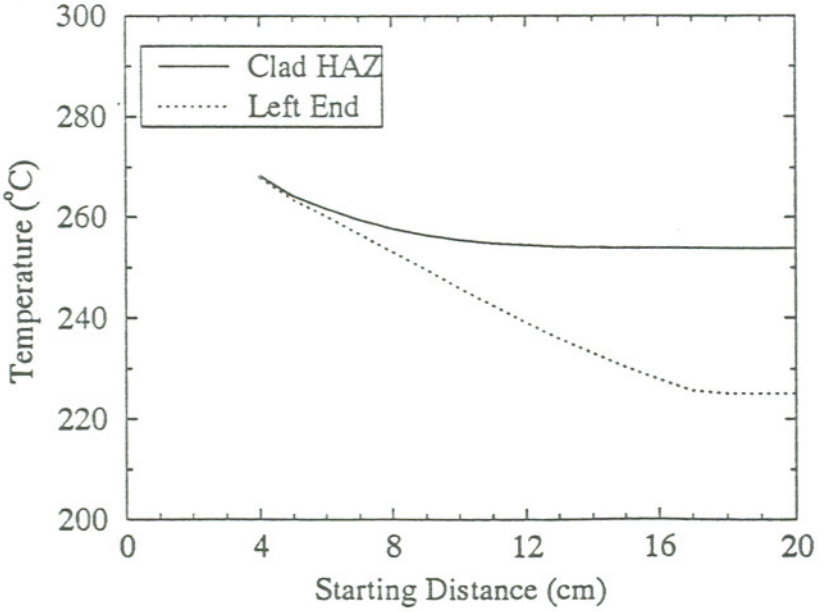

Figure 4.8 Temperature in the heat affected zone and at left end of a shaft versus starting distance of cladding.

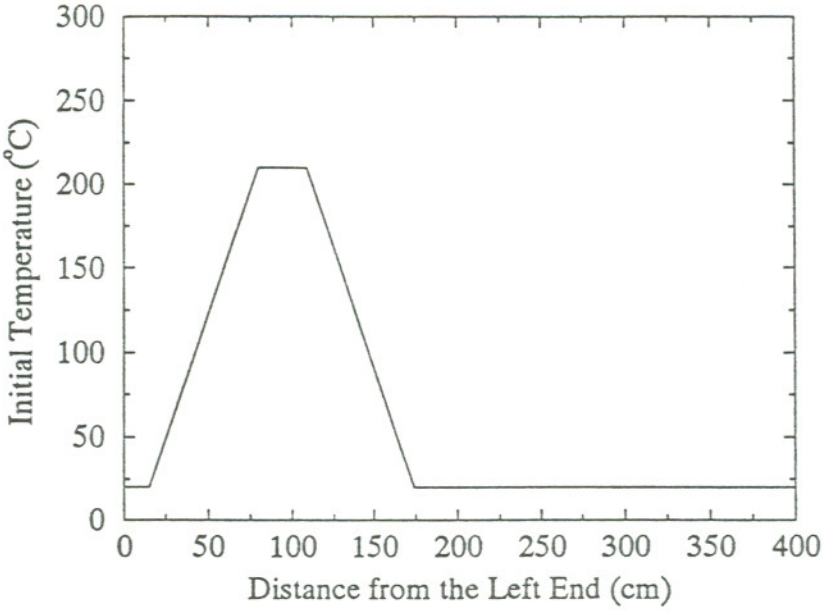

Figure 4.9 Assumed Optimal preheating temperature distribution for cladding onto a long shaft.

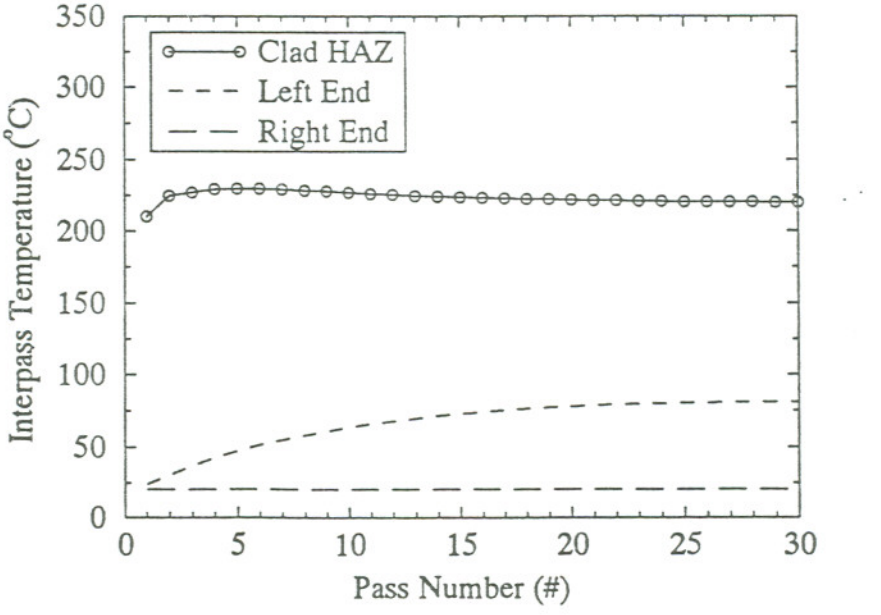

Figure 4.10 Predicted interpass temperatures before cladding each pass onto a long shaft.

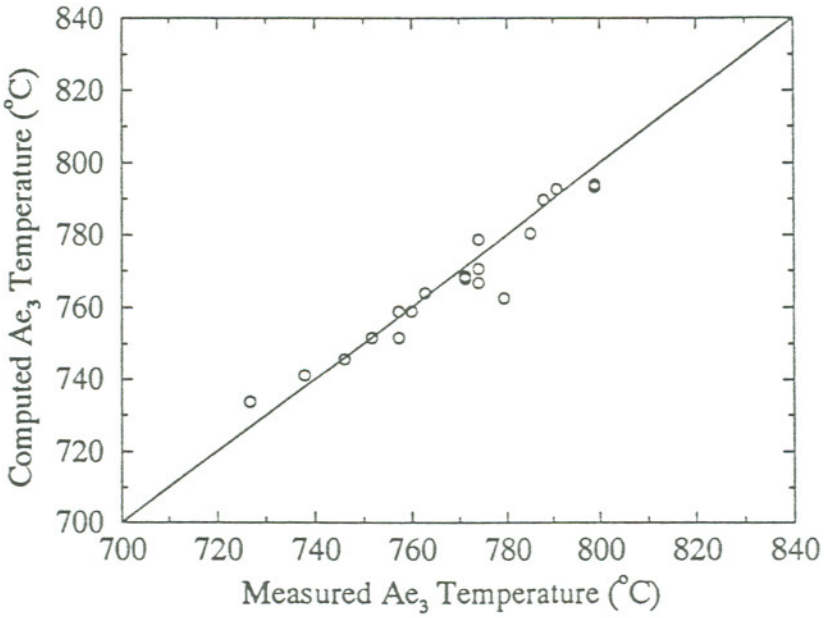

Figure 5.1 Predicted and experimental Ae_3 temperatures. Data from Grange.[259]

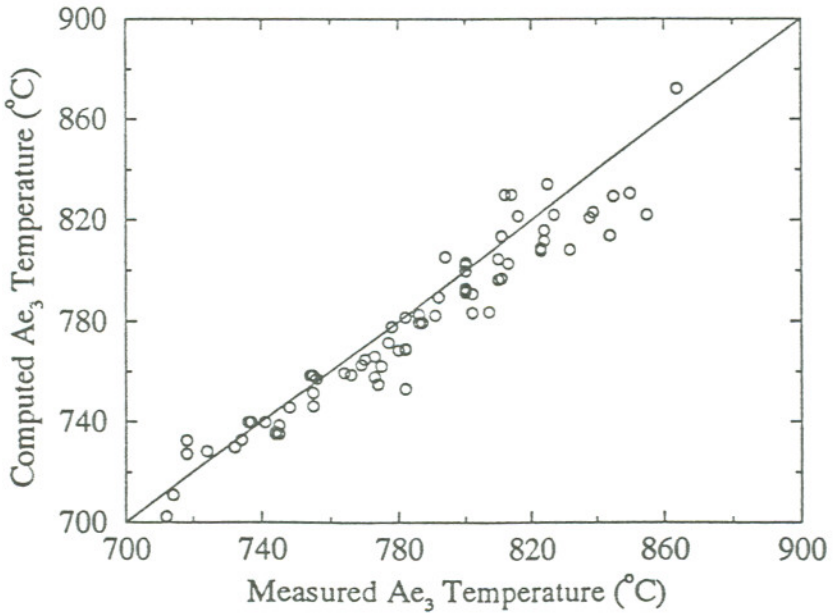

Figure 5.2 Predicted and experimental Ae_3 temperatures. data from U.S. Steel Atlas.[156]

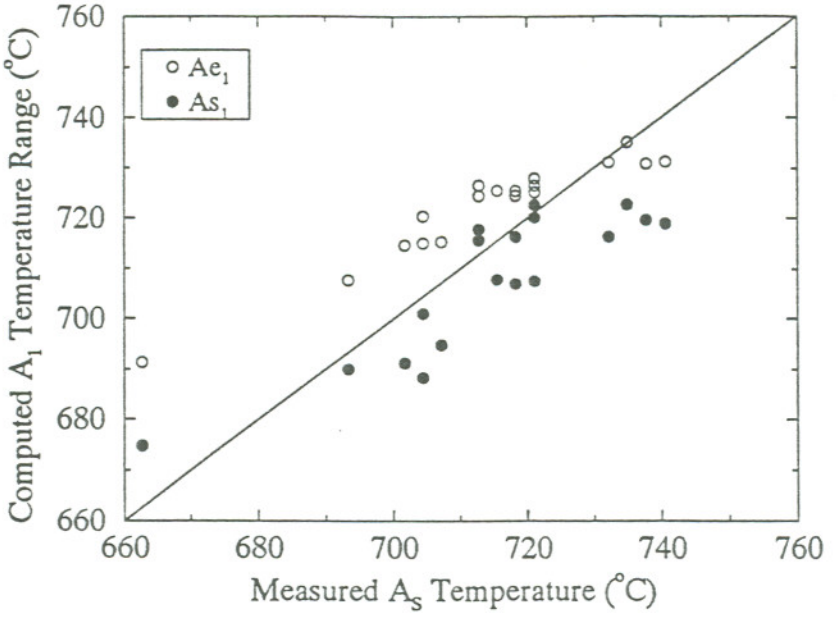

Figure 5.3 Predicted Ae_1, As_1 and experimental A_s temperatures. data from Grange.[254]

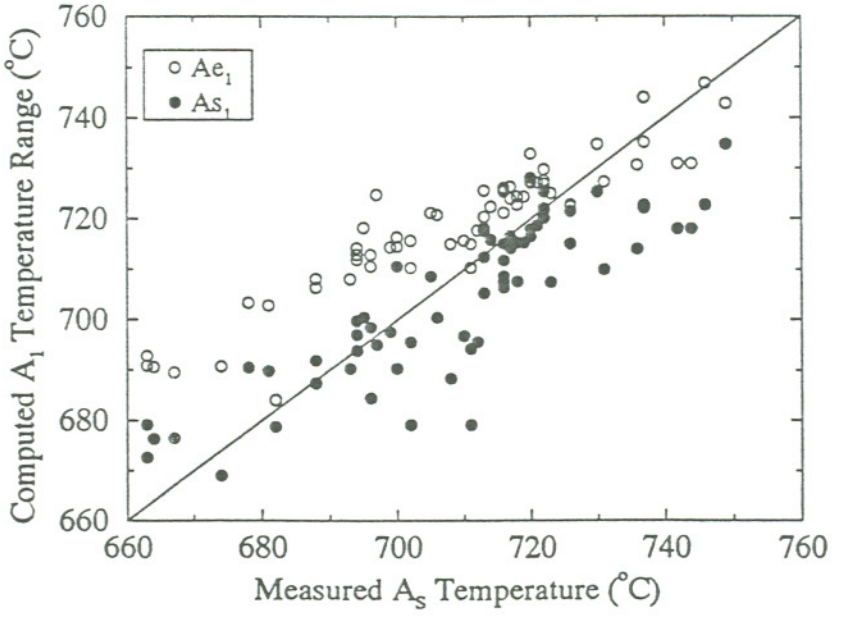

Figure 5.4 Predicted Ae_1, As_1 and experimental A_s temperatures. Data from U.S. Steel Atlas.[156]

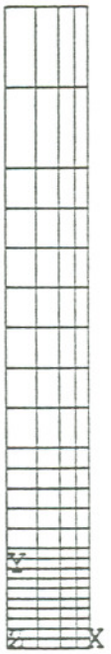

Figure 5.5 Finite element mesh for modeling Jominy end-quench bars.

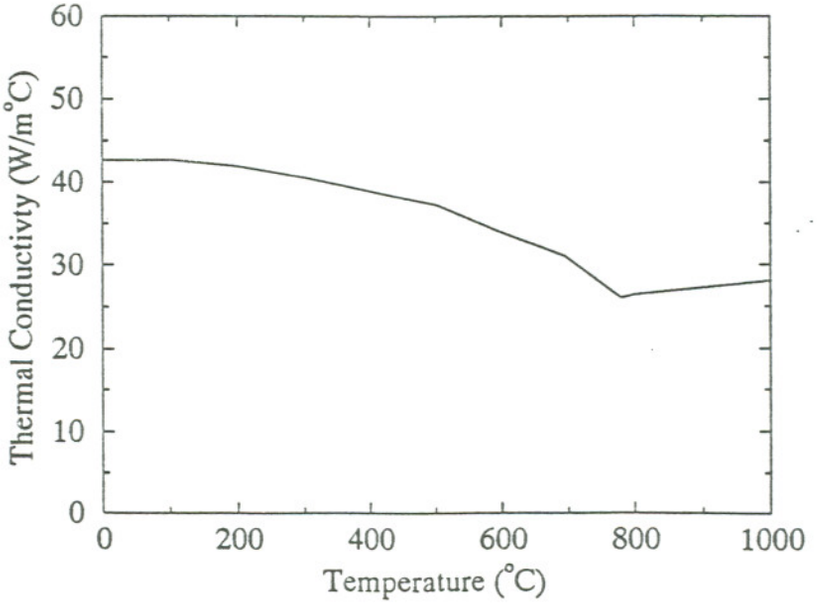

Figure 5.6 Thermal conductivity of steels used in the finite element analysis.

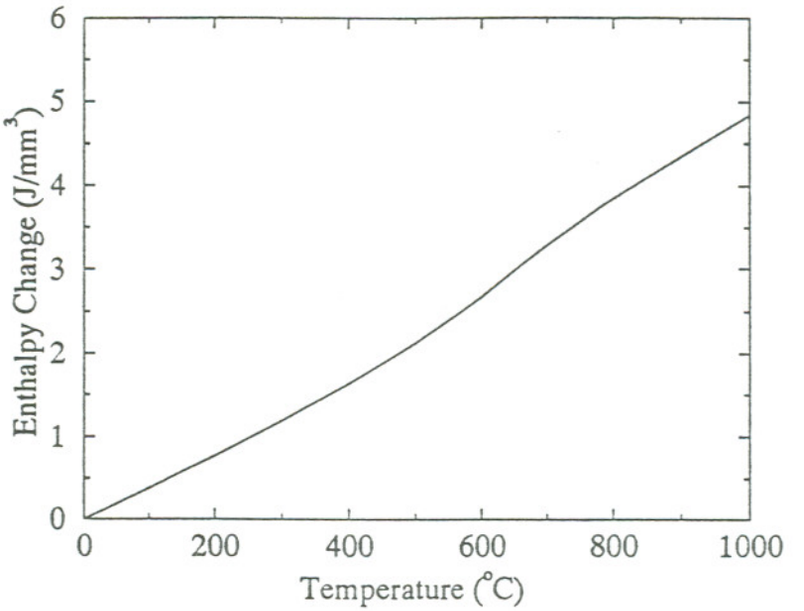

Figure 5.7 Enthalpy change of the steels used in the finite element analysis.

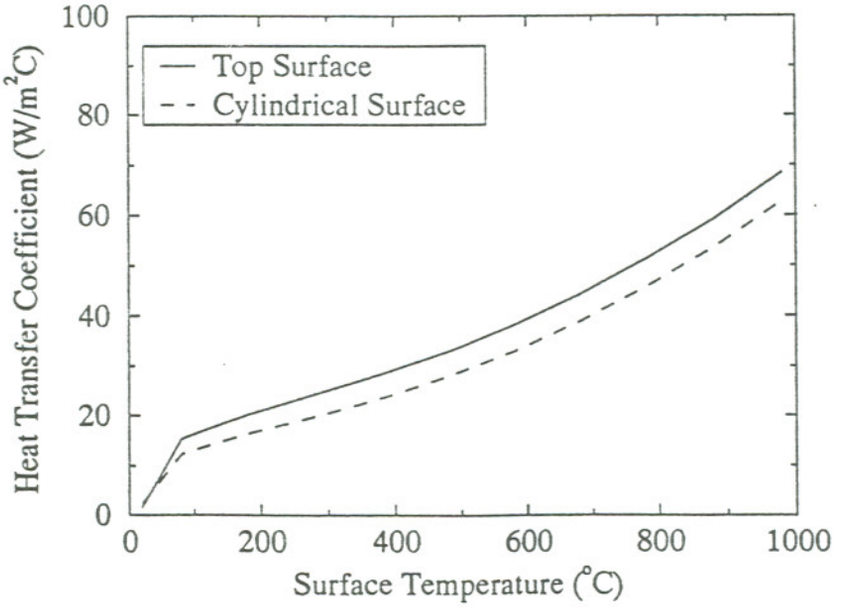

Figure 5.8 Convective heat transfer coefficient at the cylindrical surface of Jominy bars.

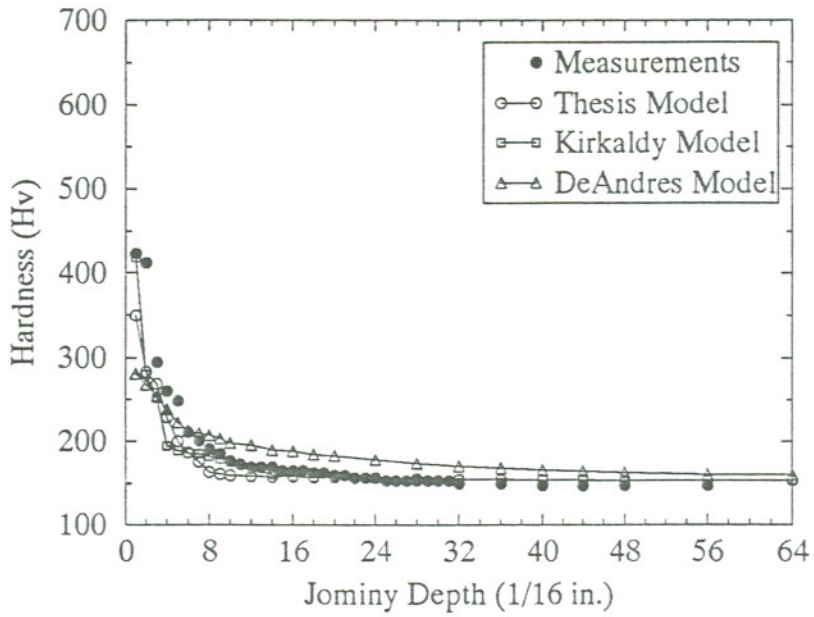

Figure 5.9 Predicted and measured Jominy hardness curve of A36 steel.

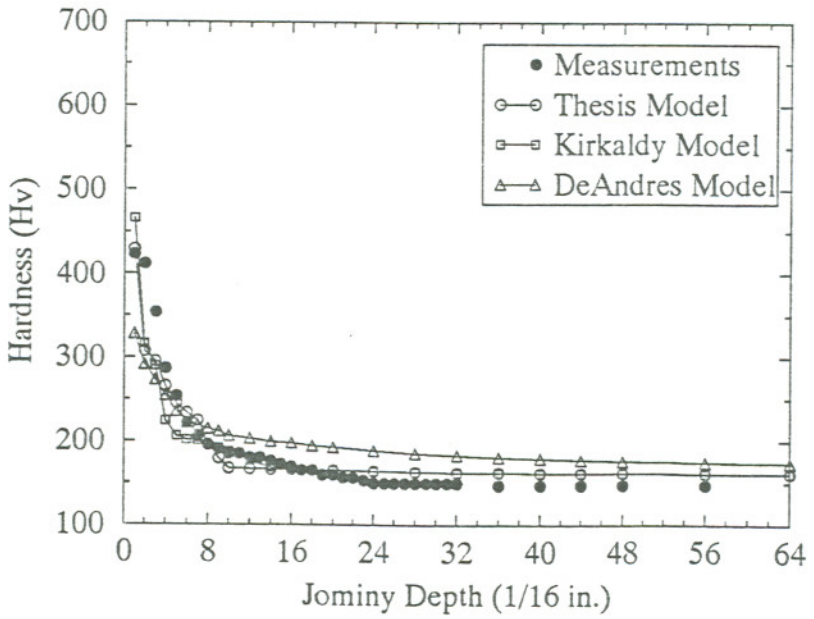

Figure 5.10 Predicted and measured Jominy hardness curve of A588 steel.

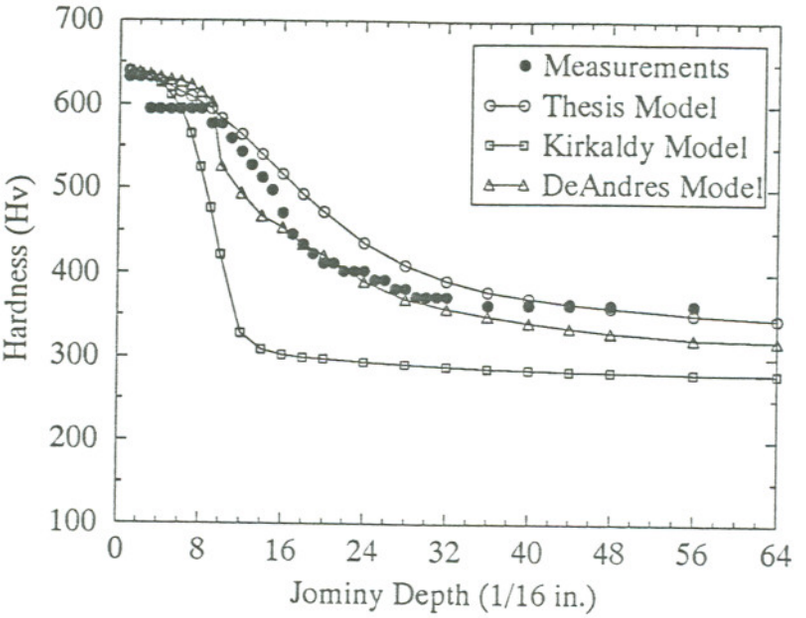

Figure 5.11 Predicted and measured Jominy hardness curve of 4140 steel.

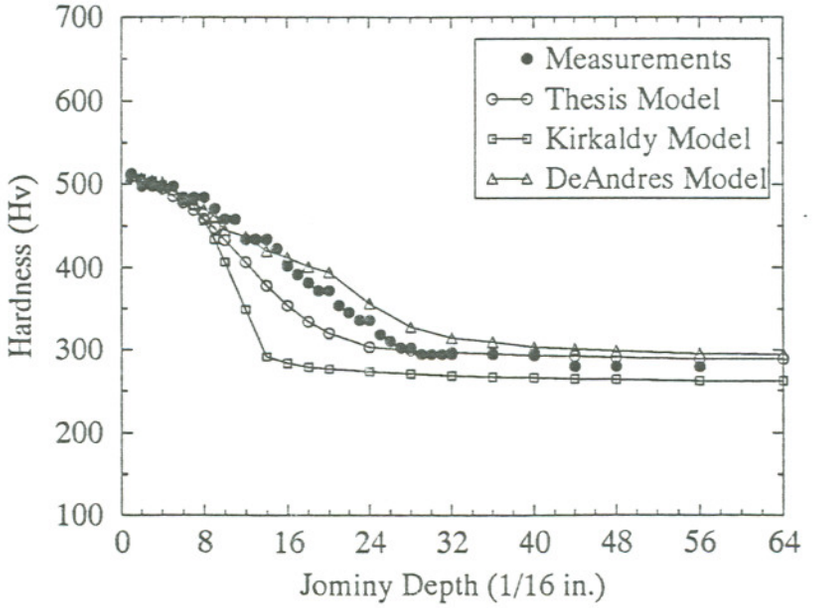

Figure 5.12 Predicted and measured Jominy hardness curve of Class 1 steel.

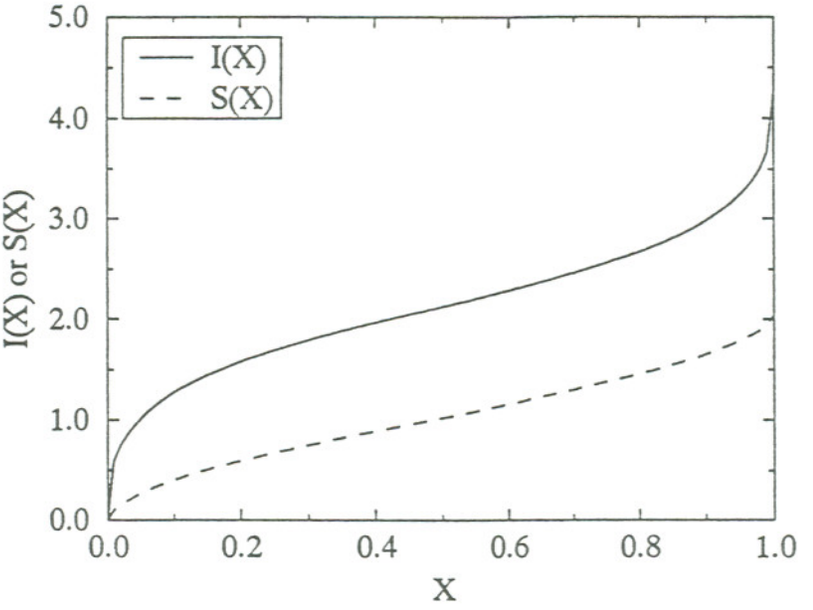

Figure 5.13 Characteristics of I(X) and S(X) terms.

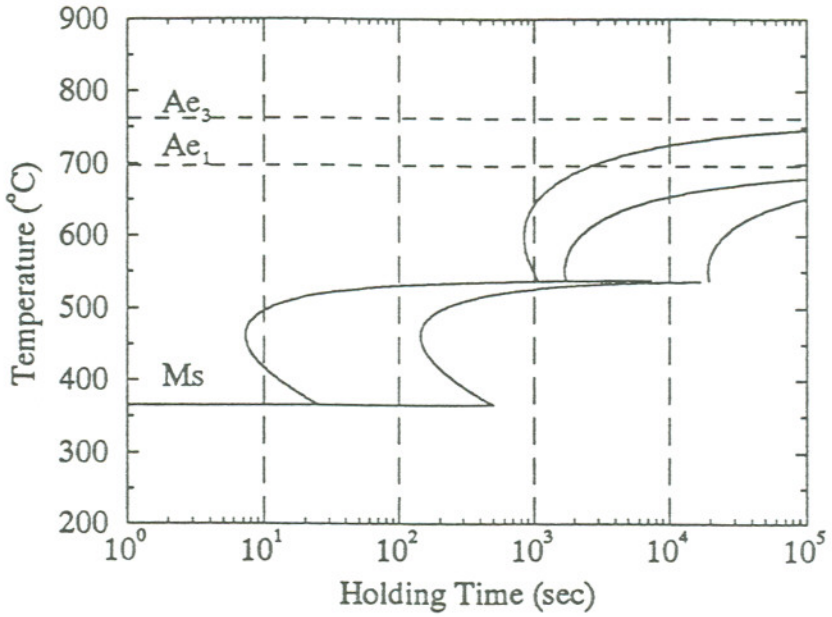

Figure 6.1 Predicted TTT diagram for the gain coarsened HAZ (G.S. = 105 μm).

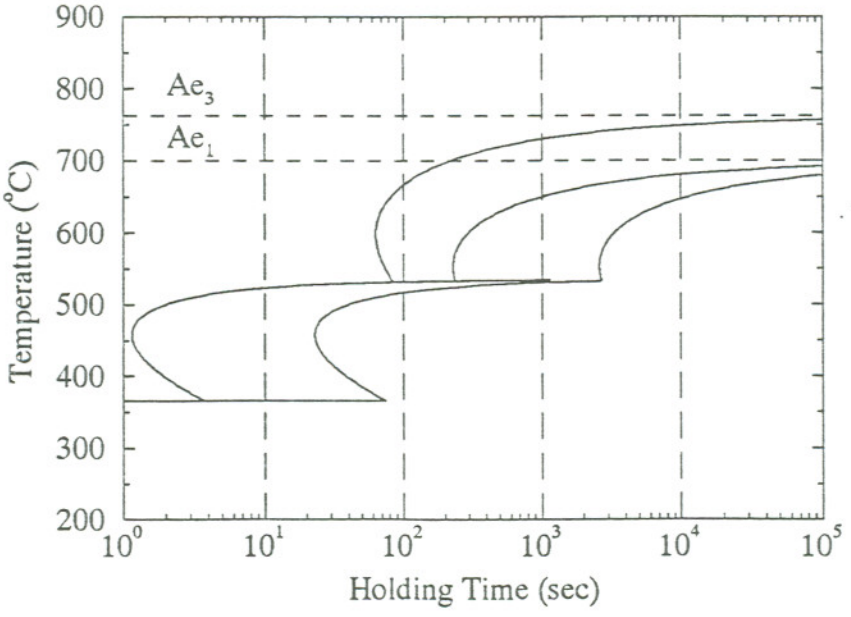

Figure 6.2 Predicted TTT diagram for the grain refined HAZ (G.S. = 5 μm).

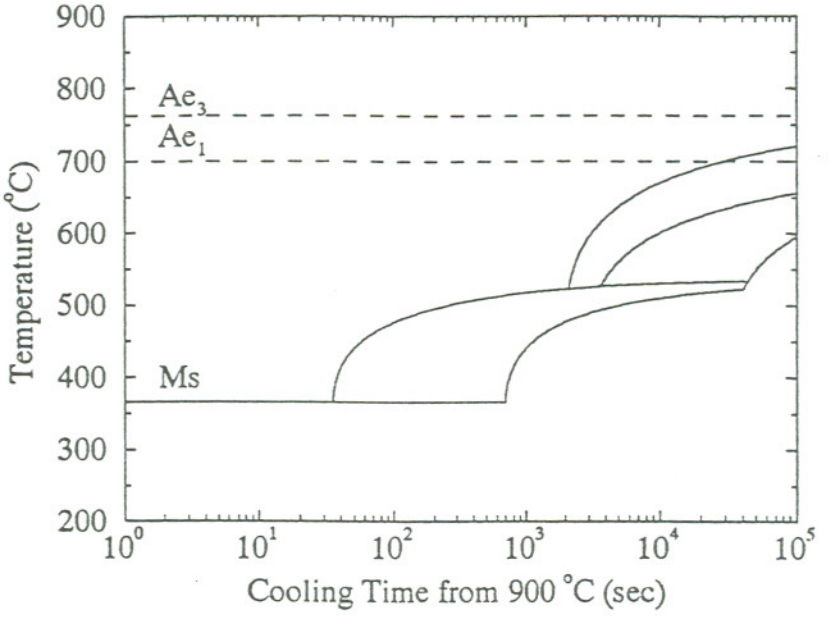

Figure 6.3 Predicted CCT diagram for the grain coarsened HAZ (G.S. = 105 μm).

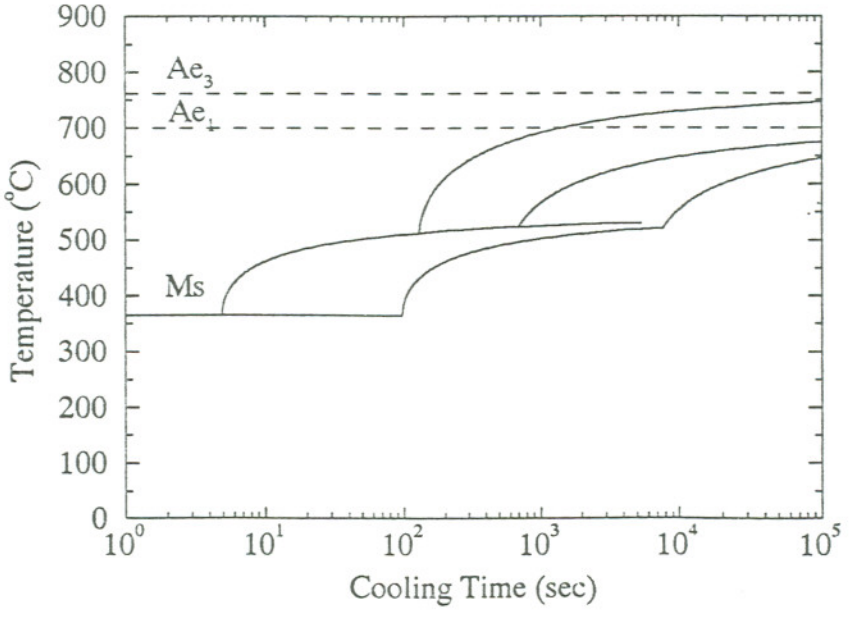

Figure 6.4 Predicted CCT diagram for the grain refined HAZ (G.S. = 5 μm).

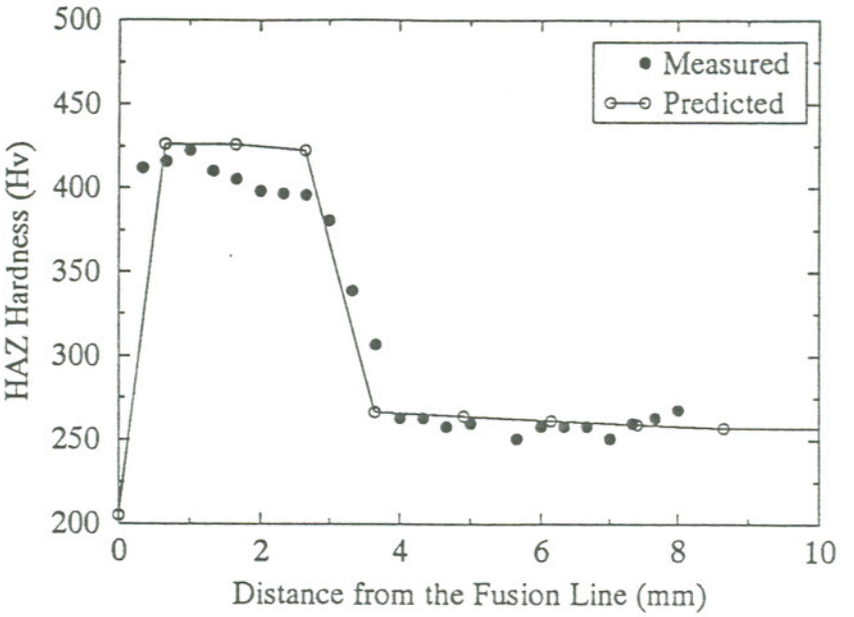

Figure 6.5 Predicted and measured HAZ hardness profile (T_0=93 °C).

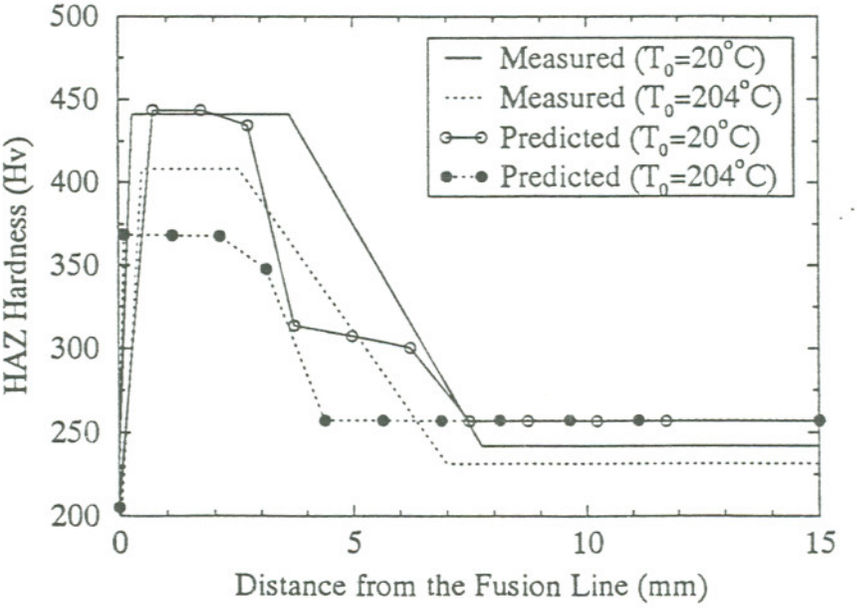

Figure 6.6 Predicted and measured HAZ hardness.

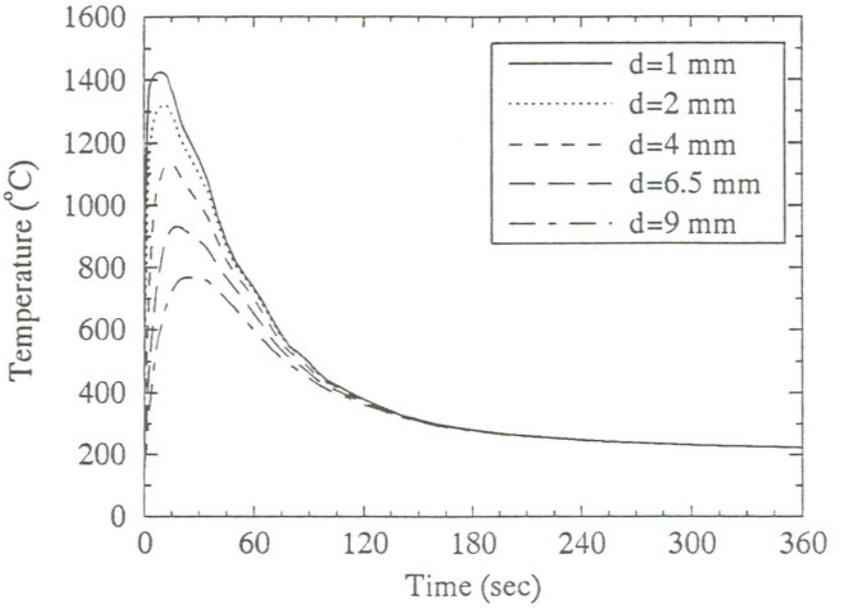

Figure 6.7 Computed thermal cycles in the HAZ versus distances from the original clad/substrate interface (T_0=150 °C).

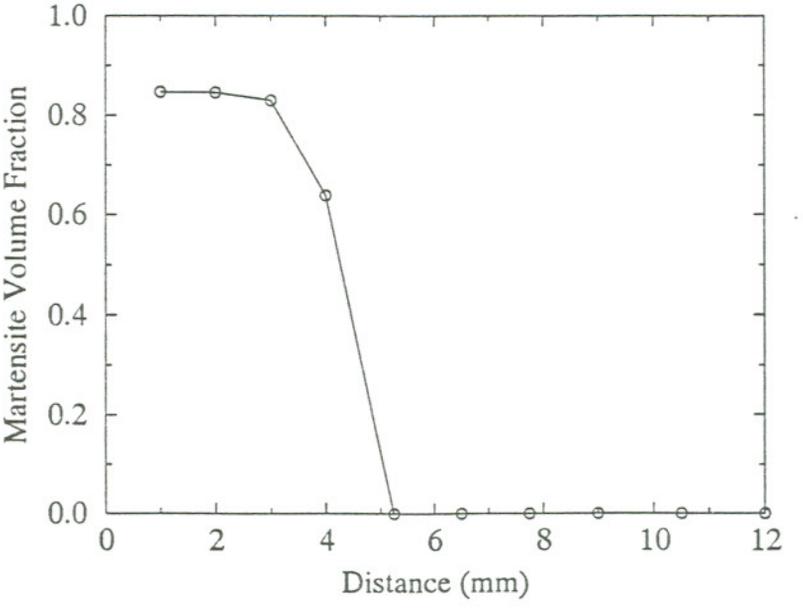

Figure 6.8 Predicted martensite volume fraction in the HAZ versus distances from the original clad/substrate interface (T_0=150 °C).

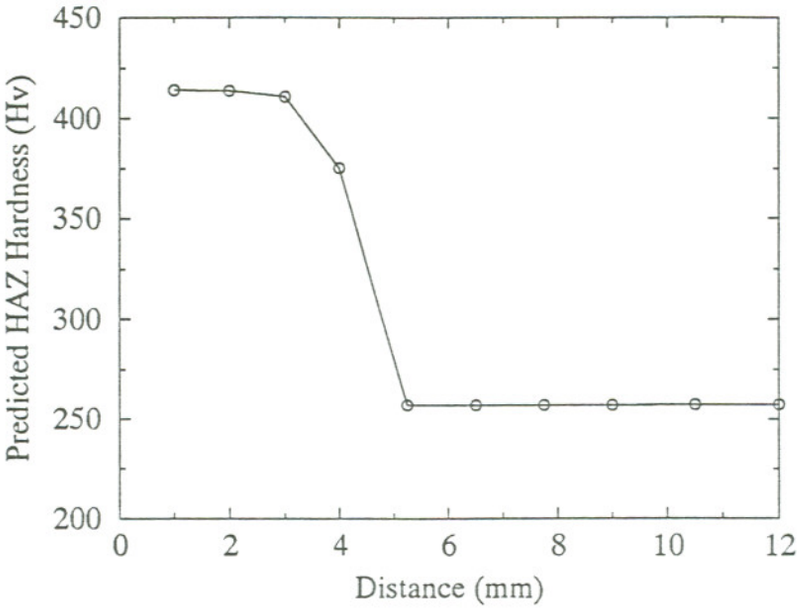

Figure 6.9 Predicted hardness in the HAZ versus distances from the original clad/substrate interface (T_0=150 °C).

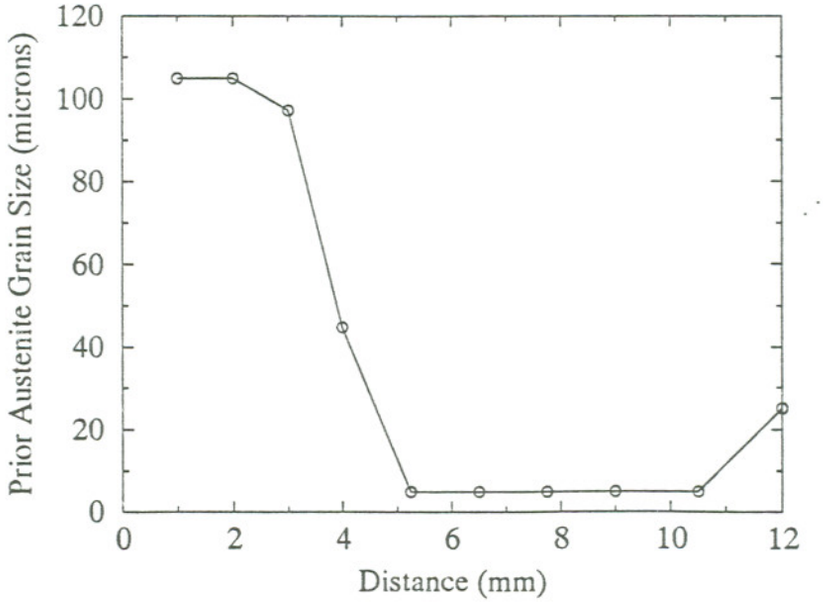

Figure 6.10 Predicted austenite grain size in the HAZ versus distances from the original clad/substrate interface (T_0=150 °C).

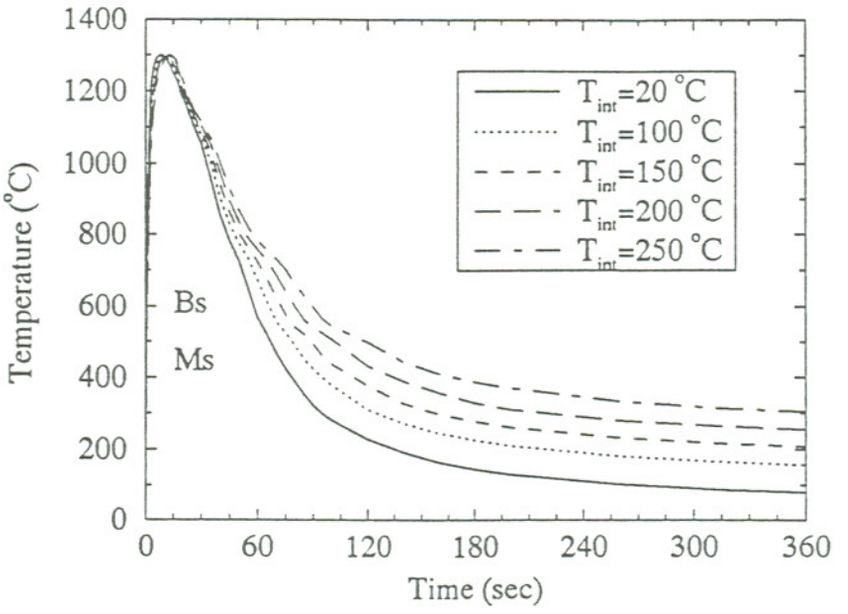

Figure 6.11 Representative thermal cycles in the grain coarsened region of HAZ as functions of interpass temperature.

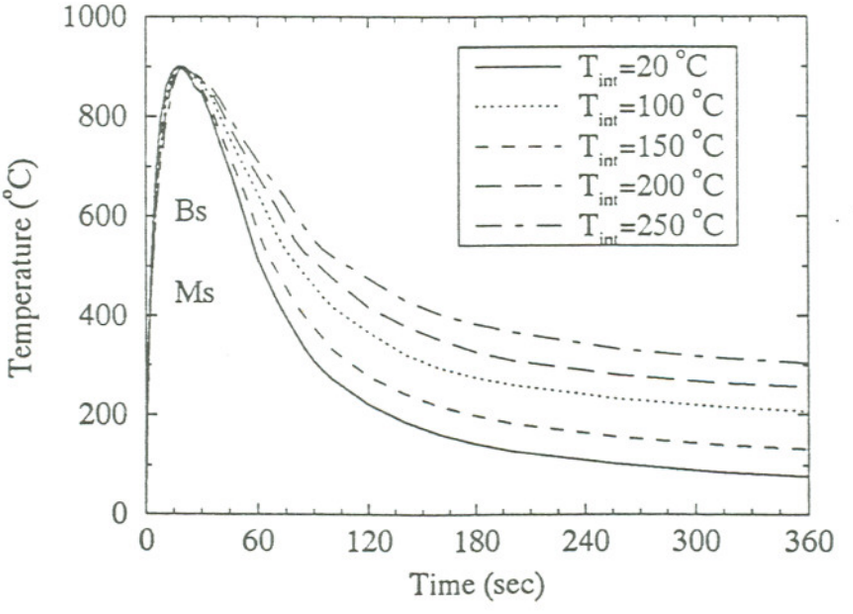

Figure 6.12 Representative thermal cycles in the grain refined region of HAZ as functions of interpass temperature.

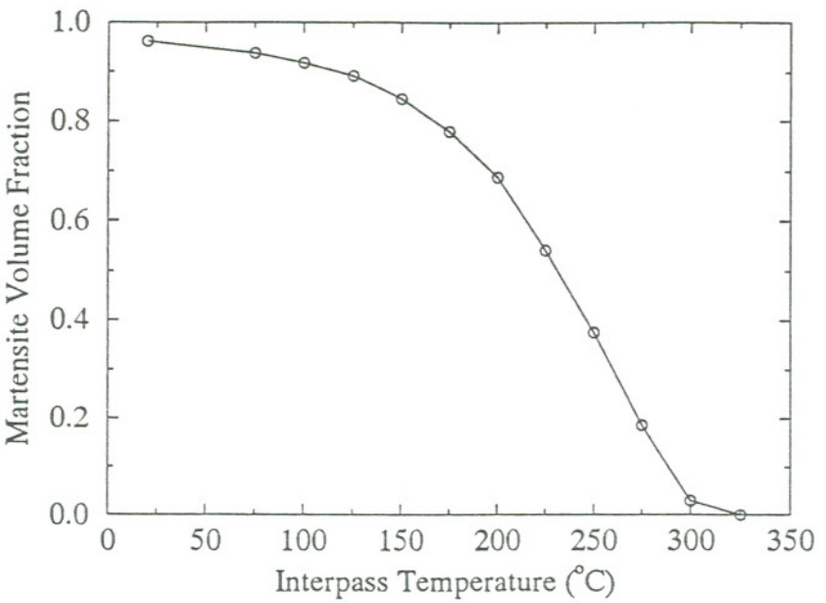

Figure 6.13 Predicted martensite volume fractions in the grain coarsened HAZ as a function of interpass temperature.

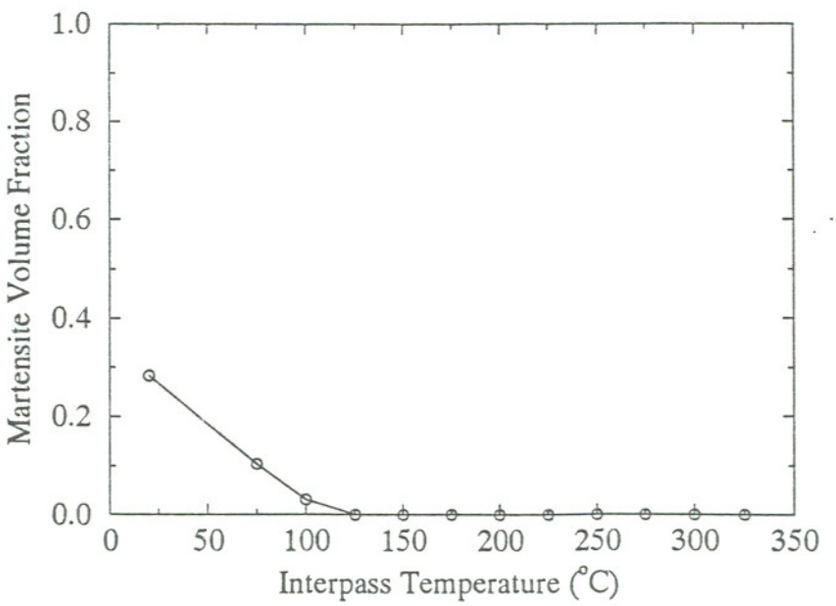

Figure 6.14 Predicted martensite volume fractions in the grain refined HAZ as a function of interpass temperature.

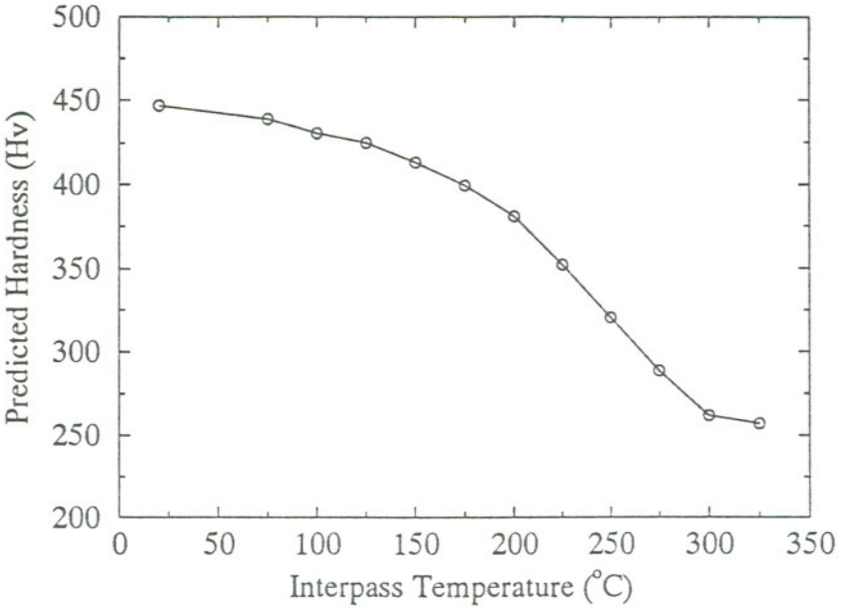

Figure 6.15 Predicted hardness in the grain coarsened HAZ as a function of interpass temperature.

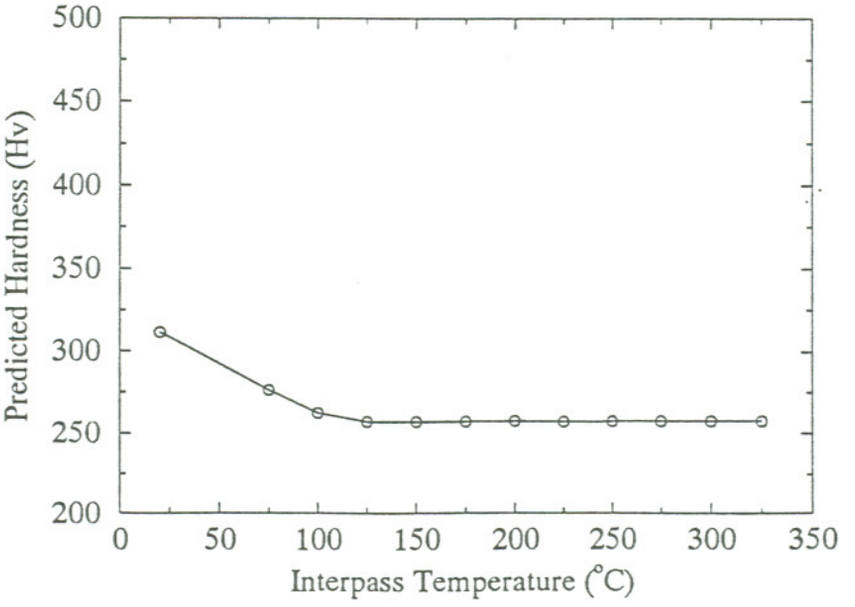

Figure 6.16 Predicted hardness in the grain refined HAZ as a function of interpass temperature.

REFERENCES

1. Seidal, G., and Hess, H., "Investigation of the Electroslag Strip Cladding with Strip Electrodes," **Schweissen Schneiden**, vol. 23(10), 1971, pp. 410-411.
2. Barger, J. J., "Welding Overlay," in **Welding Technology in Japan**, 1982, Welding Research Council, New York, pp. 16-22.
3. Nakano, S., and Nishiyama, N. T., and Tsuboi, J., "Maglay Process Electromagnetic Controlled Overlay Welding Process with ESW," **Kawasaki Steel Technical Report**, No. 2, March 1981, p. 31.
4. Bemst, A. Van and Dargent, Ph., "Electroslag Cladding Using Nickel Base Alloys," **Metal Construction**, vol. 15(10), 1983, pp. 730-733.
5. Killing, R., "Performance Characteristics of Electroslag Weld Cladding with Strip Electrodes," **Schweissen Schneiden**, vol. 40(6), 1988, pp. 283-288.
6. Killing, R., "Influence of Welding Powder and Welding Parameters on the Welding Process in Electroslag Strip Cladding with Strip Electrodes," **Schweissen Schneiden**, vol. 40(10), 1988, pp. 500-504.
7. Oh, Y. K., Devletian, J. H., and Chen, S. J., "Low Dilution Electroslag Cladding for Shipbuilding," **Welding Journal**, vol. 69(8), 1990, pp. 37-44.
8. Devletian, J. H., Gao, Y. P., Zhao, Q. H., and Wood, W. E., "Strip Cladding of Propeller Shafts with Nickel Alloy 625 by Electroslag Surfacing," **Journal of Ship Production**, vol. 9(3), 1993, pp. 173-180.
9. Gao, Y. P., Devletian, J. H., and Wood, W. E., "Electroslag and Submerged Arc Cladding with Nickel Alloy Strip," in **International Trends in Welding Science and Technology**, Edited by S. A. David and J. M. Vitek, ASM International, June 1992, pp. 449-453.
10. Zhao, Q. H., Gao, Y. P., McCarthy, J. M., Devletian, J. H., and Wood, W. E.,

"Microstructure Study of Ni Alloy 625 Cladding over Carbon Steel," in **International Trends in Welding Science and Technology**, Edited by S. A. David and J. M. Vitek, ASM International, June 1992, pp. 339-343.

11. Gooch, T. G. and Hart, P. H. M., "Keynote Address: Solid State Phase Transformations in Steel During Welding," in **Advances in Welding Science and Technology**, Edited by S. A. David, May 1986, pp. 161-176.
12. Easterling, K. E., "Keynote Address: Predicting Heat-Affected Zone Microstructures and Properties in Fusion Welds," in **Advances in Welding Science and Technology**, Edited by S. A. David, May 1986, pp. 177-184.
13. Bhadeshia, H. K. D. H., Svensson, L., and Gretoft, B., "Prediction of Microstructure of the Fusion Zone of Multicomponent Steel Weld Deposits," in **Advances in Welding Science and Technology**, Edited by S. A. David, May 1986, pp. 225-228.
14. Easterling, K. E., "Keynote Address: Microstructure and Properties of the Heat Affected Zone," in **Recent Trends in Welding Science and Technology**, Edited by S. A. David, ASM, 1990, pp. 177-188.
15. Bhadeshia, H. K. D. H., "Keynote Address: Modeling the Microstructure in the Fusion Zone of Steel Weld Deposits," in **Recent Trends in Welding Science and Technology**, Edited by S. A. David, ASM, 1990, pp. 189-198.
16. Goldak, J., Bibby, M., Moore, J., House, R., and Patel, B., "Computer Modeling of Heat Flow in Welds," **Metallurgical Transactions**, vol. 17B(9), 1986, pp. 587-600.
17. Goldak, J., Bibby, M., and Moore, J., "Computational Weld Mechanics," Invited Opening Paper for **AGARD Workshop — Structures and Materials 61st Panel Meeting**, Oberammergau, Germany, September 8-13, 1985, 32p.
18. Radaj, D., **Heat Effects of Welding — Temperature Field Residual Stress Distortion**, Springer-Verlag, 1992.
19. Goldak, J., Oddy, A., Gu, M., Ma, W., Mashaie, A., and Hughes, E., "Coupling Heat Transfer, Microstructure Evolution and Thermal Stress Analysis

in Weld," **Mechanical Effects of Welding**, Edited by L. Karlsson, L. -E Lindgren, and M. Jonsson, 1991, pp. 1-30.

20. Ueda, Y. and Murakawa, H., "Application of Computer and Numerical Analysis Techniques in Welding Research," **Transactions of JWRI**, vol. 13(2), 1984, pp. 337-346.
21. Alberry, P. J., and Jones, W. K. C., "Comparison of Mechanical Properties of 2Cr-Mo and 0.5Cr-Mo-V Simulated Heat-Affected Zones," **Metals Technology**, vol. 4(1), 1977, pp. 45-51.
22. Christensen, N., Davis, V. de L., and Gjermundsen, K., "The Distribution of Temperatures in Arc Welding," **British Welding Journal**, vol. 12(2), 1965, pp. 54-75.
23. Spraragen W., and Claussen, G. E., "Temperature Distribution During Welding – A Review of the Literature to January 1, 1937," **Welding Journal**, vol. 16(9), 1937, pp. 4s-10s.
24. Hess, W. F., Merrill, L. L., Nippes, E. F., and Bunk, A. P., "The Measurement of Cooling Rates Associated with Arc Welding and Their Application to the Selection of Optimum Welding Conditions," **Welding Journal**, vol. 22(9), 1943, pp. 337s-422s.
25. Doan, G. E., and Stout, R. D., "A Tentative System for Preserving Ductility in Weldments" **Welding Journal**, vol. 22(8), 1943, pp. 278s-294s, 294s-299s,
26. Mahla, E. M., Rowland, M. C., Shook, C. A., and Doan , G. E.,."Heat Flow in Arc Welding," **Welding Journal**, vol. 20(10), 1941, pp. 459s-468s.
27. Paschkis, V., "Establishment of Cooling Curves of Welds by Means of Electrically Analogy," **Welding Journal**, vol. 22, 1943, pp. 462s-483s.
28. Wilson, H. A., "On Convection of Heat," **Proceedings of Cambridge Philosophy Society**, vol. 12, 1940, pp. 406-423.
29. Carslaw, H. S., and Jaeger, J. C., **Conduction of Heat in Solids**, Clarendon Press, Oxford, 1947.
30. Roberts, O. F. T., "The Theoretical Scattering of Smoke in a Turbulent

Atmosphere," **Proceedings of the Royal Society**, A, vol. 104, 1923, pp. 640-654.

31. Rosenthal, D., "Mathematical Theory of Heat Distribution During Welding and Cutting," **Welding Journal**, vol. 20(5), 1941, pp. 220s-234s.
32. Rosenthal, D., "The Theory of Moving Sources of Heat and Its Application to Metal Treatments," **Trans. ASME**, vol. 68(11), 1946, pp. 849-865.
33. Boulton, N. S., and Lance-Martin, H. E., "Residual Stresses in Arc-welded Plates," **Proceedings of the Institution of Mechanical Engineers**, vol. 133, 1936, pp. 296-347.
34. Myers, P. S., Uyehara, O. A., and Borman, G. L., "Fundamentals of Heat Flow in Welding", **Welding Research Council Bulletin**, No. 123, July 1967, pp. 1-46.
35. Tanaka, S., "A Study on Heat Conduction of a Moving Heat Source," **Journal of the Japan Welding Society**, vol. 13(9), 1943, pp. 347-359.
36. Naka, T., and Masubuchi, K., "Temperature Distribution of Welded Plates – Part 1," **Journal of the Japan Welding Society**, vol. 16(7) 1947, pp. 281-290.
37. Naka, T., and Masubuchi, K., "Temperature Distribution of Welded Plates – Part 2," **Journal of the Japan Welding Society**, vol. 16(12) 1947, pp. 374-378.
38. Masubuchi, K., and Kusuda, T., "Temperature Distribution of Welded Plates," **Journal of the Japan Welding Society**, vol. 22(5), 1953, pp. 14-17.
39. Wells, A. A., "Heat Flow in Welding," **Welding Journal**, vol. 31(5), 1952, pp. 263s-267s.
40. Nippes, E. F., Merrill, L. L., and Savage, W. F., "Cooling Rates in Arc Welds in 1/2-in Plate," **Welding Journal**, vol. 28(11), 1949, pp. 556s-564s.
41. Nippes, E. F., Savage, W. F., and Allio, R. J., "Studies of the Weld Heat-Affected Zone of T-1 Steel," **Welding Journal**, vol. 36(12), 1957, pp. 531s-540s.
42. Adams, C. M. Jr., "Cooling Rates and Peak Temperatures in Fusion Welding," **Welding Journal**, vol. 37(5), 1958, pp. 210s-215s.
43. Jhaveri, P., Moffatt, W. G., and Adams, C. M. Jr., "The Effect of Plate

Thickness and Radiation on Heat Flow in Welding and Cutting," **Welding Journal**, vol. 41(1), 1962, pp. 12s-16s.

44. Grosh, R. J., Trabant, E. A., and Hawkins, G. A., "Temperature Distribution in Solids of Variable Thermal Properties Heated by Moving Heat Sources," **Quarterly of Applied Mathematics**, vol. 13(2), 1955, pp. 161-167.

45. Grosh, R. J., and Trabant, E. A., "Arc-welding Temperatures," **Welding Journal**, vol. 35(8), 1956, pp. 396s-400s.

46. Kazimirov, A. A., Nedoseka, A. Y., and Sanchenko, V. A., "Calculating the Distribution of Heat During the Butt Welding of Plates Allowing for the Effect of Temperature on Their Physical Properties," **Automatic Welding**, vol. 26(11), 1973, pp. 30-32.

47. Nunes, A. C. Jr., "An Extended Rosenthal Weld Model," **Welding Journal**, vol. 62(6), 1983, pp. 165s-170s.

48. Ashby, M. F. and Easterling, K. E., "The Transformation Hardening of Steel Surface by Laser Beams — I Hypo-Eutectoid Steels," **Acta Metallurgica**, vol. 32(3), 1984, pp. 1935-1948.

49. Kasuya, T. and Yurioka, N., "Analysis of Three Dimensional Heat Conduction in Welding by Dispersed Point Heat Sources," **IIW Doc**. IX-1554-89, May 1989, 24p.

50. Kasuya, T. and Yurioka, N., "Prediction of Welding Thermal History by a Comprehensive Solution," **Welding Journal**, vol. 72(3), 1993, pp. 107s-115s.

51. Kou, S., "Welding, Glazing, and Heat Treating — A Dimensional Analysis of Heat Flow," **Metallurgical Transactions**, vol. 13A(3), 1982, pp. 363-371.

52. Bonacina, C., Comini, G., "On the Solution of the Nonlinear Heat Conduction Equation by Numerical Method," **International Journal of Heat and Mass Transfer**, vol. 16, 1973, pp. 581-589.

53. Bonacina, C., Comini, G., Fasano, A., and Primicerio, M., "Numerical Solution of Phase-change Problems," **International Journal of Heat and Mass Transfer**, vol. 16, 1973, pp. 1825-1832.

54. Comini, G., Del Guidice, S., Lewis, R. W., and Zienkiewicz, O. C., "Finite Element Solution of Non-linear Heat Conduction Problems with Special Reference to Phase Change," **International Journal for Numerical Method in Engineering**, vol. 8, 1974, pp. 613-624.

55. Kohler, W., and Pittr, J., "Calculation of Transient Temperature Fields with Finite Elements in Space and Time Dimension," **International Journal for Numerical Method in Engineering**, vol. 8, 1974, pp. 625- 631.

56. Thomas, B. G., Samarasekera, I. V., and Brimacomber, J. K., "Comparison of Numerical Modeling Techniques for Complex, Two-Dimensional, Transient Heat-Conduction Problems," **Metallurgical Transactions**, vol. 15B(6), 1984, pp. 307-318.

57. Westby, O., **Temperature Distribution in the Work-Piece by Welding**, Department of Metallurgy and Metals Working, The Technical University of Norway, Trondheim, Norway, 1968.

58. Pavelic, V., Tanbakuchi, R., Uyehara, O. A., and Myers, P. S., 'Experimental and Computed Temperature histories in Gas Tungsten-Arc Welding of Thin Plates," **Welding Journal**, vol. 48(7), 1969, pp. 295s-305s.

59. Parley, Z. and Hibbert, P. D., "Computation of Temperatures in Actual Weld Designs," **Welding Journal**, vol. 54(11), 1975, pp. 385s-392s.

60. Hibbitt, H. D. and Marcal, P. V., "A Numerical, Thermomechanical Model for the Welding and Subsequent Loading of a Fabricated Structure," **Computers and Structure**, vol. 3, 1973, pp. 1145-1174.

61. Friedman, E., "Thermomechanical Analysis of the Welding Process using the Finite Element Method," **Transactions of ASME, Journal of Pressure Vessel Technology**, vol. 97(3), 1975, pp. 205-214.

62. Friedman, E., "An Iterative Procedure for Including Phase Change in Transient Heat Conduction Programs and Its Incorporation into the Finite Element Method," **Proceedings of the 17th National Heat Transfer Conference,** AIChE, August, 1977.

63. Glickstein, S. S., Friedman, E., and Yeniscavich, W., "Investigation of Alloy 600 Welding Parameters," **Welding Journal**, vol. 54(4), 1975, pp. 113s-122s.

64. Friedman, E., and Glickstein, S. S., "An Investigation of the Thermal Response of Stationary Gas Tungsten Arc Welds," **Welding Journal**, vol. 55(12), 1976, pp. 408s-420s.

65. Friedman, E., "Analysis of Weld Puddle Distortion and Its Effect on Penetration," **Welding Journal**, vol. 57(6), 1978, pp. 161s-166s.

66. Krutz, G. W. and Segerlind, L. J., "Finite Element Analysis of Welded Structures," **Welding Journal**, vol. 57(7), 1978, pp. 211s-216s.

67. Inagaki, M., and Sekiguchi, H., "Continous Cooling Transformation Diagrams of Steels for Welding and Their Applications," **Transactions of the National Research Institute for Metals (Japan)**, vol. 2(2), 1960, pp. 102-125.

68. Andersson, B. A. B., "Thermal Stresses in a Submerged-Arc Welded Joint Considering Phase Transformation," **Journal of Engineering and Technology, Transactions of ASME**, vol. 100, 1978, pp. 356-362.

69. Karlsson, L., "Thermal Stresses in Welding," **Thermal Stress I**, Edited by R. B. Hetnarski, Elsevier, 1986, pp. 299-389.

70. Argyris, J. J., Szimmat, J., Willam, K. J., "Computational Aspects of Welding Stress Analysis," **Computer Method in Applied Mech. Eng.**, vol. 33, 1984, pp. 299-305.

71. Argyris, J. J., Szimmat, J., Willam, K. J., "Finite Element Analysis of Arc-Welding Processes," **Numerical Methods in Heat Transfer**, Edited by R. W. Lewis and K. Morgan, John Wiley & Sons, 1985, pp. 1-34.

72. Goldak, J., Oddy, A., McDill, M., Bibby, M. J., House, R., and Chakravarti, A. P., "Progress in Computing Residual Stress and Strain in Welds," **Advances in Welding Science and Technology**, Edited by S. A. David, May 1986, pp. 523-527.

73. Karlsson, R. I. and Josefson, B. L., "Three-Dimensional Finite Element Analysis of Temperature and Stresses in a Single-Pass Butt Welded Pipe," **Journal of**

Pressure Vessel Technology, Transactions of ASME, vol. 112(1), 1990, pp. 76-84.

74. Lindgren, L., Karlsson, L., "Deformations and Stresses in Welding of Shell Structures," **International Journal of Numerical Method**, vol. 25, 1988, pp. 635-655.

75. Tekriwal, P. and Mazumder, J., "Finite Element Modeling of Arc Welding Processes," **Advances in Welding Science and Technology**, Edited by S. A. David, May 1986, pp. 71-80.

76. Moore, J. E., Bibby, M. J., Goldak, J. A., and Santyr, S., "A Comparison of the Point Source and Finite Element Schemes for Computing Weld Cooling," in **Welding Research: the State of Art**, Edited by E. F. Nippes and D. J. Ball, ASM International, 1986, pp. 1-9.

77. Goldak, J. and Bibby, M., "Computational Thermal Analysis of Welds: Current Status and Future Directions," in **Modeling and Control of Casting and Welding Processes**, Edited by A. F. Giamei and G. J. Abbaschian, The minerals, Metals & Materials Society, 1988. pp. 153-166.

78. Lancaster, J. F., "Energy Distribution in Argon-Shielded Welding Arcs," **British Welding Journal**, vol. 1(9), 1954, pp. 412-426.

79. Nester, O. H., "Heat Intensity and Current Density Distributions at the Anode of High Current, Inert Gas Arcs," **Journal of Applied Physics**, vol. 33(5), 1962, pp. 1638-1648.

80. Eckert, E. R. G. and Pfender, E., "Plasma Energy Transfer to a Surface with and without Electric Current," **Welding Journal**, vol. 46(10), 1967, pp. 471s-480s.

81. Rykalin, R., R., "Welding Arc Heat Flow," **Welding in the World**, vol. 9(3/4), 1971, pp. 112-132.

82. Rykalin, R., R., "Energy Sources Used for Welding," **Welding in the World**, vol. 12(9/10), 1974, pp. 227-248, (Houdrement Lecture, International Institute of Welding, London, 1974, p. 1-23).

83. Tekriwal, P., Stitt, M., and Mazumder, J., "Finite Element Modeling of Heat Transfer for Gas Tungsten Arc Welding," **Metal Construction**, vol. 19(10), 1987, pp. 599-606R.

84. Lancaster, J. F., **The Physics of Welding**, Second Edition, IIW/IIS, Pergamon Press, 1986.

85. Woods, R. A., and Milner, D. R., "Motion in the Weld Pool in Arc Welding," **Welding Journal**, vol. 50(4), 1971, pp. 163s-173s.

86. Dilawari, A. H., Szekely, J., and Eagar, T. W., "Electromagnetically and Thermally Driven Flow Phenomena in Electroslag Welding," **Metallurgical Transactions**, vol. 9B(3), 1978, pp. 371-381.

87. Dilawari, A. H., Eagar, T. W., and Szekely, J., "An Analysis of Heat and Fluid Flow Phenomena in Electroslag Welding," **Welding Journal**, vol. 57(1), 1978, pp. 24s-30s.

88. Atthey, D. R., "A Mathematical Model for Fluid Flow in A Weld Pool at High Currents," **Journal of Fluid Mechanics**, vol. 98(Part4), 1980, pp. 787-801.

89. Oreper, G. M., Eagar, T. W., and Szekely, J., "Convection in Arc Weld Pools," **Welding Journal**, vol. 62(11), 1983, pp. 307s-312s.

90. Oreper, G. M., and Szekely, J., "Heat- and Fluid-Flow Phenomena in Weld Pools," **Journal of Fluid Mechanics**, vol. 147, October 1984, pp. 53-79.

91. Chan, C., Mazumder, J., and Chen, M. M., "A Two-Dimensional Transient Model for Convection in Laser Melted Pool," **Metallurgical Transactions**, vol. 15A(11), 1984, pp. 2175-2183.

92. Lin, M. L. and Eagar, T. W., "Influence of Arc Pressure on Weld Pool Geometry," **Welding Journal**, vol. 64(6), 1985, pp. 163s-169s.

93. Lin, M. L. and Eagar, T. W., "Effects of Surface Depression and Convection in GTA Welding," in **Advances in Welding Science and Technology**, Edited by S. A. David, ASM International, May 1986, pp. 47-51.

94. Szekely, J., "The Mathematical Modelling of Arc Welding Operations," in **Advances in Welding Science and Technology**, Edited by S. A. David, ASM

International, 1986, p. 3-14.

95. Kou, S., and Wang, Y. H., "Computer Simulation of Convection in Moving Arc Weld Pools," **Metallurgical Transactions**, vol. 17A(12), 1986, pp. 2271-2277.

96. Kou, S., and Wang, Y. H., "Three-Dimensional Convection in Laser Melted Pools," **Metallurgical Transactions**, vol. 17A(12), 1986, pp. 2265-2270.

97. Kou, S. and Wang, Y. H., "Weld Pool Convection and Its Effect," **Welding Journal**, vol. 65(3), 1986, pp. 63s-70s.

98. Mills, K. C. and Keene, B. J., "Factors Affecting Variable Weld Penetration," **International Materials Review**, vol. 35(4), 1990, pp. 185-216.

99. Zacharia, T., David, S. A., Vitek, J. M., and Debroy, T., "Weld Pool Development During GTA and Laser Beam Welding of Type 304 Stainless Steel, Part I - Theoretical Analysis," **Welding Journal**, vol. 68(12), 1989, pp. 499s-509s.

100. Zacharia, T., David, S. A., Vitek, J. M., and Kraus, H. G., "Computational Modeling of Stationary Gas-Tungsten-Arc Weld Pools and Comparison to Stainless Steel 304 Experimental Results," **Metallurgical Transactions**, vol. 22B(2), 1991, pp. 243-257.

101. Ohji, T., Ohkubo, A., and Nishiguchi, K., "Mathematical Modeling of Molten Pool in Arc Welding," in **Mechanical Effects of Welding**, Edited by L. Karlsson, L. -E Lindgren, and M. Jonsson, Springer-Verlag, 1991, pp. 207-214.

102. Lu, M. and Kou, S., "Power and Current Distribution in Gas Tungsten Arcs," **Welding Journal**, vol. 67(2), 1988, pp. 29-34.

103. Kraus, H. G., "Experimental Measurement of Weld Pool Temperature - A Review," in **Modeling and Control of Casting and Welding Processes**, Edited by A. F. Giamei and G. J. Abbaschian, The Minerals, Metals & Materials Society, 1988, pp. 205-212.

104. Goldak, J., Oddy, A., McDill, M., and House, R., "A New Finite Element Model for Welding Heat Sources," **Metallurgical Transactions**, vol. 15B(6), 1984, pp. 587-600.

105. Leung, C. K., Pick, R. J., and Mok, D. H. B., "Finite Element Modeling of a Single Pass Weld," **Welding Research Council Bulletin**, No. 356, New York, 1990, pp. 1-10.

106. Leung, C. K. and Pick, R. J., "Finite Element Analysis of Multipass Welds," **Welding Research Council Bulletin**, No. 356, New York, 1990, pp. 11-33.

107. Wellford, L. C. Jr, and Ayer, R. M., "A Finite Element Free Boundary Formulation for the Problem of Multi-phase Heat Conduction," **International Journal of Numerical Method and Engineering**, vol. 11, 1977, pp. 933-943.

108. Morgan, K., Lewis, R. W., and Zienkiewics, O. C., "An Improved Algorithm for Heat Conduction Problems with Phase Change," **International Journal of Numerical Method and Engineering**, vol. 12, 1978, pp. 1191-1195.

109. Rybicki, E. F., Stonisifer, R. B., "Computation of Residual Stresses due to Multipass Welds in Piping Systems," **Journal of Pressure Vessel Technology, Transactions of ASME**, vol. 101, May 1979, pp. 149-154.

110. Easterling, K., **Introduction to the Physical Metallurgy of Welding**, Butterworths-Heinemann, 1992.

111. Buchmayr, B. and Cerjak, H., "Mathematical Description of HAZ Behavior of Low-alloyed Structural Steels," in **Weld Quality - The Role of Computers**, Pergamon Press, 1988, pp. 43-50. (Proceedings of the International Conference on Improved Weldment Control with Special Reference to Computer Technology, Vienna, Austria, July, 1988)

112. Chong, L., Bibby, M. J., and Goldak, J. A., "Predicting Heat-Affected Zone Hardness," **Fourth International Symposium of the Japanese Welding Society - Fundamental and Practical Approaches to the Reliability of Welded Structures**, Osaka, November 24, 1982, pp. 491-496.

113. Shing, G. Y., Bibby, M. J., and Goldak, J. A., "A Microprocessor Model for the Heat-Affected Zone Hardness of Steel Welds," **SAMPE Quarterly**, vol. 16(4), 1985, pp. 31-39.

114. Bayoumi, M. R., "Towards a Prediction of the hardness of the Heat-Affected

Zone of Steel Weldments," **Journal of Materials Science**, vol. 26(10), 1991, pp.2716-2724.

115. Stout, R., D., Torr, S. S., and Doan, G. E., "Quantitative Measurement of Welding Response by Bead Welds," **Welding Journal**, vol. 24(12), 1945, pp. 625s-628s.

116. Maynier, Ph., Dollet, J., and Bastien, P., "Prediction of Microstructure via Empirical Formulae Based on CCT Diagrams," **Hardenability Concepts with Applications to Steel**, Edited b D. V. Doane and J. S. Kirkaldy, 1978, pp. 163-178.

117. Maynier, Ph., Jungmann, B., and Dollet, J., "Creusot-Loire System for the Prediction of the Mechanical Properties of Low Alloy Steel Products" **Hardenability Concepts with Applications to Steel**, Edited by D. V. Doane and J. S. Kirkaldy, 1978, pp. 518-545.

118. Bastien, P., Dollet, J., Maynier, Ph., "Prediction of the Structure and Mechanical Properties in the Heat-Affected Zone of High Yield Weldable Steels," **Metal Construction and British Welding Journal**, vol. 2(1), 1970, pp. 9-20.

119. DeAndrés, M. P. and Carsí, M., "Hardenability: An Alternative to the Use of Grain Size as Calculation Parameter," **Journal of Materials Science**, vol. 22(8), 1987, pp. 2707-2716.

120. Dearden, J. and O'Neill, H., "A Guide to the Selection and Welding of Low-alloy Structural Steels," **Transactions of the Institute of Welding**, vol. 3(10), 1940, pp. 203-214.

121. Winterton, K., "Weldability Prediction from Steel Composition to Avoid HAZ Cracking," **Welding Journal**, vol. 40(6), 1961, pp. 253s-258s.

122. Kihara, H. et al, "Weld Cracking Tests of High-Strength Steels and Electrodes," **Welding Journal**, vol. 41(1), 1962, pp. 36s-48s.

123. Suzuki, H., Yurioka, N., and Okumura, M., "A New Cracking Parameter for Welded Steels Considering Local Accumulation of Hydrogen," **Welding in the World**, vol. 21(5/6) 1983, pp. 110-132.

124. Ito, Y. and Bessyo, K., "Weldability Formula of High Strength Steels Related to heat Affected Zone Cracking," **IIW Document**, IX-576-68, 1968.

125. Düren, C., "Equations for the Prediction of Cold Cracking Resistance in Field-Welding Large-Diameter Pipes," **IIW Document**, IX-1458-87, 1987.

126. Bailey, N., "The Development and Use of Carbon Equivalent in Britain," in **Hardenability of Steels — Select Conference**, The Welding Institute, May 1990, pp. 25-33.

127. DeMeester, B., "Note on the Carbon Equivalent," **Welding in the World**, vol. 28(3/4), 1990, pp. 48-54.

128. Boothhy, P. J., "Predicting Hardness in Steel HAZs," **Metal Construction**, vol. 17(6), 1985, pp. 363-366

129. Cottrell, C. L. M., "Hardness Equivalent May Lead to A More Critical measure of Weldability," **Metal Construction**, vol. 16(12), 1984, pp. 740-744.

130. Boniszewski, T. and Keeler, T., "HAZ Hardness Control in C-Mn Microalloyed Structural Steels," **Metal Construction**, vol. 16(10), 1984, pp. 608-617.

131. Arata, Y., Nishiguchi, K., Ohji, T., and Kohsai, N., "Weldability Concept on Hardness Prediction," **Transaction of JWRI**, vol. 8(1), 1979, pp. 43-52.

132. Yurioka, N., Suzuki, H., Okumura, M., Ohshita, S., and Saito, S., "Carbon Equivalents to Assess Cold Cracking Sensitivity and Hardness of Steel Welds," **Nippon Steel Technical Report**, No. 20, 1982, pp. 61-73.

133. Yurioka, N., Okumura, M., Kasuya, T., and Cotton, H. J. U., "Prediction of HAZ Hardness of Transformable Steels," **Metal Construction**, vol. 19(4), 1987, pp. 217R-223R.

134. Yurioka, N., "Weldability of Modern High Strength Steels," **IIW Document**, IIW-IX-1524-88, 1988.

135. Yurioka, N., "Carbon Equivalent for Hardenability and Cold Cracking Susceptibility of Steels', in **Hardenability of Steels — Select Conference**, The Welding Institute, May 1990, pp. 41-50.

136. Terasaki, T., "Study of Predictive Equations of Thermal Factor and Hardness

Related with Weld Cold Cracking," **Journal of ISIJ**, vol. 16, 1981, pp. 2715-2723.

137. Buchmayr, B., "'HAZ-Calculator' - A Software System for Welding Engineers," in **Recent Trends in Welding Science and Technology**, Edited by S. A. David and J. M. Vitek, ASM International, 1990, pp. 327-331.

138. Christenson, A. L., Nelson, E. C., and Jackson, C. E., "A High-Speed Dilatometer and the Transformational Behavior of Six Steels in Cooling," **Trans. AIME**, vol. 162, 1945, pp. 606-626.

139. Cottrell, C. L. M., "Assessment of Weldability by Rapid Dilatation Tests," **Journal of Iron and Steel Institute**, vol. 174(1), 1953, pp. 17-24.

140. Harrison, P. L. and Farrar, R. A., "Microstructural Development and Toughness of C-Mn and C-Mn-Ni Weld Metals, I. Microstructural Development," **Metal Construction**, vol. 19(7), 1987. pp. 392R-399R.

141. Harrison P. L. and Farrar R. A., "Application of Continuous Cooling Transformation Diagrams for Welding of Steels," **International Materials Reviews**, vol. 34(1), 1989, pp. 35-51.

142. Ohmori, Y., Ohatani, H., and Kunitake, T., "The Bainite in Low Carbon Alloy High Strength Steels," **Transactions of Iron and Steel Institute**, Japan, vol. 11(4), 1971, pp.250-259.

143. Brownrigg, A., and Boelen, R., "The Effect of Nb on Hardenability of C-Mn-Si-Al Steels," **IIW Document**, IIW-1976-MTC, 1976.

144. Eldis, G. T., "A Critical Review of Data Source for Isothermal and Continuous Cooling Transformation Diagrams," **Hardenability Concepts with Applications to Steel**, Edited by D. V. Doane and J. S. Kirkaldy, Metallurgical Society of AIME, 1978, pp. 126-157.

145. Kirkaldy, J. S., "Quantitative Prediction of Transformation Hardening in Steels," **ASM Handbook, vol. 4, Heat Treating**, 1990, pp. 20-32.

146. Umemoto, M., Nishioka, N., and Tamura, I., "Prediction of Hardenability from Isothermal Transformation Diagrams," **Transactions of ISIJ**, vol. 22(8), 1982,

pp. 629-636.

147. Scheil, E., "Anlaufzeit der Austenitumwandlung," **Archiv für das Eisenhüttenwes**, vol. 8, 1935, pp. 565-567.

148. Avrami, M., "Kinetics of Phase Change I," **Journal of Chemical Physics**, vol. 7, 1939, pp. 1103-1112.

149. Avrami, M., "Kinetics of Phase Change II," **Journal of Chemical Physics**, vol. 8, 1940, pp. 212-224.

150. Grange, R. A. and Kieffer, J., "Transformation of Austenite on Continuous Cooling and Its Relation to Transformation at Constant Temperature," **Transactions of ASM**, vol. 29, 1941, pp. 85-116.

151. Markowitz, L. M. and Richman, M. H., "The Computation of Continuous Transformation Programs from Isothermal Data, **Transactions of AIME,** vol. 239, 1967, pp. 131-132.

152. Hildenwall, B., and Ericsson, T., "Prediction of Residual Stresses in Case Hardening Steels," **Hardenability Concepts with Applications to Steel**, Edited by D. V. Doane and J. S. Kirkaldy, AIME, 1978, pp. 578-605.

153. Johnson, W. A. and Mehl, R. F., "Reaction Kinetics in Processes of Nucleation and Growth," **Transactions of AIME**, vol. 135, 1939, pp. 416-442.

154. Cahn, J. W., "The Kinetics of Grain Boundary Nucleated Reactions," **Acta Metallurgica**, vol. 4, 1956, pp. 449-459.

155. Saito, Y., Saeki, M., Nishida, M., Ito, Y., Tanaka, T., and Takizawa, S., "Optimum Designing of Mechanical Properties of Hot-Rolled Steel Coils by controlled Rolling and cooling," **Proceedings of the International Conference on Steel Rolling, vol. 2, Science and Technology of Flat Rolled Products**, Tokyo, Japan, 1980, The Iron and Steel Institute of Japan, pp. 1309-1320.

156. **Atlas of Isothermal Transformation Diagrams**, U.S. Steel, 3rd edition, 1963.

157. Kirkaldy, J. S., "Prediction of Alloy Hardenability from Thermodynamic and Kinetic Data," **Metallurgical Transactions**, vol. 4, 1973, pp. 2327-2333.

158. Kirkaldy, J. S. and Sharma, R. C., "A New Phenomenology for IT and CCT

Curves," **Scripta Metallurgica**, vol. 16, 1982, pp. 1193-1198.

159. Kirkaldy, J. S. and Venugopalan, D., "Prediction of Microstructure and Hardenability in Low Alloy Steels," **Phase Transformations in Ferrous Alloys**, Edited by A. R. Marder and J. I. Goldstein, AIME, 1984, pp. 125-148.

160. Zener, C., "Kinetics of Decomposition of Austenite," **Transactions of AIME**, vol. 167, 1946, pp. 550-583.

161. Hillert, M., "The Role of Interfacial Energy During Solid State Transformations," **Jernkont. Ann.**, vol. 141, 1957, pp. 557-585.

162. Ikawa, H., Shin, S., and Oshige, H., "Grain Growth of Commercial-Purity Nickel in Weld-Heat Affected Zone," **Transactions of the Japan Welding Society**, vol. 6(1), 1975, pp. 17-22.

163. Ikawa, H., Oshige, H., and Noi, S., "Austenite Grain Growth of Steel in Weld-Heat Affected Zone," **Transactions of the Japan Welding Society**, vol. 8(2), 1977, pp. 52-57.

164. Ikawa, H., Oshige, H., Noi, S., and Kanda, K., "Calculation of Grain Size in Weld-Heat Affected Zone using Heat Conduction Equation," **Transactions of the Japan Welding Society**, vol. 9(1), April 1978, pp. 41-46.

165. Ikawa, H., Oshige, H., Noi, S., Date, H., and Uchikawa, K., "Relation between Welding Conditions and Grain Size in Weld Heat-Affected Zone," **Transactions of the Japan Welding Society**, vol. 9(1), April 1978, pp. 47-51.

166. Savage, W. F., "1980 Houdremont Lecture: Solidification, Segregation and Weld Imperfections," **Welding in the World**, vol. 18(5/6), 1980, pp. 89-114.

167. Alberry, P. J., Chew, B., and Jones, W. K. C., "Prior Austenite Grain Growth in Heat-Affected Zone of a 0.5Cr-Mo-V Steel" **Metals Technology**, vol. 4(6), 1977, pp. 317-325.

168. Alberry, P. J. and Jones, W. K. C., "Computer Model for Prediction of Heat-Affected-Zone Microstructures in Multipass Weldments," **Metals Technology**, vol. 9(10), 1982, pp. 419-426.

169. Alberry, P. J., Brunnstrom, R. R. L., and Jones, K. E., "Computer Model for

Prediction Heat-Affected-Zone Structures in Mechanized Tungsten-Inert Gas Weld Deposits," **Metals Technology**, vol. 10(1), 1983, pp. 28-38.

170. Ashby, M. F. and Easterling, K. E., "A First Report on Diagrams for Grain Growth in Welds," **Acta Metallurgica**, vol. 30(11), 1982, pp. 1969-1978.

171. Ion, J. C., Easterling, K. E., and Ashby, M. F., "A Second Report on Diagrams of Microstructure and Hardness for Heat-Affected Zones in Welds," **Acta Metallurgica**, vol. 32(11), 1984, pp. 1949-1962.

172. Buchmayr, B., "Modeling of Microstructural Changes During Welding of HSLA Steels," in **Third International Conference on Computer Technology in Welding**, Edited by Lucas, W., June 1990, Abington Publishing, pp. 162-171.

173. Suzuki, S., Weatherly, G. C., and Houghton, D. C., "The Response of Carbo-Nitride Particles in HSLA Steels to Weld Thermal Cycles," **Acta Metallurgica**, vol. 35, 1987, pp. 341-352.

174. Sellars, C. M., "Options and Constraints for Thermomechanical Processing of Microalloyed Steel," in **Proceedings of International Conference on HSLA Steel: Metallurgy and Application**, ASM International, Beijing, China, 1986, pp. 73-81.

175. Suárez, J. C., Molleda, F., "Numerical Modeling of Microstructural Changes in the Heat-Affected Zone of a HSLA Microalloyed Steel During the Weld Thermal Cycle," in **Eurojoin 1: First European Conference on Joining Technology**, France, 1991, pp. 181-188.

176. Suárez, J. C., Molleda, F., and Gómez de Salazar, J. M., "Modeling of Grain Growth During Arc Welding of High Strength Low Alloy Steels," **Materials Characterization**, vol. 28(1), 1992, pp. 3-13.

177. Watt, D. F., Coon, L., Bibby, M. J., Goldak, J. A., Henwood, C., "An Algorithm for Modelling Microstructural Development in Weld Heat-Affected Zones (Par A) - Reaction Kinetics," **Acta Metallurgica**, vol. 36(11), 1988, pp. 3029-3035.

178. Henwood, C., Bibby, M. J., Goldak, J. A., and Watt, D., "Coupled Transient

Heat Transfer-Microstructure Weld Computations (Part B)," **Acta Metallurgica**, vol. 36(11), 1988, pp. 3037-3046.

179. Bibby, M. J., Goldak, J. A., Szyszkowicz, M. S., and Jefferson, I., "Computational Developments in the Watt Transient HAZ Microstructure Algorithm," in **Modeling and Control of Casting and Welding Processes IV**, Edited by A. F. Giamei, and G. J. Abbaschian, 1988, pp. 81-91.
180. Holman, J. P., **Heat Transfer**, Sixth Edition, McGraw-Hill, 1986.
181. Chapman, A. J., **Fundamentals of Heat Transfer**, Macmillan Publishing Co., New York, 1987.
182. Churchill, S. W., and Chu, H. H. S., "Correlating Equations for Laminar and Turbulent Free Convection from a Horizontal Cylinder," **International Journal of Heat and Mass Transfer**, vol. 18, 1975, pp. 1049-1053.
183. Churchill, S. W., and Chu, H. H. S., "Correlating Equations for Laminar and Turbulent Free Convection from a Vertical Plate," **International Journal of Heat and Mass Transfer**, vol. 18, 1975, pp. 1323-1329.
184. McAdams, W. H., **Heat Transmission**, Third Edition, New York, McGraw-Hill, 1954.
185. Goldstein, R. J., Sparrow, E. M., and Jones, D. C., "Natural Convection Mass Transfer Adjacent to the Horizontal Plates," **International Journal of Heat and Mass Transfer**, vol. 16, 1973, pp. 1025-1034.
186. Lloyd, J. R. and Moran, W. R., "Natural Convection Adjacent to Horizontal Surfaces of Various Planforms," **ASME Paper** 74-WA/HT-66, 1974.
187. Siegel, R. and Howell, J. R., **Thermal Radiation Heat Transfer**, Second Edition, Hemisphere Publishing Corporation, McGraw-Hill Book Company, 1980.
188. Incropera, F. P. and DeWitt, D. P., **Fundamentals of Heat and Mass Transfer**, John Wiley & Sons, 1985.
189. **Thermophysical Properties of Matter - vol. 7 Thermal Radiative Properties of Metallic Elements and Alloys**, Edited by Touloukian, Y. S. and Ho, C. Y.,

Plenum Press, New York, 1972.

190. **Smithells Metals Reference Book**, Edited by Brandes, E. A. and Brook, G. B., Seventh Edition, Butterworths-Heinemann, 1992.

191. **Thermophysical Properties of Matter - vol. 1 Thermal Conductivity of Metallic Solids**, Edited by Touloukian, Y. S. and Ho, C. Y., Plenum Press, New York, 1972.

192. The British Iron and Steel Research Association, **Physical Constants of Some Commercial Steels at Elevated Temperatures**, London, Butterworths Scientific Publications, 1953.

193. **Inconel 625**, Inco Alloy International, Huntingto, West Virginia.

194. Rolphe, W. D. III, and Bathe, M., "An Efficient Algorithm for Analysis of Nonlinear Heat Transfer with Phase Changes," **International Journal of Numerical Method in Engineering**, vol. 18, 1982, pp. 119-134.

195. Hillert, M., "Prediction of Iron-Base Phase Diagrams," in **Hardenability Concepts with Applications to Steel**, Edited by D. V. Doane and J. S. Kirkaldy, AIME, 1978, pp. 5-27.

196. Wagner, C., **Thermodynamics of Alloys**, Addison-Wesley Press Inc., 1952.

197. Hillert, M., and Staffansson, L. I., "The Regular Solution Model for Stoichiometric Phases and Ionic Melts," **Acta Chemistry Scandivanian**, vol. 24(10), 1970, pp. 3618-3626.

198. Hultgren, A., "Isothermal Transformation of Austenite," **Jernkontorets Annaler**, vol. 135(8), 1951, pp. 403-483.

199. Hillert, M., "The Use of Isoactivity Lines in Ternary Phase Diagram," **Jernkontorets Annaler**, vol. 136 (2), 1952, pp. 25-37.

200. Aaronson, H. I., Domian, H. A., and Pound, G. M., "Thermodynamics of the Austenite→Proeutectoid Ferrite Transformation. II, Fe-C-X Alloys," **Trans. AIME**, vol. 236, 1966, pp. 768-781.

201. Hillert, M., "The Role of Interfaces in Phase Transformations," **The Mechanism of Phase Transformations in Crystalline Solids**, Institute of Metals, Monograph

No. 33, 1969, p. 231-247.

202. Popov, A. A., and Mikhalev, M. S., "On the Kinetics of Ferrite Formation in the Decarburization of Carbon and Alloy Steels," **The Physics of Metals and Metallography**, vol. 7, 1959, pp. 36-45.

203. Purdy, G. R., Weichert, D. H., and Kirkaldy, J. S., "The Growth of Proeutectoid Ferrite in Ternary Iron-Carbon-Manganese Austenites," **Trans. AIME**, vol. 230, 1964, pp. 1025-1034.

204. Kirkaldy, J. S. and Baganis, E. A., "Thermodynamic Prediction of the Ae_3 Temperature of Steels with Additions of Mn, Si, Ni, Cr, Mo, Cu," **Metallurgical Transactions**, vol. 9A(4), 1978, pp. 495-501.

205. Kirkaldy, J. S., Thomson, B. A., and Baganis, E. A., "Prediction of Multicomponent Equilibrium and Transformation Diagrams for Low Alloy Steels," in **Hardenability Concepts with Applications to Steel**, Edited by D. V. Doane and J. S. Kirkaldy, AIME, 1978, pp. 82-125.

206. Hashiguchi, K., Kirkaldy, J. S., Fukuzumi, T., and Pavaska, V., "Prediction of the Equilibrium and No-Partition Local Equilibrium Phase Diagrams for Multicomponent Fe-C Base Alloys," **CALPHAD**, vol. 8(2), 1984, pp. 173-186.

207. Kroupa, A. and Kirkaldy, J. S., "Computed Multicomponent Phase Diagrams for Hardenability (H) and HSLA Steels with Application to the Prediction of Microstructure and Mechanical Properties," **Journal of Phase Equilibrium**, vol. 14 (2), 1993, pp. 150-161.

208. Sugden, A. A. B. and Bhadeshia, H. K. D. H., "Thermodynamic Estimation of Liquidus, Solidus, Ae_3 Temperatures, and Phase Compositions for Low Alloy Multicomponent Steels," **Materials Science and Technology**, vol. 5(10), 1989, pp. 977-984.

209. Uhrenius, B., "A Compendium of Ternary Iron-Base Diagrams," in **Hardenability Concepts with Applications to Steel**, Edited by D. V. Doane and J. S. Kirkaldy, AIME, 1977, pp. 28-81.

210. Richardson, F. D., "The Thermodynamics of Metallurgical Carbides and of

Carbon in Iron," **Journal of Iron and Steel Institute**, vol. 175, 1953, pp. 33-51.

211. Hillert, M., Wada, T., and Wada, H., "The α-γ Equilibrium in Fe-Mn, Fe-Mo, Fe-Ni, Fe-Sb, Fe-Sn and Fe-W Systems," **Journal of Iron and Steel Institute**, vol. 205, 1967, pp. 539-546.

212. Gilmour, J. B., Purdy, G. R., and Kirkaldy, J. S., "Thermodynamics Controlling the Proeutectoid Ferrite Transformations in Fe-C-Mn Alloys," **Metallurgical Transactions**, vol. 3, 1972, pp. 1455-1464.

213. Weiss, R. J., and Tauer, K. J., "Components of the Thermodynamic functions of Iron," **Physical Review**, vol. 102(6), 1956, pp. 1490-1495.

214. Smith, R. P. and Darken, L. S., "The Iron-Carbon Eutectoid Temperature," **Trans. AIME**, vol. 215, 1959, pp. 727-728.

215. Kaufman, L., Clougherty, E. V., and Weiss, R. J., "The Lattice Stability of Metals — III. Iron," **Acta Metallurgica**, vol. 11(5), 1963, pp. 323-335.

216. Orr, R. L. and Chipman, J., "Thermodynamic Functions of Iron," **Trans. AIME**, vol. 239, 1967, pp. 630-633.

217. Harvig, H., "The Iron-Carbon System in the Temperature Range 500-1150 °C," **Jernkont. Ann.**, vol. 155, 1971, pp. 157-161.

218. Porter, D. A. and Easterling, K. E., **Phase Transformations in Metals and Alloys**, Van Nostrand Reinhold Company, 1980, pp. 110-139.

219. Burke, J. E. and Shiau, Y. G., "The Effect of Mechanical Deformation on Grain Growth in Alpha-Brass," **Metal Technology**, vol. 14(9), 1947, T.P. pp. 2265-2278.

220. Burke, J. E., "Some Factors Affecting the Rate of Grain Growth in Metals," **Trans. of AIME**, vol. 180, 1949, pp. 73-91.

221. Feltham, P., "Grain Growth in Metals," **Acta Metallurgica**, vol. 5(2), 1957, pp. 97-105.

222. Cole, D. G., Feltham, P., and Gillam, E., "On the Mechanism of Grain Growth in Metals, with Special Reference to Steel," **Proceedings of the Physical Society**, 1954, vol. B68, pp.131-137

223. Beck, P. A., Kremer, J. C., and Demer, L., "Grain Growth in High Purity Aluminum," **Physical Review**, vol. 71, 1947, pp. 555.

224. Beck, P. A., "Grain Growth in High-Purity Aluminum and in an Aluminum-Magnesium Alloy," **Transactions of AIME**, vol. 175, 1948, pp. 372-400.

225. Ralph, B., "Grain Growth," **Materials Science and Technology**, vol. 6, (11), 1990, pp. 1139-1144.

226. Rath, B. B. and Hu, H., "Driving force Dependence of Rate of Boundary Migration in Zone-Refined Aluminum Crystals," **Transactions of AIME**, vol. 245, 1969, pp. 1243-1252.

227. Hu, H., and Rath, B. B., "On the Time Exponent in Isothermal Grain Growth", **Metallurgical Transactions**, vol. 1(11), 1970, pp. 318-3184.

228. Hannerz, N. E., and Kazinczy, R. De, "Kinetics of Austenite Grain Growth in Steel," **Journal of Iron Steel Institute**, vol. 208, 1970, pp. 475-481.

229. Myers, J., "Technical Note: Grain Growth in Vacuum-Melted Steels During Weld HAZ Simulations," **Metals Technology**, vol. 4(8), 1977, pp. 411-412.

230. Rad, T., Bobok, G., and Gergely, M., "Computing Method for Nonisothermal Heat Treatments," **Heat Treatment 81**, The Metals Society, 1983, pp. 91-96.

231. Gergely, M., Somogyi, S., Reti, T., Konkonly, T., "Computerized Properties Prediction and Technology Planning in Heat Treatment of Steels," ASM Handbook, vol. 4, **Heat Treating**, 1990, pp. 638-656.

232. Akselsen, O. M., Grong, Ø, Ryum, N., and Christensen, N., "HAZ Grain Growth Mechanisms in Welding of Low Carbon Microalloyed Steels," **Acta Metallurgica**, vol. 34(9), 1986, pp. 1807-1815.

233. Kirkaldy, J. S., "Diffusion-Controlled Phase Transformations in Steels: Theory and Applications," **Scandinavian Journal of Metallurgy**, vol. 20, 1991, pp. 50-61.

234. Cahn, J. W., "Transformation Kinetics during Continuous Cooling," **Acta Metallurgica**, vol. 4(11), 1956, pp. 572-575.

235. Tzitzelkov, I., Hougardy, H. P., and Rose, A., "Mathematical Description of the

TTT Diagram for Isothermal Transformation and Continous Cooling," **Archiv für das Eisenhüttenwesen**, vol. 45, 1974, pp. 525-532.

236. Umemoto, M., Komatsubara, N., and Tamura, I., "Prediction of Hardenability Effects from Isothermal Transformation Kinetics," **Journal of Heat Treating**, vol. 1(3), 1980, pp. 57-64.

237. Fernandes, F. N. B., Denis, S., and Simon, A., "Mathematical Model Coupling Phase Transformation and Temperature Evolution during Quenching of Steels," **and Technology**, vol. 1, 1985(10), pp. 838-844.

238. Buza, G., Hougardy, H. P., and Gergely, M., "Calculation of the Isothermal Transformation Diagram from Measurements with Continous Cooling," **Steel Research**, vol. 57(12), 1986, pp. 650-653.

239. Feldman, S. E., "The Minitech Computerized Alloy Steel Information System," in **Hardenability Concepts with Applications to Steel**, Edited by D. V. Doane and J. S. Kirkaldy, AIME, 1978, pp. 546-567.

240. Kennon, N. F., "Schematic Transformation Diagrams for Steel," **Metallurgical Transactions**, vol. 9A, 1978, pp. 57-66.

241. Steven, W. and Haynes, A. G., "The Temperature of Formation of Martensite and Bainite in Low-Alloy Steels," **Journal of Iron and Steel Institute**, vol. 183(8), 1956, pp. 349-359.

242. Bhadeshia, H. K. D. H., "Thermodynamic Analysis of Isothermal Transformation Diagrams," **Metal Science**, vol. 16(3), 1982, pp. 159-165.

243. Bhadeshia, H. K. D. H., Svensson, L. -E., and Gretoft, B., "A Model for the Development of Microstructure in Low-Alloy Steel (Fe-Mn-Si-C) Weld Deposits," **Acta Metallurgica**, vol. 33(7), 1985, pp. 1271-1283.

244. Lee, J. L. and Bhadeshia, H. K. D. H., "Assessment of TTT Diagrams: A New Methodology," **China Steel Technical Report**, No. 7, 1993, pp. 16-25.

245. Russell, K. C., "Linked Flux Analysis of Nucleation in Condensed Phase," **Acta Metallurgica**, vol. 16(5), 1968, pp. 761-769.

246. Russell, K. C., "Grain Boundary Nucleation Kinetics," **Actal Metallugica**, vol.

TTT Diagram for Isothermal Transformation and Continous Cooling," **Archiv für das Eisenhüttenwesen**, vol. 45, 1974, pp. 525-532.

236. Umemoto, M., Komatsubara, N., and Tamura, I., "Prediction of Hardenability Effects from Isothermal Transformation Kinetics," **Journal of Heat Treating**, vol. 1(3), 1980, pp. 57-64.

237. Fernandes, F. N. B., Denis, S., and Simon, A., "Mathematical Model Coupling Phase Transformation and Temperature Evolution during Quenching of Steels," **and Technology**, vol. 1, 1985(10), pp. 838-844.

238. Buza, G., Hougardy, H. P., and Gergely, M., "Calculation of the Isothermal Transformation Diagram from Measurements with Continous Cooling," **Steel Research**, vol. 57(12), 1986, pp. 650-653.

239. Feldman, S. E., "The Minitech Computerized Alloy Steel Information System," in **Hardenability Concepts with Applications to Steel**, Edited by D. V. Doane and J. S. Kirkaldy, AIME, 1978, pp. 546-567.

240. Kennon, N. F., "Schematic Transformation Diagrams for Steel," **Metallurgical Transactions**, vol. 9A, 1978, pp. 57-66.

241. Steven, W. and Haynes, A. G., "The Temperature of Formation of Martensite and Bainite in Low-Alloy Steels," **Journal of Iron and Steel Institute**, vol. 183(8), 1956, pp. 349-359.

242. Bhadeshia, H. K. D. H., "Thermodynamic Analysis of Isothermal Transformation Diagrams," **Metal Science**, vol. 16(3), 1982, pp. 159-165.

243. Bhadeshia, H. K. D. H., Svensson, L. -E., and Gretoft, B., "A Model for the Development of Microstructure in Low-Alloy Steel (Fe-Mn-Si-C) Weld Deposits," **Acta Metallurgica**, vol. 33(7), 1985, pp. 1271-1283.

244. Lee, J. L. and Bhadeshia, H. K. D. H., "Assessment of TTT Diagrams: A New Methodology," **China Steel Technical Report**, No. 7, 1993, pp. 16-25.

245. Russell, K. C., "Linked Flux Analysis of Nucleation in Condensed Phase," **Acta Metallurgica**, vol. 16(5), 1968, pp. 761-769.

246. Russell, K. C., "Grain Boundary Nucleation Kinetics," **Actal Metallugica**, vol.

17(8), 1969, pp. 1123-1131.

247. Li, M. V., Niebuhr, D., Atteridge, D., and Meekisho, L., "Computing Jominy Hardness Curves of Steels," **Proceedings of the 34th Annual Conference of Metallurgists**, CIM, 1995.

248. Li, M. V., Atteridge, D., Meekisho, L., and Niebuhr, D., "A Critical Review of Hardenability Prediction Methods and A New Model for Hardenability Predictions," submitted to **Materials and Metallurgical Transactions** in May, 1995.

249. Li, M. V., Atteridge, D., "Prediction of Carbon Steel Heat Affected Zone Microstructure Induced by Eleectroslag Cladding," presened at the **75th Annual AWS Convention**, Philadelphia, Pennsylvania, April 14, 1994.

250. Koistinen, D. P., and Marburger, R. E., "A General Equation Prescribing the Extent of the Austenite-Martensite Transformation in Pure Iron-Carbon Alloys and Plain Carbon Steels," **Acta Metallurgica**, vol. 7, 1959, pp. 59-60.

251. Payson, P., and Savage, C. H., "Martensite Reactions in Alloy Steels," **Trans. ASM**, vol. 33, 1944, pp. 261-275.

252. Carapella, L. A., "Computing A or Ms (Transformation Temperature on Quenching) from Analysis," **Metal Progress**, vol. 46, 1944, p. 108.

253. Rowland, E. S. and Lyle, S. R., "The Application of Ms Points to Case Depth Measurement," **Trans. ASM**, vol. 37, 1946, pp. 467-490.

254. Andrews, K. W., "Empirical Formulae for the Calculation of Some Transformation Temperatures," **Journal of The Iron and Steel Institute**, vol. 203, 1969, pp. 721-727.

255. Krauss, G, "Martensitic Transformations, Structure, and Properties in Hardenable Steels," **Hardenability Concepts with Applications to Steel**, Edited by D. V. Doane and J. S. Kirkaldy, AIME, 1978, pp. 229-248.

256. Kung, C. Y. and Rayment, J. J., "An Examination of the Validity of Existing Empirical Formulae for the Calculation of Ms Temperature," **Metallurgical Transactions**, vol. 13A(2), 1982, pp. 328-331.

257. Chaillet, J. M., Chevet, F., Bocquet, P., and Dollet, J., "Prediction of the Microstructure and Tensile Properties of Weld Metal Deposits," **Welding of HSLA (Microalloyed) Structural Steels**, Edited by A. B. Rothwell and J. M. Cray, ASM, 1976, pp. 299-321.

258. Bourges, Ph., Jubin, L., and Bocquet, P., "Prediction of Mecahnical Properties of Weld Metal Based on Some Metallurgical Assumptions," **Mathematical Modeling of Weld Phenomena**, Edited by H. Cerjak and K. E. Easterling, The Institute of Materials, 1993, pp. 201-212.

259. Grange, R. A., "Estimating Critical Ranges in Heat Treatment of Steels," **Metal Progress**, vol. 70(4), 1961, pp. 73-75.

260. Bain E. G. and Paxton, H. W., **Alloying Elements in Steels**, ASM, 1961.

261. Buchmayr, B. and Kirkaldy, J. S., "Modeling of the Temperature Field, Transformation Behavior, Hardness and Mechanical Response of Low Alloy Steels during Cooling from the Austenite Region," **Journal of Heat Treating**, vol. 8(2), 1990, pp. 127-136.

262. Buchmayr, B., and Kirkaldy, J. S., "A Fundamental Based Microstructural Model for the Optimization of Heat Treatment Processes," **Proceedings of the First International Conference on Quenching & Control of Distortion**, 1990, pp. 221-227.

263. **Atlas of Isothermal Transformation Diagram**, American Society for Metals, 1977.

264. G. F. Vander Voort, (Ed.) **Atlas of Time-Temperature Diagrams for Irons and Steels**, ASM International, 1991.

265. Austin, J. B. and Rickett, R. L., "Kinetics of the Decomposition of Austenite," **Trans. AIME**, vol. 135, 1939, pp. 396-415.

266. Grossmann, M. A., "Hardenability Calculated from Chemical Composition," **Trans. AIME**, vol. 150, 1942, pp. 227-257.

267. Yurioka, N. and Kasuya, T., "Carbon Equivalent and Multiplying Factor for Hardenability of Steel," **Welding Journal**, vol. 72(6), 1993, pp. 263s-268s.

268. Kirkaldy, J. S., Pazionis, G. O., and Feldman, S. E., "An Accurate Predictor for the Jominy Hardenability of Low-Alloy Hypoeutectoid Steels," **Heat Treatment '76, Proceedings of the 16th International Heat Treatment Conference**, The Metals Society, 1976, pp. 169-175.

269. Kirkaldy, J. S., "Quantitative Prediction of Transformation Hardening in Steels," **ASM Handbook**, vol. 4, Heat Treating, 1990, pp. 20-32.

270. Kirkaldy, J. S., "Development of Thermodynamic and Kinetic Models for Microscopic and Mechanical Property Prediction in Steels," **Proceedings of International Conference on Computer-Assisted Materials Design and Process Simulation**, Tokyo, Japan, September, 1993, pp. 17-24.

271. Kirkaldy, J. S., "Amalgamation of Fundamentals and Empiricism for Prediction of Microstructure and Mechanical Properties," **Phase Transformations During the Thermal/Mechanical Processing of Steel**, Edited by E. B. Hawbolt and S. Yue, CIM, 1995, pp. 3-18.

272. Zhao, Q. H., **Microstructural Analysis of NI Alloy Cladding onto Low Alloy Steel**, M.S. Thesis, Oregon Graduate Institute of Science & Technology, 1993.

273. Gao, Y. P., Devletian, J. H., and Wood, W. E., "Electroslag and Submerged Arc Cladding Ni Alloy 625," presented at the **73rd Annual AWS Convention**, Chicago, Illinois, 1992.

274. Wood, W. E., Devletian, J. H., Atteridge, D. G., Meekisho, L. L., Turpin, R. B., Johnsen, J. L., Parthasarathy, R., and Dikshit, V., **Electroslag Surfacing Technology Technical Reference Guide**, Oregon Graduate Institute of Science & Technology, October, 1995.

VITA

The author was born on May 23, 1964 in Sichuan Province, China. He received his Bachelor of Engineering degree in welding engineering from Tsing Hua (Qinghua) University, Beijing, China, in 1984, and his Master of Engineering degree in materials science and engineering from Beijing Institute of Aeronautical Materials, Beijing, China, in 1987.

He had worked in the Beijing Institute of Aeronautical Materials for three years as a research engineer until he joined Oregon Graduate Institute of Science & Technology, Portland, Oregon, in 1990. He finished the requirements for the degree of Doctor of Philosophy in materials science and engineering in September, 1995.